Interlayer effect on the hydrogen uptake in Vanadium films: Stress development, surface topography and optical behavior changes

Dissertation

zur Erlangung des mathematisch-naturwissenschaftlichen Doktorgrades
„Doctor rerum naturalium“
der Georg-August-Universität Göttingen

im Promotionsprogramm ProPhys
der Georg-August University School of Science (GAUSS)

vorgelegt von
Anshu Tyagi
aus Ghaziabad, Indien

Göttingen, 10.10.2022

Betreuungsausschuss

Prof. Dr. Astrid Pundt
Institut für Materialphysik, Georg-August-Universität Göttingen
Present Institut: Karlsruher Institut für Technologie (KIT)

Prof. Cynthia A. Volkert
Institut für Materialphysik, Georg-August-Universität Göttingen

Prof. Dr. Reiner Kirchheim
Institut für Materialphysik, Georg-August-Universität Göttingen

Mitglieder der Prüfungskommission

Prof. Dr. Astrid Pundt
Institut für Materialphysik, Georg-August-Universität Göttingen

Prof. Cynthia A. Volkert
Institut für Materialphysik, Georg-August-Universität Göttingen

Prof. Dr. Reiner Kirchheim
Institut für Materialphysik, Georg-August-Universität Göttingen

Weitere Mitglieder der Prüfungskommission

Prof. Dr. Hans Christian Hofsäss
II. Physikalisches Institut, Georg-August-Universität Göttingen

Prof. Dr. Michael Seibt
IV. Physikalisches Institut, Georg-August-Universität Göttingen

Prof. Dr. Martin Wenderoth
IV Physikalisches Institut, Georg-August-Universität Göttingen

Datum der Promotion:10.10.2022

Contents

Chapter 1

Introduction

1.1 Motivation

Human development and the earth's health need to go hand in hand for humanity's survival. Global energy demand is growing fast because of the fast-increasing population and rapid economic development across the world. Earlier centuries witnessed enormous development at the cost of the environment with a significant impact on its health. With increasing awareness, the demand arose for energy sources with a minimal footprint on the environment, such as the low-carbon footprint of electricity originating from renewable energy sources. Nowadays, 81% of the energy demand globally is fulfilled through fossil fuels, 14% is met through renewable energy sources (with a major contribution coming from biomass and wood followed by solar, wind turbine, geothermal and other sources, and about 5% is met by nuclear energy [1]. With the phenomenal, expected rise from the current 8.02 billion to about 9.20 billion in the world population in the year 2040, there is immense pressure to develop and transform this energy sector, despite numerous challenges. In 2016, the share of renewable energy in global energy consumption was 20.4% [2]. This percentage of share is based on the installed renewable technologies, which enhance the net energy generating capacity by 61% [3].

Hydrogen is the most abundant element in the universe and constitutes about 90% of all atoms in the universe. It is a clean secondary energy carrier because it stores and transports energy produced from other resources (fossil fuels, water, biomass, and solar). Hydrogen plays a vital role in the decarbonization of the energy sector. The energy storage potential of hydrogen with immense possibilities, also comes with many challenges. Hydrogen is not economically competitive with its fossil counterparts and requires significant cost reduction in its production and distribution sections [4]. To diversify the sources of the energy sector and play an important role in replacing oil, there is a dire need for the development of storage techniques for hydrogen-related society in the near future. The hydrogen economy can combine different renewable energy systems, especially needed for several high-grade energy-demanding areas, such as transportation and construction industries (see Figure 1) where complete carbonization is extremely difficult. Figure 1 depicts how hydrogen can fit into the renewable energy chain as an energy carrier.

Compared to the combustion of traditional fuels, the heat combustion of hydrogen demonstrates better efficiency for the same amount of fuel (Table 1) [5]. For meeting the short and long-term imbalances in the energy demand and supply, heat combustion of hydrogen is especially useful for countries with seasonal high-energy demands. Therefore, hydrogen can work as a missing link between hard-to-decarbonize sectors.

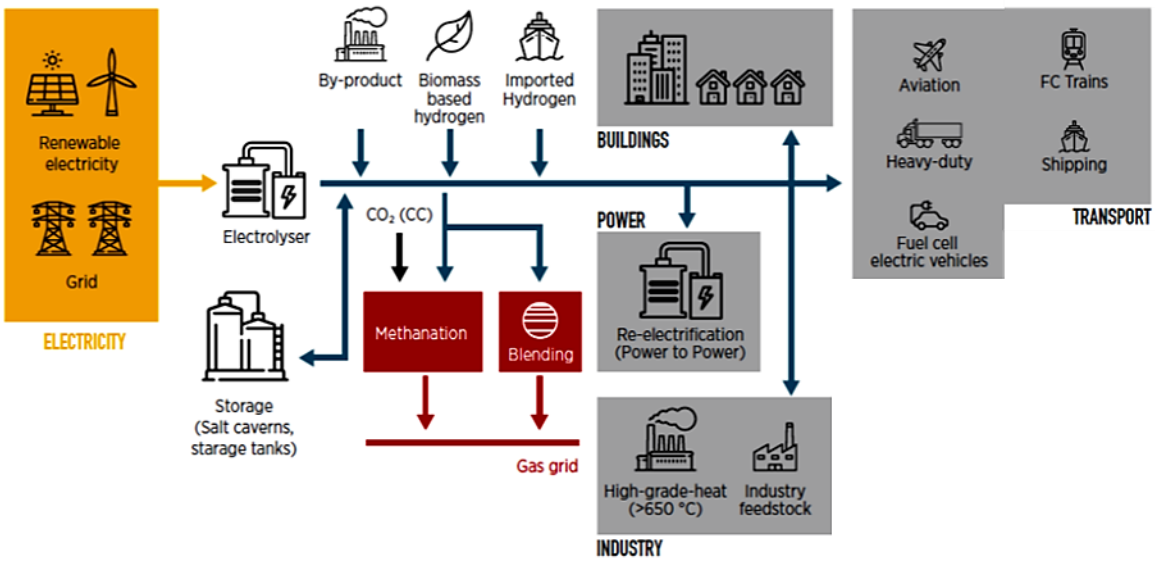

Figure 1: Representation showing end uses of energy, including hydrogen in the chain of variable renewable energy (VRE). [4] copyright 2018 International Renewable Energy Agency.

Table 1: Energy densities of different fuels upon combustion [5]**.**

Fuel type	The energy density (kcal/gram)
Hydrogen	34.0
Petroleum	10.3-8.4
Paraffin	10.3-9.8
Graphite(coal)	7.8
Wood	4.2

Price is the major driving force for renewable energy, which is expected to decrease with increasing research into renewable resources. The energy density in hydrogen is the highest per unit mass (34 kcal/gram) compared to other known fuels (see Table 1). Besides, hydrogen has the advantage of pollution-free combustion, and greater efficiency, with no limitation on quantity available, as in the case of fossil fuels which are exhaustible and nonrenewable. Resultantly, the development of hydrogen technology using renewable resources can produce 100% environment-friendly fuels. An energy-dispersive society around the world gives more energy security to developing nations. Effective storage and transport of energy will reduce the dependency on fossil fuels of a few nations, in case of crises and disasters, such as the 1970s energy crisis and the ongoing Russia-

Ukraine war (since 2022) when Europe is facing a huge energy crisis because of blockage and non-supply of energy from Russia due to ongoing conflict state.

Hydrogen gas can be obtained by using an electrolyser operating with water (an electrolyser converts water into hydrogen and oxygen through electrolysis). Hydrogen can be used at room temperature (300 K) and has high mobility. It can be loaded and unloaded easily and safely, especially when using nanomaterial hydride systems with very small diffusion lengths.

For hydrogen storage, metal hydrides (MH) are powerful options. The challenging tasks are to improve the kinetics and tailor the MH's thermodynamic properties. MH can be studied at the nano-metric scale to examine these characteristics; at the nano-metric scale alloy compositions can be easily modified. By studying fundamental properties, we add useful knowledge to developing systems with desired requirements. Nanostructures have the advantage of fast kinetics, different thermodynamics, and interaction with hydrogen in comparison to bulk, leading to a greater possibility of better control over the performance of MH. At the nano-metric scale, various interesting properties changes, such as in optical and electrical properties, are observed compared to the bulk. Semiconductor-metal transitions have also been observed at the nanoscale [6].

Absorption of hydrogen in bulk metals commonly occurs in interstitial sites, which leads to in a three-dimensional lattice expansion. In the nanoscale system of a thin film that adheres to a solid and rigid substrate, hydrogen absorption-related compressive stresses are developed in the in-plane direction because of the constraint condition [7]. These in-plane stresses can reach up to the GPa range, while in out-of-plane, they have zero value [7]. As opposed to freely expandable bulk metals in all three orthogonal dimensions, thin films attached to the rigid substrate can expand freely only in the out-of-plane direction. The amplitude of this out-of-plane expansion can be calculated using linear elastic theory; expansion changes linearly with applied in-plane stress [8, 9]. This results in an anisotropic stress field, which gives rise to anisotropic position shifts of the lattice atoms in the metal in x-, y-, and z-directions. Hence, the interaction between hydrogen atoms in the metal lattice (H-H interaction) appears with directional dependency, impacting the thermodynamics of the phase transition in the metal-hydrogen system of interest [10, 11]. For this purpose, a metal system with well-studied bulk properties like niobium (Nb) [12, 13], vanadium (V) [13, 14, 15], palladium (Pd) [13, 16], or yttrium (Y) [13] will offer the advantage of having repeatedly verified reference data for vigorous comparison; of these metallic elements, vanadium is the lightest element for energy storage devices weight consideration.

Against the above backdrop, the present thesis focuses on the study of vanadium thin metal films and their hydrogen absorption behavior. It evaluates the changes in properties due to hydrogen uptake. From the application point of view, thin films have several advantages over bulk metals counterparts due to their large surface area, fast charging and discharging rate, and good heat transfer [17]. Modified properties can be easily achieved by decreasing the thickness of the adhered film: for metal-hydrogen thin films, the critical temperature closing the miscibility gap can be significantly lowered, which may be beneficial for some applications [18, 19].

For many metal-hydrogen systems, protection from oxidation poses a challenge. Exposure of vanadium films to oxygen partial pressures of 10^{-7} mbar [17] can result in hydrogenation and dehydrogenation rates dropping to zero within a few seconds. For thin vanadium films, oxidation can be prevented by adding protective surface coatings, like Pd-layers [17].

After the system size changes from bulk to the nanometer scale, the surface-to-volume ratio changes, and for nanocrystalline materials offering additional grain boundaries, the interface-to-volume ratio becomes large. Compared to the bulk metals, these contributions from the surface and the interface become more relevant in nanometer dimensions and are expected to change the properties of the system [7].

Bloch et al. [20] documented that vanadium films with thickness ranging from 50 nm to 100 nm show bulk-like behavior for hydrogen absorption. Therefore, it will be interesting to study the behavior of vanadium film having a thickness of <50 nm. Thickness-correlating effects are expected to modify the V-H thermodynamics. Stress arises out of the mismatch between the metallic film and the rigid substrate, whose release depends on the film's thickness. The elastic strain energy can affect the hydrogen site occupancy. In the case of Fe/V multilayers, Andersson et al. reported on hydrogen, preferring to occupy in-plane (xy) interstitial sites of a (100) oriented V film. Only when all the allowed interstitial sites in the xy plane have filled the sites along the out-of-plane (z)-direction start to be occupied [21, 22].

Nanocrystalline vanadium films are developed and used in this work by depositing them on glass substrates at room temperature to facilitate faster reaction rates. The adhesion between the film and the substrate is modified, allowing for different constraint conditions and lateral stress situations. The effect of biaxial compressive stress between the substrate and the thin film leads to different H-H interactions compared to the bulk system and the different conditions. The change in the electromotive force (EMF) and optical properties induced by hydrogen uptake is studied with the help of EMF measurements and optical light transmittance and reflectance (hydrogenography). To gain insights into the sample behavior on a local scale, scanning tunneling microscopy (STM) was performed. It allows visualization of the stress release mechanism surface traces.

1.2 Outline of the thesis

The current thesis focuses on the hydrogenation of thin vanadium films with special emphasis on the influence of different adhesion interlayers, including interlayers with different special adhesion (mixed-adhesion interlayers). The corresponding adhesion is considered, and the stress development, the optical and electromotive force behavior, and local surface changes are studied in depth in this thesis.

This thesis is structured into the following chapters:

- **Chapter 1** describes the current status of the research work, its challenges, and the objective of the thesis.
- **Chapter 2** contains the theoretical background of metal-hydrogen systems, which includes the stress-induced volume expansion and the elastic stress increase related to hydrogen absorption (linear elastic theory).
- **Chapter 3** briefly describes the experimental techniques used in this research and shows the state of as-prepared samples.
- **Chapter 4** presents the experimental results of *in-situ* hydrogen loading (performed by gas phase or electrochemical loading) on 30 nm vanadium thin films with different interlayers. This chapter is divided into four sub-chapters by experimental techniques: 4.1 **Hydrogenography**, 4.2 **Electromotive Force (EMF),** 4.3 **Stress Measurement,** and 4.4 **Application of the thermodynamical DOS model to the data**. The results of individual experiments are briefly explained in each section.
- **Chapter 5** presents the results of Scanning Tunneling Microscopy (STM) measurements on V-films with no interlayer.
- **Chapter 6** combines all results and presents a global interpretation of the results. This chapter provides the essence of the stress development and the microstructural changes occurring in V-H thin films and their influence on the optical behavior,
- **Chapter 7** summarizes this thesis and provides an outlook and future direction for the next steps.

Chapter 2

Hydrogen in Metals Films

This chapter presents a comprehensive theoretical introduction to the thermodynamic and kinetic aspects of hydrogen absorption in metal-hydrogen (Me-H) systems. The solubility of H in vanadium and palladium, and the related phase diagrams (section 2.1) are also presented. This chapter also evaluates the differences between thin films and bulk material (section 2.2) and presents the calculation of the mechanical stress in V-films by using the theory of linear elasticity (section 2.3). Common stress release mechanisms of thin films are also addressed (section 2.4). Section 2.5 of this chapter focuses on the optical properties of metals with an emphasis on thin films.

2.1 Hydrogen in Metals

2.1.1 Interstitial sites solution

Due to their small size, hydrogen atoms introduced in a metal host lattice are absorbed in interstitial sites of the host lattice, typically known as tetrahedral sites (T-sites) and octahedral sites (O-sites). The preferred occupancy of these interstitial sites depends on the host metal-lattice structure. For the case of a body center cubic (bcc) crystal structure, like the vanadium metal, the hydrogen atoms have the availability of three octahedral and six tetrahedral sites per host metal atom, see Figure 2.1 [13]. Figure 2.1 shows an anisotropy exist between the Me-H distance from the O-sites, in the bcc crystal structure. The preferential position hydrogen atoms occupied in the bcc lattice are usually T- sites, not all sites are available to be occupied according to Westlake's criterion [23]. At low concentrations, hydrogen occupies T-sites randomly. At higher concentrations (discussed in the following sections) hydrogen changes its occupancy from T-sites to O-sites.

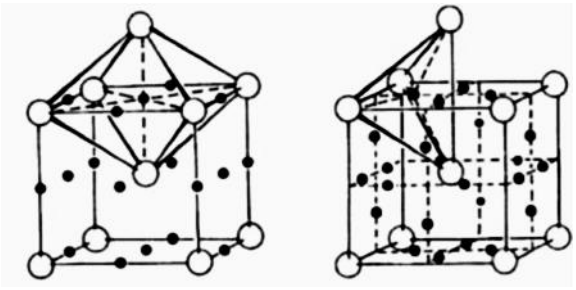

Figure 2.1: Bcc crystal structure showing the interstitial octahedral (O-sites, left image) and tetrahedral sites (T-sites, right image), available for hydrogen occupation [13]. The big hollow circles present the host metal atoms in the unit cell, the dark small circles present the theoretically

possible interstitial sites that hydrogen can occupy. Reproduced with permission [13]. Copyright 2005 Springer.

2.1.2 Hydrogen absorption-induced lattice expansion in bulk Me-H systems

The introduction of the hydrogen atom in an isotropic metal crystal lattice that can freely expand in all spatial directions induces a volume expansion ΔV. If it is assumed that the volume occupied by one hydrogen atom is Δv and the number of hydrogen atoms dissolved in the metal crystal is n, then the volume change of the metal due to the presence of hydrogen atoms is $\Delta V = \Delta v \cdot n$. The initial volume of the metal crystal (without hydrogen) can be roughly calculated using the following formula $V = N \cdot {}'\Omega$, where N is the number of metal atoms in a metal crystal with the volume of ${}'\Omega$. Thus, the relative change of volume caused by the hydrogen absorption can be given as $\frac{\Delta V}{V} = c_H \cdot \frac{\Delta v}{{}'\Omega}$ where $c_H = \frac{n}{N}$. Besides this relative volume change for interstitial hydrogen randomly distributed in a cubic crystal, can also be approximately expressed in terms of the lattice parameter 'a' of the host metal [14]:

$$\frac{\Delta V}{V} \approx 3 \cdot \frac{\Delta a}{a} = c_H \frac{\Delta v}{{}'\Omega} \tag{2.1}$$

Equation (2.1) presents a linear relationship between the relative volume change and the hydrogen concentration c_H [H/M], applicable for the defect-free metal. This linear increase of lattice parameter is experimentally verified for most of the metals [14]. Experimentally, ratios $\frac{\Delta v}{{}'\Omega}$ and $\frac{\Delta a}{a}$ can be measured by X-ray diffraction (XRD) via lattice parameter measurement or by dilatometrically measurement at several concentrations c_H.
For a V single crystal and for low H concentrations (up to the solubility limit of about 0.03 H/V ($VH_{0.03}$) at room temperature, the following dependency was determined by using dilatometry [24]:

$$\frac{\Delta a}{a} = 0.063 \cdot c_H \text{ and } \quad \frac{\Delta V}{V} = 0.189 \cdot c_H \tag{2.2}$$

For the Pd metal, the expansion coefficient is $\frac{\Delta V}{V} = 0.19$ [14].

2.1.3 Mechanical stress due to hydride formation in bulk Me-H systems

Equation 2.2 given above suggests a jump in the lattice expansion in two-phase region because as the local hydrogen concentration differs according to the equilibrium concentration. Therefore, misfit or interface stress can be released by dislocations. Schober (1973) [25] and Makenas and Birnbaum (1980) [26] showed the occurrence of dislocations for the Nb samples surrounding the

hydride positions by electron microscopy. They even confirmed the emission of extrinsic dislocation loops into the matrix, as shown in Figure 2.2 given below.

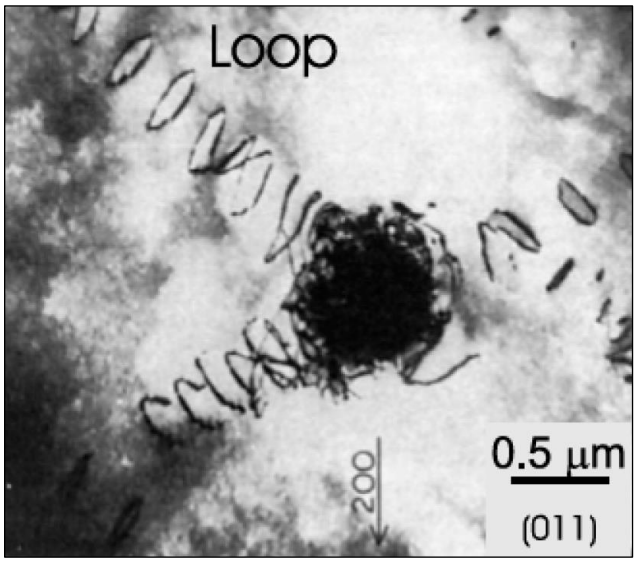

Figure 2.2: TEM image of dislocations generated at the location of the hydride in a Nb-sample. Also, dislocation loops are visible. *Source: Makenas and Birnbaum* [26]. Adapted with permission from [26] , copyright 1979 Elsevier.

2.1.4 V-H binary bulk system

The phase diagram of vanadium-hydrogen (V-H) had been intensively studied and investigated in the 1970s via XRD, differential scanning calorimetry (DSC), and differential thermal analysis (DTA) [27, 28], as summarized in [29, 30, 31]. Different graphical presentations of the V-H phase diagram are present in various textbooks on metal hydrogen systems and are also presented in this chapter briefly. Figure 2.3 presents the V-H phase diagram reproduced from the study by Pesch [32]. Here, c_H= H/V is the hydrogen concentration (0 H/V < c_H < 1 H/V), and T is the temperature of the system (0 K < T < 500 K).

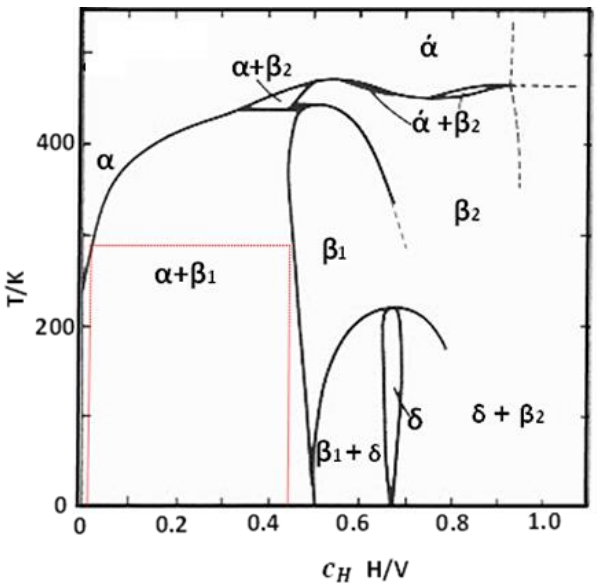

Figure 2.3: The phase diagram of hydrogen in bulk V crystal reproduced from [32], different areas having different phases are labeled as α, ά, β_1, β_2 , and δ. Phase boundaries at room temperature 298 K are plotted with the red line: H-V α-solubility = 0.03 H/V, $\alpha+\beta_1$= 0.03 -0.47 H/V, β_1 = 0.47 – 0.67 H/V, and so on. Copyright 1982 W.Pesch.

The low-concentration phase α is considered to be a lattice gas while the high-concentration phase ά is described as a lattice liquid phase [33]. The only difference between these two disordered interstitial alloy phases is that the lattice parameter increases linearly with the rise in hydrogen concentration. Both phases are bcc lattice structures. β_1 is called the lattice crystal/ordered hydride phase. It possesses a bct lattice structure, with a c/a-ratio of c/a ~1.1 [13]. β_1 differs from β_2 by an order-to-disorder transition: in the ordered β_1 phase half of the interstitial sites are occupied statistically [31]. For the bulk V-H system, the critical temperature T_c is around close to ~ 200°C/ 473 K which separates the homogeneous phase from the two-phase region.

Figure 2.4 shows the location of interstitial sites in the body-centered cubic/ body-centered tetragonal (bcc/bct) lattices because the hydrogen occupancy changes from the T-sites in the α phase to the O_z -sites in the β_1 and the β_2 phases. This shift of site occupancy from the T-site to the O_z site occurs through a reconfiguration of four T sites to a laterally distorted 4T site, as presented in Figure 2.4 [34]. The origin of this effect is a change in the self-trapping energy with increasing hydrogen concentration.

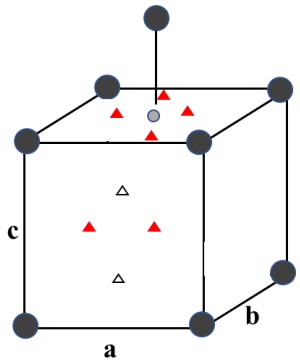

Figure 2.4:

Schematic drawing of the interstitial sites in a bcc/bct lattice. The geometrical locations of the O_z, T_z, and $T_{x(y)}$ interstitial sites are indicated by the symbols ○, △ , and ▲ , respectively.

At room temperature marked by the red line in Figure 2.3, three different phases, labeled as α, β_1, and β_2 are relevant. In the solid solution α-phase, hydrogen occupies T sites randomly. Above the solid solution limit, β_1 starts to nucleate and turn into phase β_2, for higher concentrations. In the bct structure, hydrogen preferentially occupies the O_z sites, as reported by previous studies [35, 36, 37].

At room temperature, there exists a two-phase region (miscibility gap, labeled as $\alpha+\beta_1$) in the concentration range between 0.03 H/V and 0.47 H/V. In this miscibility gap, the phase transformation from α to β_1 occurs with increasing concentration. All other phases of higher concentrations are out of the scope of this work.
The formation of vanadium hydride V_2H (0.5 H/V) occurs at 10^{-5} mbar hydrogen partial pressure, at room temperature.

2.1.5 Pd-H binary bulk system

A thin Pd cap layer is used to cover the sample surface to avoid oxidation of the underlying vanadium layer and improve the hydrogen absorption reaction. Therefore, the bulk Pd-H Phase diagram is briefly discussed in this section. More details on the H adsorption by Pd can be found in Ref. [13].
The Pd-H lattice has an fcc lattice structure that upon hydrogen uptake results in a hydrogen filling of the interstitial O-sites. The α-phase of the Pd-H bulk system solves up to c_H = 0.01 H/Pd at 298 K [13, 38], as shown in Figure 2.5. Further uptake of hydrogen gives rise to the ά phase. At room temperature, the miscibility gap during the presence of two-phase region α+ ά exists between 0.01 H/Pd to about 0.6 H/Pd.
At room temperature of about 298 K, the formation of ά palladium hydride occurs at a pressure of 20 mbar (2×10^3 Pa) hydrogen partial pressure, which is much higher than the formation pressure of vanadium hydride V_2H at 10^{-5} mbar (10^{-3} Pa). At room temperature and 10^{-5} mbar hydrogen partial pressure, the calculated concentration in the Pd is only $c_H = 1.3\times10^{-5}$ H/Pd. The ratio in the solubility defined as k= [c_H in Pd]/[c_H in V] is about k~10^{-4}. Thus, at 10^{-5} mbar partial pressure, the hydrogen concentration (c_H) in Pd can be ignored compared to c_H in V.

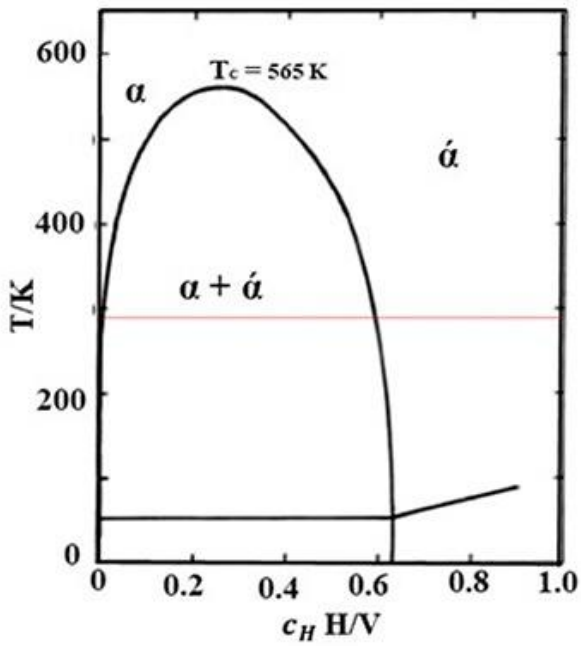

Figure 2.5: Phase diagram of the palladium-hydrogen system [39, 38]**.** The red line marks 298 K. Source: Reproduced with permission [13]. Copyright 2005 Springer Nature.

2.2 Me-H thin films

2.2.1 Difference between the bulk and the thin film system

Many differences emerge in the physical behavior of bulk and thin film systems for the same composition and metal, arising from the difference in microstructure, and the presence of a stabilizer needed for the film stability [7, 16]. For the thin film system, a reduction in the system dimension changes the related boundary conditions. Therefore, the elastic properties show anisotropies and high mechanical stress in the GPa range arise in the thin film system [7, 40, 41].

For thin films deposited on flat substrates, mechanical stress appears mainly in the in-plane direction. It can affect different material properties such as the chemical potential and width of a semiconductor band gap [7, 42, 43]. For metal hydride systems it can change thermodynamic properties such as the hydrogen-hydrogen interaction [10, 21, 44], thereby affecting the solubility limits [7] or the critical temperature of the miscibility gap between two phases [45, 46]. Besides, very high mechanical stress can destabilize the hydride phase itself, as reported by Wagner et al. [44].

2.2.2 Intrinsic stress in thin films

Thin films usually experience mechanical stress in their as-deposited condition, also defined as intrinsic stresses, due to the deposition process or the mismatch between the thin film and the substrate lattice parameter. When high temperatures are used in the deposition process, different thermal expansion coefficients of the different materials result in additional mechanical stress. Intrinsic stress commonly occurs in the order of $\pm$100 MPa for thermally evaporated films, up to ±800 MPa for sputtered deposited films [47, 48], or in the range of ±2 GPa for laser-deposited films [49, 50]. These latter methods can result in atom peening or ions forming intrinsic defects [51]. The kinetic energy of the deposited material and the working pressure of deposition can change the film stress state from compressive to tensile [49, 52, 53, 54]. Therefore, due to the above-mentioned reasons, the intrinsic stress of the film should be considered as a factor affecting the film's properties. Nevertheless, intrinsic stress is not determined in this thesis, as all the films were deposited under the same conditions. Thus, hydrogen-related effects were considered. In forthcoming works, intrinsic stress contribution should be added.

2.2.3 Mechanical stress due to interstitial absorption and hydride formation

Thin metal films deposited on the rigid substrates are subjected to high in-plane stresses upon hydrogen absorption. As mentioned before, this stress can have remarkable influence on the thermodynamics of the Me-H systems [7, 55]. Furthermore, the thin film microstructure can change the terminal solubility of hydrogen compared to the common bulk microstructure [7]. This part presents fundamental aspects of Me-H systems while focusing on V-H and Pd-H systems. Further details regarding this topic can be obtained from Ref. [29].

2.3 V-H thin films

2.3.1 Linear elastic theory of hydrogen-loaded V-films adhered to the substrate

In section 2.1.2 of this chapter, it was discussed how (homogeneous) hydrogen absorption in bulk Me-H systems can lead to hydrogen-induced lattice expansion ε_0. This lattice expansion takes place homogeneously in all three-orthogonal directions (x, y, and z). Thus, this situation can be regarded as stress-free, see Figure 2.6 (a). In contrast, in case of a thin film clamped to a rigid substrate, the in-plane expansion is restricted due to adhesion to the substrate, see Figure 2.6 (b). This results in compressive in-plane stress that increases with increasing hydrogen concentration. Because of the Poisson effect, this gives rise to an additional expansion in the out-of-plane direction, as shown in Figures 2.6 (b) and (c). This compressive stress can be as of several GPa [7, 8, 12].

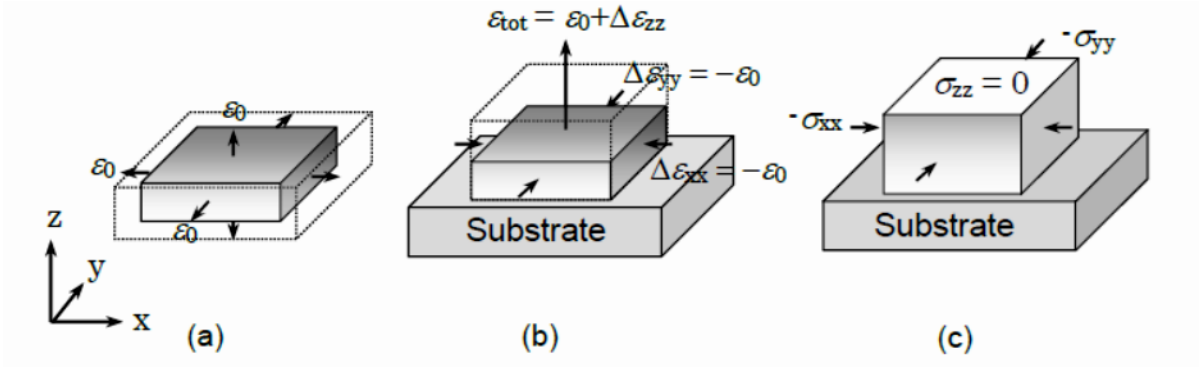

Figure 2.6: Schematic presentation of stress and strain developed during hydrogen-induced lattice expansion: **(a)** 3-dimensional volume expansion of bulk metal by ε_0 upon hydrogen absorption, **(b)** one-dimensional expansion of film clamped to a rigid substrate, **(c)** Biaxial-stress working in the film and the resulting expansion in the out-of-plane direction. Adapted with permission from [56]. copyright 2014 Elsevier.

Figures 2.6 (a), (b), and (c) demonstrate how the above-mentioned biaxial compression originating from the expansion of a hydrogen-absorbing film, leads to the film one-dimensional expansion: The stress and the strain of a freely expanded metal film that is ideally adhered onto a rigid substrate can be calculated by doing a Gedanken experiment [8, 56]. In Figure 2.6 (a) the bulk metal or the free-standing film is allowed to strain freely in all directions ($\varepsilon_0 = \varepsilon_{xx} = \varepsilon_{yy} = \varepsilon_{zz}$) upon hydrogen absorption in a completely stress-free state ($\sigma_{xx} = \sigma_{yy} = \sigma_{zz} = 0$).

In Figure 2.6 (b) the metal film adhered to a substrate and due to this boundary constraint in the in-plane directions, the film upon hydrogen absorption has to be compressed, by $-\varepsilon_0 = \Delta\varepsilon_{xx} = \Delta\varepsilon_{yy}$ to fit in the initial lateral dimension. This leads to biaxial compressive stress in such a sample in the lateral direction [8]. The normal direction still is in a stress-free state ($\sigma_{zz} = 0$) and expands freely. But due to the Poisson response to the in-plane biaxial stress, an additional expansion $\Delta\varepsilon_{zz}$ happens in the out-of-plane direction [38, 56].

The compressive biaxial in-plane (x-y) stress ($\sigma^{\text{in-plane}}$) that is induced by hydrogen absorption can be calculated [41], using Young's modulus *E* and Poisson's ratio υ, according to Hooke's law.

$$\sigma^{\text{in-plane}} = -\frac{E}{1-\upsilon} \cdot (\Delta\varepsilon_0) \tag{2.3}$$

where $\sigma < 0$ presents the compressive stress state of the sample.
Above given relation hold good as far as the following assumptions are fulfilled:

(i) The film material is elastically isotropic [57].
(ii) The in-plane grain is homogeneous in configuration [58].

Thus, using the above knowledge, average in-plane stress for a V-film is calculated < σ > as -12.8· c_H [GPa H/V]. For this calculation $\varepsilon_0 = 0.063 \cdot c_H$ [24] is assumed and *E*= 128 GPa, $\upsilon = 0.37$ taken. The corresponding total expansion ε_{tot} in the z-direction can be calculated as:

$$\varepsilon_{tot} = \varepsilon_0 + \Delta\varepsilon_{zz} = \left(1 + \frac{2\upsilon}{1-\upsilon}\right) \cdot \varepsilon_0 \qquad (2.4)$$

Thus, for V-H, the total expansion for the isotropic case is, $\varepsilon_{tot} = 0.137 \cdot c_H$. But, for most metals, condition (i) cannot be fulfilled [57, 59]. As the thin V film grows in <110> out-of-plane direction, elastic properties are anisotropic. More detailed presented in chapter 3. It allows us to determine the relevant elastic out-of-plane expansion that is relevant for the scanning tunneling microscopy (STM) measurements on V-H films.

2.3.2 Hydrogen-induced lattice/volume expansion and stress in thin V-films: direction dependency

To determine comprehensively the strain in z-direction and the mechanical stress in the x- and y-directions arising from hydrogen absorption in films adhered to rigid substrates, the theory of linear elasticity can be applied with direction dependency [60]. The following treatment of the next 3 ½ pages follows the description in V. Burlaka's thesis [61] and A. Pundt and R. Kirchheim's review article [56].
For the linear elastic regime, Hooke's law holds with the following equation:

$$\sigma_{ij} = C_{ijkl}\varepsilon_{kl} \qquad (2.5)$$

where stress and strain in the deformed crystal are denoted by the symmetric second-rank tensors σ_{ij} and ε_{kl}, respectively, and C_{ijkl} denotes the fourth-rank tensor of the elastic stiffness constants. Thus, this elastic stiffness tensor couples the strain matrix ε_{kl} to the stress matrix σ_{ij}, the subscripts *i, j, k,* and *l* run from 1 to 3. This C_{ijkl} fourth-order tensor contains 81 components. For the present case of cubic lattice structures, symmetry gives $\sigma_{ij} = \sigma_{ji}$ and $\varepsilon_{ij} = \varepsilon_{ji}$. This implies that the components of the stiffness tensor must be $C_{ijkl} = C_{ijlk} = C_{jikl}$. Three independent elastic constants C_{11}, C_{12}, and C_{44} are enough to completely describe the elastic properties of the cubic system [62]. For convenience, instead of the matrix notation, the simpler Voigt notation is used here. Therefore, we can describe the direction-dependent stress and strain relations by xx =1, yy =2, zz = 3, xy (yx) =4, xz(zx) =5, zy(yz) =6. It will be much better for the understanding, as shear strains are $\varepsilon_4, \varepsilon_5, \varepsilon_6 = 0$ (Equation 2.5).

$$\sigma_\alpha = C_{\alpha\beta}\varepsilon_\beta \tag{2.6}$$

For cubic systems, the stiffness tensor $C_{\alpha\beta}$ is given by [62].

$$\mathrm{C}_{\alpha\beta}^{cub} = \begin{pmatrix} C_{11} & C_{12} & C_{12} & 0 & 0 & 0 \\ C_{12} & C_{11} & C_{12} & 0 & 0 & 0 \\ C_{12} & C_{12} & C_{11} & 0 & 0 & 0 \\ 0 & 0 & 0 & C_{44} & 0 & 0 \\ 0 & 0 & 0 & 0 & C_{44} & 0 \\ 0 & 0 & 0 & 0 & 0 & C_{44} \end{pmatrix} \tag{2.7}$$

The elastic energy density f_{el}, is given in matrix notation by [57, 63].

$$f_{el} = \frac{1}{2} \cdot \mathrm{C}_{ijkl} \cdot \varepsilon_{ij} \cdot \varepsilon_{kl} \tag{2.8}$$

This can be represented in Voigt notation for convenience as given below:

$$f_{el} = \frac{1}{2} \cdot \mathrm{C}_{11}(\varepsilon_1^2 + \varepsilon_2^2 + \varepsilon_3^2) + \frac{1}{2} \cdot \mathrm{C}_{44}(\varepsilon_4^2 + \varepsilon_5^2 + \epsilon_6^2) + \mathrm{C}_{12}(\varepsilon_1\varepsilon_2 + \varepsilon_2\varepsilon_3 + \varepsilon_3\varepsilon_1) \tag{2.9}$$

The stress in a bcc thin film system have to calculated by considering the fact that the film usually grows (110) oriented. This means the external z-direction of the thin film coincides with the [110] internal crystallographic direction of the metal lattice. A transformation matrix (a_{ij}) allows correlation of the internal coordinate system of the crystal system with the external coordinate system of the thin film. Thus, strain in the internal coordination system (ε_{ij}) can be correlated to strain in the external coordinate system (ε'_{mn}) using the following equation [64].

$$\varepsilon_{ij} = a_{im}^T \cdot \varepsilon'_{mn} \cdot a_{jn} \tag{2.10}$$

The transformation needed is a rotation by φ = -90° around the x-axis and after that θ = -135° around the reorientated z-axis which gives the new external coordinates x', y', z' in [1-10], [001], and [110] crystallographic and orthogonal directions.
Hence, to link the external strain with the internal strain tensor, a rotational matrix for x and z rotation axis multiplication has to be determined.

$$a_{ij} = \begin{pmatrix} 1 & 0 & 0 \\ 0 & cos\varphi & -sin\varphi \\ 0 & sin\varphi & cos\varphi \end{pmatrix} \cdot \begin{pmatrix} cos\theta & -sin\theta & 0 \\ sin\theta & cos\theta & 0 \\ 0 & 0 & 1 \end{pmatrix} \quad (2.11)$$

For $\varphi = -90^{o}$ and $\theta = -135^{o}$ rotation [65]

$$a_{ij} = \begin{pmatrix} 1 & 0 & 0 \\ 0 & 0 & 1 \\ 0 & -1 & 0 \end{pmatrix} \cdot \begin{pmatrix} -\frac{1}{\sqrt{2}} & \frac{1}{\sqrt{2}} & 0 \\ -\frac{1}{\sqrt{2}} & -\frac{1}{\sqrt{2}} & 0 \\ 0 & 0 & 1 \end{pmatrix} = \begin{pmatrix} -\frac{1}{\sqrt{2}} & \frac{1}{\sqrt{2}} & 0 \\ 0 & 0 & 1 \\ \frac{1}{\sqrt{2}} & \frac{1}{\sqrt{2}} & 0 \end{pmatrix} \quad (2.12)$$

Now, the a_{ij} in the transformation, the matrix can be substituted by using equations from (2.12) to (2.10). With this tensor transformation, any strain in the external coordinate system can be directly visualized in the form of strain in the internal coordinate:

$$\varepsilon_{ij} = \begin{pmatrix} \frac{1}{2}(\varepsilon_1' + \varepsilon_3') & \frac{1}{2}(\varepsilon_3' - \varepsilon_1') & 0 \\ \frac{1}{2}(\varepsilon_3' - \varepsilon_1') & \frac{1}{2}(\varepsilon_1' + \varepsilon_3') & 0 \\ 0 & 0 & \varepsilon_2' \end{pmatrix} \quad (2.13)$$

Combining equations (2.13) and (2.9) gives us the following strain energy density:

$$f_{el} = \frac{1}{4} \cdot \mathrm{C}_{11}\left(\varepsilon_1'^2 + 2\varepsilon_2'^2 + +2\varepsilon_1'\varepsilon_3' + \varepsilon'^2_3\right) + \frac{1}{2} \cdot \mathrm{C}_{44}(\varepsilon_3' - \varepsilon_1')^2 + \frac{1}{4} \cdot \mathrm{C}_{12}\left(\varepsilon_1'^2 + 4\varepsilon'_2\,\varepsilon'_3 + 2\varepsilon'_1\varepsilon'_3 + 4\varepsilon'_1\,\varepsilon'_2 + \varepsilon'^2_3\right) \quad (2.14)$$

By definition, stress σ'_i in an external coordinate system is given by the strain derivative of the free energy density:

$$\sigma'_i = \frac{\partial f_{el}}{\partial \varepsilon'_i} \quad (2.15)$$

The assumption of free expansion for ε_3' , as shown in Figure 2.6, gives $\frac{\partial f_{el}}{\partial \varepsilon_3} = \sigma_3 = 0$. For V (110) hydrogen-induced vertical expansion, ε_3' or $\Delta\varepsilon_{zz}$ is given by

$$\Delta\varepsilon_{zz} = \varepsilon'_3 = -\frac{(\mathrm{C}_{11} + \mathrm{C}_{12} - 2\mathrm{C}_{44})\varepsilon'_1 + 2\mathrm{C}_{12}\,\varepsilon'_2}{(\mathrm{C}_{11} + \mathrm{C}_{12} + 2\mathrm{C}_{44})} \quad (2.16)$$

The biaxial strain ($\varepsilon'_1 = \varepsilon'_2 = -\varepsilon_0$) for a film adheres to a rigid substrate (Figure 2.6 (c)), gives total vertical strain represented by

$$(\varepsilon_{zz})_{total} = \varepsilon_0 + \Delta\varepsilon_{zz} = \left(1 + \frac{(C_{11} + 3C_{12} - 2C_{44})}{(C_{11}+C_{12}+2C_{44})}\right) \cdot \varepsilon_0 \quad (2.17)$$

For the vanadium-hydrogen system, $\varepsilon_0 = 0.063 \cdot c_{H\left(\frac{H}{V}\right)}$ [24]

$$(\varepsilon_{zz})_{total} = \varepsilon_0 + \Delta\varepsilon_{zz} = 0.135 \cdot c_{H\left(\frac{H}{V}\right)} \quad (2.18)$$

This total strain occurs in the out-of-plane direction of the film, by considering linear elastic expansion. This value is slightly smaller than the $\varepsilon_{tot} = 0.137 \cdot c_H$, obtained for the isotropic metal in chapter 2.3.1.

The biaxial in-plane stress σ_1 [1-10] and σ_2 [001] arising at the film and substrate interface can be calculated by substituting equation (2.17) in (2.14).

$$\sigma'_1[1-10] = \frac{\partial f_{el}}{\partial \varepsilon'_1} = \frac{4C_{44}(C_{11} + C_{12})\varepsilon'_1 + 4C_{12}C_{44}\varepsilon'_2}{(C_{11}+C_{12}+2C_{44})} \quad (2.19)$$

$$\sigma'_2[001] = \frac{\partial f_{el}}{\partial \varepsilon'_2} = \frac{4C_{44}C_{12}\varepsilon'_1 + \{C_{11}^2 - 2C_{12}^2 - C_{11}(C_{12} + 2C_{44})\}\varepsilon'_2}{(C_{11}+C_{12}+2C_{44})} \quad (2.20)$$

For the biaxial expansion, $\varepsilon'_1 = \varepsilon'_2 = -\varepsilon_0 = -0.063 \cdot c_{H\left(\frac{H}{V}\right)}$, and with the published stiffness values for V bulk $C_{11} = 229\ GPa$, $C_{12} = 119\ GPa$ and $C_{44} = 43\ GPa$, [66] the direction-dependent biaxial stress in V(110) film can be determined [66].

$$\sigma'_1[1-10] = \frac{\partial f_{el}}{\partial \varepsilon'_1} = -4 \cdot \frac{(C_{11} + 2C_{12})C_{44}}{C_{11}+C_{12}+2C_{44}} \cdot \varepsilon_0$$

$$= -11.7\ \text{GPa} \cdot c_H \quad (2.21)$$

$$\sigma'_2[001] = \frac{\partial f_{el}}{\partial \varepsilon'_2} = -\frac{2(C_{11}+2C_{12})C_{44}+C_{11}^2-2C_{12}^2+C_{11}C_{12}}{C_{11}+C_{12}+2C_{44}} \cdot \varepsilon_0$$

$$= -13.3\ \text{GPa} \cdot c_H \qquad (2.22)$$

Equations (2.21) and (2.22) give the extrema range of compressive stress that can be expected in the elastic regime in V (110) film upon hydrogen absorption. It varies between -11.7 GPa·c_H and -13.3 GPa·c_H. In this manner, the obtained stress value may vary depending on the crystallographic direction of the stress measurement, for in-plane oriented films. If the vanadium film is fiber-textured, then in-plane randomness can be expected. Here, average stress is expected to be: $\langle\sigma'\rangle = -12.5 \cdot c_H$ [GPa]. This average stress is smaller than what was calculated for the isotropic case $<\sigma> = -12.8 \cdot c_H$ [GPa], given in part 2.3.1 above.

2.3.3. Stress influence on the H-site occupancy

Hjörvarsson et al. [10, 11] documented that the site occupancy of hydrogen in vanadium is highly sensitive to the stress state of the metal lattice. This effect becomes large in the case of the thin films grown on rigid substrates as they experience large in-plane stress. According to Hjörvarsson et al., this finally leads to a preferential occupation of the sites arranged in out-of-plane orientation. However, in this work, two sets of sites are occupied because the films are oriented in <110> direction, and not in <100> direction as in the study by Hjörvarsson et al. [10]. Furthermore, in this work, nanocrystalline films are used, and not epitaxial films that are study by Hjörvarsson et al. So, if any anisotropy effect occurs in the nanocrystalline fiber textured V-films, it will be hard to observe.

2.3.4. Local strain in the two-phase region

According to equations 2.4 and 2.18, the lattice strain depends on the hydrogen content. In thin films, the vertical lattice expansion is about 2.1 times larger than in the bulk system, compared to Eq. 2.18 with $\varepsilon_0 + \Delta\varepsilon_{zz} = 0.135 \cdot c_H$ and the bulk value of $\varepsilon_0 = 0.063 \cdot c_H$ [24].
In the two-phase field of a system, the local hydrogen content depends on the local phase and the position in the sample. In a thin film, the local lattice expansion varies with the phase in the film. Nörthemann et al. [12] showed that local lattice expansion allows the detection of the position of phases in epitaxial thin films and monitoring the hydride formation and growth, using STM. This kind of study requires constant pressure conditions and precise pressure control during the STM measurements. As will be shown in chapter 3, these conditions are experimentally not achievable for here regarded the V-H films, as the hydride formation pressure of the V-films overlaps with the corona-discharge pressure region of the STM. Changes in the morphology of grains, in their size,

and in their lateral distributions can be monitored by this technique, after hydrogen loading. More details regarding the measurement protocol are provided in chapter 3.

2.4 Mechanical Stress relaxation in thin films

As discussed before, mechanical stress in thin films can arise from different types, such as thermal stress, intrinsic stress, or misfit stress due to the different lattice parameters between the film and the substrate (see section 2.2). For the nanocrystalline V-films, sample preparation was done at room temperature and, thus, the thermal stress is expected to be small. Intrinsic stress expected to be in the range of 100 MPa. As amorphous glass and amorphous polymer substrates or interlayers are used in this work, these misfit stresses are expected to be small. However, for fiber-textured Pd-interlayers, misfit stress may arise because the lattices might match the Nishiyama-Wassermann relationship between the fcc (111) plane and the bcc (110) plane.
In thin films, the largest mechanical stress contribution of -12.5 GPa/c_H is induced by hydrogen absorption (see section 2.3.2). These highly compressive stresses usually are released by different mechanisms such as dislocation formation, film buckling, or grain sliding.

2.4.1 Stress relaxation by dislocations

Measurements on the stress and the strain developing during hydrogen absorption in thin metal films show the linear dependency, for small hydrogen concentrations [8]. With further hydrogen uptake, deviations from the linear elastic behavior accompanied by plastic deformation, occur. The extent of plastic deformation depends on the thickness and the morphology of the film [7, 8, 61, 67]. Intensive studies on the lattice expansion of films upon hydrogen absorption were carried out by Miceli et al. [40] and Burlaka et al. [61]. The plastic deformation is related to misfit dislocations, located close to the film-substrate interface and, in the case of phase transformation, in form of extrinsic dislocation loops surrounding the precipitating phase [61]. Dislocations connected to the film surface result in surface steps [38].
According to Miceli et al. [40], the related vertical expansion of hydrogen-loaded thin films is higher for films attached to rigid substrates than that of films adhered to mechanically soft substrates. However, this also depends on the thickness of the substrate [68, 69].
The effect of the microstructure on the stress development is shown in Figure 2.7, for Nb-H films. The epitaxial film (marked with $MBE_{900°C}$) behaves linear elastically up to the α phase concentration limit and then deforms plastically. This microstructure presents the most effective way of stress relaxation. Due to the large grain size, hardening by dislocation pile-up is negligible.

(a) **(b)**

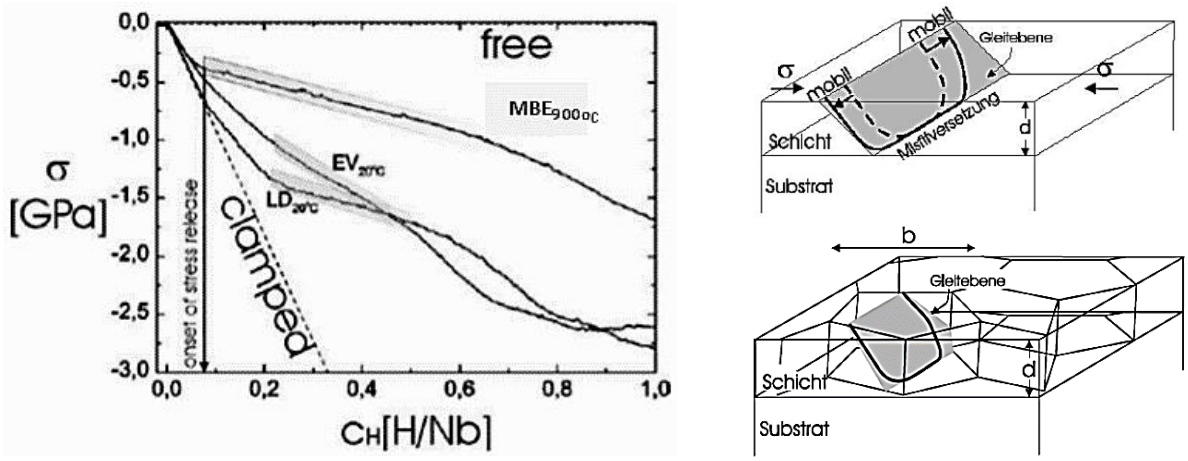

Figure 2.7: (a) Hydrogen-related stress development of metal films of different microstructure, shown for the case of 200 nm Nb films (on rigid substrates) and different grain size d_G with $MBE_{900}{}^{o}C$: $d_G > 1$ µm, $EV_{20}{}^{o}C$: d_G~100 nm, $LD_{20}{}^{o}C$: $d_G < 20$ nm. The vertical line presents the critical concentration of 0.08 H/Nb, above which the dependency deviates from linear elastic theory (clamped). **(b)** dislocation evolution in an epitaxial film and in a nanocrystalline film with lateral grain size b. Figure 2.7 (a) Reprinted with permission from A. Pundt [70] and Figure 2.7 (b) from [38, 70]. copyright 2004 wiley-VCH GmbH.

For nanocrystalline films having small grain sizes, dislocations pile up at the grain boundaries. Therefore, stress relaxation is small due to hindered formation of misfit dislocations, according to the Hall-Petch mechanism [71]. This is visible by the final stress σ= - 1.7 GPa remaining in the epitaxial film, while σ = - 2.6 GPa arises in the nanocrystalline film, as presented in Figure 2.7. As the above-referred vanadium films have a nanocrystalline grain structure, large compressive stresses are expected to result from the dislocations mechanism.
In the next sections, two other kinds of stress release mechanics to be observed in this work are presented.

2.4.2 Stress relaxation by buckle formation

Metal films and coatings used in the electronic industry are required to have good adhesion to the substrate for successful device operation. Thus, in many technologies film detachment and buckle appearance have to be avoided. However, intentional buckling can be used to study the physical behavioral changes in a film with the change in the adhesive condition. For hydrogen-loaded thin metal films grown on rigid substrates with low adhesion, GPa stresses can result in local or global film detachment, as shown in Figure. 2.8 (a)-(c) in-side-view. The optical micrograph of a single buckle (dark line) formed in a 30 nm V film is shown in Figure 2.8 (d), in the top-view. Other

reasons for film detachment and buckling are film oxidation or different thermal expansion coefficients of film and substrate.

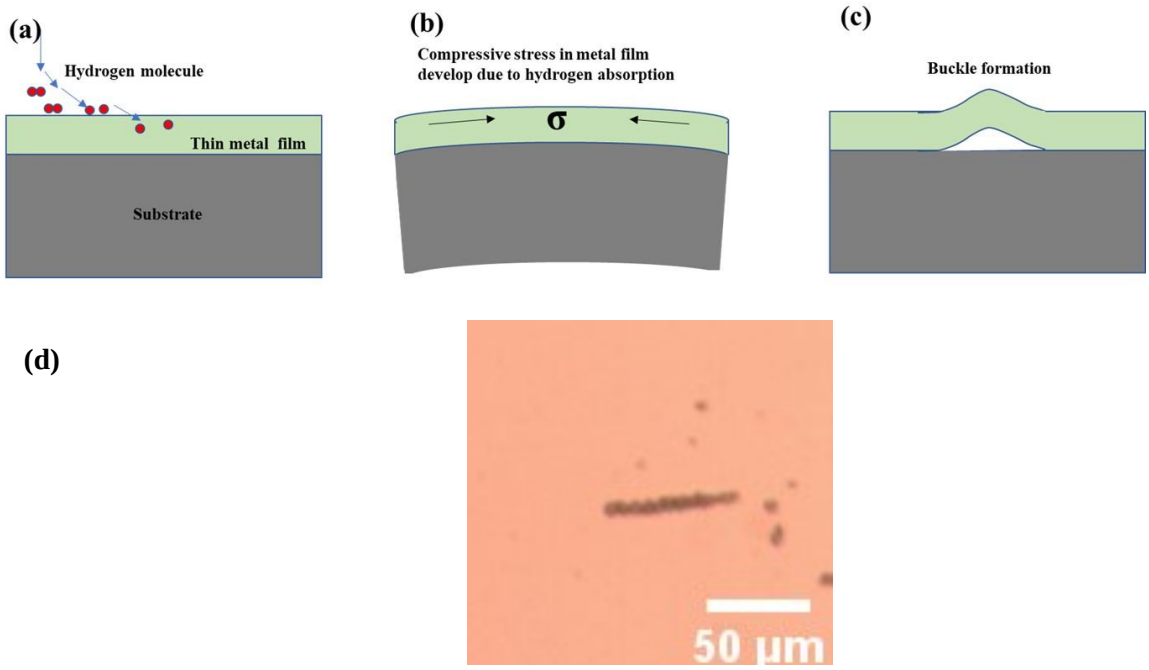

Figure 2.8: Schematic drawing shows V-films buckling during hydrogen absorption, in-side view. **(a)** adsorption and absorption of hydrogen on and in the metal film, **(b)** compressive stress developing with hydrogen absorption due to film adhesion to the substrate, **(c)** local film detachment due to high compressive stress resulting in buckle formation, (**d)** presents a micrograph of a single buckle (dark line) in a V film, in top-view.

For hydrogen-loaded films, detachment occurs above a critical in-plane stress, resulting in crack formation at the interface of the metal film and the substrate. Different kinds of buckle morphologies, such as the straight-sided buckle, the telephone cord buckle, or the varicose mode buckle describe a transition between the other two mentioned morphologies [68] . Which type of buckle morphology will appear depends on the adhesion between the film-substrate interface, the film thickness, the film's Poisson ratio, and the stress state of the film. In the present thesis, straight-side buckles were seldom detected for the 30 nm V-films.

In this work, V-films are grown on rigid glass substrates and polycarbonate (PC) substrates. Also, different interlayers (Pd and PC) are used to change the adhesion conditions between the V-films and the glass substrates. Thus, hydrogen absorption in V thin film results in stress development which depends on the adhesion condition. Strong adhesion leads to high in-plane stress of up to several GPas while weak adhesion results in buckle formation. As the adhesion energy between the metal and the PC substrate (or interlayer) is observed to be small (see table 2.1), buckling is expected for these samples upon hydrogen uptake.

Table 2.1: Adhesion energy γ for different film/substrate combinations

Film/substrate	γ [J/m^2]	Source
Niobium$_{poly}$/Sapphire (0001)	26	[72]
Palladium/Sapphire	2.8	[73]
Niobium(oxide)/PC	0.05	[68]
Palladium/PC	0.4	[68]
Chromium/PC	0.1	[68]

Higher stress is expected for the films directly deposited on the glass or on the Pd interlayer, because of the considered higher adhesion energy.

2.4.3 Stress relaxation by grain sliding

For the nanocrystalline thin film, grain-boundary sliding has been found by several investigators to contribute to plastic deformation. Grain-boundary sliding defines the translative motion of two grains, under shear stress in parallel to the common grain boundary [74, 75]. Initially, grain sliding is reported for materials deforming at higher temperatures. As this research was performed at room temperature, we discuss the grain sliding effect by solute atoms, such as hydrogen atoms according to a previous study [76]. Solute atoms can act in two ways by trapping at grains-boundaries: (i) hydrogen atoms can segregate at the grain boundaries and result in hardening. Thus, decreasing grain boundary sliding increases the resistance against deformation of the material. (ii) Segregation of the hydrogen atoms at the grain boundary may cause faceting of the grain-boundary plane. A faceted grain boundary behaves like a corrugated grain boundary for grain sliding. This drastically decreases the grain-boundary sliding rate.

Grain sliding mechanism model proposed for nanocrystalline thin films

Figures 2.9 (a) – (d) show the schematic general way of grain sliding that is observed for nanocrystalline or microcrystalline metals, such as in a previous study [77]. Under tensile stress, the grain microstructure of the metal changes by grain sliding, resulting in grains' elongation in the direction of the applied tensile stress while normal to that direction the grains shrink [see Figure 2.9 (b)]. Ashby and Verral describe the process in detail [78]. The intermediate stage results in an increase in the grain boundary area. The sliding originates from vacancy flux and thus, a metal atom flux along the grain boundaries, deforming the grains perpendicular to the applied biaxial mechanical stress.

When grain boundary sliding (GBS) happens in nanocrystalline thin films, some boundary conditions have to be considered as the film is adhered to a rigid substrate. Figure 2.9 (e) presents the top view of such a nanocrystalline film with grain boundaries. When this type of V-film is loaded with hydrogen, it cannot expand freely in the in-plane direction, and thus develops strong compressive stress (see also chapter 2.3.2).

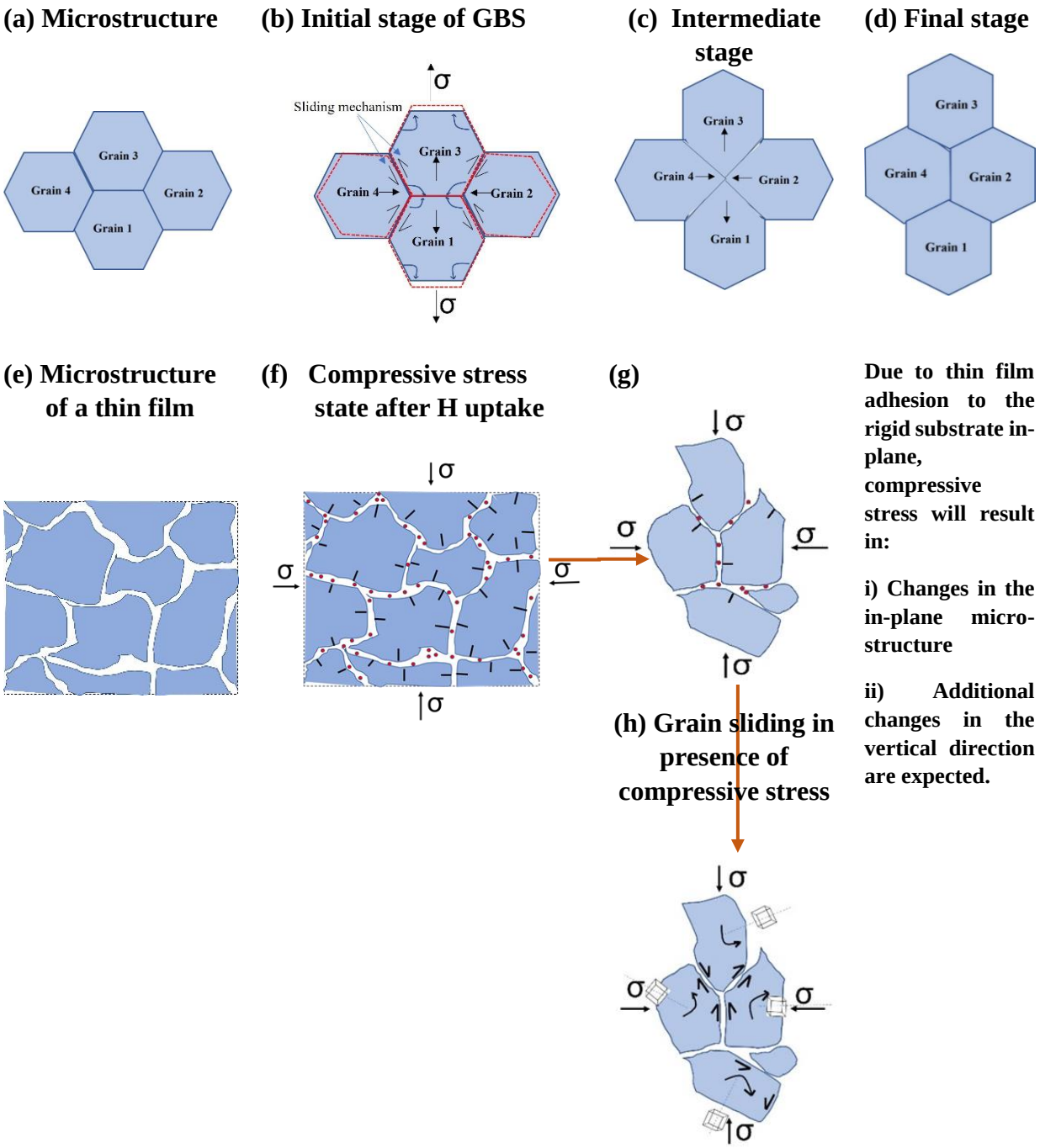

Figure 2.9: The grain boundary sliding mechanism (GBS) for nanocrystalline metals presented at different stages during tensile stress loading from **(a-d)**. **(a)** presents the grain morphology [78]. **(b)** the initial stage of GBS, **(c)** shows the intermediate stage with increasing grain boundary area, **(d)** presents the grain morphology after process completion. Parts **(e-h)** present the thin film model in top view. **(e)** nanocrystalline thin film **(f)** and **(g)** present the compressive stress state of the thin film due to hydrogen loading (black line at the grain boundary presents local slip). **(h)** presents the GBS process in the thin film and the grain morphology modification. Due to the adhesion state of the thin film to the substrate, vertical changes are also expected. Figure 2.9 (a-d) adapeted with permission from [78], copyright 1972 Elsevier.

Figures 2.9 (f) and (g) present the hydrogen-loaded situation of the film, depiction is focus on the hydrogen absorbed in the grain boundaries region only, not the hydrogen in the grains. In these figures, black arrows represent the compressive stress state in the film. Grain boundary deformation can happen normally or tangentially to the grain boundary plane. With respect to the macroscopic stress or strain, both can result in shear stress due to the arbitrary orientation of the grain boundary to them. Black marks across the grain boundaries present the local slip. Further, stress concentrations at triple points of three meeting grain boundaries can result in stress accommodation by plastic deformation.

As mentioned earlier, the presence of hydrogen atoms can pin the dislocation motion, or hydrogen segregation at grain boundaries may cause faceting. Different orientations of grains with respect to the in-plane compressive stress can deform the grains by GBS and due to in-plane constraints for such kind of nanocrystalline sample, grain sliding should be observed in the vertical direction. The strength of these vertical changes will depend on grain size, material properties, stress value, and strain rate [77].

2.5 Optical properties of metals

Metals often display drastic changes in their optical properties upon hydrogen absorption. Pd, Mg, La, Gd, and Y have been well-studied [79, 80, 81, 82, 83, 84, 85, 86], but many other metals such as V have been studied only in a very limited range. The change in the optical properties can be used to monitor phase formation upon hydrogen loading in thin films. Gremaud et al. [87, 88] named this method "Hydrogenography''. It is based on the fact that metallic films change their optical properties depending on the hydrogen concentration. Further, hydrogen absorption and desorption can be monitored by measuring the optical transmission of the films while hydrogen can be cyclically loaded and unloaded.
In this work, electrochemically hydrogen loading, and unloading are done to accurately determine the hydrogen concentration in the film and to correlate this with the optical changes in, reflection and transmission.

2.5.1 Optical properties of M-H systems

Metal hydrides of many metals show profound changes in their optical properties, such as switchable mirrors [89] and hydrogen sensors [90]. Many metals can absorb hydrogen such as reaching and exceeding a metal-to-hydrogen atom ratio of 1:1. This results in significant changes in the lattice constant or, after phase transition, often also in the crystallographic structure. This alters the electronic band structure. In addition to this, the added electron contributed by hydrogen and the addition of resonances associated with the binding of hydrogen to the metal lattice results in changes in the metal's optical behavior. By measuring the transmission, the reflectivity, the absorption, or the light scattering, the dielectric function ε(ω) of the optical conductivity or the frequencies that are excitation frequencies can be deduced.

The frequency-dependent complex dielectric function ε(ω) can be used to show the behavior change upon hydrogen uptake. The influence of hydrogen on the optical properties of metals can be studied by using the Drude-Lorents model [91, 92].
The complex dielectric constant ε(ω) and the complex index of refraction n_c are defined as [93]

$$\varepsilon(\omega) = \varepsilon_1 + i\varepsilon_2 = n_c^2 = (n + ik)^2 \tag{2.23}$$

where ε_1 and ε_2 are real and imaginary parts of the dielectric constant; n and *k* are real and imaginary parts of the refractive index, respectively.

According to the Drude-Lorentz model, when an electric field (due to electromagnetic radiation) falls on a dielectric material its material particle response can be approximated by a damped harmonic oscillator with the mass m, charge e, damping Γ, eigenfrequency $\omega_T = 2\pi\sqrt{\frac{f}{m}}$, and restoring force f.
Now, the complex dielectric function ε(ω) for N oscillators that exist per unit volume is given by [94]:

$$\varepsilon(\omega) = 1 + \frac{s(\omega_0^2 - \omega^2)}{(\omega_T^2 - \omega^2)^2 + \omega^2\Gamma^2} + i\frac{s\omega\Gamma}{(\omega_T^2 - \omega^2)^2 + \omega^2\Gamma^2} \tag{2.24}$$

where $s = e^2$ N//m, presents oscillator strength and

$$\varepsilon_1 = 1 + \frac{s(\omega_0^2 - \omega^2)}{(\omega_T^2 - \omega^2)^2 + \omega^2\Gamma^2}, \qquad \varepsilon_2 = \frac{s\omega\Gamma}{(\omega_T^2 - \omega^2)^2 + \omega^2\Gamma^2}$$

For metal having free charge carriers (electron gas model), there will be no restoring force f=0, and only damping of incident intensity happens. Thus equation (2.24) is modified as

$$\varepsilon(\omega) = 1 - \frac{\omega_p^2}{\omega(\omega^2+\Gamma^2)} + i\frac{\omega^2\Gamma}{\omega(\omega^2+\Gamma^2)} \quad (2.25)$$

Where $\omega_p = \sqrt{\frac{Ne^2}{m}}$ is the plasma frequency

$$\varepsilon_1 = 1 - \frac{\omega_p^2}{\omega(\omega^2+\Gamma^2)}, \qquad \varepsilon_2 = \frac{\omega^2\Gamma}{\omega(\omega^2+\Gamma^2)}$$

Figure 2.10 presents the dielectric index variation with hydrogen. It explains the optical behavior changes for Pd, Mg, and V upon hydrogen uptake. According to Figure 2.10 (a), for Pd the dielectric function of the imaginary and the real parts shows that upon hydrogen loading, Pd becomes less metallic. The real part of the dielectric function increases by up to 39% in the infrared region while the imaginary part decreases by a similar percentage [95]. This implies that the optical transmission of palladium increases upon hydrogen uptake.

For Mg, shown in Figure 2.10 (b), the real part of the dielectric function shows that Mg abruptly changes its optical properties from that of a metal to that of an insulator. The real part of the dielectric function decreases and the imaginary part increases with loading hydrogen.

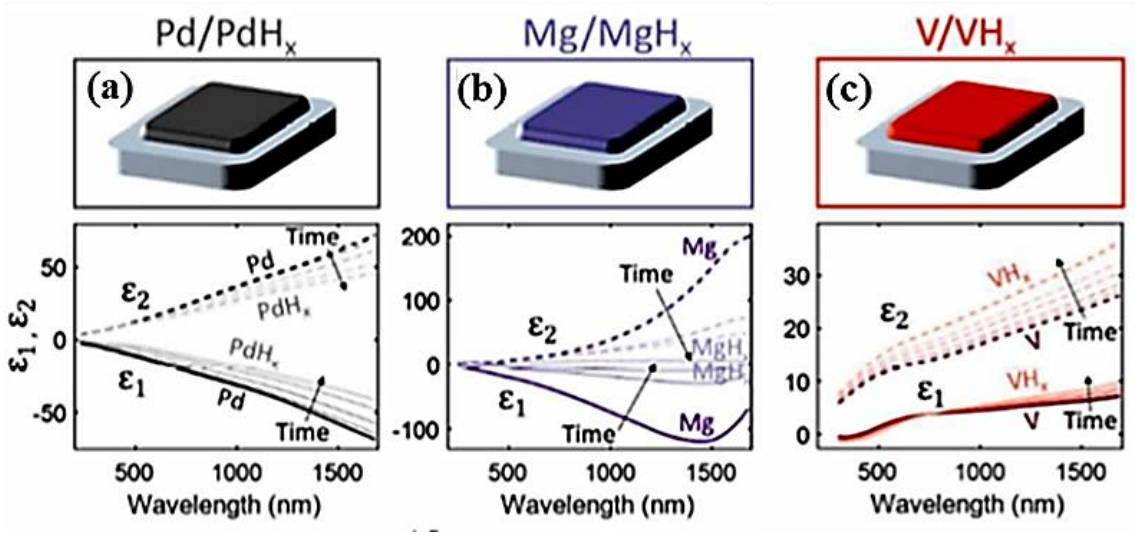

Figure 2.10: (a), **(b)**, and **(c)** presents the Pd, Mg, and V optical properties, respectively, without and with hydrogen for different loading states. The top row sketches the samples in their thin film states, while the lower row presents the dielectric functions of each metal before hydrogen loading in, its hydride state and intermediate loading states, as presented by arrows. Reprinted with permission from [95]. Copyright 2018 American Chemical Society.

For vanadium, shown in Figure 2.10 (c), hydrogen loading only slightly changes the real part of the dielectric function. However, the imaginary part shows a large and significant change, with hydrogen loading increasing by more than 38% in the infrared part. This demonstrates that the optical transmission of vanadium decreases upon hydrogen uptake.

2.5.2 Band structure changes in the V-H system

Hydrogen absorption in metal marginally affects the electronic band structure. This change happens due to the hydrogen donation of its one electron to the host conduction band. This leads to the hybridization of the 1s-state of the hydrogen and the host metal 3d-states. They form bonding and anti-bonding states, the bonding state lies below the d-band, and the anti-bonding state lies above the Fermi energy of the vanadium and remains unoccupied. This was verified for hydrogenated V by Fukai et al by using x-ray emission spectroscopy [96], see Figure 2.11.

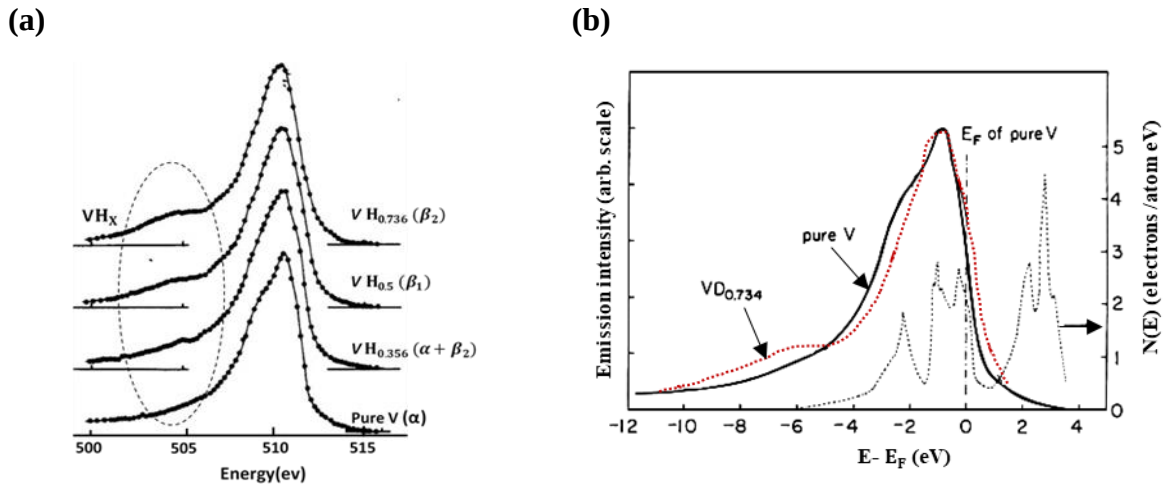

Figure 2.11: (a) Soft x-ray emission spectra of vanadium and **(b)** vanadium deuteride $VD_{0.734}$ emission spectra that includes the calculated density of state of V. **(b)** with increasing hydrogen concentration in V a bulge appears around ~6 eV below the Fermi energy, and d band has shifting of energy state above fermi energy see the dash red line. Data in this figure reprinted with permission from [96]. copyright 1976 Elsevier.

Figure 2.11 (a) shows that with increasing hydrogen concentration a bulge starts to appear ~6 eV below the Fermi energy indicating the formation of new states. Figure 2.11 (b) presents the vanadium deuteride $VD_{0.734}$ emission spectra, showing that the low energy side of the d-band is diminished in intensity and the high energy side is shifted above the Fermi level (red curve). This change in the electronic density of states can lead to a change in the optical behavior. Energies between 1 eV to 3 eV can result from metal d-band electrons being excited to the s or p states and vice versa. Such change in the absorption coefficient γ (λ), shows optical light frequency dependency and thus also affects the transmission intensity (see Figure 2.12).

The transmission behavior changes with film thickness. A 5 times lower transmission is expected due to a decrease in thickness. Instead, a 30% increase in the transmission is detected for 400 nm wavelength.

(a) **(b)**

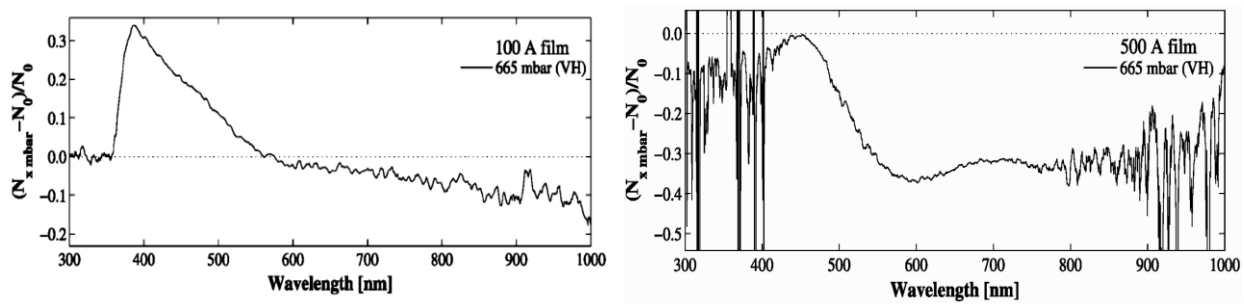

Figure 2.12: Change in transmission intensity of a 10 nm **(a)** and a 50 nm vanadium film **(b)** due to hydrogen uptake at 150°C and 665 mbar hydrogen pressure. N_0 and N_{xmbar} give the numerical count in the spectrometer, with and without hydrogen. For wavelengths below 350 nm, the result is inaccurate. This Figure was taken from [97]. Copyright 2010 J.Prinz.

The optical properties like transmission, reflection, and absorption of a material depend on the frequency of the incident light and its angle, the dielectric constant of the material, and its shape. For this work, during hydrogenography measurement, thin films of thickness d with refractive index n_c are used while incident visible light falls normal to be probed sample [88].

Lambert-Beer law describes changes in transmission as observed in studies of Pd-H [88] and V-H [98]. According to Lambert's law, the rate of Intensity *I* loss of light, transmitted through an infinitesimally thin layer *x* of homogeneous medium is proportional to the intensity of light

$$-\frac{dI}{dx} \propto I \; or \; \frac{dI}{dx} = -k_1 \cdot I \tag{2.26}$$

Integrating equation (2.26) between limits $I = I_o$ for $x = 0$ and $I = I_t$ when $x = d$, gives

$$\int_{I_o}^{I_t} \frac{dI}{I} = -k_1 \int_0^d dx \Rightarrow \; ln\left(\frac{I_t}{I_o}\right) = -k \cdot \mathrm{d} \tag{2.27}$$

Where k_1 and k are proportionality constants. As $T = \frac{I_t}{I_o}$, equation (2.27) presents Lambert's law

$$T = e^{-kd} \tag{2.28}$$

The light that does not get reflected or absorbed will get transmitted

$$T = \frac{I_t}{I_o} = \frac{I_o - I_o \cdot R}{I_o} \cdot e^{-\alpha d} = (1-R) \cdot e^{-\alpha d} \tag{2.29}$$

where α is the attenuation coefficient, and

$$T = (1 - R) \cdot e^{-\alpha d} \tag{2.30}$$

From equation (2.27), Lambert's law can be rewritten as Lambert-Beer's law, which required the addition of a parameter for the light attenuation such as concentration dependency and extinction coefficient. Absorption in a gaseous, liquid, or a sample having solute and solvent parts can be split as

$$\alpha = \alpha_0 + \sum_i \epsilon_i c_i \tag{2.31}$$

Where α_0 is absorption due to solvent only and c_i is the solute concentration with the extinction coefficient ϵ_i.

Inserting equation (2.31) in equation (2.30) gives

$$T = (1 - R) \cdot e^{-(\alpha_0 + \varepsilon c) \cdot d} = T_M \cdot e^{-\varepsilon c d} \tag{2.32}$$

For a thin metallic layer of thickness d, the transmission T_M in the metallic state transforms in Lambert-Beer's law, after the addition of solute of concentration c, as

$$ln \frac{T(c,d)}{T_M} = -\epsilon c d \tag{2.33}$$

For this model to be applicable, it is required that the solute atom is homogeneously distributed. This condition is fulfilled by the metal solid solution phase before the phase transformation into the hydride phase.

Chapter 3

Experimental methods

In this chapter, the used experimental techniques are briefly described. Section 3.1 gives the details regarding the ultrahigh vacuum (UHV) system used for film preparation. Section 3.2 provides the detail on the electrochemical and gas phase hydrogen loading. Section 3.3 gives the description of hydrogenography, and electrochemical hydrogen loading with the simultaneous optical measurement with the light microscope. Section 3.4 explains the in-situ stress measurements that were used in combination for the studies of this thesis. Section 3.5 gives the details on the hydrogen loading system used for in-situ Scanning Tunneling microscopy (STM) experiments and includes the Atomic Force microscopy (AFM) technique. Section 3.6 briefly explains the applied X-ray diffraction (XRD) and X-ray reflectivity (XRR) techniques.

3.1 Sample Preparation

The deposition of V films for this thesis was done in an ultra-high vacuum (UHV) cathode beam sputter system. Details about the method are provided previously [53]. The UHV system shown in Figure. 3.1 consists of three different chambers: the pre-evacuation chamber (pre-chamber), the cathode ion beam sputtering chamber, and the UHV-STM loading chamber. The system is equipped with two sample transfer rods, to transfer the sample from the pre-chamber to, the sputter chamber or the STM chamber. The sputtering chamber has a z-manipulator which facilitates the translation motion of the substrate in x, y, and z direction as well as its rotation with respect to the target.

The sputtering system has the potential of mounting four different targets (V, Pd, Mg, Nb) on a rotational holder, a cubic metal block with a cooling unit attached to it. Thus, without removing the substrate or target from the deposition chamber, different materials can be sputtered. Attached to the sputter chamber is the in-situ STM chamber which is equipped with a four-probe resistivity stage. During measurement, the STM chamber is isolated from the sputter chamber via a gate valve. The background pressure inside the sputter chamber is better than 5×10^{-10} mbar. For preparing the samples, an RF ion source from Plasma Consult was used [12]. Sputtering was performed via argon plasma (Ar purity 99.9999%) at $p_{Ar}= 2.2 \times 10^{-4}$ mbar. High-purity vanadium (99.99%) was used as a target material. (110) textured V films of different thicknesses were prepared by Ar+ ion-beam sputtering on the glass substrates. The details regarding the typical sputtering parameters are summarized in Table 3.1. The sputtering rate is stable during one single deposition but varies with the running time of the source (0-10,000 h). Therefore, two limiting values are given in Table 3.1.

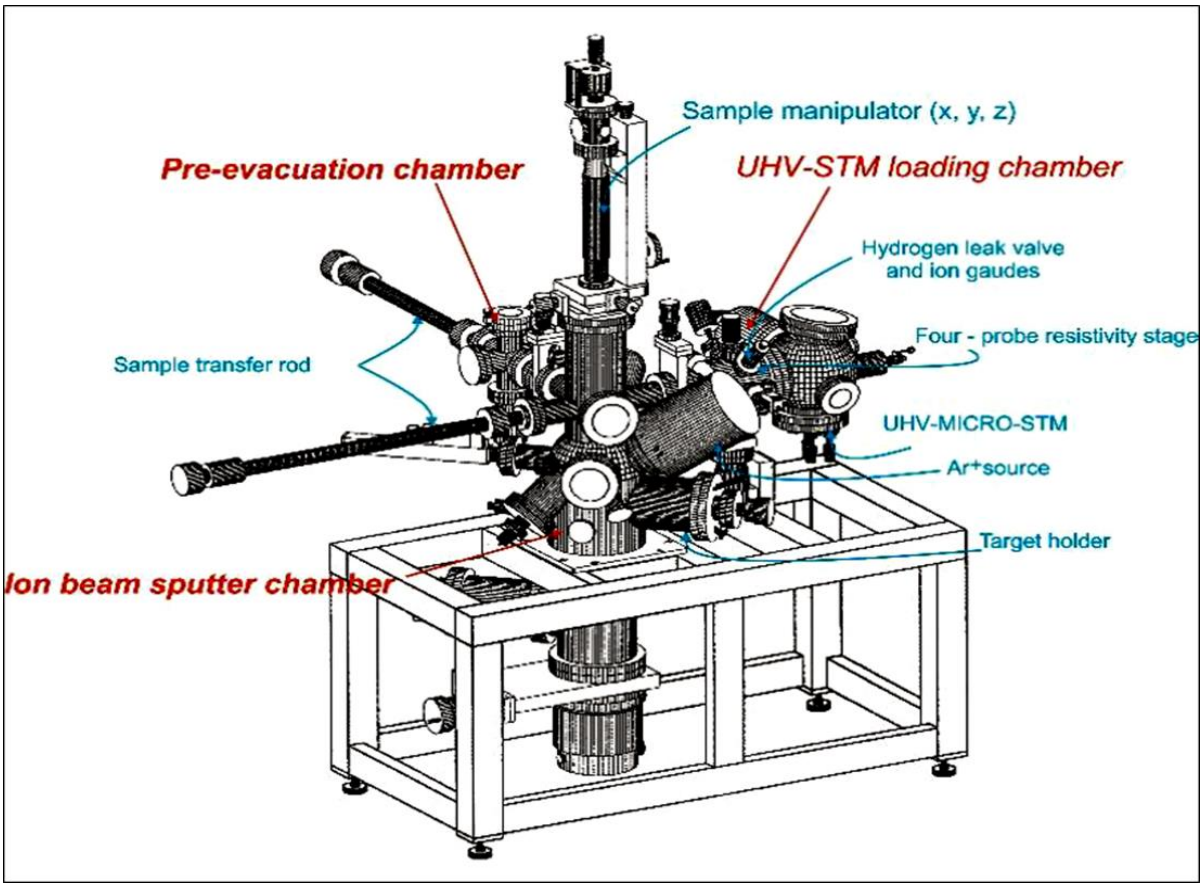

Figure 3.1: Schematic diagram of the UHV system used in this work (picture taken from Ref. [12]), showing three main parts: the pre-evacuation chamber, the sputter chamber, and the STM chamber. It has two sample transfer rods and one manipulator arm which can do translation motion in x, y, and z directions. The UHV STM chamber is equipped with the hydrogen dose valve for hydrogen loading experiments, in addition to a four-probe resistivity stage. The system is equipped with a quadrupole mass spectrometer, a full-range gauge, and other sets of vacuum gauges. This Figure reprinted from [12]. Copyright 2006 K.Nörthemann.

Table 3.1 Experimental conditions for sputter depositions

Sputtering gas	Ar purity 99.9999%
Sputtering gas pressure (mbar)	2.0×10^{-5}-2.4×10^{-4}
Substrate target distance (cm)	5-12
Target purity (V, Pd in %)	>99.9
Energy of Ar^+ (eV)	880

RF power (w)	76
Substrate	Glass (specific type from Schotts), Si
Deposition rate (nm/min)	Pd 0.61-0.86
	V 0.67-1.12
Deposition temperature	Room temperature

In order to facilitate hydrogen absorption at 20°C, a Pd catalyst capping layer of 1 nm to 15 nm layer thickness (depending on the measurement) was deposited onto the V films. This Pd layer is required to prevent subsequent film oxidation upon air exposure and to improve hydrogen uptake in the sample. Figure 3.2 presents the schematic representations of different geometries of the samples interlayer that were grown and used in this work. Samples that were studied by *in-situ* STM were transferred into the UHV-STM loading chamber (see Figure. 3.1, right side) with a thin Pd cap layer, directly after film preparation without breaking the vacuum conditions, see Figure 3.2 (a). Thus, rapid oxidation of the V surface, occurring in the atmosphere at 20°C, is prevented.

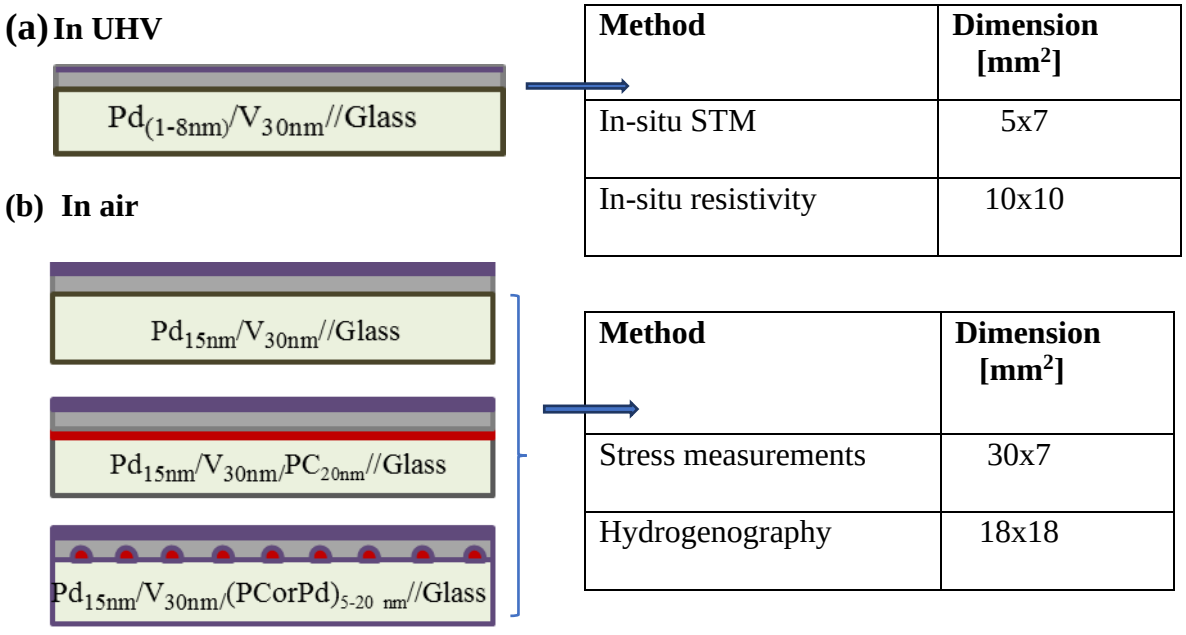

Method	Dimension [mm²]
In-situ STM	5x7
In-situ resistivity	10x10

Method	Dimension [mm²]
Stress measurements	30x7
Hydrogenography	18x18

Figure 3.2: Sample configurations used in this work. **(a)** The sample used under UHV conditions has a 1-8 nm Pd cap layer. **(b)** Samples that were exposed in air have a 15 nm Pd cap layer. Different interface layers (Pd, PC, no-layer) with 5-20 nm thickness are deposited between the V film and the substrate.

For the samples that were studied outside of the UHV system, namely used in hydrogenography and in-situ stress measurements techniques, V films are covered alternatively with a 15 nm Pd capping layer, as shown in Figure 3.2 (b).

For adhesion modification, some of the samples contained an interfacial layer between the V-film and the substrate. These interfacial layers are (a) sputter-deposited Pd layers or dots of about ~1.4 mm in diameter, or (b) laser-deposited polycarbonate (PC) layers or dots of about ~1 mm in diameter. The thickness of the interfacial layer varied between 20 nm and 5 nm. The dots were prepared by using a mask consisting of a drilled hole array. Figure 3.3 shows the mask used to deposit Pd dots of hole size of 1 mm and resultant dots with a dimension of 1.4 mm in diameter.

Figure 3.3: Sputter holder with the mask used to deposit the Pd dot pattern onto the glass substrate. Hole sizes of 1 mm (left-hand side) result in deposited dot pattern of 1.4 mm (right-hand side).

Laser deposition of PC was done in collaboration with Florian Döring under the supervision of H.U. Krebs. For the deposition, a KrF Excimer laser source of 248 nm wavelength with pulse duration of 30 ns was used. Laser deposition was done at room temperature in a background vacuum condition 10^{-8} mbar. Details about the method are available in Ref. [50, 99]. Figure. 3.4 shows two atomic force microscopy (AFM) images presenting the PC surface when deposited at two different laser fluences of (a) 80 mJ/cm^2 and (b) 310 mJ/cm^2. F. Döring [100] documented that higher laser fluence results in higher roughness. Therefore, for the growth of PC dotes here, a low laser fluence of 80 mJ/cm^2 was used.

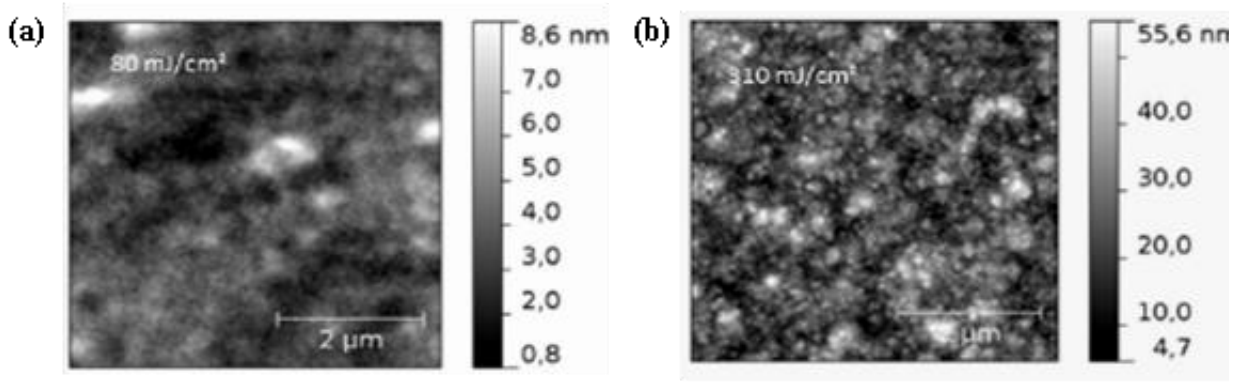

Figure 3.4: AFM images of the surface topography of laser-deposited thin PC films, deposited at laser fluences of 80 mJ/cm^2 **(a)** and 310 mJ/cm^2 **(b)**. The higher laser fluence results in a higher roughness. This Figure reprinted from [100]. Copyright 2017 F.Döring.

3.2 Hydrogen loading

Hydrogen loading can be carried out in two major ways: from the gas phase by varying the pressure or electrochemically by setting the hydrogen concentration as explained below. It also allows measuring the electromotive force with respect to a known potential.

3.2.1 Electrochemical hydrogen loading

In comparison to gas-phase, electrochemical loading has the advantage that a desired amount of hydrogen can be dosed into the sample. In this regard, a specially designed PC-cell is developed (Figure 3.8) which provides hydrogen loading in an oxygen-free environment. For hydrogen loading, the sample was placed in this cell containing the electrolyte of phosphoric acid and glycerine in volume ratios of 1:2 [101]. The hydrogen loading requires the electrochemical cell to be connected to an electronic setup which consists of a reference electrode ($Ag/AgCl_{sat}$, Schotte Instruments GmbH), a current source, an impedance converter, and a counter electrode (Pt wire), as described in Ref [56]**.** The sample works as one electrode, and the Pt wire works as the counter electrode. With each hydrogen loading step, hydrogen ions are adsorbed at the sample surface and further get absorbed in sample, this process is observed as a change in the electromotive force (EMF). With each loading step, the EMF is allowed to equilibrate. The change of the EMF was observed with the help of a standard reference electrode $Ag/AgCl_{sat}$. The hydrogen concentration c_H ([H]/[V]) was determined by using a loading current pulse with current I and time t, as described by Faraday's law:

$$\Delta c_H = \frac{I \cdot \Delta t \cdot V_M^V}{F \cdot V^V} \tag{3.1}$$

where V^V is the sample volume exposed to hydrogen loading; V_M^V represents the molar mass of the sample's material; and F denotes the Faraday constant. By controlling the loading time t and the loading current I, a chosen amount of hydrogen can be charged into the sample.

Electrochemical loading can be done in two modes: continuous or step-by-step. Continuous mode (continuous loading) requires a fixed charging current (constant current) to be applied, for a calculated amount of time. For step-wise loading, each charging step and time can be calculated separately, making it easy to control the hydrogen concentration c_H with each loading step. Loss of hydrogen is minimized by the design of the electrochemical cell. However, the charging current density should be low (<50 mA/cm^2) [8], otherwise hydrogen ions can combine to form H_2 instead of diffusing into the sample. To further minimize the loss of hydrogen ions, the electrolyte is bubbled with Ar gas for 12 hours, to reduce its oxygen content. In step-wise loading, the EMF value is allowed to equilibrate for each loading step before setting the next step. The EMF value of hydrogen in loaded film in the equilibrium is a measure of the chemical potential of hydrogen μ_H via [102]:

$$E = E_0 + \frac{\mu_H}{F} \tag{3.2}$$

where E is the measured EMF of the sample, and E_0 is the standard potential of the reference electrode (at 298 K Ag/AgCl$_{sat}$, electrode has a potential of 0.2223V) [41].

It is possible to calculate the hydrogen partial pressure by using the Nernst equation [103]

$$p_{H_2} = p_o \cdot \frac{exp\left((E-E_0)n_{eF}\right)}{RT} \tag{3.3}$$

where P_0 is the standard pressure (1 bar); R is the gas constant; T is the temperature; and n_e is the number of electrons related to the reaction (n = 1 for hydrogen).

Hydrogen loading ranges from 0 hydrogen atom per vanadium metal atom (denoted 0 H/V) to 1 H/V. We neglect a small amount of hydrogen present before loading. Loading for hydrogenography is done step-wise and generally, 50 loading steps are used between c_H = 0 H/V and c_H =1 H/V. This range is divided in step sizes of Δc_H = 0.01 H/V between c_H = 0 H/V and c_H = 0.3 H/V, Δc_H = 0.02 H/V between c_H = 0.3 H/V and c_H = 0.5 H/V, and Δc_H = 0.05 H/V between c_H = 0.5 H/V and c_H = 1 H/V. The EMF was recorded 1 minute after the electric pulse, resulting in EMF stabilization and, thus, in a quasi-equilibrium state.

For stress measurements, mostly continuous loading is used. That means, for stress measurements the measured EMF value includes the voltage applied for hydrogen charging. This results in EMF plateau values that were artificially higher than the equilibrium values derived by step-wise loading. However, the stress measurements were only slightly affected by the different charging conditions, as will be shown later.

The two kinds of aforementioned loadings have their advantages and disadvantages: long measurements required for multiple loading and unloading cycles can be easily done by continuous loading in automatic mode, and step-wise loading needs to be done manually but gives information about changes occurring with each loading step.

For *in-situ* stress measurements, a cell setup (with components of the electrochemical loading cell) was combined with an induction gauge required for the stress measurements arising in the film upon hydrogen loading.

Thus, electrochemical loading is a very useful tool of hydrogen loading for thin films but needs precautions such as (1) the proper choice of the electrolyte, as the metal can be attacked by the electrolyte, (2) the proper protection layer, and (3) the removal of oxygen from the electrolyte to avoid hydrogen loss in the form of water. Under proper conditions, the hydrogen concentration in the measured sample can be accurately determined.

3.2.2 Gas-phase hydrogen loading

The UHV sputter system is directly attached to the STM hydrogen loading chamber (see Figure 3.1), allowing for film deposition and film measurement without breaking the vacuum conditions. In the STM chamber, the sample can be exposed to hydrogen in a pressure range of 10^{-10} mbar to 900 mbar. The corona discharge pressure range of 10^{-3} mbar to 10 mbar is avoided for working, to exclude the risk of damaging the internal electronics of the STM system [12]. During measurement, hydrogen was introduced via a dosing valve. Once it was introduced, it was possible to have a constant hydrogen pressure for long-term measurements in constant flow conditions, by using a nearly closed valve on top of the turbo pump. The pressure range used in this work is 10^{-10} mbar to 660 mbar. To avoid the corona discharge pressure range, a gas mixture of $Ar+H_2$ (0.01%) was used. The absolute was measured by using two Baraton type (MKS) pressure. Gauges (MKS Baratron® capacitance manometers) in the sensitivity range of 10^{-4} mbar to 1 mbar and of 10^{-1} mbar to 1 bar. These gauges are independent of the gas species. Additionally, for rough pressure control, a full-range gauge (Pfeifer pressure gauge is strongly gas species-dependent ranging from 5×10^{-9} mbar to 1000 mbar) is also mounted in the UHV STM camber. Figure 3.5 shows the hydrogen pressure sensitivity of the full-range gauge for pressures above 1 mbar strongly decays.

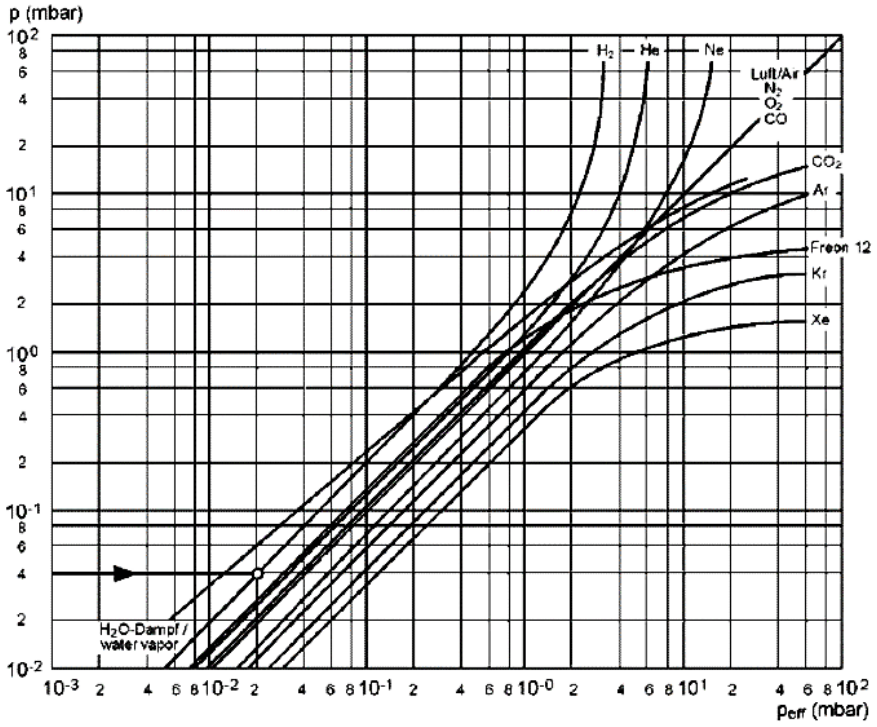

Figure 3.5: Sensitivity curve of the full-range gauge for hydrogen. Above 1 mbar, the sensitivity for hydrogen drops. The range (5×10^{-9} mbar – 1000 mbar) is out of reach, in the STM measurements, due to the corona discharge. Figure copyright Pfeiffer vacuum GmbH[1]).

3.3 Hydrogenography

Hydrogenography is an optical technique applicable to thin metal films, based on the fact that hydrogen loading and unloading affect the optical properties of metallic films. For a thin metal film, electrochemical hydrogenography allows measurements of the EMF as well, so it allows for measurements of the optical transmission and the reflection as a function of the hydrogen concentration $c_{H,}$ which is determined by step-wise loading (for more details, please see section 3.2.1).

By absorbing hydrogen, the metallic film's optical properties can change from metallic to insulator or from opaque to transmission. This is shown in Figure. 3.6 where an Mg-Ti film is used as a mirror for a flower in the metallic state, after hydrogen loading (Mg-Ti-H) film does not show the reflection anymore [104]. The film remains dark in this state.

According to Lambert-Beer law [105], see equation 3.4, for most metals, the normalized transmission is proportional to the hydrogen concentration. So generally, the transmission also increases with increasing the hydrogen content for most metals. This depends on the used light

[1] This Figure reprinted from:
(https://www.idealvac.com/files/brochures/Pfeiffer_PKR_251_Pirani_ColdCathode.pdf)

Figure 3.6: Mg0.7Ti0.3 thin film in, the metallic (left) and the hydride (right) state during hydrogenation [104]. Reprinted with permission from [104]. copyright 2008 Elsevier.

wavelength [106, 107]. Figure 3.8 (a) presents the wavelength dependency of V films, in the range of 400 nm to 500 nm transmission have maxima [97]. Figure 3.8 (b) shows the wavelength spectrum of the light microscope (Leica DM1750, Leica Microsystems) used in this work.

In the case of Pd the normalized transmittance T/T_0 changes (increases) by a factor of 10, on increasing the hydrogen concentration c_H = 0 H/Pd to c_H = 0.8 H/Pd Ref [108]**.**

Lambert–Beer law gives [105]:

$$c_H = -\frac{1}{\epsilon.d} \cdot \ln\left(\frac{T}{T_0}\right) \tag{3.4}$$

where T_0 and T are the transmittance in the metallic and the hydrogen loaded state, respectively, ϵ is the extinction coefficient, and d is the thin film thickness. This result seems to hold well for thin films as demonstrated by Kooij et al. [86].

Hydrogenography offers the possibility to study the local and the global hydrogen concentration within a defined area of the film and thus gives information on the lateral hydrogen distribution on a micrometer scale. It is limited by the resolution of the light microscope and the thickness of the film because of the light absorption. For V, studies on films below 70 nm are promising with conventional light sources. Their strength is to monitor the growth of large hydrides on short-time scales.

In the case of our V thin films, we found evidence of deviations from the general findings, as the transmission decreases with increasing hydrogen content, see Figure 3.7 (a) transmission of the deposited film and (b) the film darkens after hydrogen loading during transmission. However, these deviations will not affect the general message.

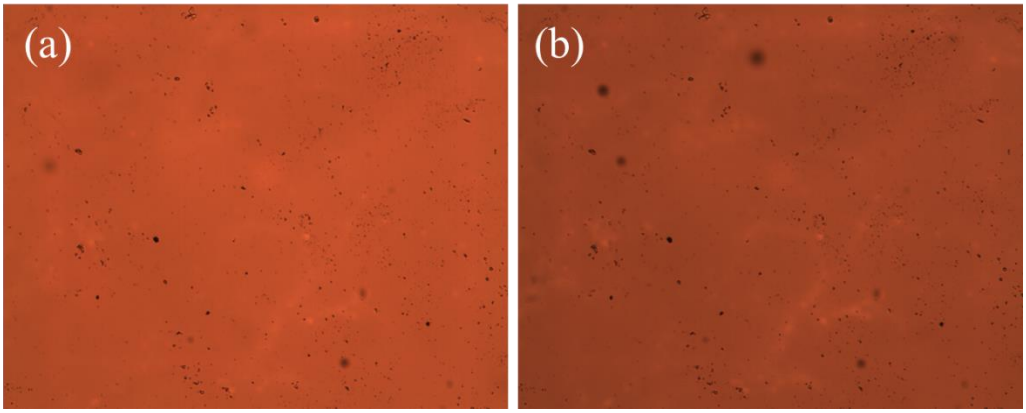

Figure 3.7: Hydrogen-induced changes in the absorptance of a 30 nm vanadium film of 1x1mm surface area, **(a)** before and **(b)** after absorption. With increasing hydrogen content, the film turns darker representing less transmission as compared the to intrinsic film.

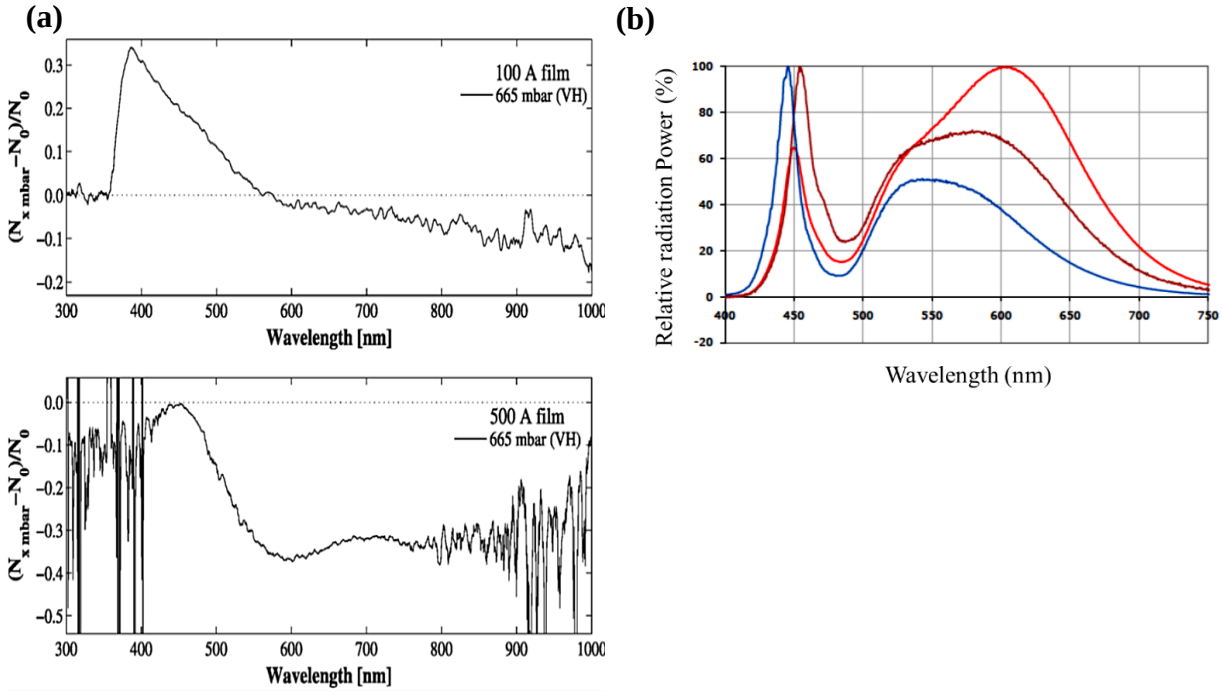

Figure 3.8: (a) Represents the wavelength dependency of the transmission of Vanadium film on hydrogenation at 150°C and 665 hydrogen pressure. where $N_{xmbar/0}$ stands for spectroscopic number count for the hydrogenated and intrinsic film [97], **(b)** wavelength spectra for the source of the Light microscope Leica DM1750 used in this work. Figure 3.8 (a) was taken from [97]. Copyright 2010 J.Prinz. Figure 3.8 (b) copyright 2010-2011 cree, INC.

For hydrogenography measurements, thin V films with a thickness of 30 nm (Ortho Lux) and 70 nm (Leica 1750), capped with 15 nm of Pd, were used. This allows for measurements in transmission and reflection.
To perform the hydrogenography, the PC-cell (electrochemical loading cell, see Figure 3.9) was mounted in the light microscope with normal incident radiation (see Figure 3.10). A sample of 1.8x1.8 mm^2 in size was glued to the sample holder and mounted in the cell (Figure 3.9 central area). Before mounting to the PC cell, the sample was seal-packed between two epoxy O-rings, so that only an area of 0.6486 cm^2 was exposed to the electrolyte and also available for hydrogen loading (details of the sample loading can be seen in sect. 3.2.1).

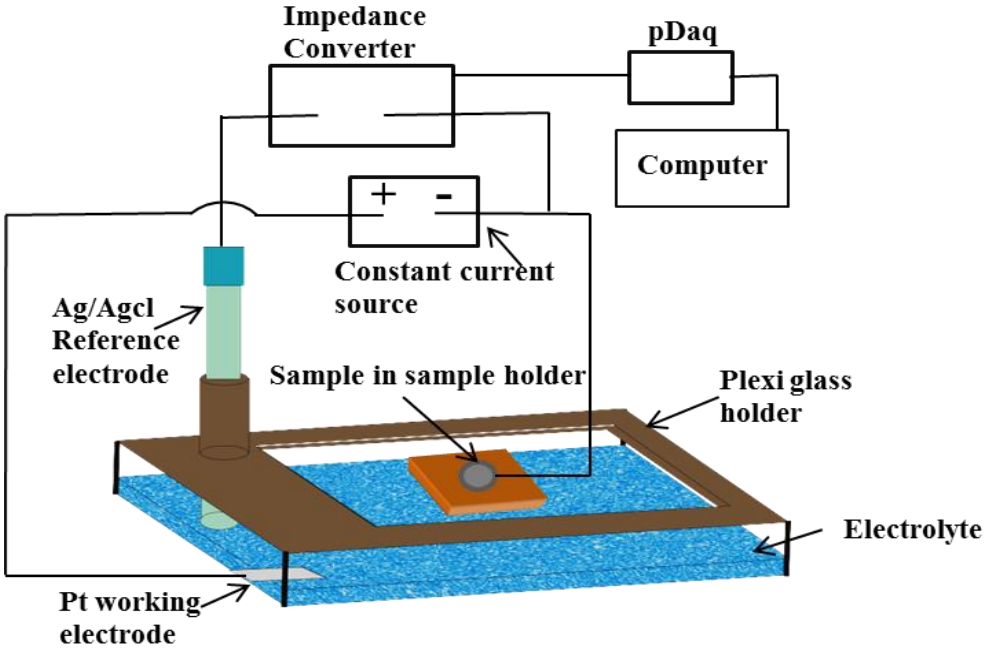

Figure 3.9: Schematic diagram of the electrochemical cell, representing the electrochemical setup required for hydrogen loading. The sample is mounted in the sample holder positioned in the center of the cell. The cell is equipped with a fixed counter electrode, Pt. After filling the electrolyte, a reference electrode ($Ag/Agcl_{sat}$) is mounted in the holder. For hydrogen-loading connections are done using cu wires, as shown in the image.

With electrochemical loading, the transmission and the reflection signals were observed and recorded. There are five different magnifications available (1000, 500, 200, 100, and 50 times), but mostly 100 × and 50 × were used to have a wide view. The maximum resolution of the light microscope is approximately 0.2 μm. In the Ortho Lux II light microscope, two tungsten-helium light sources of 50 Watts were used: one for the reflection study and the other for the transmission study. These intensities are recorded by a three-channel (RGB) charge-coupled device (CCD) camera. Also, a Leica 1750 microscope is used for thicker samples. This microscope is equipped with a more intense light source with a high-power LED lamp.

The system is also equipped with a CCD camera (Leica MC 170 HD). Figure. 3.10 shows the two different microscopes, the Ortho Lux II (a) and Leica 1750 (b) equipped with the loading cell.

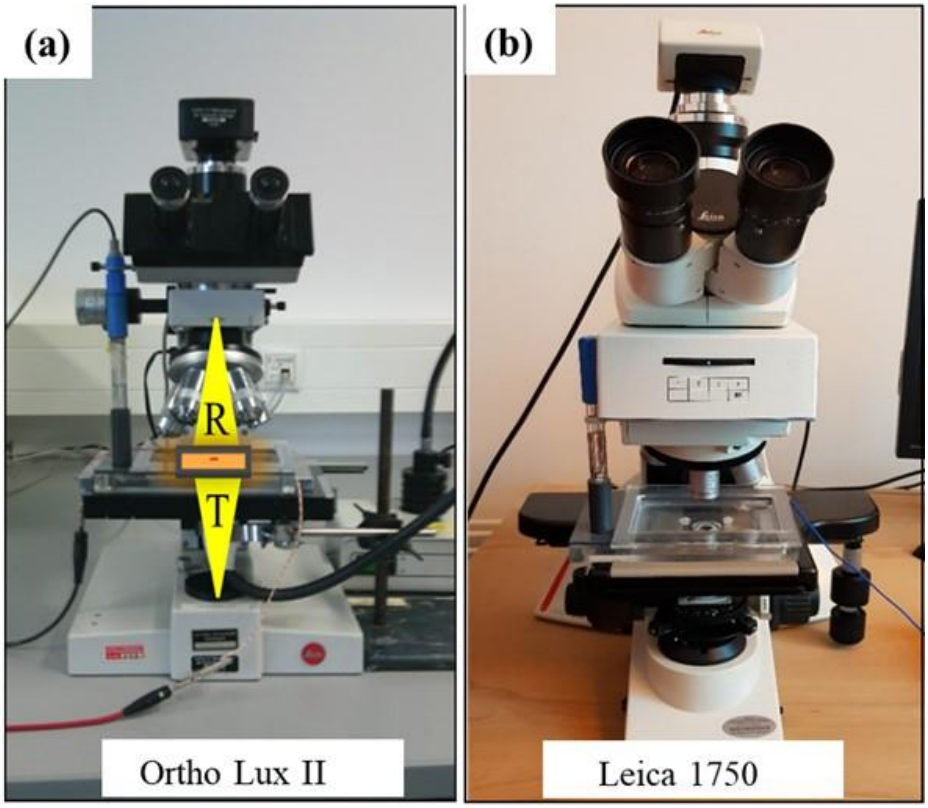

Figure 3.10: Photos of the two light microscopes used in this work during the measurement of Hydrogenography. For a sample of thickness less than 40-50 nm (vanadium + capping layer thickness), Ortho Lux II was used **(a)**, while for thicker samples Leica 1750 was used **(b)**.

To further analyze the transmission intensity of the measurement, the image intensity of grey and, in some cases, of the green channel are plotted with respect to the concentration. These diagrams are defined as transmission pixel intensity diagrams (see chapter 4). These diagrams have two y-axes, showing the intensity (left scale) in the waterfall diagram and the hydrogen concentration with increasing order (right side). In short, pixel intensity diagrams are deduced from each transmission image by plotting the number of pixels (measured with a certain intensity i_t) against the pixel intensity i_t.

3.4 In-situ stress measurements

Hydrogen absorption in the sample leads to a stress state in the sample whose magnitudes depend on the hydrogen concentration. While XRD can measure changes in strain normal to the sample surface, *in-situ* stress can show the in-plane stress response during electrochemical hydrogen loading. This kind of measurement works only for the sample firmly adhered to the substrate, as with hydrogen charging stress can be observed. To study the stress development during hydrogen

absorption, during phase transformation, and during its release by plastic deformation or other processes, *in-situ* stress measurement was conducted. The initial stress state was artificially set to zero, as intrinsic stresses are not measured.

From linear elastic theory, the compressive stress developed due to hydrogen absorption should lead to a known slope in the elastic range. Its deviation from this slope represents plastic deformation.

The schematic of the setup used for stress measurements is shown in Figure 3.11, see Ref [41]. The cell (shown as a blue line) consists of a substrate holder (black squire) and an induction gauge (at the bottom of the cell (Dornier Company)). To have sufficient bending (for theory, see chapter 2.2.), V films were deposited on a long and thin glass substrate of 30 x 7 x 0.1 mm^3. For the measurements, the sample was mounted (firmly) on a sample holder such that the substrate was facing the induction gauge. A small metal plate (Pd) was glued to the substrate, facing the induction gauge. One side of the sample was now fixed in the sample holder and the other side was free so that it could behave as a cantilever. The distance between the sample and the induction gauge can be measured via the voltage. The distance has to be adjusted so the induction gauge works in the range over which the voltage has a linear relation to the distance (precisely calibrated for the particular sensor). The cell is filled with the electrolyte of H_3PO_4 and glycerine mixed in a 1:2 ratio.

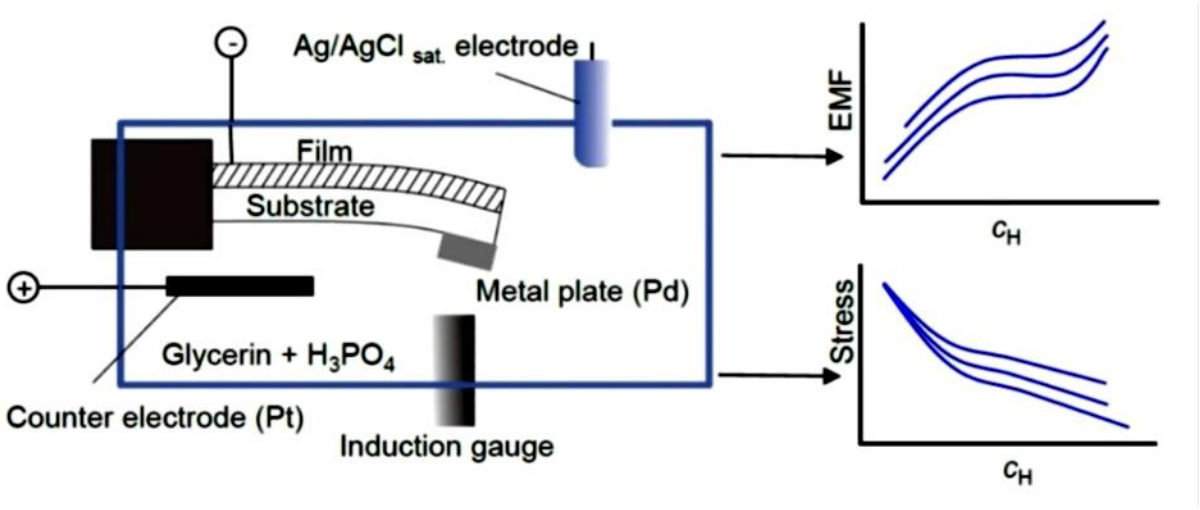

Figure 3.11: Schematic diagram of the in-situ stress measurement. Picture taken from Ref. [41]**.** In-situ stress arises during electrochemical hydrogen loading (schematic bottom right corner) and change in EMF can be measured simultaneously (schematic top right corner). Reprinted from [41]. copyright 2011 R.Gemma.

The calibration factor of the sensor used in this work τ was 3.95 Volt/mm. When hydrogen loading was done, the sample bends (thin substrate < 0.3 mm) due to the development of compressive stress. The radius of curvature R changes due to sample bending. This changes the distance z

between the Pd plate (sample) and the induction gauge which records this change in terms of voltage ΔU, such that:

$$Z = \frac{\Delta U}{\tau} \tag{3.5}$$

With Z derived from the calculation and the known sample length, R can be calculated as required for the stress calculation [68]**:**

$$R \approx \frac{L^2}{2Z} \tag{3.6}$$

Stoney's formula [109] allows to calculate the in-plane stress arising due to the hydrogen loading/unloading

$$\sigma = \frac{E_S \cdot t_S^2}{6t_f(1-v_S)} \cdot \frac{1}{R} \tag{3.7}$$

where E_s is the Young's Modulus of the substrate; v_s is the Poisson ratio of the substrate; t_s is the thickness of the substrate; and t_f is the thickness of the film.

The V films were capped with a Pd layer, but for the thickness of the film t_f, only the thickness of the V layer is considered. This was done because hydrogen absorption in Pd is negligible, and hydrogen is only absorbed practically in V (see hydrogen solubility data in chapter 2).

3.5 STM and AFM

Two different scanning probe microscopy techniques, namely scanning tunneling microscopy (STM) and atomic force microscopy (AFM), were used in this work. These techniques are employed to observe the morphological change arising on the film surface after hydrogen loading.

3.5.1 Scanning Tunneling Microscopy (STM)

STM technique was invented in 1981 by G Binnig and H Rohrer and implemented by G Binnig, H Rohrer, C Gerber, and E Weibel [110]**.** This technique is based on the tunneling effect of electrons through an insulator region between two electrodes: STM Tip (one conductor) to the probed surface (second conductor).

The operational principle of STM is illustrated in Figure 3.12. It involves a sharp metal tip, often made of tungsten or Pt_xIr_{1-x} (x= 0.1 used in this work), which is brought to proximity (in a range of 0.3 to 1 nm) to the sample surface. A voltage of 10 mV-1.5 V applied between the tip and the

sample results in a tunnel current of 0.2 nA to 10 nA. The tunneling current which is an exponential function of the width of the tunneling barrier (i.e. the tip-sample distance z), varies strongly, as shown below in equation 3.8,

$$I \propto |\varphi|^2 e^{-2k \cdot z} \tag{3.8}$$

where $|\varphi|^2$ is the probability of density of electronic states at the sample surface, and k is the wave vector. A detailed description of this technique can be found in previous works. [111, 112].

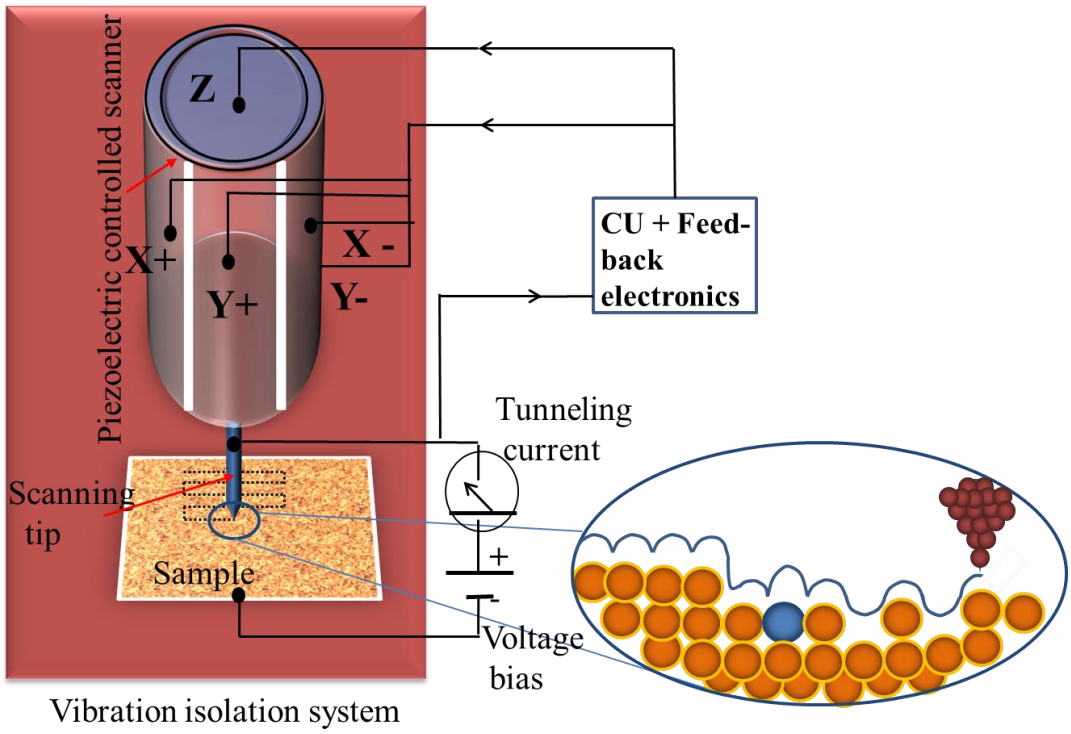

Figure 3.12: Schematic diagram of the STM includes the scanning tip, the piezoelectrically controlled scanner, the feedback electronics, the computer, and the vibration isolation system. On applying the tunneling voltage, a tunneling current flows between the sample and the tip, considering they are close enough with 0.3 nm to 1 nm. The feedback loop monitors that the tunneling current remains constant, and the piezoelectrically controlled scanner expands and contracts very slightly to control the horizontal position x, y, and the height z of the scanning tip. The computer records the tunneling currents as well as controls the voltage applied to the piezo tubes to create the 3D map of the sample surface.

The measurement of the surface features can be done by operating STM in either constant height mode or constant current mode. In our thesis, the constant current mode was used. A feedback network changes the sample-tip distance to maintain the tunneling current constant. This was

achieved by moving the tip towards or away from the sample surface, by applying a voltage to the piezoelectric driver (the scanner to which the tip is mounted). As a function of coordinate (x, y) the z displacement of the tip, given by the applied voltage to the piezo, was stored in a file. These stored files can be analyzed later by an SPM software i.e. Gwyddion or WSxM.

The STM instrument used in this study is the Micro-STM (OMICRON). Furthermore, all STM studies of this work were done at room temperature. As a small temperature variation normally affects the piezo elements, it leads to thermal drift. It requires some time for the system to be thermally equilibrated. For the first hour, a thermal drift of 25 nm/h is observed, reducing to less than 5 nm image shift in a frame of 500 x 500 nm^2, after a few hours. The hydrogen loading is performed in a pressure range from 10^{-9} mbar to 600 mbar, in the STM chamber with the mounted sample.

Some setup and measurement limitations are encountered for gas phase loading of the vanadium thin film: (1) Proper pressure control was not possible as four different pressure gauges had to be used: the ion gauge ranging from 10^{-9} to 10^{-5} mbar, two Baratron type (MKS) pressure gauges ranging from 10^{-4} to 1 mbar and 10^{-1} mbar to 1 bar, and a full range gauge ranging from 5×10^{-9} mbar to 1000 mbar (See chapter 3.2.2 for more details). (2) As the pressure was increased manually with a leak valve, precise changes in the pressure were not possible.

The vanadium thin film used in this work showed hydride formation in the pressure region of corona discharge. This issue was solved by using gas mixtures of Ar and hydrogen, as explained in chapter 3.2.2 in detail. Also, it was observed that with high hydrogen pressure, the STM normal motion (coarse sample approach) did not work.

The schematic drawing in Figure 3.13 illustrates the measurement protocol, developed for hydrogenated sample scanning by crossing the corona discharge region. Step I show the STM measurement of the sample before loading. In step II, the STM measurement has to be stopped (with one coarse step in the backward direction) and followed by shutting down the ion gauge. This is followed by a gradual hydrogen pressure increase (passing through the corona discharge region).

In the III stage, the sample stays for 30 minutes or longer (up to 2 hours) in the hydrogen gas pressure. The duration required depends on the thickness of the capping layer. IV: With fast hydrogen gas removal in the fourth stage, the corona discharge region is crossed again, and the STM is still not running. As the pressure reached $\leq10^{-5}$ mbar, the STM is started again, and with one coarse step forward, it starts measuring the sample.

Due to these aforementioned limitations, it is not possible for STM to stay in the same position before and after hydrogen loading. But, as will be shown later, in special cases some surface features exist that help to locate the previous scanning position.

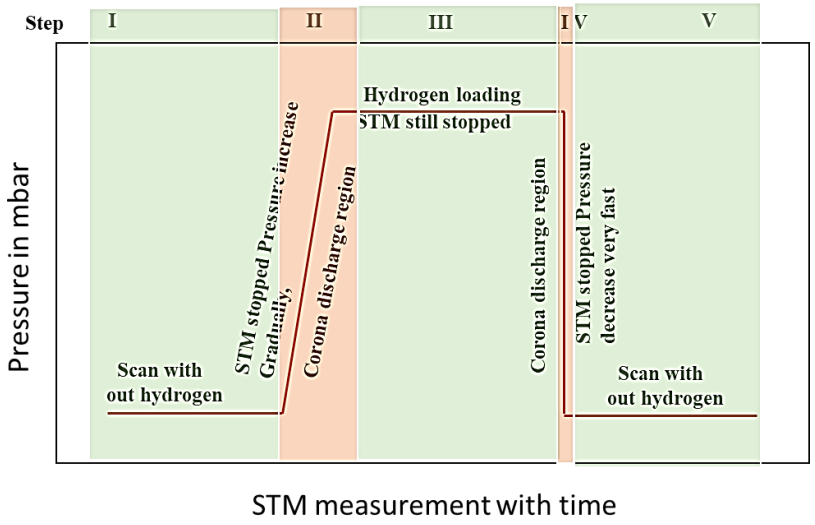

Figure 3.13: Schematic drawing presenting the measurement protocol on hydrogen loading and the corresponding STM working conditions.

To verify the reality of the surface topography changes, forward and backward scans are performed. Figure 3.14 (a) and (c) present this exemplarily for a surface with drastic surface topography with corresponding line scans (b) and (d). Two-line scans are drawn , one on a rather flat surface (blue line) and one going from high to low ground (green line). The scan on the flat surface region has the same feature existing with similar height, in the forward and backward directions. The same result is shown for the green line profile. By this kind of measurement, the true existence of features with strong height changes has been confirmed.

(a) **(b)**

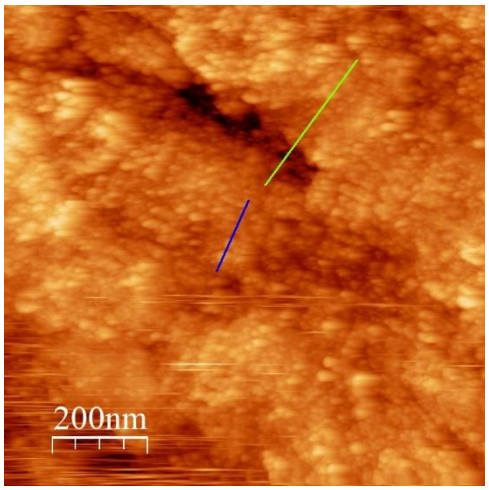

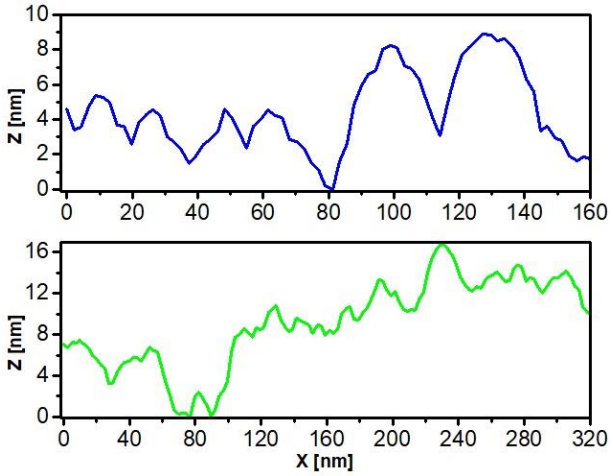

(c) **(d)**

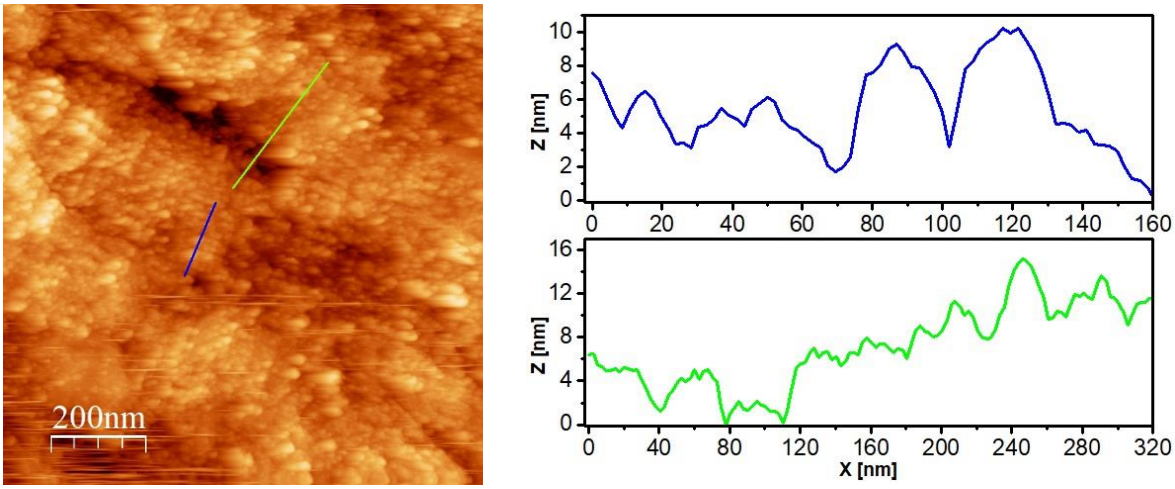

Figure 3.14: STM measurement on an 8 nm Pd/ 30 nm V// glass sample, **(a)** and **(c)** presenting the forward and backward scan done after loading with hydrogen partial pressure at p_H = 6.7×10^{-2} mbar. Line profile **(b)**, **(d)** confirm the same scale of the surface topography.

3.5.2 Atomic Force Microscopy (AFM)

Atomic force microscopy (AFM) is another kind of scanning probe microscopy. It is applicable for all material type samples for atomic scale surface information i.e. surface roughness. Detailed information about this technique can be found in Ref. [113].

Figure. 3.15 shows the schematic drawing of AFM, which represents the operating principle. In the AFM imaging mode, a flexible cantilever is usually raster-scanned over the sample surface to get a 3D image. A sharp tip (e.g. SiN) is mounted at one end of the cantilever. When this tip is brought close to the sample surface, an atomic scale force (van der Waals force) interaction between the tip and the sample surface takes place. A laser beam is focused on the reverse side of the cantilever. The reflected beam from it falls onto a position-sensitive 4-quadrant photodetector. During raster scanning of the tip on the sample surface, varying van der Waals force interaction give rise to deflections of the cantilever. As a result, the reflected laser spot position on the photodetector changes, which can be monitored and can give relative height changes of the sample topography.

There are three different imaging modes of the AFM. For this work, the tapping imaging mode is used. In the tapping mode, the force between the tip and the sample is very low with only 10^{-12} N. The cantilever is stiffer than that used in contact mode (a soft cantilever can be pulled into contact with the sample surface). The small valve of force and the greater cantilever stiffness result in a small signal detection and require a sensitive AC detection scheme. In the tapping mode, the cantilever is allowed to vibrate near its resonant frequency (typically from 100 to 400 KHz) with an amplitude of a few tens of an Angstrom (Å).

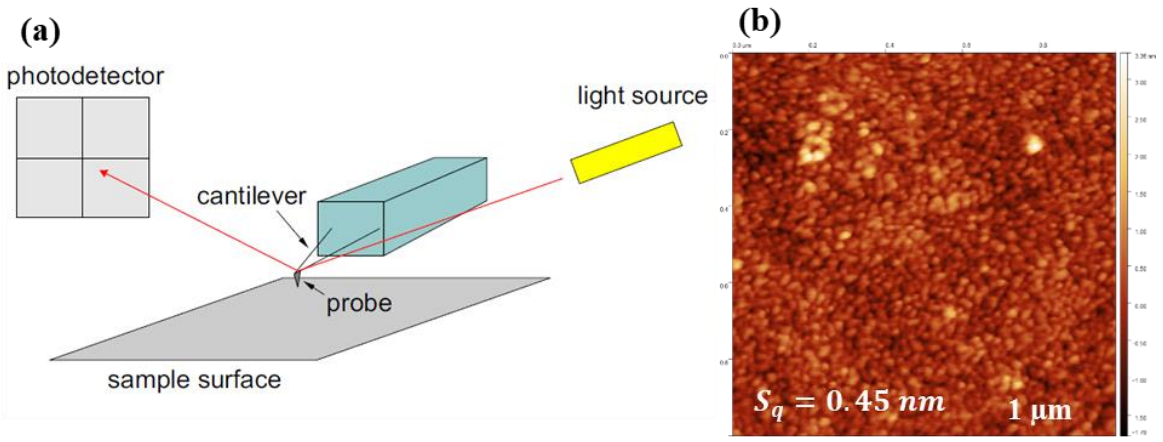

Figure 3.15: (a) Schematic drawing of an AFM setup, **(b)** AFM image (1×1 µm^2) of the vanadium film surface covered with 15 nm Pd. The rms value of the roughness (S_q) is 0.45 nm.

The sample-tip interaction results in a change in the vibration frequency or its amplitude. A monitoring system with help of a feedback system moves the scanner up or down, to keep the resonant frequency or the amplitude constant. This method does not suffer from tip or sample degradation effects that are observed after taking several scans in contact mode. The AFM used in this work is procured from Oxford Instruments Asylum Research, Inc MFP-3D^{TM} connected to the SPM controller ARC2^{TM} from Oxford Instruments. An AFM probe of type AC160TS (from Oxford Instruments) is used with a tip radius of 7 to 8 nm.

3.6 XRD and XRR measurement

In this work, XRD and XRR were used to study the V film microstructure, the film thickness, and the surface (or interface) roughness. These measurements were done using the Bruker Discovery D8 diffractometer equipped with a Cu ($\lambda_{K\alpha}$=1.54 Å) source. Details on XRD and XRR theory can be found in the book Ref. [114].

3.6.1 X-ray Diffraction

The crystal structure of the thin film can be identified by XRD studies, using Bragg's law [114],

$$2d_{hkl}sin\theta_{hkl} = n\lambda \tag{3.9}$$

where $d_{hkl}$is the interplanar distance between (h,k,l) planes in the normal direction, θ_{hkl} is the Bragg angle of reflection, n is a positive integer called diffraction order and λ is the wavelength of the incident beam. All parameters are shown schematically in Figure 3.16. The diagram shows that

waves 1 and 2 are scattered from atoms A and B of a crystal having the interplanar distance d. The diffracted beam interferes constructively if the path difference of the beams (2dsinθ) is equal to a positive integer n, for the wavelength λ. The constructive interference results in interference maxima measured by the detector as a peak, which is plotted in the θ-2θ scan. Figure 3.17 presents the nanocrystalline V film XRD pattern, consist of broad peak of (110).

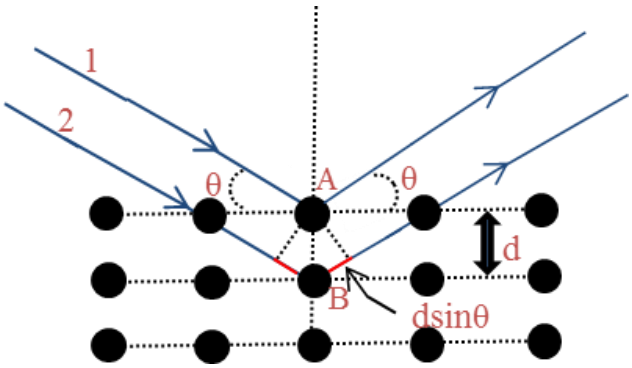

Figure 3.16: Schematic drawing representing Bragg's equation, indicating the parameters such as lattice plane distance d, path difference 2dsinθ, Bragg's angle θ, and beams, represented by lines 1 and 2, having a wavelength λ.

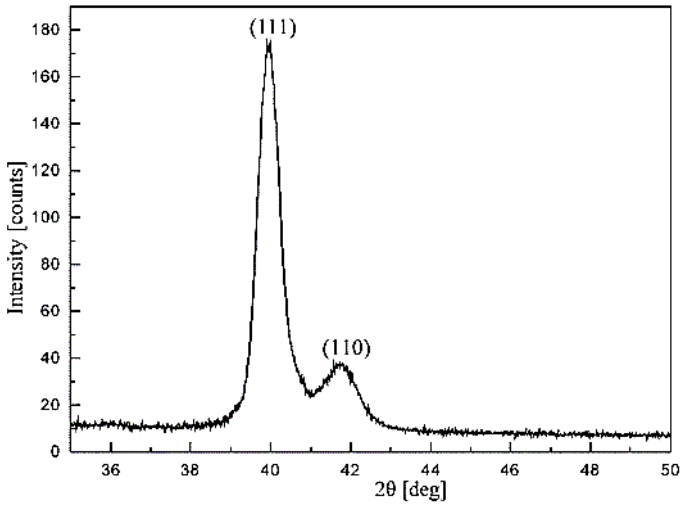

Figure 3.17: X-ray diffraction pattern of the V film deposited on glass at RT. The peaks are assigned to the (110) vanadium and the (111) palladium lattice reflection. No other lattice reflections are obtained, thus justifying the fiber textures of the films.

To get information on the domain size (normal to surface) one can use the Debye-Scherrer formula, by fitting the shape of the peak and calculating the full width at half maximum (FWHM), as [114].

$$t = \frac{K \cdot \lambda}{B \cdot cos\theta_{B}} \tag{3.10}$$

where K denotes the shape factor with a value of 0.9 or 1 depending on the shape of the crystallites in the sample; λ is the wavelength; θ is the Bragg angle; B is the FWHM; and t is domain size. This formula is applicable to very small crystalline grains only and not applicable to grain sizes above 0.1 μm [114].

3.6.2 X-ray Reflectometry (XRR)

X-ray Reflectometry is performed to study film thickness, surface roughness, and interface roughness in film stacks and to deduce oxide layers or some additional interface layers (alloying regions) between the film and the substrate. In XRR, the interference of the electromagnetic wave takes place not only at the surface but also between the different layers. The X-rays are completely reflected below a critical angle θ_{cr}, and normal reflection occurs above it. The value of the critical angle depends on the density of the material and the wavelength used, and the reflectivity is also related to the refractive index of the material. For X-rays, reflection for most materials has refractive indexes of less than 1. More details about the XRR method are available in Ref. [115]**.**

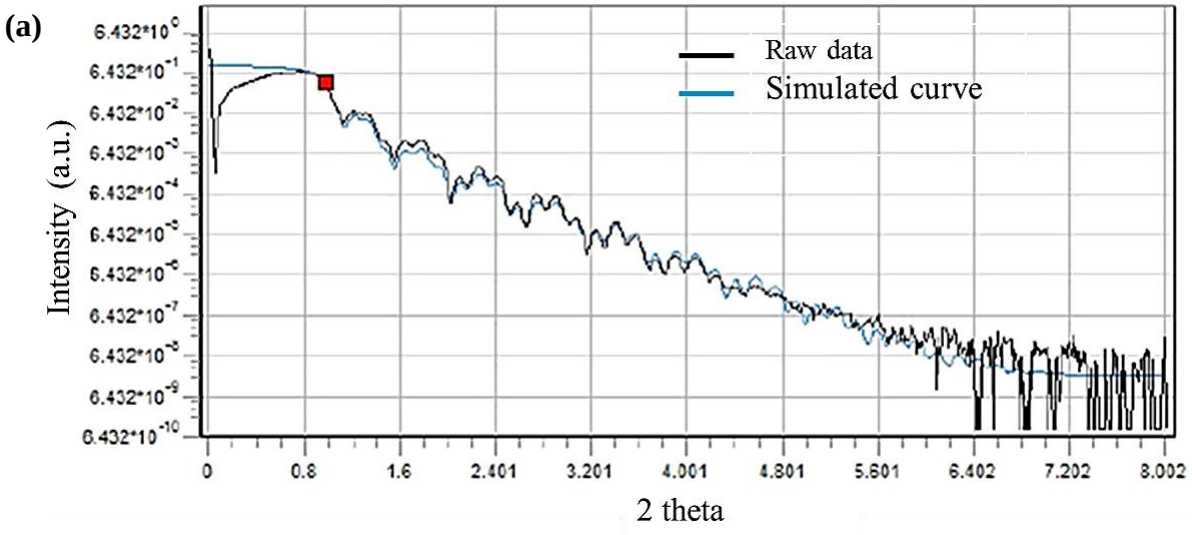

(b)

Simulated Parameter			
Material	**Thickness (nm)**	**Roughness (nm)**	**Density(g/cm^3)**
PdO	1.42	0.16	8.3
Pd	14.53	0.59	12.01
V	37.27	0.70	6.11
SiO_2	0.0	0.59	2.65

Figure 3.18: (a) Representation of XRR measurement of a sample (black curve) Pd(14.5nm)/V(37.2nm) on the glass substrate. Superimposed is the simulated curve (blue curve). **(b)** Table of parameters calculated by simulation.

The film thickness was checked for exemplary films. The thickness deduced from XRR was also used to calibrate the sputter rate. This rate was used to calculate the deposition rate to obtain films of desired thicknesses. Figure 3.18 (a) exemplarily shows an XRR pattern of a 37 nm V film capped with 14.5 nm Pd (black curve) and the fitted simulation curve (blue curve). The match quite well.

Figure 3.18 (b) presents a table of parameters calculated by the LAPTOS software 7.7, by fitting a simulated curve to the measured graph provided by Bruker Company [116]. A Pd-oxide layer has to be added to the simulated curve. It adds up to the effect of the interaction of the atmosphere with the sample surface.

XRR roughness is measured over a large area of mm^2 while for AFM, roughness is measured over a small area in the µm^2 range. XRR has the advantage of being a non-destructive and non-contact mode technique that can measure 2 nm to 200 nm thick film with an accuracy of 0.1-0.2 nm. This method also has its limitation. It bases on the grazing angle reflection of X-rays and, thus, XRR can be measured up to $2\theta = 10^o$. The measurement end of $2\theta = 8^o$ is shown in Figure 3.18 (a). Additionally, the absorption of X-rays in the material also limits the achievable film stack thickness.

Chapter 4

Result and Individual Experiment discussion

4.1 Optical Transmission and Reflection

This chapter represents the optical *in-situ* results of hydrogen loading on vanadium films. Measurements have been performed on different film thicknesses of 30 nm, 50 nm and 70 nm, but the results presented here focus on the 30 nm films. To modify the adhesion between the vanadium films and the substrates, the vanadium films were grown on different interface layers (interlayer) name as no-interlayer, Pd-interlayer, or PC-interlayer. To locally modify the adhesion Pd, and PC were also deposited in the shape of a dots pattern (mixed adhesion). The thickness of the Pd-interlayer varied between 5 nm and 7 nm to check for any thickness dependency. At the start, optical transmission studies upon hydrogen loading on a pure Pd film of 30 nm thickness are presented (the latter in collaboration with Dr. S. Wagner). This study serves as background information, as a Pd film is present in all samples at least as a capping layer. Its optical change can be neglected for chemical potentials below 120 mV because, for Pd, buckle phase transition potential is above it [117].

The following chapter subgroups the results of the optical microscopy images (hydrogenography, see chapter 3.3) in, transmission and reflection as well as the pixel intensity diagram as a function of the hydrogen concentration. Finally, corresponding EMF and stress measurements are also shown at the end of the current chapter.

4.1.1 Pd(30nm)//sapphire

During electrochemical loading (ECL), transmission and reflection images of the samples are recorded, to observe optical changes and to correlate them with phase transitions induced by ECL.

Figure 4.1.1.1 shows the selected transmission images of a Pd 30 nm thin film grown on a sapphire substrate {of (11-20) orientation} with c_H or H/Pd, from c_H = 0.0 H/Pd to c_H = 0.99 H/Pd. Images in reflection mode are not shown here.

Homogeneously bright **transmission images** are measured for the initial Pd-film and low hydrogen contents, as exemplarily shown in Figure 4.1.1.1. The hydrogen contents ranging from 0.00 H/Pd to 1 H/Pd, are shown in the upper part of the images. The first sign of hydride precipitation is observed at c_H = 0.12 H/Pd. In the case of Pd, hydrides are visible as lighter regions in the images [108]. These hydride precipitates are more visible at c_H = 0.16 H/Pd and higher concentrations. With higher concentrations, more small precipitates emerge while others grow, see Figure 4.1.1.1 second row. Above a concentration of c_H = 0.49 H/Pd hydride phase growth dominates within the

frame. At the concentration of c_H = 0.79 H/Pd the whole frame area is covered by the hydride phase. In the center of the hydride regions, appear a dark spot from which dark lines are running radially toward the boundary of the hydride region. They look like dendrites. The spot in the center appears dark; it is the onset of film buckling at around c_H = 0.44 H/Pd. This can be observed more clearly for the images of higher concentration loaded samples.

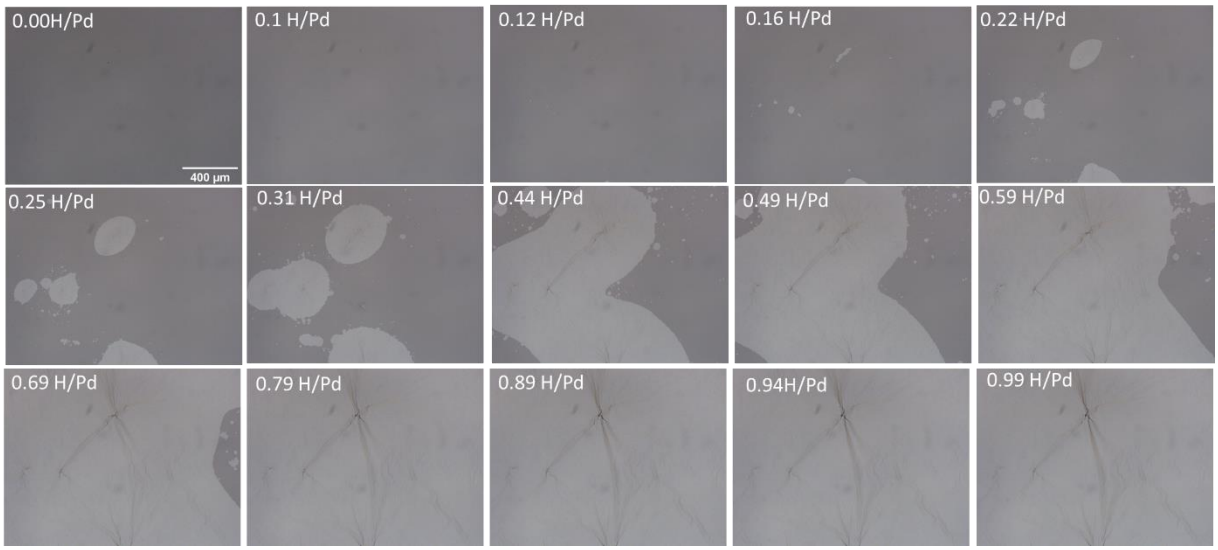

Figure 4.1.1.1: Selection of transmission images of a Pd 30 nm film on a sapphire substrate with 50 × magnification, loaded with different hydrogen concentrations c_H. The c_H is given in the upper left corner of each image. Hydride-containing film regions appear in light grey.

Pixel intensity diagrams are deduced from each transmission image by plotting the number of pixels measured with a certain intensity i_t against the pixel intensity i_t. As shown by the graph in Figure 4.1.1.2, the initial Pd film c_H = 0 H/Pd, shows a peak with a maximum value of i_t= 124. Hydrogen concentration increase leads to a shift of the highest peak intensity toward higher values, starting at i_t= 124 at c_H = 0 H/Pd and ending at i_t= 155 for c_H = 0,99 H/Pd. In Figure 4.1.1.2, the intensity distribution moves toward the right side of the intensity scale. The peak shifts non-linearly with c_H and becomes broader. On top of this, at a concentration of c_H = 0.16 H/Pd, a second peak appears at higher intensity. This peak continues to grow while the first peak shrinks. This can be related to the hydride phase nucleation and α-phase disappearance, according to the lever rule in the two-phase region of the Pd-H system (see chapter 2 and [118]). At c_H = 0.79 H/Pd only one peak remains. Alternative measurements of Jara Kürschner give c_H = 0.62 H/Pd, for hydrogen loaded 30 nm Pd films on Si [108]. This suggests a little hydrogen loss, in our measurement. However, it also means that the hydride phase formation is completed. Further hydrogen loading slightly shifts this peak to higher intensity, to the right. The distribution slightly changes its shape, in this high-concentration regime. As already mentioned, this high-concentration regime is not relevant for the following data interpretations.

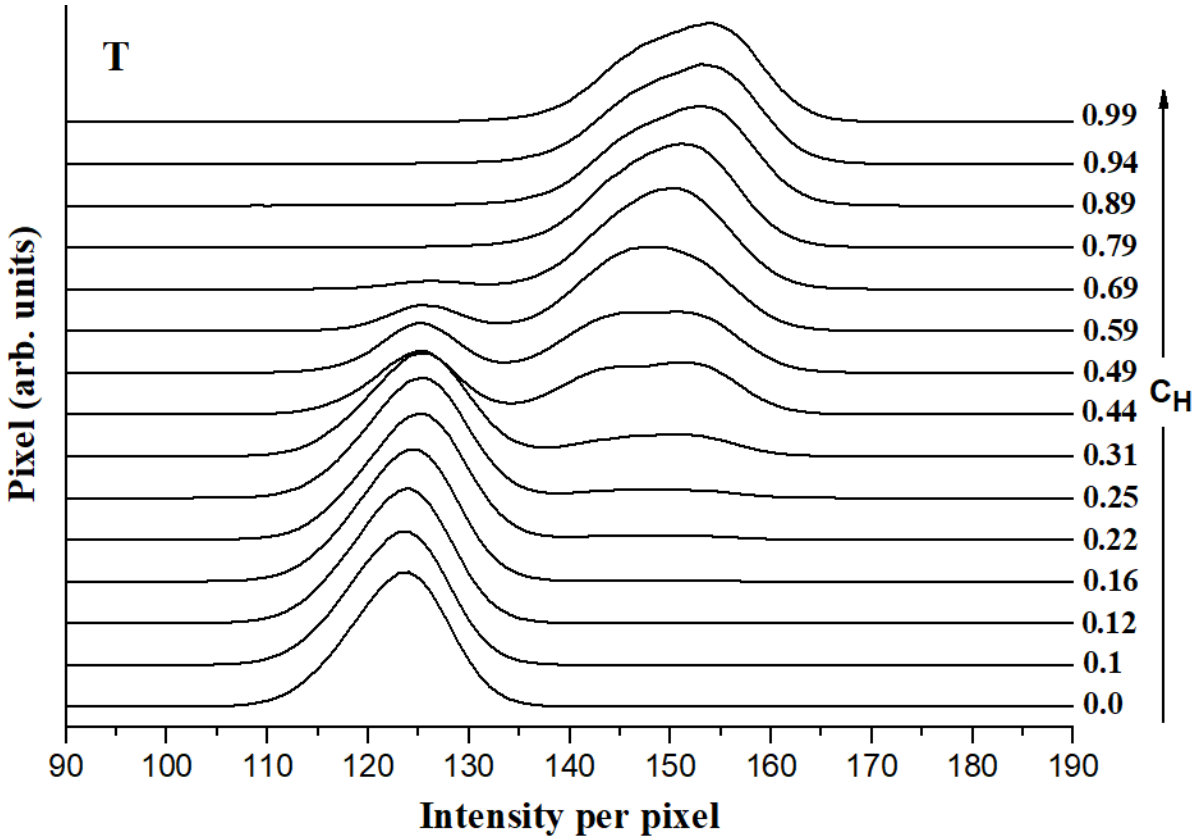

Figure 4.1.1.2: Transmission pixel intensity diagrams deduced from the transmission images of the hydrogen loaded 30 nm Pd film grown on sapphire substrate, Figure 4.1.1.1, with 50× magnification.

4.1.2 Pd(15nm)/V(30nm)//glass

Figure 4.1.2.1(a) shows the reflection images of the Pd(15nm)/V(30nm)//glass substrate upon hydrogen loading. The hydrogen concentration c_H is given in each figure in H/V. As discussed in chapter 3, reflection images inform about buckle formation. All images in Figure 4.1.2.1(a) show a film without buckles from $c_H = 0$ H/V up to $c_H = 1$ H/V. Only a few concentrations are seen in the figure chosen from a large number of measurements, presenting the initial to final sample state. The slight lateral lines result from scratches on the surface of the samples and do not originate from the expected film detachment from the flat part of the substrate. Scratch lines can be seen get darker with increasing c_H. Overall, the whole film stays adhered to the substrate.

The corresponding optical **transmission images** are shown in Figure. 4.1.2.1(b). The images of the sample get noticeably darker upon hydrogen loading. This indicates the increase in the hydrogen content in the V-film. The dot in the middle relates to a hydrogen gas bubble that was formed on a morphological defect in the film. This was visible in the real images during the measurement.

There is no conspicuous sign of isolated hydride precipitates (which would appear locally darker for vanadium) at this magnification of 100× or higher, for this kind of sample with strong adhesion to the substrate. EMF measurements (see Figure 4.2.2) done simultaneously confirm a phase transformation by a plateau-like region and, thus, hydride formation for this sample. Thus, hydrides have to be very small and beyond the light microscope resolution of detection.

The related frequency distribution of the transmission intensity is shown in Figure 4.1.2.2. **Transmission pixel intensity diagrams** more clearly visualize hydrogen concentration changes by optical modifications (see chapter 3).

(a)

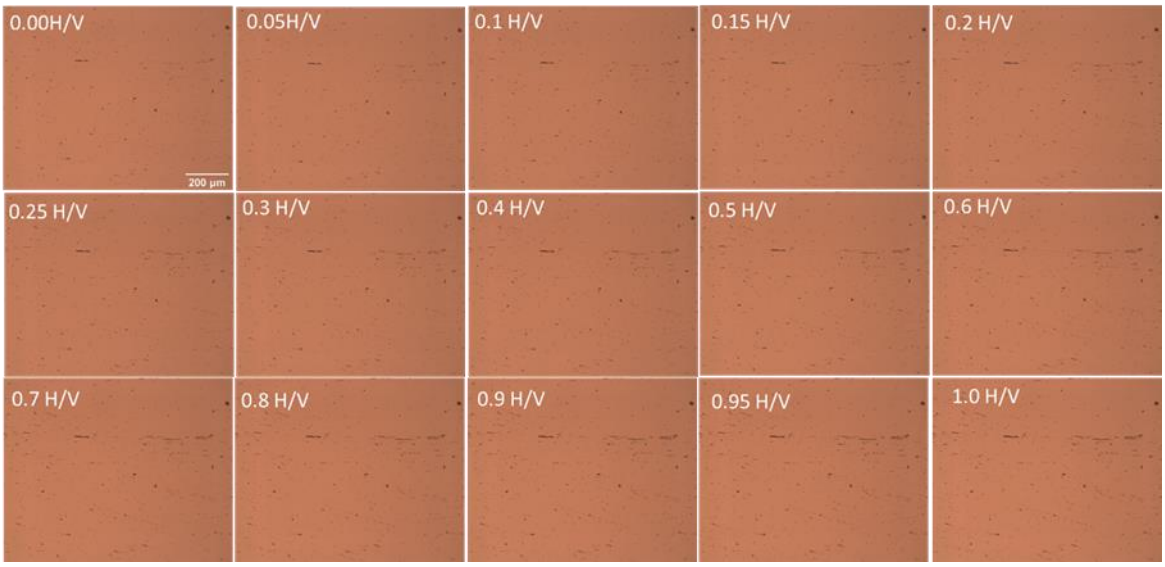

(b)

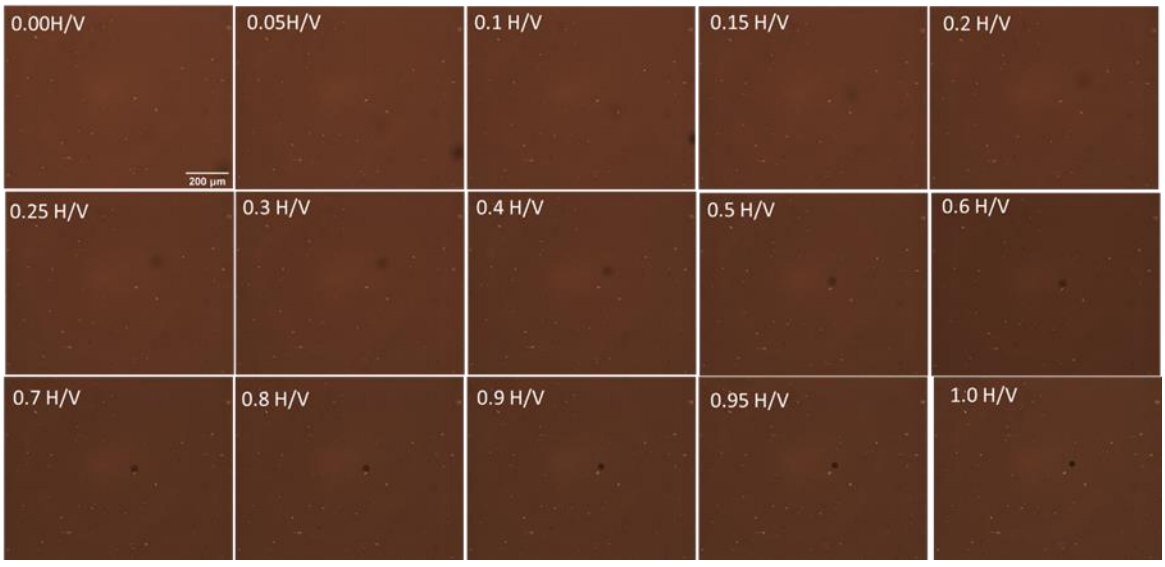

Figure 4.1.2.1: Optical measurements on Pd(15nm)/V(30nm)//glass film in **(a)** Reflection mode and **(b)** Transmission mode, both with 100× magnification. The images were subsequently taken at the same concentration's steps, first in reflection and then in transmission.

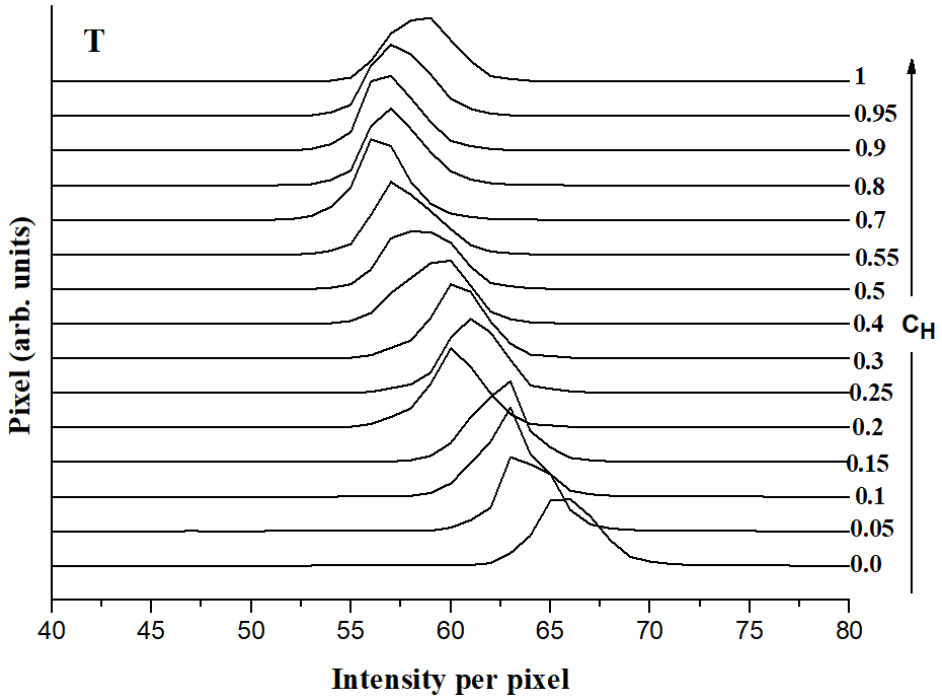

Figure 4.1.2.2: Transmission pixel intensity diagrams of the Pd(15nm)/V(30nm)//glass film, transmission images taken with 100× magnification

Figure 4.1.2.2 shows the transmission pixel intensity diagrams obtained on selected non-linearly increasing loading steps. At $c_H = 0$ H/V a broad peak is detected at about $i_t = 66$. Upon hydrogen loading the peak shifts to a lower intensity. Between $c_H = 0.15$ H/V and $c_H = 0.7$ H/V, the peak shifts strongly towards lower intensity. From $c_H = 0.8$ H/V to $c_H = 0.95$ H/V it then remains at a constant position and gets broader. The step size of the hydrogen loading was increased from $c_H = 0.01$ H/V (for $c_H < 0.3$ H/V) to $c_H = 0.02$ H/V (for $c_H \geq 0.3$ H/V till $c_H \geq 0.5$) and after this from $c_H \geq 0.5$ to $c_H = 1$ H/V step size $c_H = 0.05$ H/V, see appendix A.1. The intensity changes upon hydrogen loading opposes to that of the Pd film, where the peak shifts towards higher intensity, as shown in section 4.1.1.1.

When loading is done for the V sample, the optical effect of hydrogen loading of the Pd film can be slightly observed at high concentrations. At $c_H = 1$ H/V the peak shifts to the right, showing a total intensity increase. This can be interpreted by the higher transparency of the H-loaded Pd film, upon hydrogen uptake.

It is noted briefly that the transmission spectrum at c_H = 0.6 H/V is replaced with that at c_H = 0.55 H/V (see appendix A.1), on account of an unexpected jump in the whole image brightness. This effect is related to an external factor.

Phase separation in the V-H film is not detectable from the hydrogenography transmission pixel intensity diagrams. For this information, the simultaneously taken EMF curve (see Figure 4.2.2) gives details. By using linear fitting for the EMF curve [119] (shown later in Figure 4.2.2), phase boundaries for solid solution and hydride phase are deduced at c_H = 0.08 H/V and c_H = 0.48 H/V, respectively.

4.1.3 Pd(15nm)/V(30 nm)/Pd(7nm) layer//glass

The adhesion between the V film and the substrate can be changed by adding an interface layer: for this measurement, a 7 nm Pd layer is grown on the glass substrate. Figure 4.1.3.1 (a) shows the **optical reflection images** of Pd(15nm)/V(30 nm)/Pd(7nm) layer//glass film.

Only the images for a few chosen concentrations from a bigger measurement concentration range are shown here. For c_H = 0.0 H/V the image shows the as-deposited film which has some surface features in the shape of small circles. Above a concentration of c_H = 0.4 H/V, small dark spots start to grow at the right corner of the image. This suggests local film detachment, as a concentration increase is not visible by such a strong change in the reflected brightness (see Figure 4.1.2.1 (a)). At a concentration of c_H = 0.42 H/V many small, detached regions start to appear see Figure 4.1.3.1 (a). The number of such regions increases up to c_H= 0.7 H/V. At this concentration, the existing regions start to grow. The very rapid growth of the dark regions appears at c_H= 0.8 H/V and till c_H= 0.95 H/V. It appears that the whole regarded region of the film has changed. From the folded appearance of the film, it can be concluded that the dark film regions relate to film regions that are detached from the substrate.

Figure 4.1.3.1 (b) displays **the transmission images** of the same sample, at low hydrogen concentrations which do not show any buckle-related change. As already described for Pd(15nm)/V(30nm)//glass in chapter part 4.1.2, hydrogen loading results in overall image darkening. Only above c_H= 0.7 H/V (at c_H= 0.8 H/V few of such images are shown by red circles) buckle growth can be observed in the transmission images, Figure 4.1.3.1 (b). Above c_H= 0.9 H/V, the film buckling resulting in folds also appears in the transmission image. However, the buckle visibility is very small, in the transmission images.

(a)

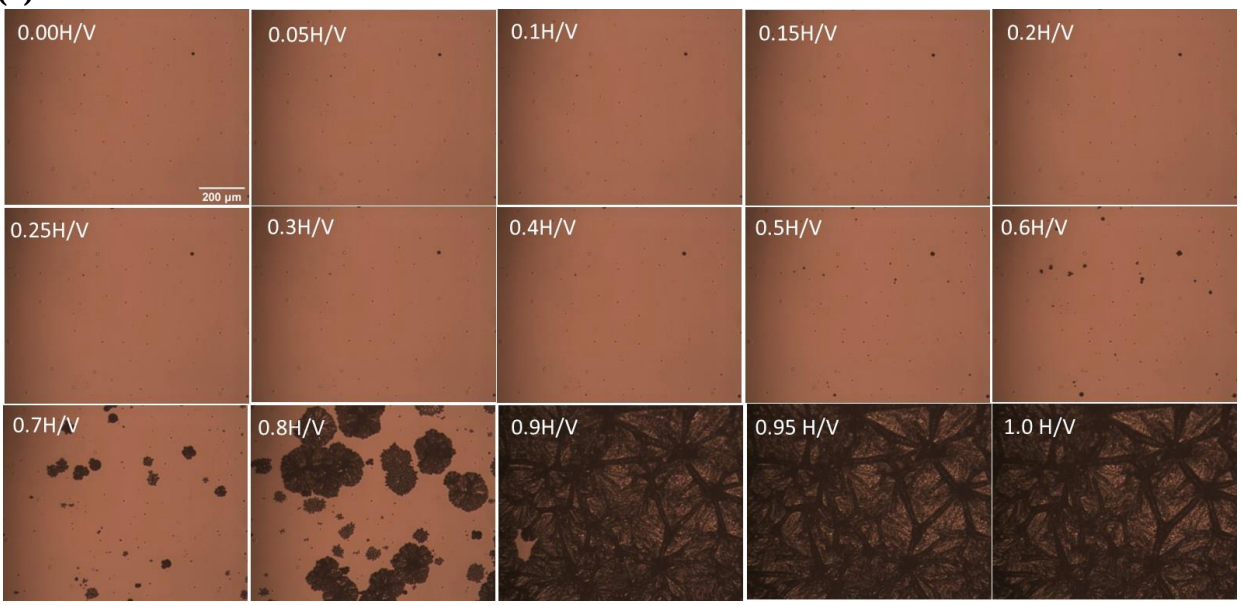

(b)

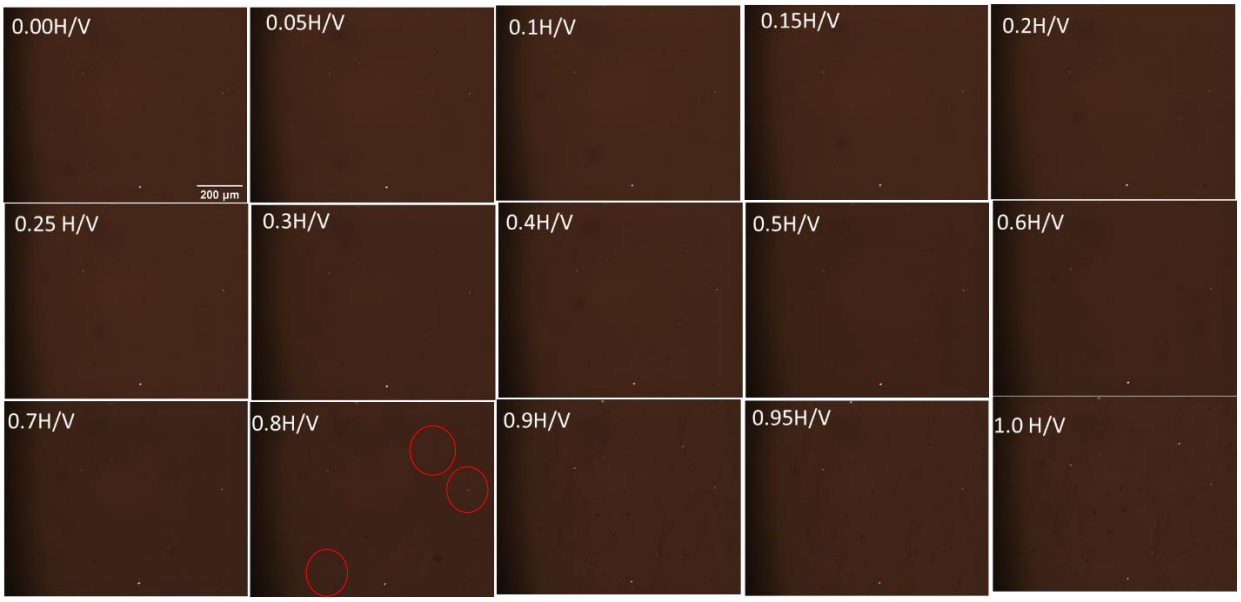

Figure 4.1.3.1: Optical measurement of Pd(15nm)/V(30 nm)/Pd(7nm) layer//glass film in **(a)** reflection mode and **(b)** transmission mode, both with 100× magnification. Both observation modes are taken at the same concentration's steps, first in reflection and then in transmission.

Transmission pixel intensity diagrams are deduced from each transmission image (Figure 4.1.3.2). The increase in concentration leads to an increase in the width of the peak while the peak

position remains fixed at i_t= 44 from c_H = 0 H/V to i_t= 44 for c_H = 0.2 H/V. Above a concentration of c_H = 0.25 H/V, the peak position at i_t= 43 (the highest peak intensity) starts to move toward lower values and continues to do so, until c_H = 0.8 H/V, i_t= 39. The intensity distribution moves towards the left side of the intensity scale for concentrations from c_H = 0.25 H/V till c_H = 0.8 H/V. As shown in Figure. 4.1.3.1, the buckle growth happens very rapidly between c_H = 0.8 H/V to c_H = 0.9 H/V. At this concentration, the peak shift in Figure. 4.1.3.2 starts to move toward the right side, from i_t= 39 to i_t= 41, respectively. As the buckle growth in the frame of Figure 4.1.3.1 is completed at a concentration c_H = 0.95 H/V, the peak position remains locked at i_t= 41 for c_H = 0.9 H/V and c_H = 0.95 H/V. The only remaining difference is a peak broadening at a concentration c_H = 0.95 H/V. For the fully loaded film at c_H = 1 H/V, the peak shifts to the right i_t= 42. This indicates the H-loading of the Pd film, which gets more transparent upon hydrogen absorption. This effect also contributes at high concentrations.

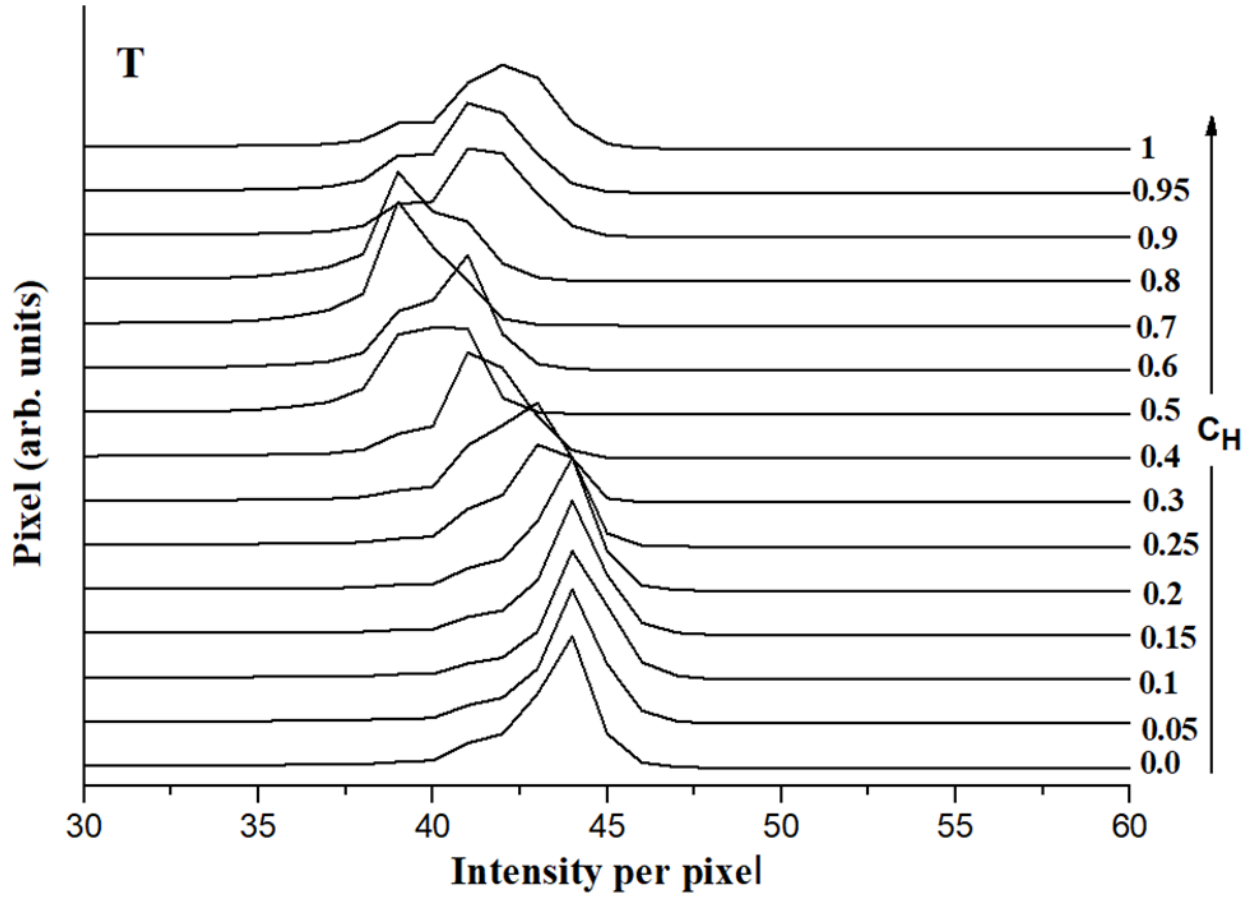

Figure 4.1.3.2: Transmission pixel intensity diagrams of the Pd(15nm)/V(30 nm)/Pd(7nm) layer//glass film, transmission images taken with 100× magnification.

The stable peak position in Figure 4.1.3.2 during the first loading steps up to a concentration of c_H =0.2 H/V is remarkable. It cannot be accounted for the α-phase low H-solubility, solely. It is hypothesized here that the change in the missing intensity results from the large intrinsic stress in

the V-sample. The EMF shows a solid solution phase boundary at c_H =0.09 H/V (while the hydride phase boundary is deduced to be at c_H = 0.38 H/V), see Figure 4.2.3. Different intrinsic stress may result from the 7 nm Pd film which strongly binds the Pd/V/Pd-film package to the substrate. Comparison of the first and second loading EMF-curve shows a shift of the curve by about -0.03 V with respect to the second loading EMF, see image A.2 in the appendix. This may result from strong intrinsic compressive mechanical stress in the V-film, prior to the first loading. During the first hydrogen loading, stress release may result in a different stress condition for the second loading. Other samples show a similar effect but on a smaller scale.

From c_H = 0.2 H/V to c_H = 0.8 H/V, the optical transmission peak starts to shift to a lower-intensity with each hydrogen loading step. Till c_H = 0.6 H/V no strong buckling is observed, but for c_H = 0.7 H/V and c_H = 0.8 H/V, there is a clear sign of buckling. Nevertheless, the transmission pixel intensity behaves similar to that in absence of buckling. In the almost buckled situation, from c_H = 0.9 H/V to c_H = 1H/V, the transmission pixel intensity behavior changes, and the peak shifts to a higher value. From the EMF curve, (shown later in this chapter Figure 4.2.3) an effect of hydrogen absorption in the Pd cap layer is expected for the last two concentrations. In presence of the 7 nm Pd interlayer, something happens that pins the peak position for low concentrations. The effect of hydrogen loading on the peak shift only appears at higher concentrations. Also, the presence of the 7 nm Pd interlayer leads to buckling with hydrogen concentration increase. Nucleation and rapid buckle growth appear in the hydride phase and result in complete film buckling.

4.1.4 Pd(15nm)/V(30 nm)/Pd(5nm) layer//glass

The interface layer thickness is reduced here to 5 nm of Pd. This is not expected to differ in V-film adhesion with respect to the 7 nm Pd interlayer if the Pd-layer is closed. However, it can differ if the interlayer consists of Pd-islands.

The **optical reflection images** of the Pd(15nm)/V(30 nm)/Pd(5nm) layer//glass film are shown in Figure 4.1.4.1 (a). The reflection image in Figure 4.1.4.1 (a) at c_H = 0.0 H/V shows the as-deposited state of the film with small amount of initial surface topography. Upon hydrogen loading, these uneven topographies provide nucleation centers. In the two-phase region at about c_H = 0.3 H/V, the small centers get darker and darker with an increase in both concentration and number till c_H = 0.65 H/V. Above a concentration of c_H = 0.65 H/V, the hydride phase appears to grow up to c_H = 1 H/V. At c_H = 1 H/V, buckled regions are not as pronounced as in the case of the 7 nm Pd interlayer.

(a)

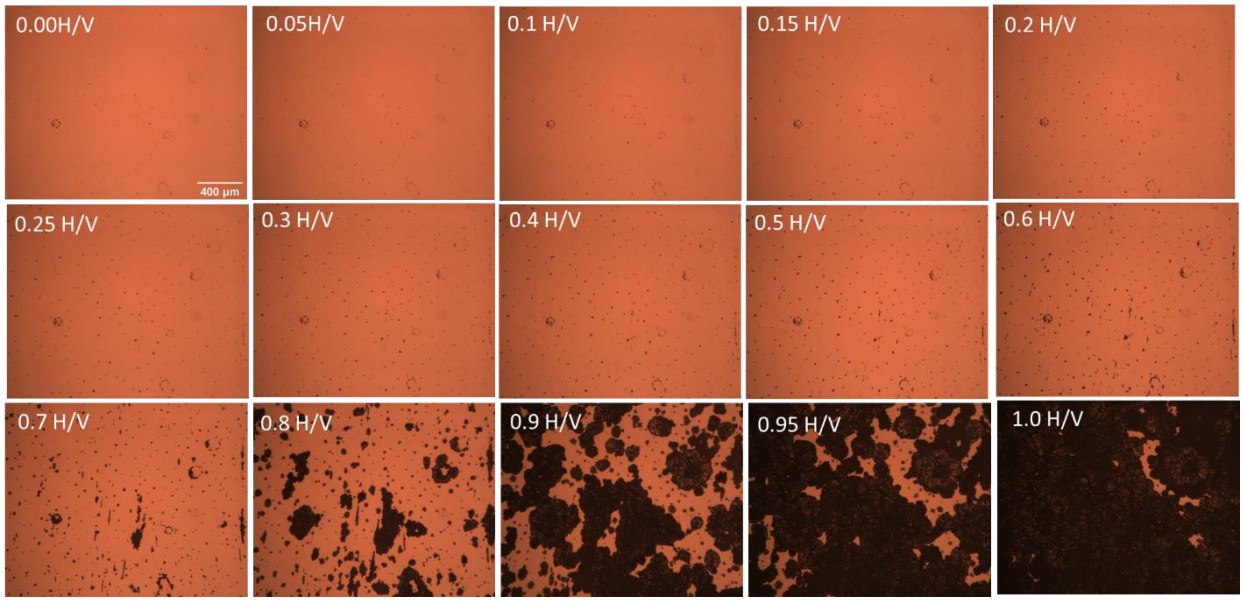

(b)

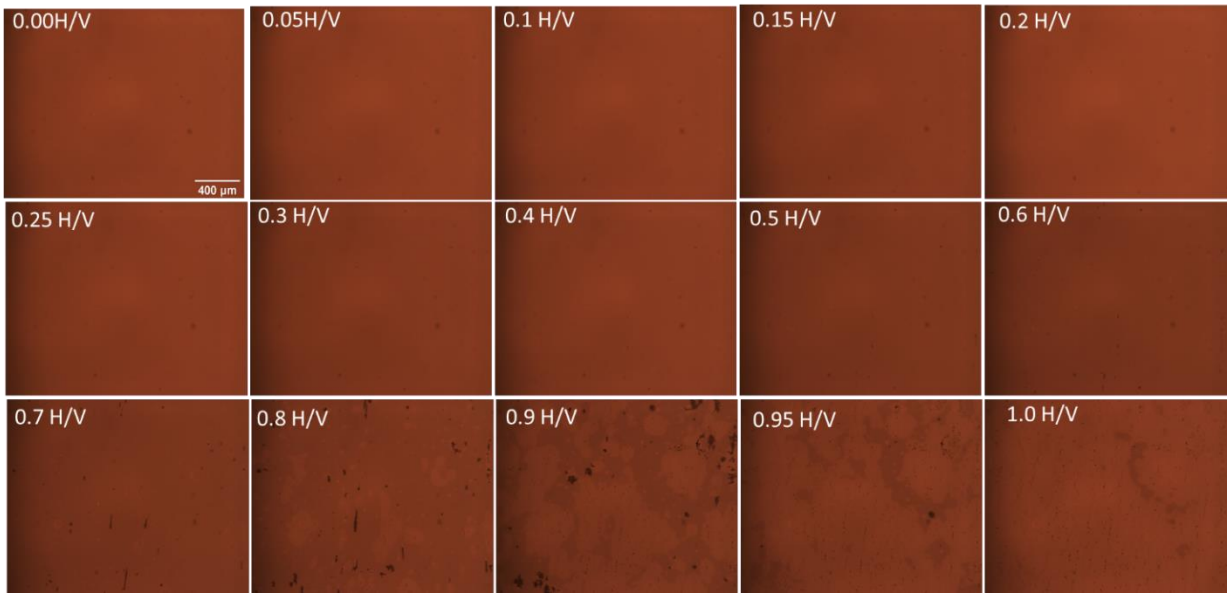

Figure 4.1.4.1 Optical measurements on Pd(15nm)/V(30 nm)/Pd(5nm) layer//glass film in **(a)** Reflection mode and **(b)** Transmission mode, both with 50× magnification the images were taken at the same concentration's steps, first in reflection and then in transmission.

Transmission images during hydrogen loading of the Pd(15nm)/V(30 nm)/Pd(5nm) layer//glass film are presented in Figure 4.1.4.1 (b). Starting from concentration $c_H = 0$ H/V to $c_H = 0.6$ H/V the film gets darker. Above that, from $c_H = 0.7$ H/V to $c_H = 1$ H/V, this sample shows buckle nucleation and growth. It results in most of the area under observation in film buckling. The information from these images is converted into the respective **transmission intensity diagrams**, as depicted in Figure 4.1.4.2. Compared to the reflection images, the transmission images appear smoother, the

transmission pixel intensity diagrams reveal the effect of the surface inhomogeneities by having two peaks, the smaller and the darker peak (at lower intensity) must be the contribution of these dark spots on the film surface. From the as-deposited state at $c_H = 0$ H/V to the first loading step at $c_H = 0.05$ H/V, the transmission intensities move to slightly higher intensity (to the right side), Figure 4.1.4.2, shows the peak at, $i_t = 79$ and $i_t = 81$, respectively. Peak shift at $c_H = 0.05$ H/V and $c_H = 0.15$ H/V toward high value are unaccounted for. The peaks jump to $i_t = 77$ for $c_H = 0.19$ H/V. After this shift again the whole spectrum moves towards the lower intensity of $i_t = 68$ at $c_H = 0.7$ H/V. Transmission images Figure 4.1.4.1 (b) also show the growth of the buckles, at $c_H = 0.65$ H/V, by slight intensity changes. Above $c_H = 0.9$ H/V the whole spectrum moves towards higher intensity.

This is due to the effect of the Pd loading and Pd-hydride formation at higher concentrations. EMF shows, see Figure 4.2.4 that the last four concentrations can have an effect due to hydrogen absorption in Pd. The two peaks now merge to almost one broad peak, as shown in Figure 4.1.4.2 $c_H = 0.9$ H/V, $c_H = 0.95$ H/V, and $c_H = 1$ H/V. The match between the positions of the buckles visible in Figure 4.1.4.1 (a) and the brighter regions in Figure 4.1.4.1 (b) suggest hydride formation in the Pd-cap layer in the buckled regions. Thus, the merging and broadening of the peak in Figure 4.1.4.2 at 0.9 H/V and 1.0 H/V may be attributed to the local detachment of the underlying V-film.

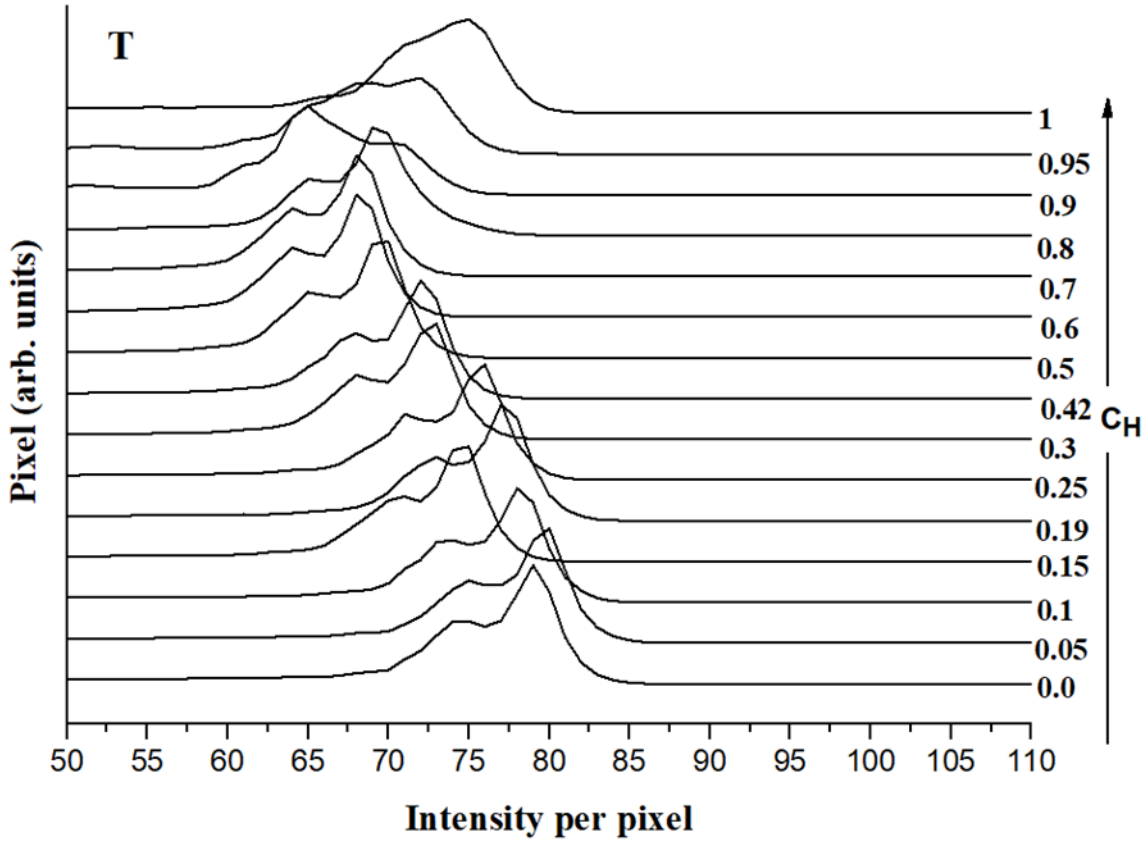

Figure 4.1.4.2: Transmission intensity diagrams of the Pd(15nm)/V(30 nm)/Pd(5nm) layer//glass film, transmission images taken with 50× magnification.

This film with 5 nm of Pd interlayer is in general behaving like the no-interlayer V-film, for low concentrations. Hydrogen loading is changing the transmission and the peak shifts towards lower intensity gradually from c_H = 0.19 H/V till c_H = 0.7 H/V. With high hydrogen concentration, this sample starts to form buckles that grow with each hydrogen charging step and result in film buckling. This film at c_H = 1 H/V is still not fully buckled.

4.1.5 Mixed adhesion samples with Pd dots

To look further into the detail of how an interface layer modifies the hydride phase formation of a V-film, a pattern of circles of the interface layer is grown, as shown in Figure 4.1.5. Further, Figure 4.1.5 (a) shows the mask (with a hole size of 1 mm) that was used to create the pattern, and Figure 4.1.5 (b) shows the interface layer pattern after deposition on the substrate by using the mask. The interface layer circle size is about 1.4 mm which is slightly larger than the hole size of the mask. Figure 4.1.5 (c) represents the as-deposited state of the vanadium film with the Pd cap layer. The interface layer pattern is not visible anymore and the film surface appears uniform. Figure 4.1.5 (d) shows the state of the film in a fully hydrogen-loaded condition after taking it out from the electrochemical loading cell. The interface pattern is now visible again due to buckling. This will be addressed in the following.

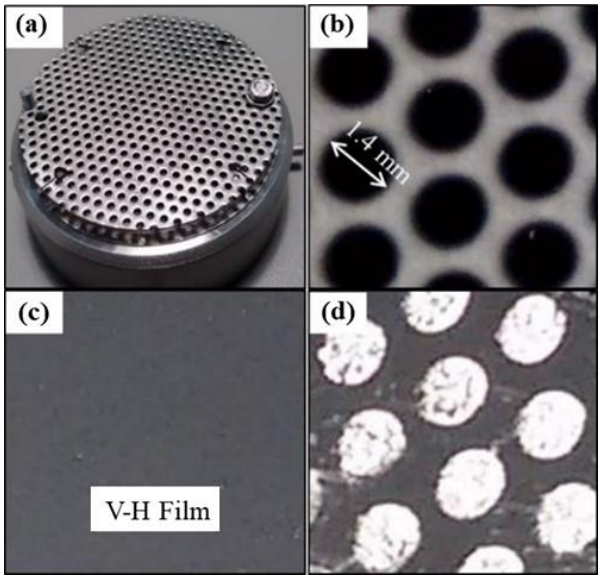

Figure 4.1.5: Interface layer pattern and film deposition of Pd_{15}/V_{30}/ Pd-p or /PC-p//glass. **(a)** The mask with a hole size of 1 mm was used during the laser deposition or sputtering process, **(b)** the as-deposited pattern of 1.4 mm on the glass substrate, **(c)** after subsequent Pd/V film deposition, patterns were invisible after film deposition and **(d)** the sample after electrochemical loading.

Figure 4.1.5.1 (a) shows the **optical reflection images** of the Pd(15nm)/V(30 nm)/Pd(5nm) dots//glass film for different hydrogen concentrations. As shown above, the film deposition process generally leads to a very smooth film surface. This is shown in Figure 4.1.5.1 (a), for 50× magnification surface of the Pd(15nm)/V(30 nm)/Pd(5nm) dots//glass film which is free from unwanted surface defects. Close inspection shows no sign of the Pd dot morphology but slightly higher reflectivity (more brightness) in the areas of the Pd dots. With the hydrogen loading, the film appears to be unchanged in reflection mode imaging up to a concentration of $c_H = 0.125$ H/V. Above this concentration, small dark spots appear. This finding suggests localized buckling. The relevant area is highlighted by the red circle in Figure 4.1.5.1 (a). The growth of the dark spots continues up to $c_H = 0.7$ H/V. At this concentration, film buckling at the positions of the Pd dots appears to be completed, as can be seen in, the slow growth of the buckle front after $c_H = 0.7$ H/V. Further loading of the film makes the buckle region grow into the region of the adhered V film (the red circle always represents the finally detached area taken at 1 H/V). However, mainly the Pd-dot regions show buckles after hydrogen loading till 1 H/V.

In the comparison of the image Figure 4.1.5.1 (a) and (b), some buckles nucleate close to the border of the dots. In this region, the morphology of the V-film is slightly bent due to the height of the underlying Pd-dots. The actual lateral shape of the Pd dot region is shown in Figure 4.1.5.2. However, also in the dot interior region nucleation of buckles is visible, as shown in Figure 4.1.5.1 (a).

(a)

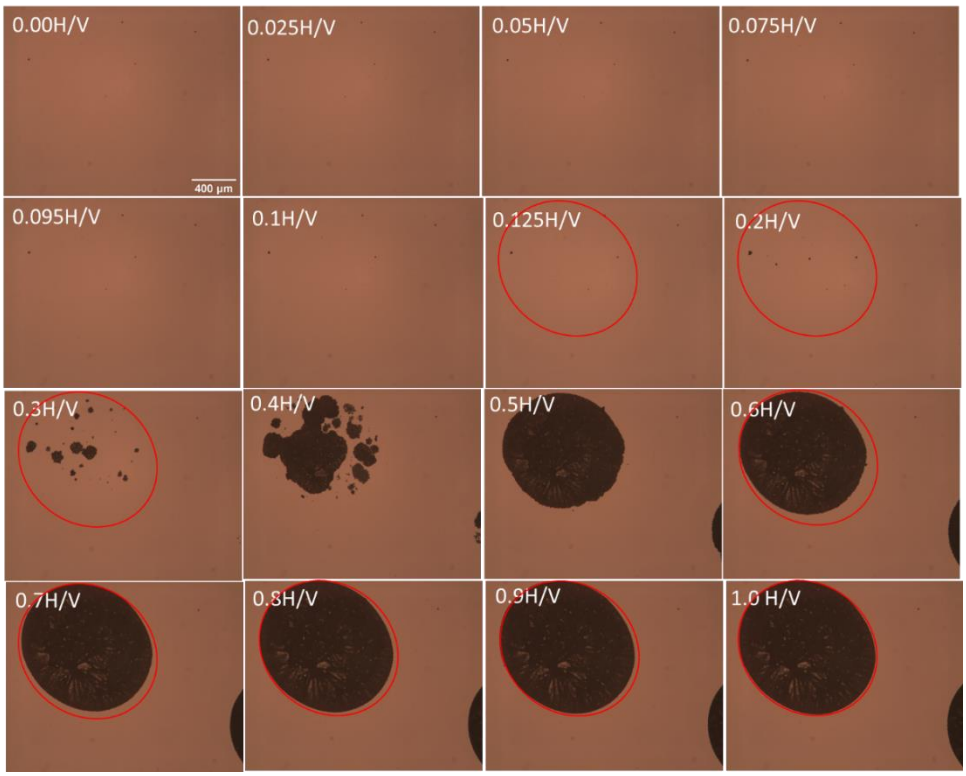

(b)

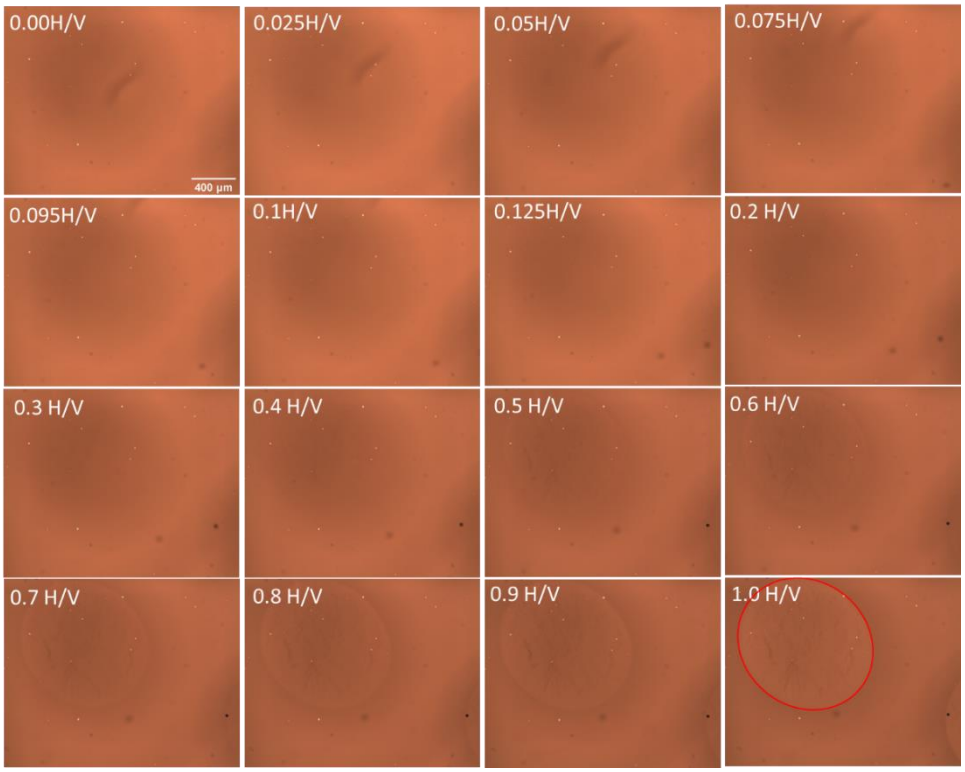

Figure 4.1.5.1: Optical measurements on Pd(15nm)/V(30 nm)/Pd(5nm) dots//glass film in, **(a)** Reflection mode and **(b)** Transmission mode, both with 50× magnification the images were taken at the same concentration's steps, first in reflection and then in transmission.

The related **transmission images** during hydrogen loading of the Pd(15nm)/V(30 nm)/Pd(5nm) dots//glass film are shown in Figure 4.1.5.1 (b). In contrast to reflection images, the transmission images show darker areas at the positions of the Pd dots, due to added extra 5 nm thickness. The Pd dots are visible in the transmission intensities because Pd is a heavy metal and absorbs light. Upon hydrogen loading, the V film gets darker, but with gradual hydrogen loading, the optical contrast between the Pd dot region and the adhered part of the V film becomes smaller.

Besides, at c_H = 0.4 H/V buckling can be observed in the Pd dot area, even in the transmission image. Above this concentration, the buckle morphology change appears more prominently and becomes slightly visible in transmission. At c_H = 0.7 H/V, buckling appears to be completed and with further loading of the V-film, existing buckles appear to grow in the area of the V-film bending region, close to the Pd dots.

Pd dots, in as deposited condition having a dimension of 1.4 mm in width and a length of 1.47 mm. With hydrogen loading V film develops buckle in the area of dots, these dots appear to have dimensions of 1.11 mm in width and 1.26 mm in length. Thus, these dots have elliptical structures, and the visible buckle area appears to be smaller than that of the Pd dots.

(a)

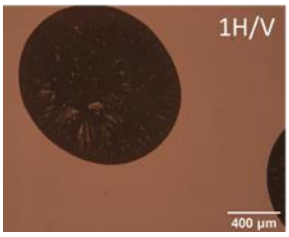

(b)

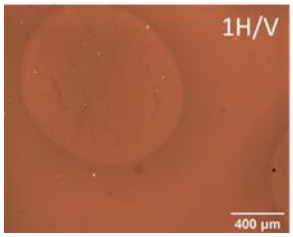

Figure 4.1.5.2: Pd dot area of the Pd(15nm)/V(30nm)/Pd(5nm) dots //glass film imaged in **(a)** reflection and **(b)** transmission mode at 1 H/V. The Pd dots are elliptical with a width of 1.4 mm and a length of 1.47 mm on average. After hydrogen loading, the width appears 1.11 mm while the length is about 1.26 mm. The dots have an elliptical shape. The size of the visible dots is slightly smaller than that of the Pd dots.

The average **transmission intensity diagrams** for this mixed-adhesion sample are scattered and broad because they contain information about the two completely different regions. While in the Pd dot area, buckles develop with hydrogen concentration increase, the adhered part behaves like the no-interlayer sample and gets darker with hydrogen loading. The resulting transmission intensity diagrams as shown in Figure 4.1.5.3 (a) present the whole sample area, and Figure 4.1.5.3 (b) present the adhered part only. The chosen areas are sketched by the green frames.

(a)

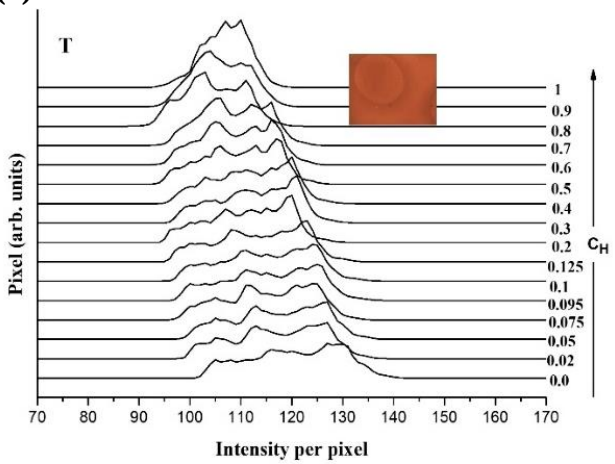

(b)

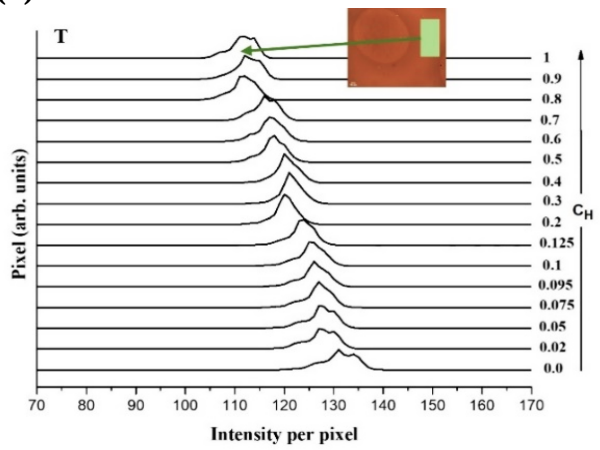

Figure 4.1.5.3: (a) Transmission pixel intensity diagrams of the Pd(15nm)/V(30 nm)/Pd(5nm) dots//glass film, measuring the whole frame. The images are taken with 50× magnification. **(b)** Transmission pixel intensity diagrams of an area that is not covered with the Pd dot.

To extract the local sample behavior from this spreading signal (Figure 4.1.5.3 (a)), a small part of the sample image information is cropped (the area without the Pd dot coverage) for all hydrogen concentrations. The transmission pixel intensity diagrams are plotted in Figure 4.1.5.3 (b). This Figure 4.1.5.3 (b) shows similarities to the original signal in Figure 4.1.5.3 (a). The related EMF measurement, presented in Figure 4.2.5, confirms the proper V-film loading and phase boundary between c_H = 0.05 H/V and c_H = 0.5 H/V. The last two images are expected to show an effect due to the Pd loading, resulting in a higher intensity shift in the transmission pixel intensity diagrams.

Figure 4.1.5.3 (b) can be used to see the general trend of the adhered V-film part. Figure A.3 (b) in the appendix shows the buckle part of the transmission pixel intensity diagrams, which are not presented here. Superposition of Figures 4.1.5.3 (a) and 4.1.5.3 (b) in Figure 4.1.5.4 clearly shows that the right-hand part of each curve has a contribution from the cropped area that adheres to the substrate and is not covered by the Pd dots while the other peaks with low pixel intensity are contributions from the sample parts influenced by the Pd dot interface layer.

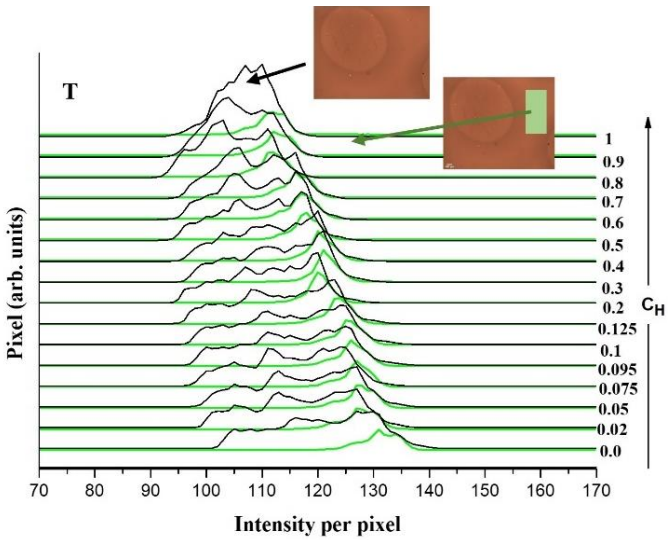

Figure 4.1.5.4: The intensity distribution of the superposition of the transmission pixel intensity diagrams of Figure 4.1.5.3 **(a)** and **(b)**. While black curves belong to pixel intensity diagrams originate from the whole sample and green curves are plotted from the crop part of the same sample.

Three-pixel intensity diagrams of concentration 0.095, 0.1, and 0.125 are shifted to the right by no physical phenomenon, so are shifted back to left with a constant value (please see image A.3 in the appendix).

4.1.6 Mixed adhesion samples with PC dots

For the Pd(15nm)/V(30nm)/PC(5nm) dots//glass sample a dot pattern interlayer of PC (poly-carbonate) of 5 nm thickness is used. The adhesion energy between a metal film and PC is very small which should, therefore, lead to film detachment above a certain mechanical stress or hydrogen concentration.

Figures 4.1.6.1 (a) and (b) show the reflection and transmission images of the V-film deposited on the de-adhesive PC pattern. In the **reflection images** of Figure 4.1.6.1 (a) it is observed that the V

film is initially detached (at c_H = 0.0 H/V) at the locations of the PC pattern. A dark-buckled region is visible already in this unloaded state. This demonstrates that the pattern is highly visible in the reflection images. The related transmission images of Figure 4.1.6.1 (b) show an overall constant brightness at c_H = 0.0 H/V, even though a part of the film is strongly buckled. The reflection images Figure 4.1.6.1 (a) taken upon hydrogen loading show that the buckling area gradually becomes darker. This is attributed to increased delamination and folding in this area. Further, with the increase in hydrogen concentration, the buckling area circumference widened.

(a)

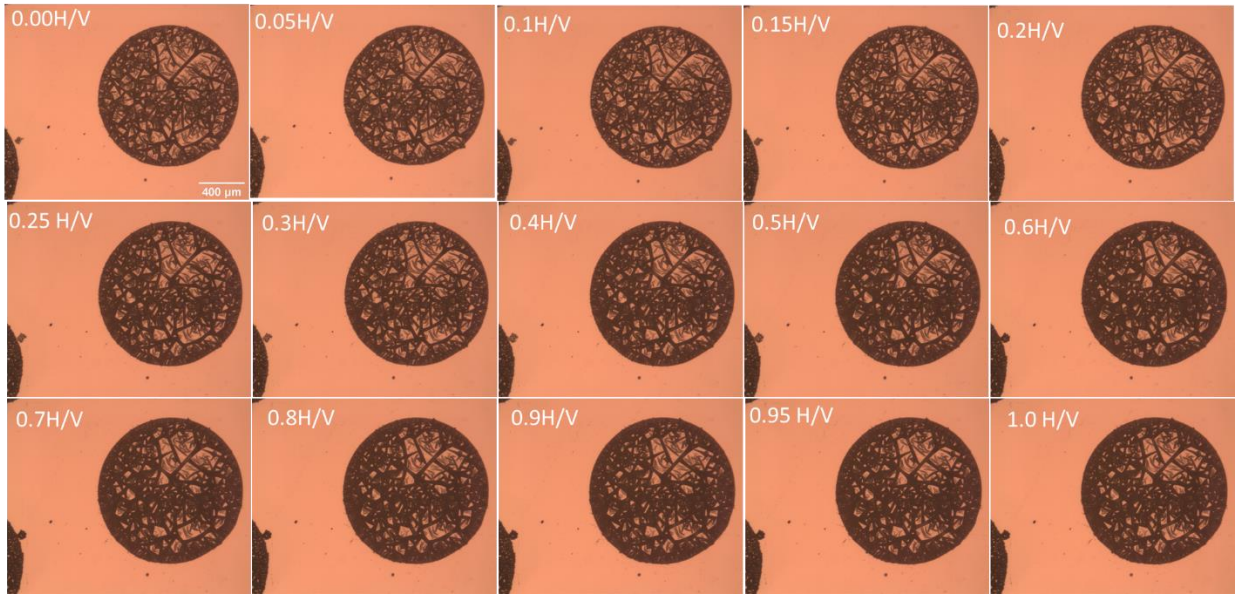

(b)

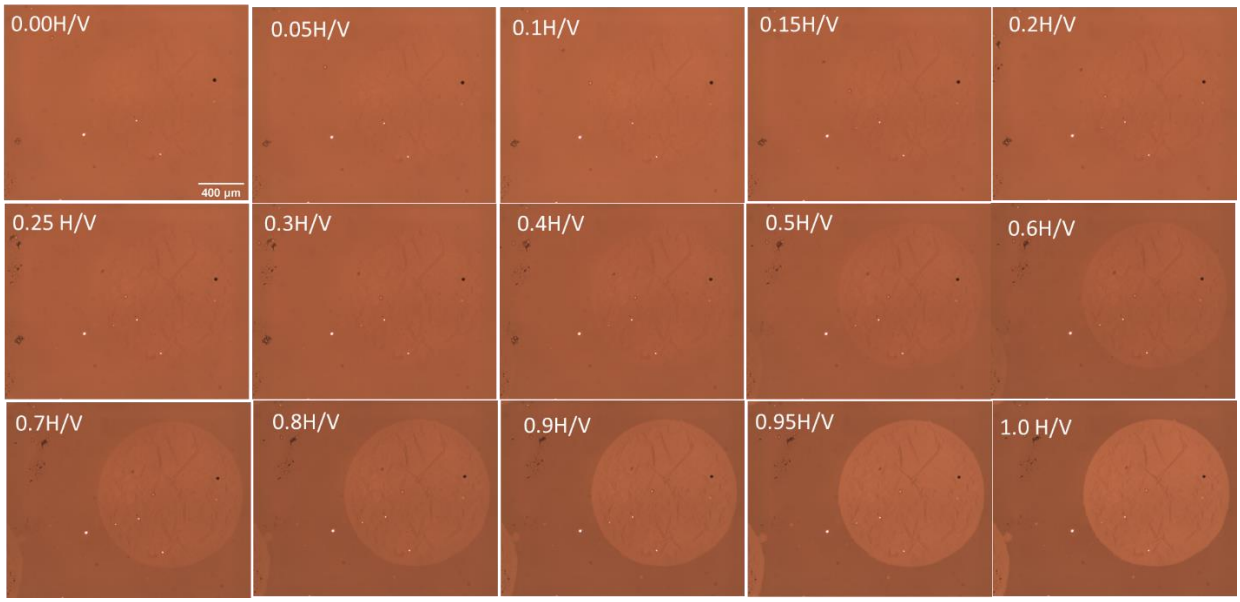

Figure 4.1.6.1: Optical measurements on Pd(15nm)/V(30 nm)/PC(5nm) dots//glass film in, **(a)** Reflection mode and **(b)** Transmission mode, both with 50× magnification the images were taken at the same concentration's steps, first in reflection and then in transmission.

The **transmission images** that were taken subsequently are shown in Figure 4.1.6.1 (b). As already mentioned, the PC dots are not visible in the initial transmission spectrum (c_H = 0 H/V). This is because it is a transparent polymer and does not absorb light. Interestingly, for this sample as the buckle area is already present in the as-deposited state of the sample. This buckling morphology seems to be not clearly visible in the transmission images.

The transmission images taken upon hydrogen loading show an increasing brightness in the buckled area. In contrast to the reflection mode, the transmission mode shows an optical contrast between adhered part and buckled area depending on the mean hydrogen content, as shown in Figure 4.1.6.1 (a) and (b). As the first image at c_H = 0.0 H/V in Figure 4.1.6.1 (b) does not show a contrast in the transmission image, this suggests a local change of the hydrogen concentration in the buckled regions compared to the adhered regions. As the buckled regions become brighter in the transmission images, the concentration in the buckles appears less than in the adhered film part.

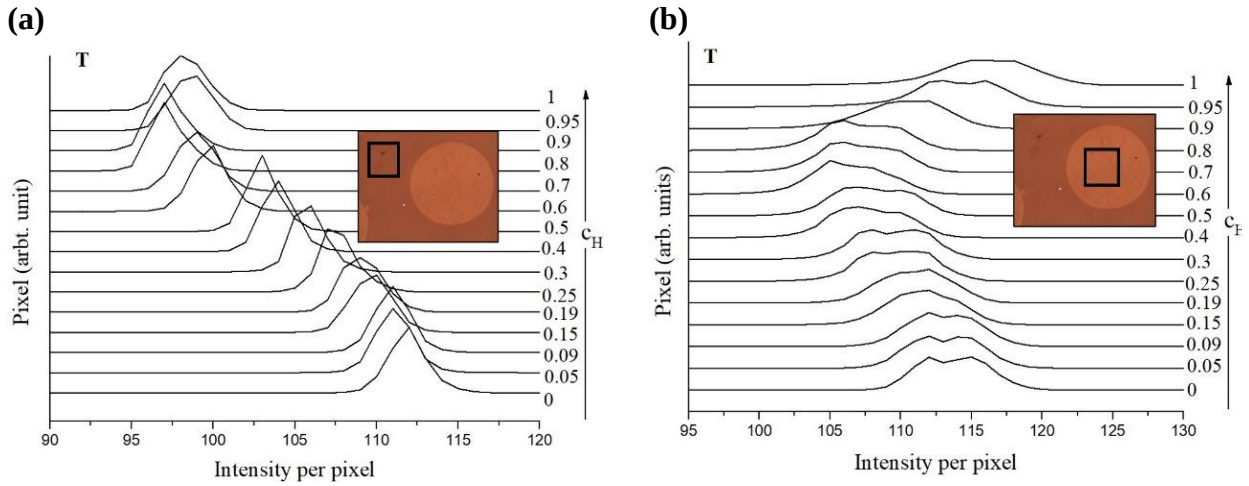

Figure 4.1.6.2: Transmission pixel intensity diagrams of the Pd(15nm)/V(30 nm)/PC(5nm) dots//glass film **(a)** at the adhered part of the film **(b)** at the buckle part of the film, as the function of the hydrogen concentration related to V-H film.

To look at the transmission intensities in more detail, the transmission images are analyzed by using two areas of interest, one at the center of the buckled area and the other at the adhered part of the film, see Figure 4.1.6.2 (a) and (b). The chosen areas are sketched by the frames in Figure 4.1.6.2. (Using the white light spectrum) and Figure 4.1.6.3 (using the green light only).

An analysis of the light source emitting color information shows that the different RGB components (red, green, and blue) have different sensitivity. It was observed that the green channel contains maximum information, showing maximum intensity change upon hydrogen absorption. Therefore, to deduce the details in the transmission signal, we focused on the green channel for this sample, as shown in Figure 4.1.6.3 (a) and (b).

By looking at the **transmission pixel intensity diagrams** of Figure 4.1.6.2 (a) and (b) at c_H = 0.0 H/V, the transmission intensity in the PC pattern area (right-hand side) resembles that of the transmission intensity in the adhered part of the film (left-hand side). Resultantly, it can be concluded that even though the buckles are present, they do not affect the transmission intensity.

According to Lambert-Beer's law (Eq. 3.4 chapter 3), the intensity of the transmitted light can be affected by a change in film thickness, a change in the extinction coefficient, and a change in the hydrogen concentration. The V-film thickness is considered constant, as the hydrogen-related film expansion is only 0.135 × 30 nm = 4.1 nm, at 1 H/V (see chapter 2 part 2.3.2). The PC pattern is optically transparent. The extinction coefficient is considered to remain constant as the film material does not change largely from start to end. Out of the three factors affecting the transmitted intensity, the above two can be mainly excluded. The remaining factor is the hydrogen concentration: Thus, the increasing concentration of hydrogen should lead to a stronger contrast arising between the adhered part of the film and the buckled area. Note, that some concentrations diagrams could not be used because of an artificial intensity jump: thus, the neighboring diagrams are plotted (for example c_H = 0.09 H/V (replacing that at 0.1 H/V) and c_H = 0.19 H/V (replacing that at 0.2 H/V), see in Figure 4.1.6.2 (a) and (b)). Details are discussed in appendix A.4.

Figures 4.1.6.3 (a) and (b) show a more detailed version of the signal (with green channel of RGB image). The inset is added to give more information on the signal behavior at low concentrations. An analysis of the transmission pixel intensity diagrams of Figure 4.1.6.3 (a) shows that the adhered-apart optical signal goes darker with increasing concentration while the buckled parts transmission pixel intensities presented in Figure 4.1.6.3 (b) are stable at the same position. Figure 4.1.6.3 (a) and (b) are plotted with the main concentration step of c_H =0.05 H/V.

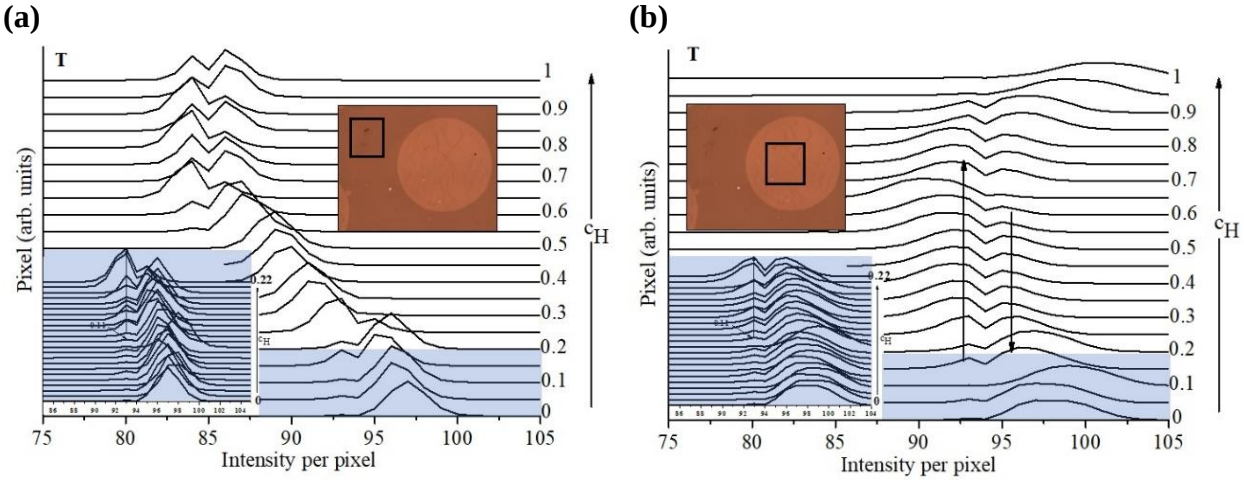

Figure 4.1.6.3: Pixel intensity distribution for the green channel of light transmission through the Pd(15nm)/V(30 nm)/PC(5nm) dots//glass film **(a)** at the adhered part of the film and **(b)** at the buckled part of the film, as the function of the hydrogen concentration related to the V-H film.

Both distributions show the peak in the intensity diagrams, which is slightly broadened for the buckled film part. With hydrogen loading, these peaks shift toward lower intensity for the adhered part, Figure 4.1.6.3 (a) and for the buckled part, they mainly stay constant 4.1.6.3 (b).

The inset image in Figure 4.1.6.3 (a) and (b) presents more detailed information for the low concentration steps of Δc_H =0.01 H/V ranging from c_H =0 H/V to c_H =0.22 H/V. Up to c_H =0.2 H/V for both regions the peak position remains constant at around intensity i_t= 97-98, see the inset of Figure 4.1.6.3 (a) and (b). A second peak starts to develop at i_t= 93 above c_H =0.1 H/V. EMF measurement recorded simultaneously with this measurement shows a value of c_H =0.09 H/V, as the solid solution limit. This value of the solid solution limit correlates with the second peak in the transmitted intensity diagrams. The above information indicates hydride phase nucleation above c_H =0.09 H/V.

As seen in the graphs for hydrogen concentrations above c_H =0.1 H/V, the buckled and the adhered part pixel intensity peaks develop differently. In the adhered region shown in Figure 4.1.6.3 (a), the second peak develops at i_t= 93 and already reaches the maximum intensity at c_H =0.25 H/V, while the first peak at i_t= 97 almost vanished at this concentration. This suggests the two-phase region for the adhered part exists between the concentration c_H =0.1 H/V and c_H =0.3 H/V.

It is suggested that due to the presence of stress in the sample (the adhered region), the critical temperature for the phase transition is reduced [18]. Reduction of the critical temperature results in the shrinking of the two-phase region for the vanadium-hydrogen system which has bulk values for the two-phase region ranging from concentration of c_H =0.03H/V to c_H =0.47H/V [14].

In the adhered part (Figure 4.1.6.3 (a)) and above a concentration of c_H =0.25 H/V, the peak at i_t= 93 shifts toward lower intensity reaching i_t= 87 for c_H =0.55 H/V. This represents either a local increase of the hydrogen or an also hydrogen-related thickness increase in the sample. The single peak in this concentration range most likely represents a single phase. Above c_H =0.6 H/V another peak start developing at i_t= 87. Above this concentration, the existing two peaks do not show any systematic intensity change trend till c_H =0.95 H/V, after which peaks shift to higher intensities. This shift can be explained as the phase change in the protecting Pd cap layer. The c_H-axis in Figure 4.1.6.3 (a) and (b) are given by taking the c_H =1 H/V, as the maximum content in the V-film and only relates to V. But as observed at the higher values of concentrations, Pd-hydride starts to form and results from hydrogen being absorbed in the Pd cap layer. Therefore, it can be concluded that the H/V concentration is overestimated for the last three concentration steps. The related EMF curve, later presented in Figure 4.2.6, confirms this statement. Hence, it is estimated that the maximum content mainly absorbed in the V-film is c_H = 0.85 H/V. The contribution of the Pd cap

layer to the transmission pixel intensities is neglected at low concentrations: This can be done as the maximum hydrogen content in the Pd cap layer is expected to be low, as for bulk Pd phase transition potential is above 120 mv [117].

In the buckled part (Figure 4.1.6.3 (b)) the peak at i_t= 93 intensity is of the maximum intensity at the high concentration of c_H = 0.65 H/V. At this concentration, the first peak existing at i_t= 97 completely vanishes. This suggests that for the buckle sample part, a two-phase region exists between c_H = 0.1 H/V and c_H = 0.65 H/V. Above this concentration, the peaks seem to redevelop. For c_H = 0.9 H/V and higher values, the intensity shifts toward higher values. This shift is more prominent in the buckled region than in the adhered region. As explained already, this shift of intensity towards higher values is due to the hydrogen absorption in the Pd cap layer. This result suggests a higher local hydrogen concentration in the Pd cap layer of the buckled regions compared to the adhered regions.

4.1.7 Pd(15nm)/V(30 nm)/PC(20nm) layer//glass

In this sample, a 20 nm interface PC layer is deposited. It can be expected for the V-film to have minimum adhesion to this layer, compared to in other substrates.

The **reflection images** are demonstrated in Figure 4.1.7.1 (a). The V film is already buckled in its as-deposited state at c_H = 0.0 H/V, indicating the very low adhesion between the film and the substrate. Thus, even though electrochemical loading requires a solid substrate to support the 30 nm vanadium film, this film can be regarded as mainly free from substrate-related stress. From the reflection images of Figure 4.1.7.1 (a), for c_H = 0.0 H/V to c_H = 1 H/V, it is observed that the film buckling morphology changes with loading, and the overall film becomes darker. At low concentrations, buckle folds are small with small folding peaks as shown in the reflection images. With increasing hydrogen concentration these folds change their shape and size. This can be observed as the image appears darker with hydrogen content increase, and deeper folds replace small folds.

(a)

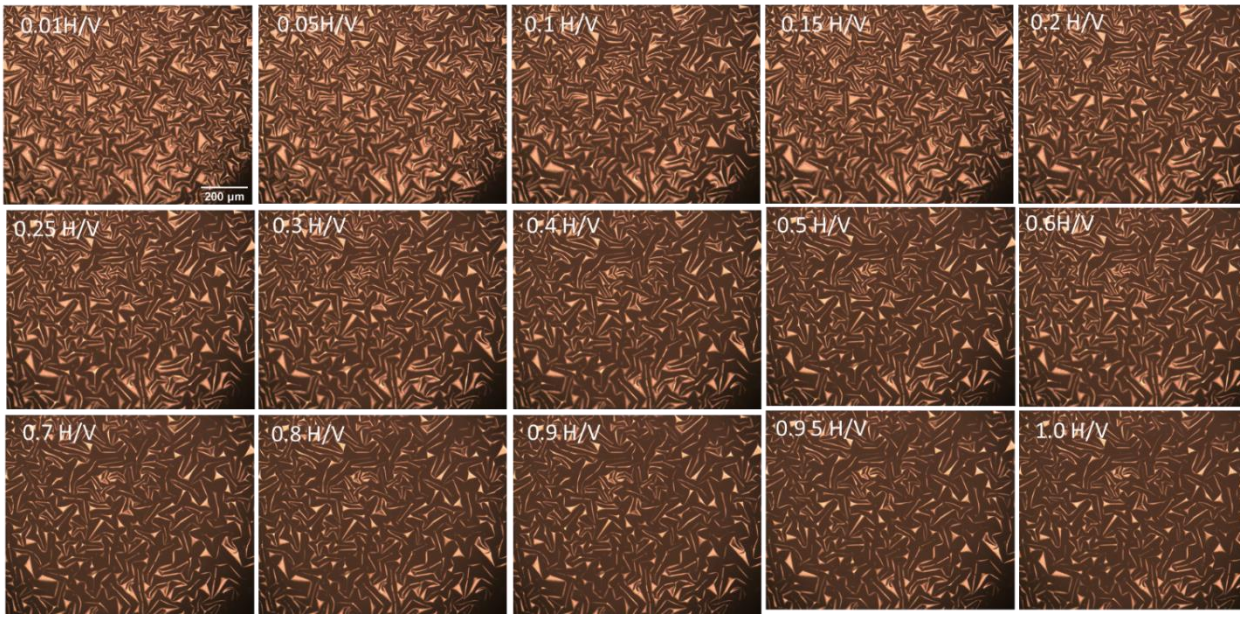

(b)

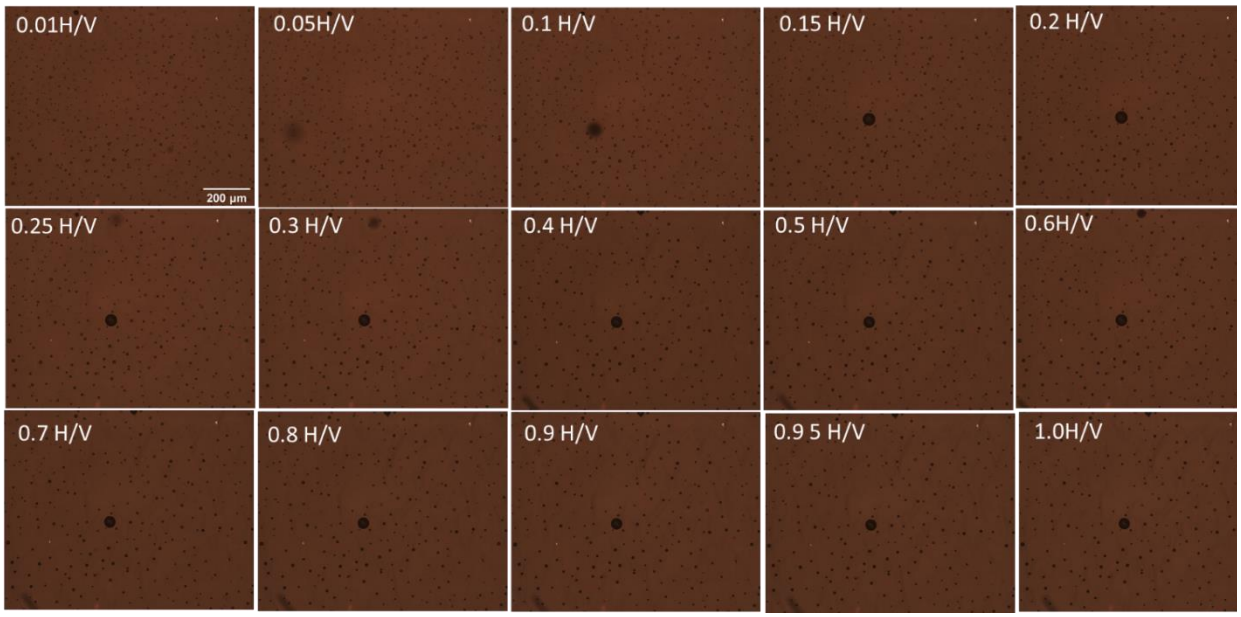

Figure 4.1.7.1: Optical measurements on Pd(15nm)/V(30 nm)/PC(20nm) layer //glass film in, **(a)** Reflection mode and **(b)** Transmission mode, both with 100× magnification. Images were taken at the same concentration's steps, first in reflection and then in transmission.

Figure 4.1.7.1(b) shows the related **transmission images**, in the concentration range from c_H = 0.0 H/V to c_H = 1 H/V. The images show lots of tiny dark dots. Dots are present already at 0 H/V. Comparison of the dark spot positions in the transmission images with the related positions in the

reflection images suggests that they relate to small folding in the buckle morphology having pointed peaks. With increasing hydrogen concentration, the size and shape of the buckles increase, and with this, the peak points increase. In accordance with this, in the transmission images, the dark dot size increases, and the distance between the dark spots also increases. This can be seen in Figure 4.1.7.1 (b) for c_H = 1 H/V. The loading state of this film is observed with the EMF curve, only. The large dark spot in the middle of the image relates to a small bubble of gas that randomly floats on the film's surface. It does not affect the measurement as only a few pixels get darker.

Transmission pixel intensities of a sample in its as-deposited state and upon hydrogen loading are shown in Figure 4.1.7.2. The sampling intensity at c_H = 0.01 H/V is i_t = 57. At a hydrogen content of c_H = 0.5 H/V, this shifts to i_t = 55. With further increase in hydrogen, concentration results in a very slight effect on the highest peak value which goes to, for c_H = 1 H/V to i_t = 57. Peaks from c_H = 0.0 H/V to c_H = 0.5 H/V, shift back and forth. This can be understood by the strong change in buckle morphology. The peaks from c_H = 0.6 H/V to c_H = 1 H/V remain mostly in one position. The change in the intensity is rather small. This may be attributed to the strong film buckling. The related EMF isotherm confirms successful film loading, see Figure 4.2.7.

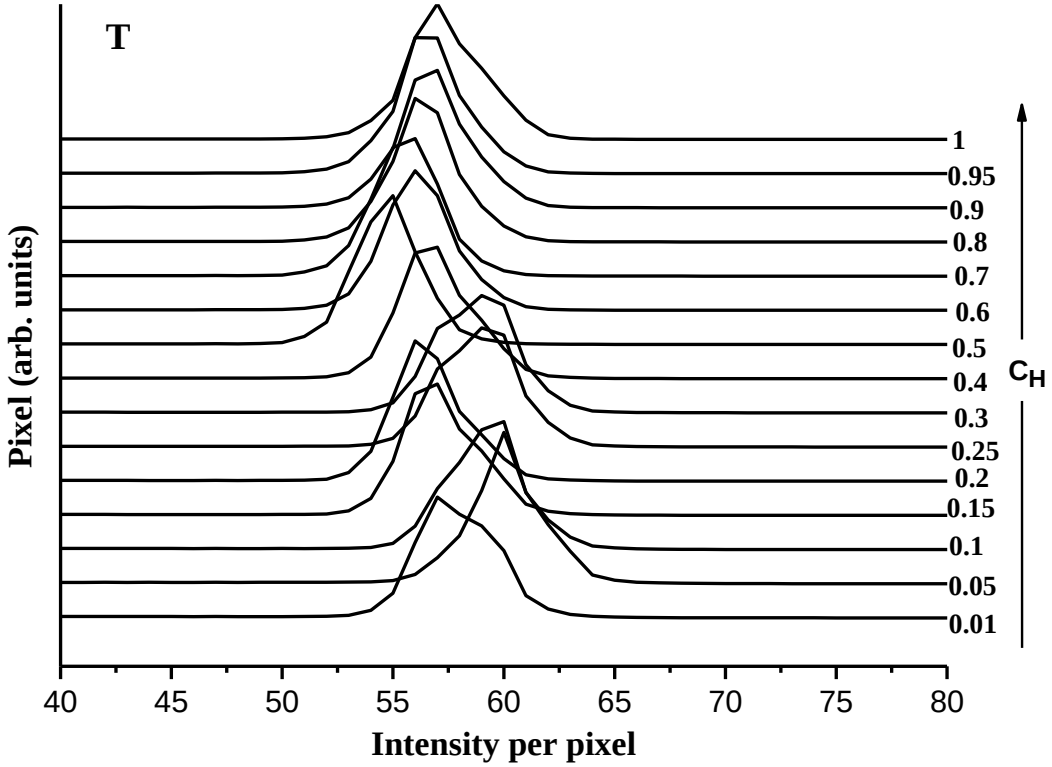

Figure 4.1.7.2: Selection of transmission Images with 100× magnification of Pd(15nm)/V(30 nm)/PC(20nm) layer//glass film. The intensity position changes only slightly with the hydrogen content in the sample.

4.2 EMF measurements

EMF data are taken simultaneously to the optical measurements (hydrogenography), in a row with loading the sample, and with taking the transmission and the reflection data. The data collected for the EMF are taken when the system reaches thermodynamic equilibrium, which takes about 1 minute after which reflection (R) and transmission (T) images are taken within a time window of 30 sec. For clarity, the EMF results are organized in the same sequence as the results in chapter 4 part 4.1.

The EMF curves for all the different samples look rather similar. This results from the fact, that all V-films have the same thickness of 30 nm. The difference between the samples is just the different adhesion to the substrate (with or without additional layers). So, the differences between the samples are comparably small.

4.2.1 Pd(30nm)//sapphire

The EMF curve obtained during electrochemical loading of the Pd(30nm)// sapphire sample is shown in Figure 4.2.1. At low c_H values, a straight line can be fitted (dashed line marked with *RT*/*F*).

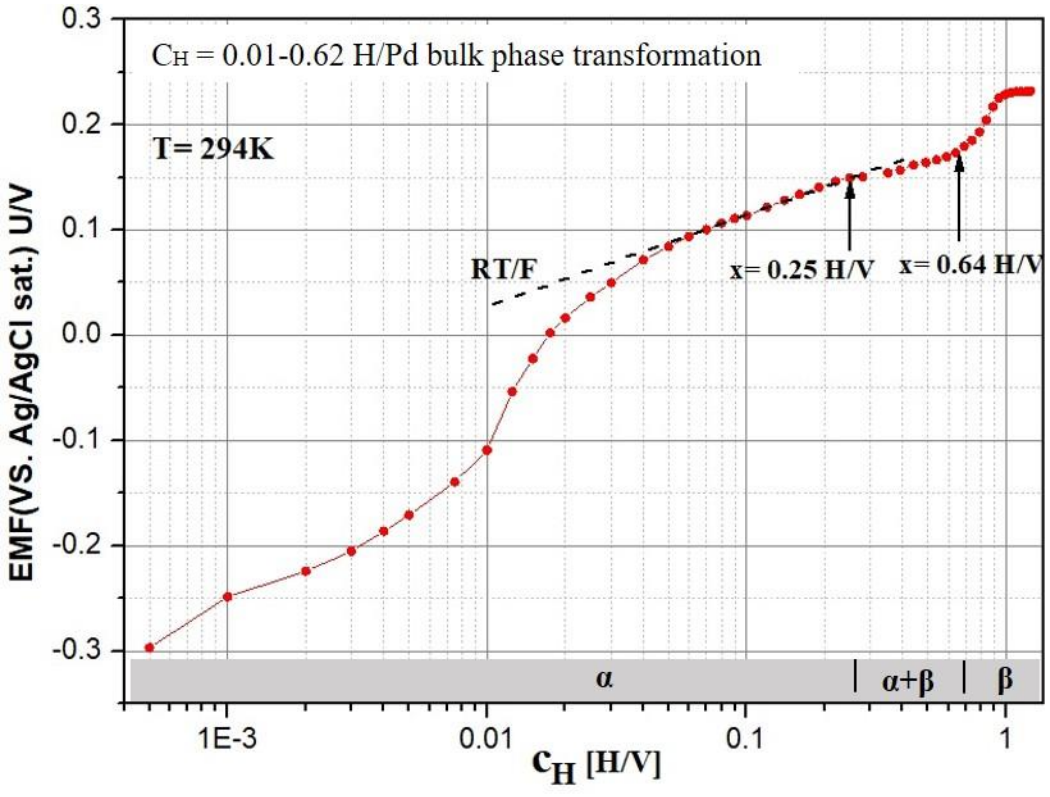

Figure 4.2.1: The EMF curve of Pd 30 nm film measured during electrochemical hydrogen loading. The black dashed line represents the linear dependency as predicted by Sievert's law. The region between two concentrations shows the two-phase region and is represented by the arrows.

This line accounts for Sieverts' law, which represents the ideal relationship between the concentration c_H and the chemical potential of hydrogen in bulk metals. For thin films, the straight-line increase may change because of mechanical stress contributions. Nevertheless, the straight line is named "RT/F", here.

All the EMF data points at lower concentrations $c_H < 0.04$ H/Pd lay below the straight line. Wagner et al. they relate trapping sites for hydrogen, to defects like dislocations, grain boundaries, and vacancies in the Pd-films [18]. At around $c_H = 0.04$ H/Pd, the EMF starts following Sieverts' law (*RT*/*F*). Thereafter, a second deviation from Sieverts' law appears at $c_H = 0.25$H/Pd. Here, the α-phase of this sample most probably ends. In the concentration range between $c_H = 0.25$ H/Pd and $c_H = 0.64$ H/Pd (marked with arrows in Fig.4.2.1), the two-phase region appears with a slanted EMF plateau region. According to Wagner et al., the mechanical stress in the sample makes the EMF again raise to higher values [55]. Above a concentration of $c_H = 0.64$ H/Pd, the rising EMF indicates hydrogen absorption happening in the β- phase (hydride phase) [13].

4.2.2 Pd(15nm)/V(30nm)//glass

The EMF curve was obtained during electrochemical loading for the Pd(15nm)/V(30nm)//glass; the sample is shown in Figure 4.2.2. Again, the dashed straight line represents Sieverts' law (marked with *RT*/*F*) and indicates that the film is in α- phase. The first three data points for concentrations of $c_H = 0.01$ to $c_H = 0.03$ lay below the *RT*/*F* line. This can be explained by the presence of trapping sites for hydrogen in the V-films, like dislocations, grain boundaries, and vacancies. In the concentration range between $c_H = 0.04$ H/V and $c_H = 0.08$ H/V, the EMF follows Sieverts' law (*RT*/*F*). At $c_H = 0.08$ H/V, the α- phase regime ends and is followed by the two-phase region from $c_H = 0.08$ H/V to $c_H = 0.48$ H/V with a slanted plateau. This, also here, hints at a nonlinear stress state in the sample, as shown with the fitted green line. Above $c_H = 0.48$ H/V, the EMF slope changes sharply and moves to higher values. This is attributed to hydrogen absorption in the hydride phase represented as a ß phase [13].

In the low hydrogen concentration range, the interaction of the hydrogen atoms with lattice defects of the sample becomes visible. It is assumed here, that the different defect densities in the sample result in variable behavior in the low concentration range.

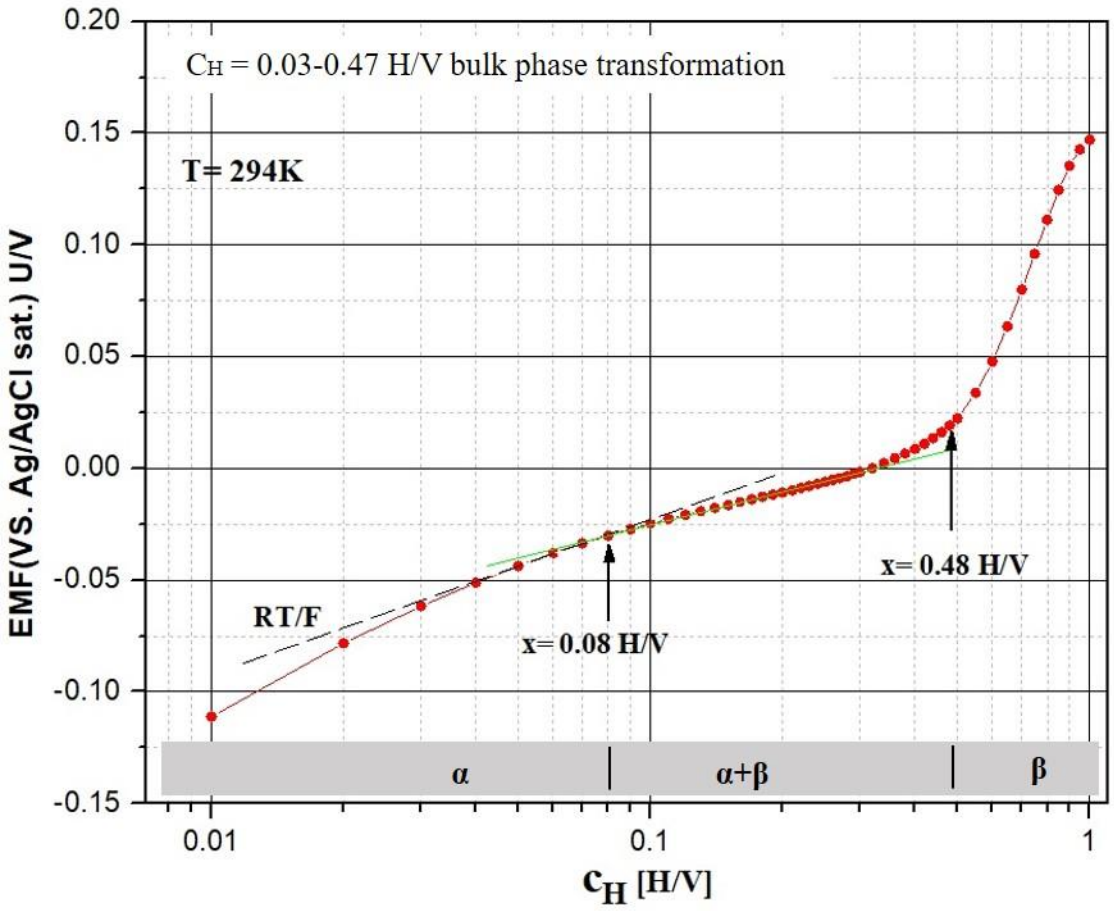

Figure 4.2.2: The EMF curve of Pd(15nm)/V(30nm)//glass film measured during electrochemical hydrogen loading. The black dashed line represents the dependency as predicted by Sievert's law. Arrows represent the deviation from Sievert's law and the end of the slanted plateau-like region. The two-phase region exists between the two related concentrations.

4.2.3 Pd(15nm)/V(30 nm)/Pd(7nm) layer//glass

In Figure. 4.2.3 the EMF measurement during hydrogen loading of the Pd(15nm)/V(30nm)/Pd(7nm)/ layer//glass sample is shown. The black dashed line representing Sieverts' law (*RT*/*F*) as described in 4.2.1, indicates the presence of the α-phase. The first two data points (c_H = 0.01 to c_H = 0.02) lay below the *RT*/*F* line according to trap sites. From a concentration of c_H = 0.03 H/V to c_H = 0.09 H/V, the EMF follows the *RT*/*F* line, and it shows that the film is in the α- phase. Above the concentration of c_H = 0.09 H/V, the two-phase region starts and ends at c_H = 0.38 H/V. The related slanted plateau suggests a nonlinear stress increase in the film. The further increase in concentration leads to a steep increase in the EMF values, indicating the hydride phase.

Therefore, all the hydrogen loaded in the sample above c_H = 0.38 H/V is absorbed in the hydride phase.

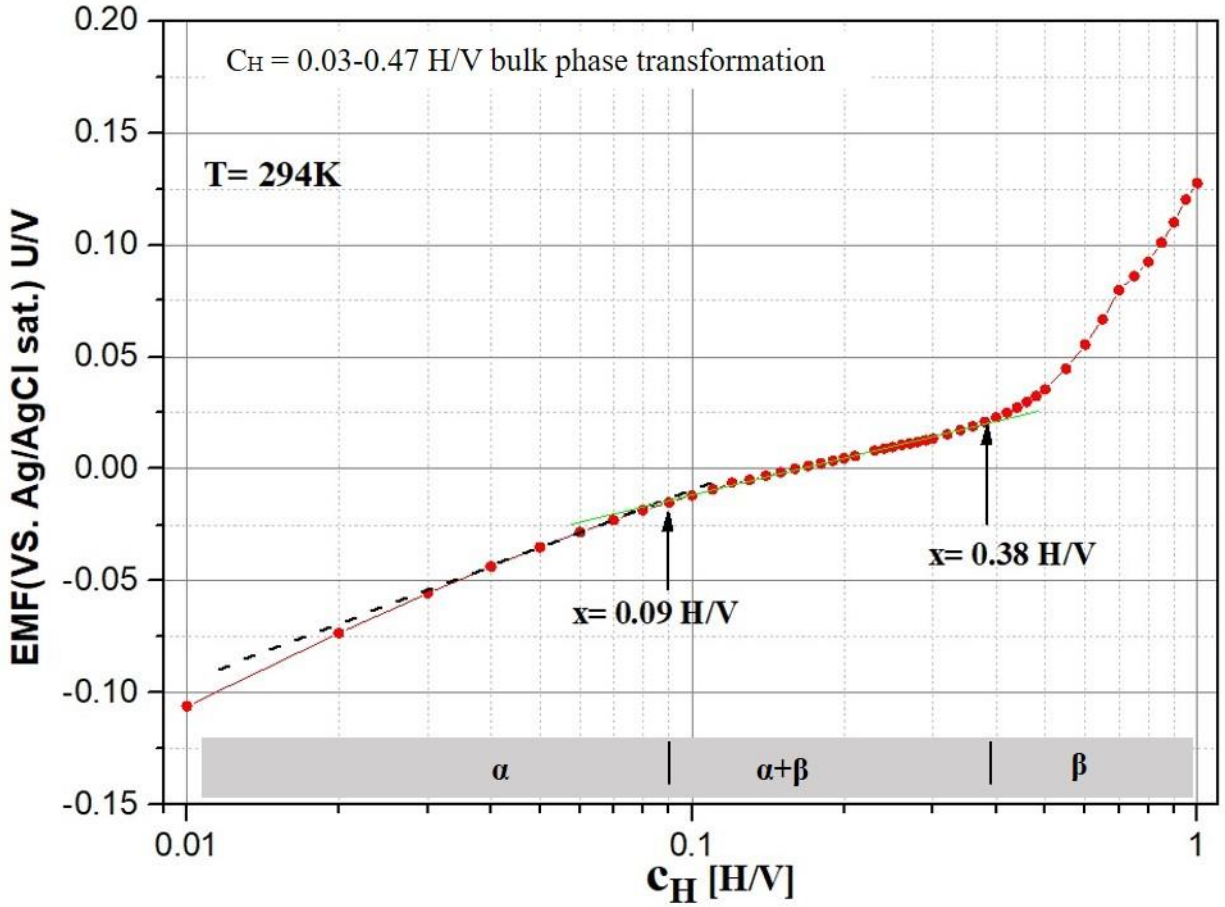

Figure 4.2.3: The EMF curve of Pd (15nm)/V(30 nm)/Pd(7nm) layer//glass film measured during electrochemical hydrogen loading. The black dashed line represents Sievert's law. Arrows represent the deviation from Sievert's law and the end of the plateau-like region, between the two related concentrations the two-phase region is expected.

4.2.4 Pd(15nm)/V(30 nm)/Pd(5nm) layer//glass

Figure 4.2.4 given below shows the EMF measurement of the Pd(15nm)/V(30 nm)/Pd(5nm) layer//glass film, during the electrochemical loading. The dashed black line representing Sieverts' law (*RT*/*F*) shows that only the first data point is affected by a side effect. This should not be the trap sites effect, as the data point lies above the ideal Sievert's dependency. Most likely, there was a small content of hydrogen already present in the film after preparation. From the concentration of c_H = 0.02 H/V to c_H = 0.08 H/V the EMF follows the Sieverts' law (*RT*/*F*) representing the α-phase. The two-phase region of this film appears between c_H = 0.08 H/V and c_H = 0.42 H/V, with

a slanted plateau showing nonlinear stress increase in the film. After c_H = 0.42 H/V, the electrochemically loaded hydrogen is absorbed in the hydride phase.

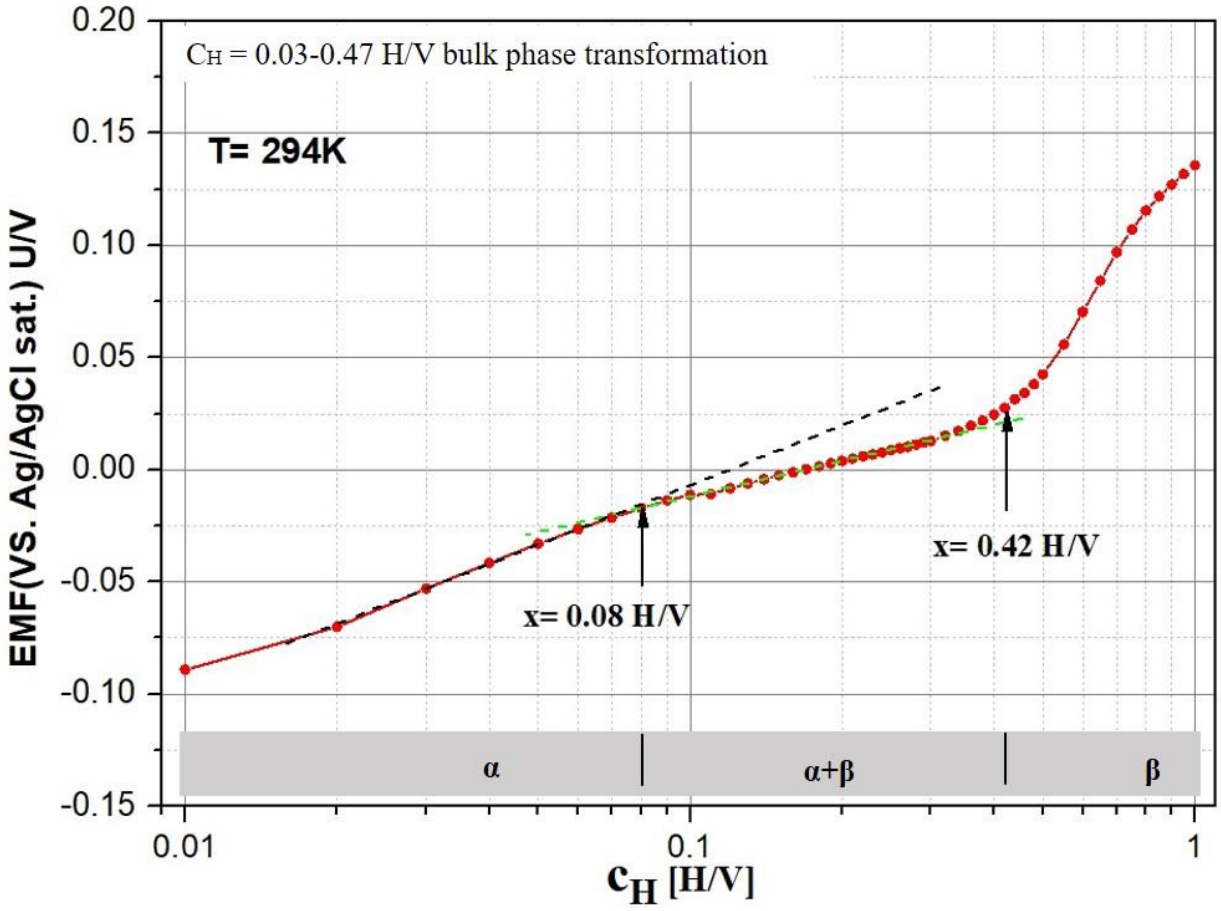

Figure 4.2.4: The EMF curve of Pd(15nm)/V(30 nm)/Pd(5nm) layer//glass film measured during electrochemical hydrogen loading. The black dashed line represents the linear dependency as predicted by Sievert's law. Arrows represent the deviation from Sievert's law and the end of the plateau-like region shows the two-phase region, between two concentrations, represented by the arrows,

4.2.5 Mixed adhesion samples with Pd dots

The EMF measurement during H-loading of the Pd(15nm)/V(30nm)/Pd(5nm) dots// glass sample is shown in Figure 4.2.5 during electrochemical hydrogen loading. The black dashed line shows the data compatibility with Sieverts' law (*RT*/*F*) representing α-phase. The EMF values for c_H = 0.01 and c_H = 0.02 lay below the *RT*/*F* line and represent the presence of trap sites. Thus, at low concentrations the hydrogen interaction with different kinds of defects such as grain boundaries, vacancies, and dislocations are significant. Therefore, the different defect density leads to the different behavior of the EMF curve in the low-concentration regime. Concentrations higher than

the c_H = 0.5 H/V represent hydrogen absorption in the hydride phase, and the related tangents steeply change to high values.

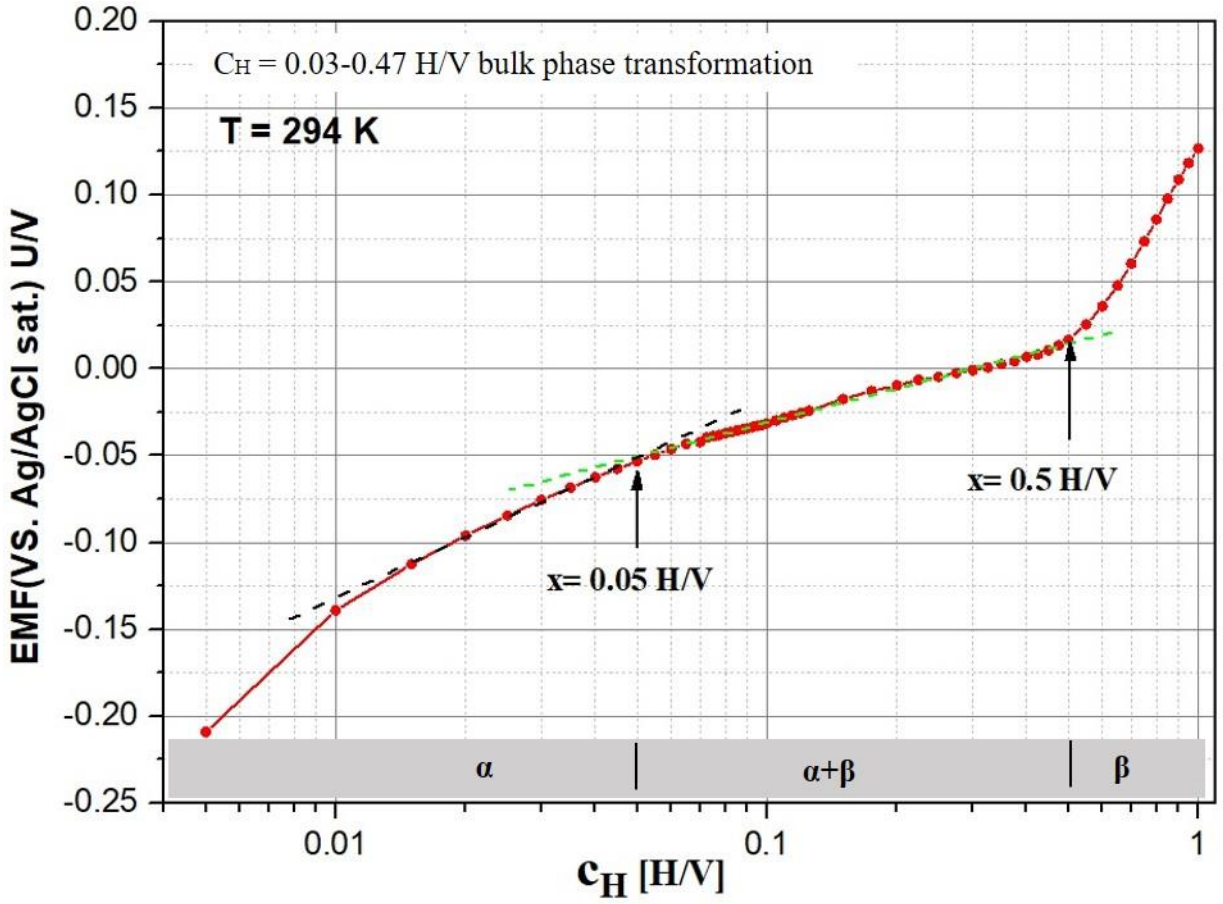

Figure 4.2.5: The EMF curve of a Pd(15nm)/V(30 nm)/Pd(5nm) dots//glass film measured during electrochemical hydrogen loading. The black dashed line represents the dependency as predicted by Sievert's law. Arrows represent the deviation from Sievert's law and the end of the plateau-like region. Between the two concentrations marked by the arrows, the two-phase region is present.

4.2.6 Mixed adhesion samples with PC dots

Figure 4.2.6 presents the EMF measurement done simultaneously on the Pd (15nm)/V(30 nm)/PC(5nm) dots//glass sample, while electrochemical hydrogen loading is performed. The black dash line represents Sieverts' law (*RT*/*F*). The first data point slightly deviates from the *RT*/*F* line, most probably due to a small content of initial hydrogen.

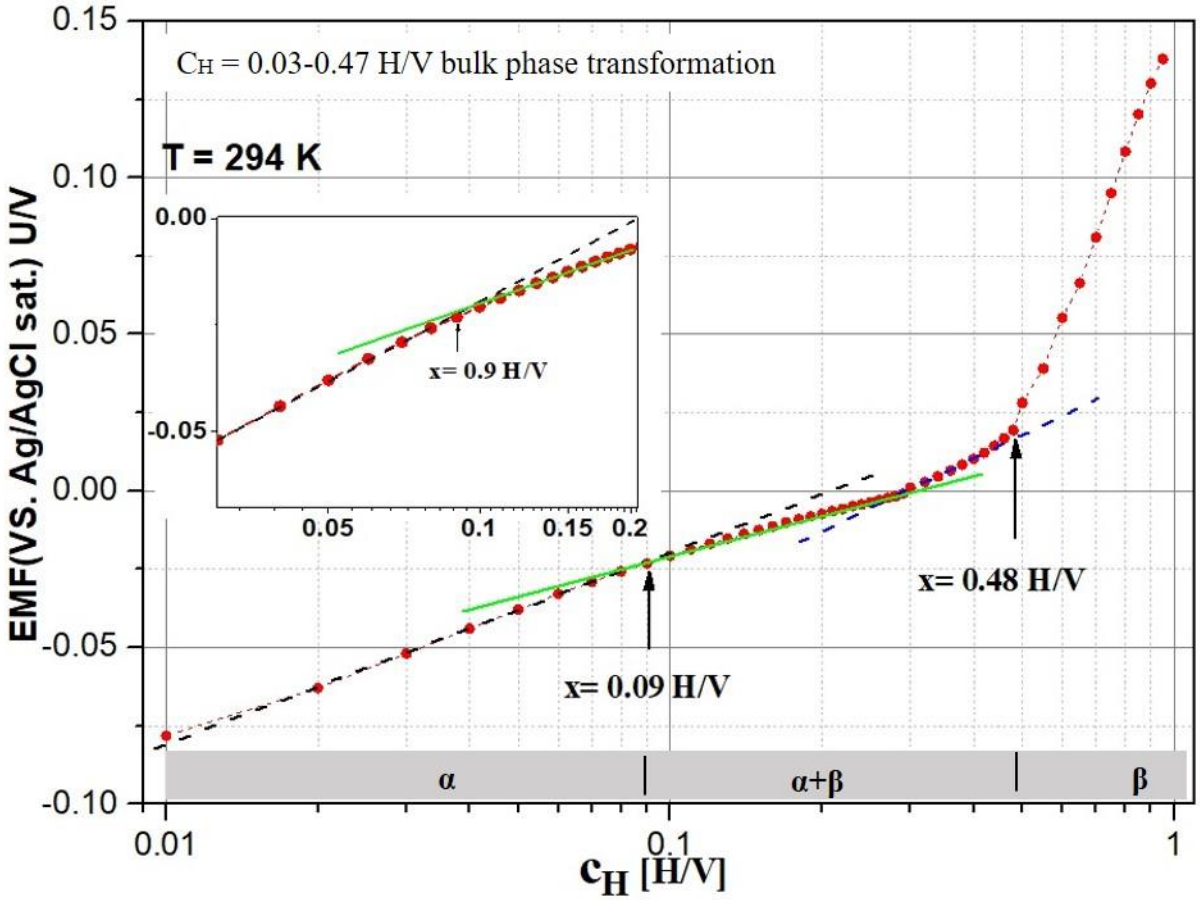

Figure 4.2.6: The EMF curve of Pd(15nm)/V(30 nm)/PC(5nm) dots//glass film measured during electrochemical hydrogen loading. The black dashed line represents the linear dependency as predicted by the Sievert's law. Arrows represent the deviation from the Sievert's law and the end of the plateau-like region. The two-phase region is present between the two concentrations marked by the arrows.

Ranging from a concentration c_H = 0.02 H/V to c_H = 0.09 H/V, EMF follows Sievert's dependency (*RT*/*F)*, representing the α- phase. This is followed by the two-phase region that has been adjusted between c_H = 0.09 H/V to c_H = 0.48 H/V. In this measurement, one thing must be noted: the plateau region shows two separate and different slopes. For all the other samples, only one slope was drawn. But in this measurement, it was difficult to get the phase boundary with one slope. This may be due to a strongly nonlinear stress as shown in Figure 4.2.6. At the end of the two-phase region at c_H = 0.48 H/V, the tangent to the EMF sharply changes to a high slope again showing hydrogen absorption in the hydride phase.

4.2.7 Pd(15nm)/V(30 nm)/PC(20nm) layer//glass

The EMF measurement, during electrochemical loading of the Pd(15nm)/V(30 nm)/PC(20nm) layer//glass sample, is shown in Figure 4.2.7 given below. The black line drawn as a tangent represents Sievert's law (*RT*/*F*) and shows data compatibility with Sievert's law.

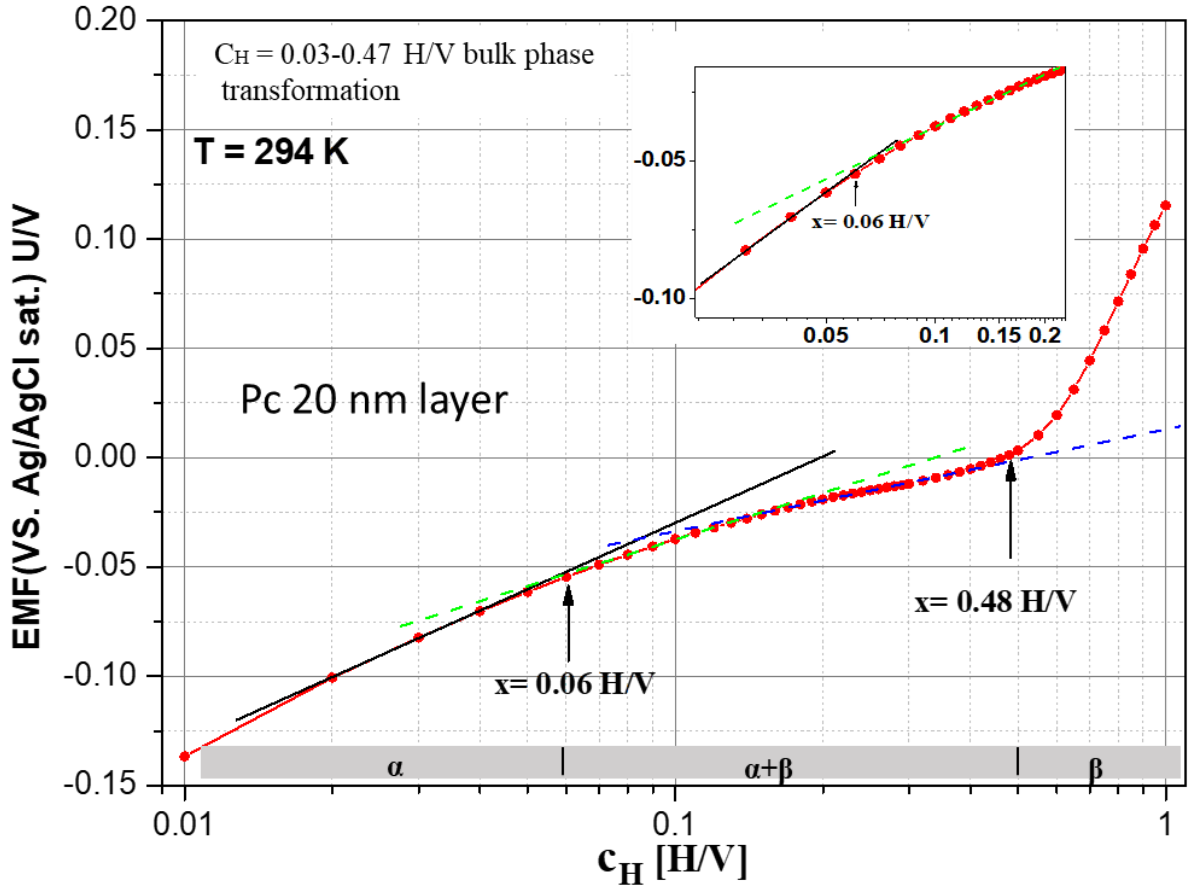

Figure 4.2.7: The EMF curve of Pd(15nm)/V(30 nm)/PC(20nm) layer//glass film measured during electrochemical hydrogen loading. The black bold line represents the linear dependency as predicted by Sievert's law. Arrows represent the deviation from Sievert's law and the end of the plateau-like region. Between these two concentrations represented by the arrows, is the two-phase region.

The first data point slightly deviating from the law shows the effect of trap sites at low concentrations. Ranging from a concentration from c_H = 0.02 H/V to c_H = 0.06 H/V the EMF follows Sievert's law and further represents the α- phase regime. This is followed by the two-phase regime, ranging from a concentration of c_H = 0.06 H/V to c_H = 0.48 H/V shown by the sloping plateau region. It is to be noted here that two tangents have to be drawn in the slanted plateau region to get the phase boundary for the two-phase region, as shown in Figure 4.2.7. This is attributed to strong nonlinear stress in the film, At the end of the two-phase regime after concentration of c_H =

0.48 H/V, the tangent to the EMF changes sharply to the high slope showing hydrogen absorption in the hydride phase.

4.2.8 EMF critical concentrations for all types of interface layers

Table 4.2.8 summarizes the EMF results, such as the phase boundaries of the alpha and the hydride phases of the related films and corresponding EMF values. The values are determined by using the logarithmic concentration axis and straight-line fitting therein.

Table. 4.2.8 Alpha and the hydride phase boundaries extracted from the EMF measurement of different interface layers.

Sample	Starting EMF (volt)	Alpha phase	EMF value [V]	Hydride phase	EMF value [V]
Pd(30nm)//sapphire	**-0.3**	**0.25**	**0.14**	**0.64**	**0.17**
Pd(15nm)/V(30nm)//glass	**-0.11**	**0.08**	**-0.03**	**0.48**	**0.019**
Pd(15nm)/V(30 nm)/Pd(7nm) layer//glass	**-0.11**	**0.09**	**-0.015**	**0.38**	**0.021**
Pd(15nm)/V(30 nm)/Pd(5nm) layer//glass	**-0.08**	**0.08**	**-0.017**	**0.42**	**0.03**
Pd(15nm)/V(30 nm)/Pd(5nm) dots//glass	**-0.21**	**0.05**	**-0.053**	**0.5**	**0.017**
Pd(15nm)/V(30 nm)/PC(5nm) dots//glass	**-0.075**	**0.09**	**-0.023**	**0.48**	**0.019**
Pd(15nm)/V(30 nm)/PC (20nm) layer//glass	**-0.13**	**0.06**	**-0.055**	**0.48**	**0.012**

4.3. Mechanical stress measured by substrate curvature

In this section, the results of stress measurement on the vanadium films are discussed. These measurements will show the development of high stress in the film, with the hydrogen charging. For these measurements many hydrogen loading and unloading cycles were performed, during which the EMF curves and the mechanical stress are measured, as discussed in chapter 3. For the stress measurements, both step-wise and continuous loading are done.

The theoretical values of stress calculated by using, linear elastic theory on the bcc vanadium film adhered to a rigid substrate, come out to be compressive stress in the direction of <1-10> (x) and <001> (y), as $\sigma \cdot c_H = -11.7\ \text{GPa}.\frac{\text{H}}{\text{V}}$ and $\sigma \cdot c_H = -13.3\ \text{GPa}.\frac{\text{H}}{\text{V}}$, respectively (see chapter 2 part 2.3.2). For a sample with isotropic grain distribution in the in-plane directions, e.g., for nanocrystalline films, the average of these compressive stresses gives a value of $< \sigma > \cdot c_H = -12.5\ \text{GPa}\ \frac{\text{H}}{\text{V}}$.

Until critical stress for plastic deformation is reached, the stress curve should depend linearly on the hydrogen concentration, as represented by the linear elastic regime. After the critical concentration is reached and as soon as the plastic deformation appears in the film, the built-up mechanical stress deviates from the linear elastic behavior, see chapter 2 for more detail.

4.3.1. Stresses development during different loading conditions

The loading conditions can change the way stress develops in thin films. It affects the stability of the film during hydrogen loading. During hydrogen loading, each current pulse is followed by a waiting time for the equilibrium to be attained. During that time the EMF is recorded, and no voltage is applied. It has the above-mentioned advantage but also has the disadvantage of taking each step manually for the required precision. This is time-consuming, limiting the number of fine concentration steps. Alternatively, **continuous loading** can be done automatically, with more detailed information. But this has the disadvantage of a continuous force being applied during hydrogen loading. This results in a higher EMF value recorded, showing in addition to the chemical potential an 'applied voltage effect' (Thus denoted c-EMF).

4.3.1.1 Effect of different current densities on the stress development during hydrogen loading

Figures 4.3.1.1(a) and (b) show stress development and corresponding c-EMF, during continuous loading in the Pd(15nm)/V(30nm)//glass sample using different current densities (black curve with j= 0.65 A/m^2, red curve with j= 0.2 A/m^2, blue j= 0.064 A/m^2), and thus different loading velocities. During these measurements, the samples adhere to the substrate up to 1 H/V. Even though multiple cycles have been done in the individual measurement, the sample stays firm at the substrate.

The stress curves show a significant difference. As shown in Figure 4.3.1.1(a), the blue curve representing the sample loading with the lowest current density shows the first decay from the linear elastic behavior at 0.06 H/V. The initial stress increase is -6.1 GPa/c_H. This sample developed -1.6 GPa stress which was the largest final compressive stress of all the presented measurements

in the current work. This curve shows the conventional type of stress release based on one deformation process, which is suggested to be dislocation formation.

The black curve in Figure 4.3.1.1(a) represents the sample loading with the highest current density and shows a final stress of -0.7 GPa. The stress curve shows the linear elastic behavior till 0.05 H/V and the initial stress increase is -5.9 GPa/c_H. The deviation from the linearity at 0.05 H/V is conventionally interpreted as the onset of the plastic deformation. The curve shows a minimum at 0.7 H/V, after which the stress curve has a positive slope. This is different from many other results and is here interpreted as a second stress release process happening.

The red curve in Figure 4.3.1.1(a) represents the sample loading with medium current density and shows a final stress of -0.1 GPa at 1 H/V. The stress curve shows that the first decay from the linear elastic behavior happens at 0.08 H/V. This onset of the first deformation process agrees well with the above-measured onset values. The initial stress increase is -7.4 GPa/c_H and it reaches a maximum compressive stress of -1.1 GPa at about 0.35 H/V. Thereafter, the curve bends strongly, hinting at a second process that sets in. This second process is very efficient in terms of stress release for this sample and even results in nearly zero final stress.

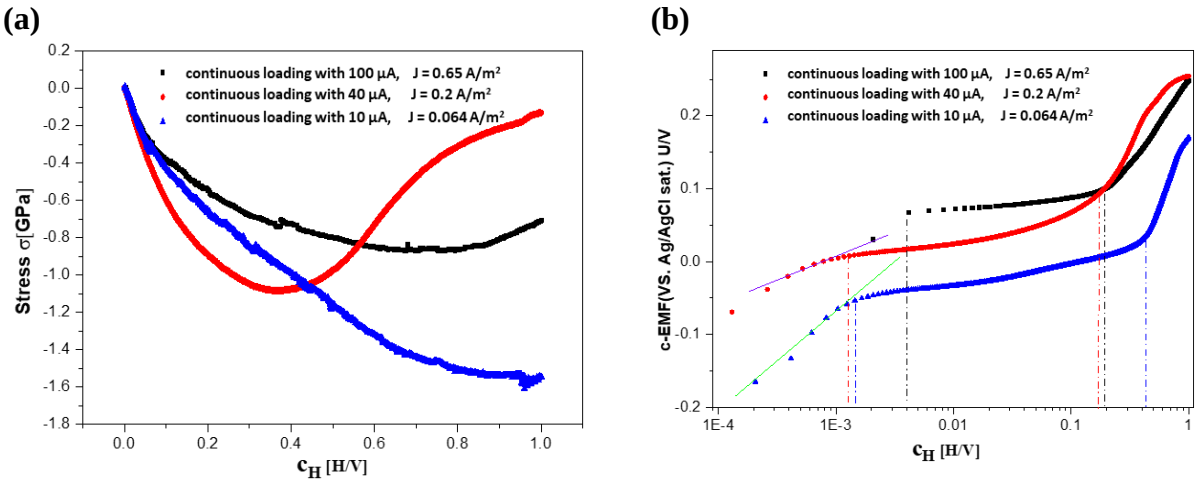

Figure 4.3.1.1: (a) Measured mechanical stress arising during hydrogen loading of Pd(15nm)/V(30nm)//glass with different applied current densities (black curve with j= 0.65 A/m^2, red curve with J= 0.2 A/m^2 and blue curve with 0,064 A/m^2). All curves deviate from linear elasticity at about 0,06 H/V, indicating plastic deformation. The black and the red curves show curve bending towards positive slopes. This indicates a second stress release process affected by the hydrogen charging speed. **(b)** Corresponding behavior of c-EMF (containing the EMF and the applied charging voltage) of the sample.

The corresponding c-EMF curves of Figure 4.3.1.1(b) show a few points that are the direct consequence of the different loading current densities (black curve with j= 0.65 A/m^2, red curve with j= 0.2 A/m^2, blue curve with j= 0.064 A/m^2). As all the measurements are done in the continuous current loading mode, it is not possible to state the exact location of the phase

boundaries. However, an overall view can be given. The order of highest current density to lowest current density shows similar order in the plateau pressures and the widths of the two-phase regions. The highest plateau pressure and the smallest two-phase region exist for the highest current density (black curve with j= 0.65 A/m^2). The red curve shows the second-highest plateau pressure while the blue curve measured for the sample loaded with the lowest current density shows the lowest plateau pressure. A similar dependency is found for the width of the two-phase regions. The width of the two-phase region of the blue curve (j= 0.064 A/m^2) is the widest, followed by that of the red curve (j= 0.2 A/m^2) and, finally, by the last black curve with the smallest width of the two-phase region.

4.3.1.2 Comparison between step-wise and continuous loading

Figure 4.3.1.2 (a) shows the effect of the hydrogen charging type on the sample behavior, while 4.3.1.2 (b) shows the c-EMF during the hydrogen loading. The applied current is 100 µA which is the same for both Pd(15nm)/V(30nm)//glass samples. Due to a small difference in the surface area of the two samples, the current density is slightly different for each sample. For loading, waiting durations of 1 minute and 30 seconds were used to reach (quasi-)equilibrium for each step. For thin films, a true equilibrium is difficult to adjust because outgassing can happen [120]. Therefore, this is called quasi-equilibrium.

The behavior has a few similarities because the overall behavior is similar, and EMF curves show the expected behavior. The loading sample having a 1 minute 30 second waiting time for reaching the quasi-equilibrium has lower EMF values as compared to the values obtained during continuous loading that is not giving any time to attain any type of equilibrium.

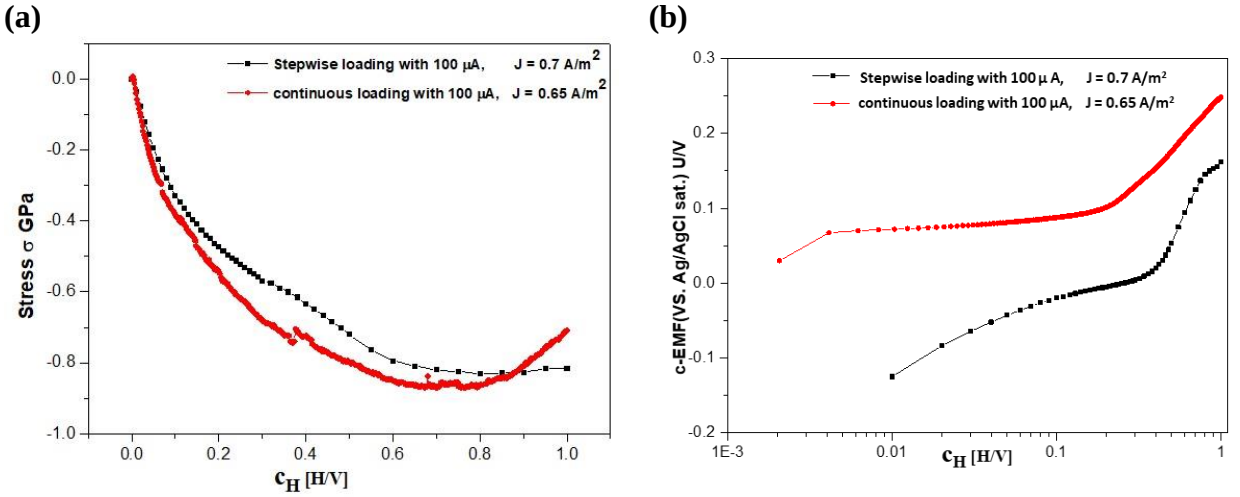

Figure 4.3.1.2: (a) Represents the influence of the hydrogen charging type on the sample behaviour, while **(b)** shows the c-EMF during the hydrogen loading. The applied current is 100 µA and is the same for both Pd(15nm)/V(30nm)//glass samples.

In addition, during step-wise loading, hydrogen is diffusing in the sample while no potential is applied. Contrary to this, there is a constant force acting on the sample in the continuous loading mode. That means when EMF is recorded; it not only includes the voltage due to hydrogen charging but also the force that is present during the hydrogen diffusion. This first factor is absent in step-wise loading. This makes the plateau rise to higher values for continuous loading. The stress increase of -4.9 GPa and linear behavior till 0.07 H/V, for step-wise loading with the hydrogen uptake are observed. For continuous loading, one observes a stress increase of -5.9 GPa and an ending of the linear behavior at 0.05 H/V. It is expected that the stress increases more strongly for the continuous loading (neglecting here the slightly different current density). Thus, increased linear elastic compressive stress is also observed. During continuous loading, a continuous loading force is present while in case of step-wise loading there is enough time in between the charging steps that hydrogen atoms can rearrange in the sample, and stress dissipation can take place. This behavior can be seen in the middle part of the Figure. 4.3.1.2 (a) for this sample while in the continuous loading mode, the compressive stress is greater.

On top of this, the continuous loading curve shows a minimum, while the step-wise loading curve does not. Minima in continuous loading followed by a positive increase in the slope indicate the existence of the second process of stress release. This process is not visible in the step-wise loading process. This may be attributed to the reason that the sample has enough time to dissipate its stress. The first stress release process starts at 0.05 H/V and 0.07 H/V for continuous and step-wise loading conditions, as observed by the deviation from the linear elastic behavior. The second process leads to a stressed minimum at 0.7 H/V for continuous loading. For the step-wise loading, this minimum is not detected, but the stress release is less than that of the continuous loading. It is suggested that the second process also happens during the waiting time, thereby lowering the compressive stress increase but not resulting in a visible stress minimum. The total stress in the sample after full loading is -0.8 GPa for step-wise and -0.7 GPa for continuous loading.

4.3.1.3 Continuous cyclic loading and unloading: stress hysteresis behavior

Some of the samples were cyclically loaded and unloaded with hydrogen (full cycle) during the stress measurement. Continuous loading with 40 μA of the Pd(15nm)/V(30nm)//glass sample shows a stress hysteresis behavior with a closed-end situation from the third cycle onwards. The first cycle shows an open hysteresis and the second one gives a distorted hysteresis, see appendix Figure A.5. A similar behavior is observed in different samples for the two starting cycles.

Figures 4.3.1.3 (a) and 4.3.1.3 (b) show the measured stress hysteresis in two different representations. Four cycles are presented in both parts. The cycle numbers are indicated by the numbers 3, 4, 5, and 6, at the loading branch because the unloading branches are too close to each other and are almost inseparable. Figure 4.3.1.3 (a) neglects the stress remaining from the previous loading cycles; thus, the starting stress is fixed to 0 GPa for each cycle. Figure 4.3.1.3 (b) presents

the stress hysteresis measurements by taking the stress of the previous loading cycles into consideration (represents the actual stress state of the sample). This leads to tensile starting stress that shifts from cycle to cycle.

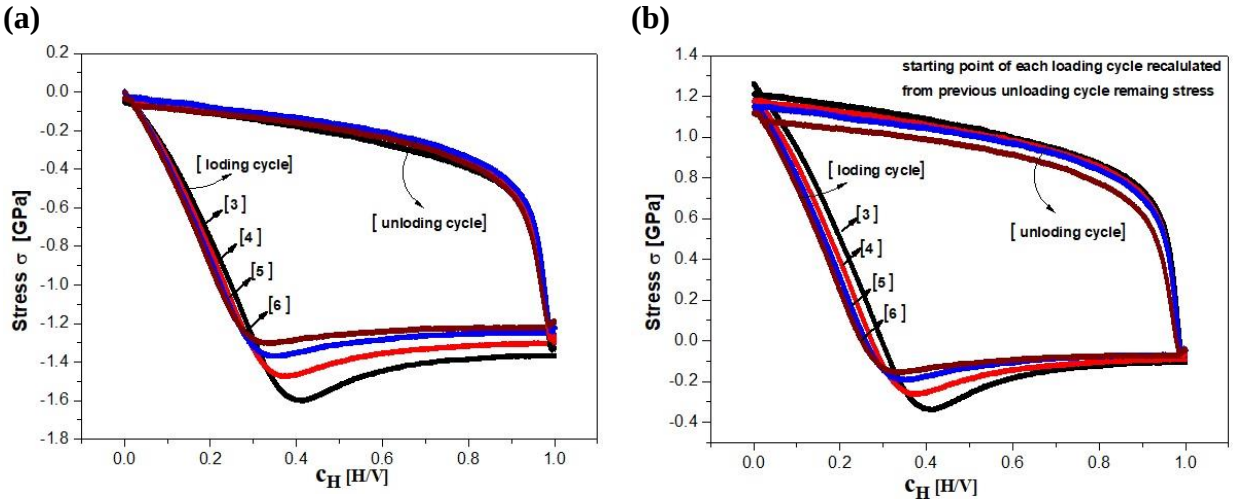

Figure 4.3.1.3: Stress hysteresis observed during multiple loading and unloading cycles of Pd(15nm)/V(30nm)//glass, as continuously loaded with 40 μA current. **(a)** presents the loading and unloading cycle by setting the initial stress condition to zero for each cycle, and **(b)** represents the actual stress state of the sample before each loading cycle, taking into account the stress left in the sample by the previous unloading.

The loading branch of the cycles shows a more or less linear behavior, with a small increase in slope that can be fitted by another linear behavior. A large dip can be seen in each loading curve (the minima represent the highest compressive stress reached during that loading cycle). The dip is followed by a stress relaxation and a linear behavior for a short range, resulting in an overall nulling effect upon hydrogen loading. After these six cycles, further, loading shows no change in the stress hysteresis shape.

It was observed in the current work that for all the cycles the deviation for all the loading cycles from the first linear behavior occurs between 0.03-0.08 H/V. After deviating from the initial linear behavior, a slight slope change is observed again before the dip (minima in each loading curve) of the loading curve. These slope changes also occur at lower and lower concentration values with the increasing number of loading cycles. The dip (minimum) in each curve represents the highest compressive stress achieved in the sample. This highest compressive stress decreases with an increasing number of loading cycles, representing the fact that lower compressive stress is achieved within the next loading cycles. Thus, the hysteresis area keeps on decreasing with the increasing number of loading cycles, which is accompanied by the shift in the dip of the curve to lower concentrations with increasing loading.

4.4. Distribution Of Sites (DOS) model of site occupation energies

DOS model provides different site occupation energy. To explain the finding of optical transmission, EMF and stress measurement data were used in the **DOS model for the distribution of sites energies** proposed by Wagner et al. [121] on a model of Kirchheim [7]. The model is applicable to a film loaded with hydrogen that has substrate-induced stress contribution in addition to grain boundary and trap defects.

The distribution of hydrogen atoms among the number of different sites is given by the density of state function:

$$Z(E) = (1 - f_1 - f_2) \cdot \delta(E - E_0) + \sum_{i=1}^{2} \frac{f_i}{\sigma_i \sqrt{\pi}} \cdot exp\left[-\left(\frac{E - E_i}{\sigma_i}\right)^2\right]$$

Where E_0 denotes the conventional interstitial lattice sites with a sharp site energy. Defect sites have a Gaussian site energy distribution, leading to delta distribution in the DOS.

$$Z(E) = (1 - f_1 - f_2)\, \delta(E - E_0). \qquad \text{(i)}$$

where $(1 - f_1 - f_2)$ is the number fraction of grain boundaries; $f_1 = N_{GB}$ and traps, $f_2 = N_{Traps}$. For defective metals, a fraction of interstitial site energy is replaced by a different kind of energy distribution. By considering sites like grain boundaries with different atomic arrangements, the DOS can be described by a Gaussian distribution

$$Z(E) = \sum_{i=1}^{2} \frac{f_i}{\sigma_i \sqrt{\pi}} \cdot exp\left[-\left(\frac{E - E_i}{\sigma_i}\right)^2\right] \qquad \text{(ii)}$$

Two kinds of defect sites are considered. They are grain boundary energy $E_1 = E_{GB}$ and trap energy $E_2 = E_{Trap}$.

(a)

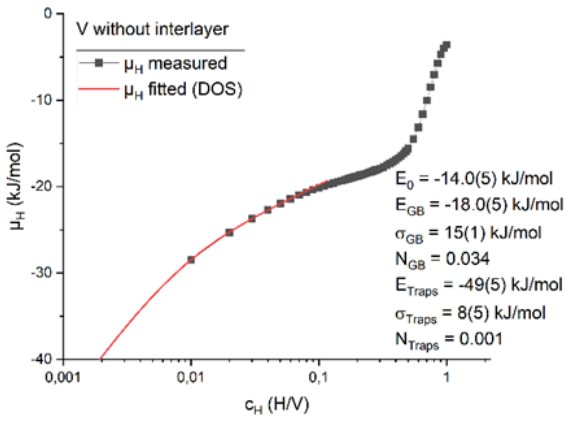

(b)

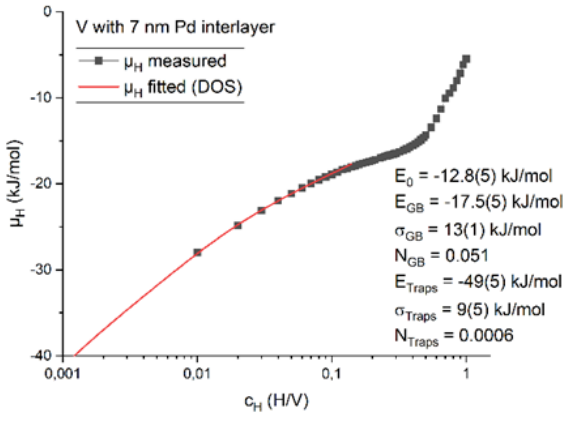

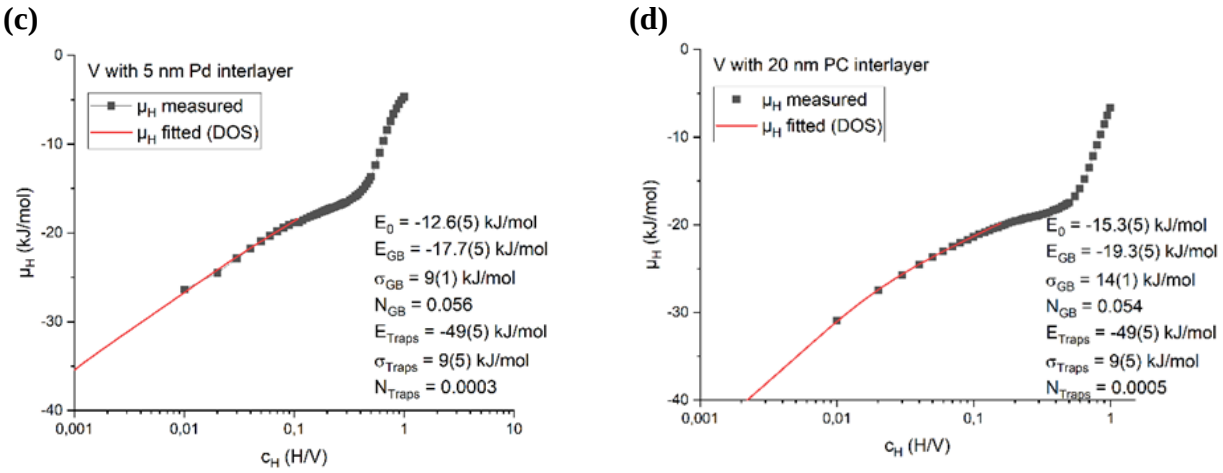

Figure 4.4.1: DOS model fitted to the measured EMF data of **(a)** no-interlayer V-film, **(b)** 7 nm Pd interlayer V-film, **(c)** 5 nm Pd interlayer V-film, and **(d)** 20 nm PC-interlayer V-film. The parameters are given in the boxes and addressed in the main text.

Application of the DOS model to the experimental data gives the results for different interlayer type V-films as shown in Figure 4.4.1. The deep traps possess an energy of -49 kJ/mol which relates to the Pd surface. The site energy E_0 becomes more negative from V with 7 nm Pd-interlayer to V no-interlayer to V with 20 nm PC-interlayer. We have -14 kJ/mol for the no-interlayer interstitial sites energy, and the PC-interlayer site energy becomes even more negative and is -15 kJ/mol. However, for the Pd-interlayer, the fit gives a site energy of -13 kJ/mol. This means, for the mixed interface samples (Pd-dots), hydrogen occupies preferentially the no-interlayer regions first, and for higher chemical potential, the interstitial sites of the Pd-dots are filled. For the mixed interface samples (PC-dots), the hydrogen should first fill the PC-dot regions and then the no-interlayer regions.

The energy levels of the "grain boundaries" also differ. They are predominantly negative for the 20 nm PC interlayer. This indicates the possibility of different kinds of grain boundaries in V for the stress-free (PC) films when compared to the stressed V-films (no-interlayer and Pd-interlayer).

Pd is not considered a trap since H does not enter Pd until V is fully loaded. Of course, the Pd/V interface might play a role as a trap. It may be noted that the number density of deep traps again is somewhat unrealistically small, questioning this parameter.

Chapter 5

STM Measurements

STM measurements during hydrogen gas phase loading with varying pressure and for different durations are used to observe the real-time change in the V-films surface morphology. They help to determine, the underlying mechanism by which mechanical stress redistributes in the sample and how it gets relaxed. In addition to STM measurements, electric resistance measurements were carried out, in the same UHV chamber. These measurements are not included in the thesis but were used for confirmation of results. The resistance measurements allow for monitoring of the phase transformation in the whole sample, while STM measurements show the situation on the local scale with 2 μm in maximum. Upon hydrogen gas exposure, the film resistance increases confirming hydrogen uptake while after pressure reduction for the STM measurement, the resistivity initially stays constant. This suggests a constant hydrogen content in the sample, during the window of the subsequently taken STM measurement.

It is not possible to load the pure V-film directly from the gas phase, as will be shown in following chapter; hence, V-films with different Pd-protective layer coverages are also used to evaluate the effect of hydrogen loading on the underlying V-films. Different surface coverage of the Pd-cap layer was chosen from partial to full coverage with 0.16 nm, 1 nm, and 8 nm in mean thickness.

The V-hydride formation pressure for the gas phase loading in the bulk sample is about 10^{-5} mbar, as determined by using pressure-composition-isotherms of V-H (see appendix A.6) [13]. This is the most interesting pressure region as it is correlated with high local stress increase due to hydride formation. However, this is exactly the pressure of gas discharge in the UHV chamber (see chapter 3). Therefore, additional strategies have been developed to observe the topographic changes in V-films. They have also been discussed in chapter 3. Due to this limitation, continuous monitoring of the same position is not possible, but in some cases, the presence of some special features or markers allows one to locate the original frame position.

5.1 Substrate preparation for deposition

The surface of the glass substrate after the cleaning procedure is shown in Figure 5.1 (AFM image). Ultrasonic cleaning of the substrate was performed using distilled water and an isopropanol bath before taking an atomic force microscopy (AFM) measurement. The overall view of the surface shown in Figure 5.1 (a) with 1×1 μm^2 size and (b) with 500×500 nm^2, size shows the close-up of the surface features. Figure 5.1 (c) presents the line scan with information that most of the surface features are below 1 nm in height. Therefore, the topography roughness is σ_{RMS}= 0.28 nm. A few brighter spots are detected and unexpected as the substrates are hand-cut. Nano-size particles that get stuck to the surface are seen in AFM images.

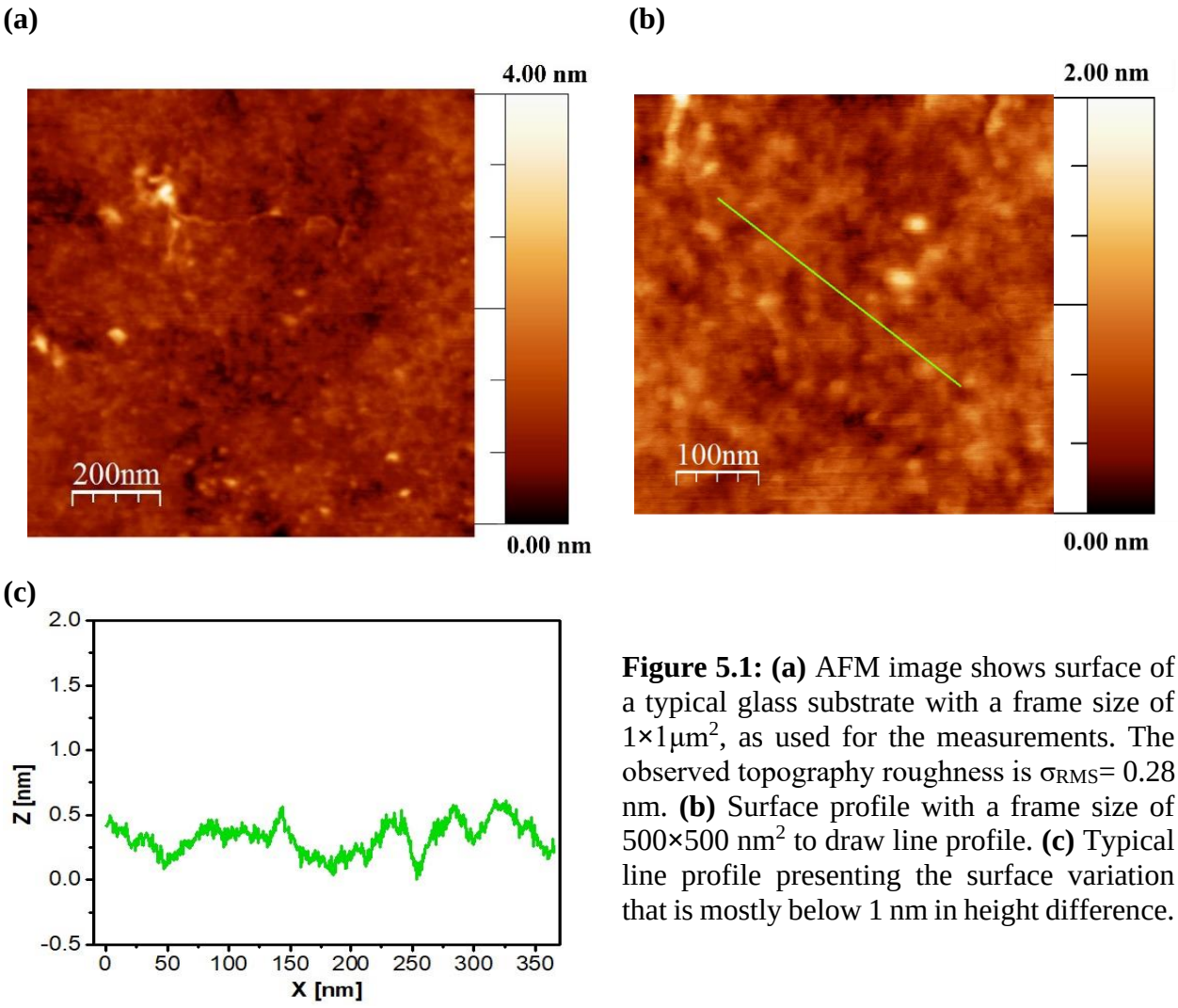

Figure 5.1: (a) AFM image shows surface of a typical glass substrate with a frame size of $1\times1\mu m^2$, as used for the measurements. The observed topography roughness is σ_{RMS}= 0.28 nm. **(b)** Surface profile with a frame size of 500×500 nm^2 to draw line profile. **(c)** Typical line profile presenting the surface variation that is mostly below 1 nm in height difference.

5.2 Sample topography: pure vanadium surface

The pure vanadium film surface is hard to monitor. Even if the background pressure of the deposition chamber and STM chamber stay in the 10^{-10}-10^{-9} mbar range, a layer of vanadium-oxide will form on the film surface within a few minutes. An oxidized V-film cannot be analyzed by STM as well as loaded with hydrogen. This issue can be solved by using a small amount of Pd, of 0.16 nm thickness deposited within 10 seconds, resulting in smooth measurements. This technique has already been successfully used for niobium films [12]. Figures 5.2 (a) and (b) present selected STM images of the Pd (0.16nm)/V(30nm)//glass sample surface morphology. This helps us, determine the topography of the V-film and the V-grain sizes.

The surface topography depicted in Figure. 5.2 shows two types of morphologies. First, a ripple structure appears locally in parallel, but on a larger scale in different directions. Regions with parallel ripples are attributed to the surface of individual grains, as their bordering size equals that is expected for V-film grown at room temperature on glass substrates. As will be shown later, this ripple structure has underlying surface topography even when thicker Pd layers are deposited. This confirms the interpretation of V-grains.

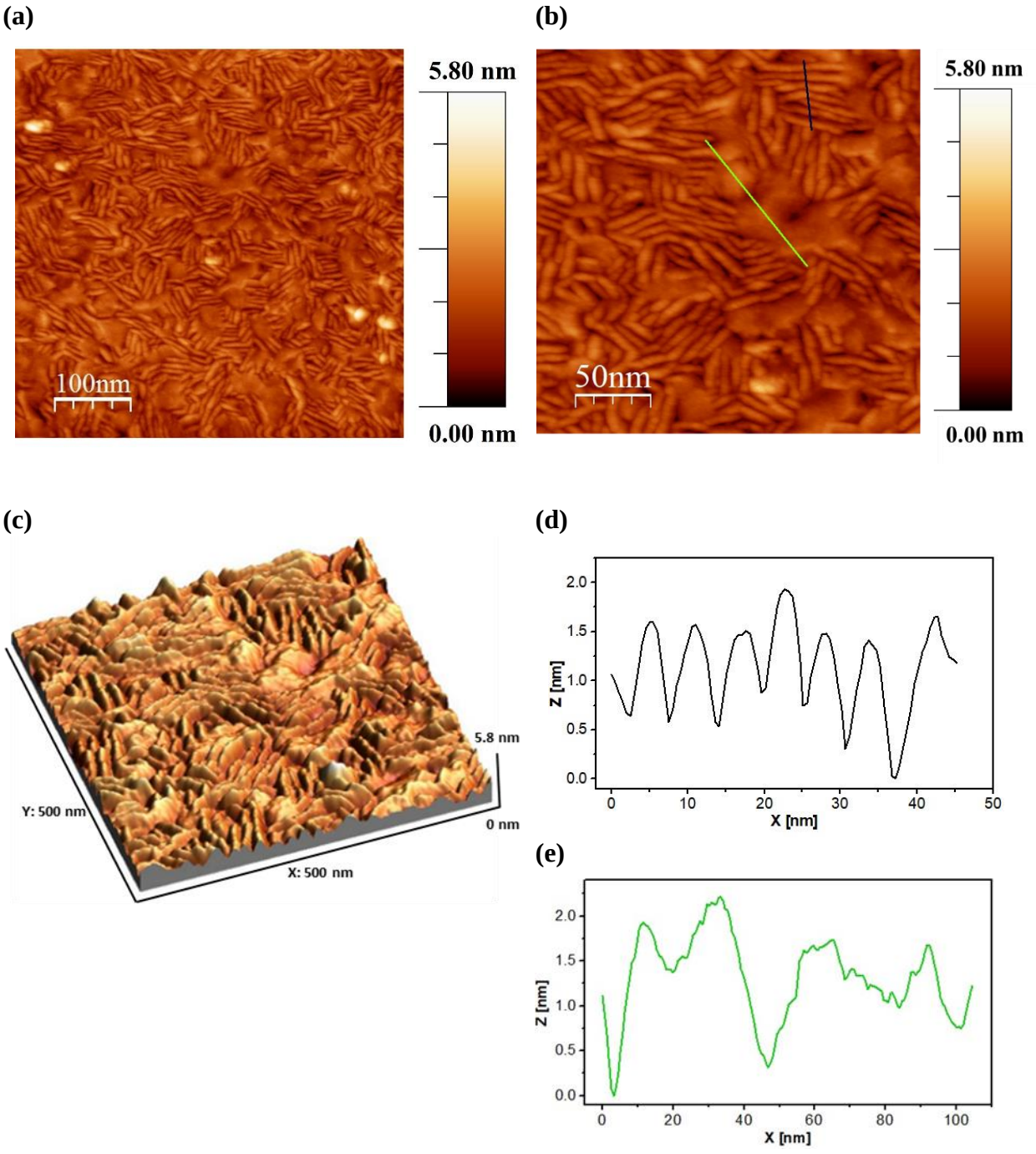

Figure 5.2: (a) STM images of the surface topography of the Pd (0.16nm)/V (30nm)//glass sample surface with a frame size of 500×500 nm^2, **(b)** STM images with higher resolution at a frame size of 250×250 nm^2, and **(c)** as 3D STM image profile show two types of surface features: ripples and dots. For a region of parallel ripple direction (grain), Figure 5.2 **(d)** shows the line profile of this substructure at the surface of the vanadium grains, having a very periodic appearance. (**e)** small islands are also visible representing Pd dots.

The substructure of the grains looks like waves with a symmetrical geometry, as shown in the line profile in Figure 5.2 (d). The dimensions of these substructures are given in Figure 5.2.1 (a). Length in the range of 25 nm to 35 nm, width ranging from 6 nm to 10 nm, and the heights of these features are below 2 nm, also see the line profile in Figure 5.2 (d). More details are furnished in Figure 5.2.1 (a) which shows STM images and the detected size (length, height, and width) of the ripple substructure.

The second kind of surface feature that can be seen in Figure 5.2.1, is blurred islands that are rather flat. Figure 5.2.1 (b) focuses on these features and (c) presents the line profile of the grains and the blurred features along the green line, as shown in part (b).

(a)

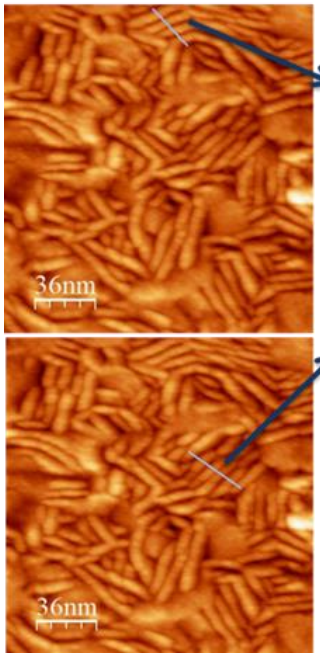

Length nm	height nm	width nm
35	1-1.6	8
25	0.45-0.7	10
35	0.8	7
35	0.3	6.4
35	1	8
28.5	1.1	8
28	1.3	6.8
27	1.3	6.9
35	1.3	6.2

(b)

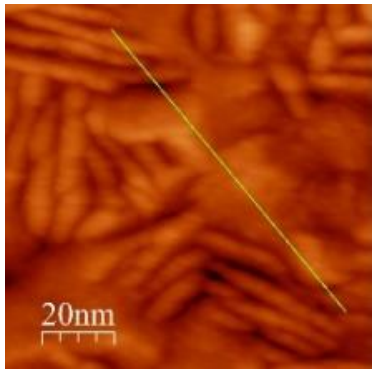

(d)

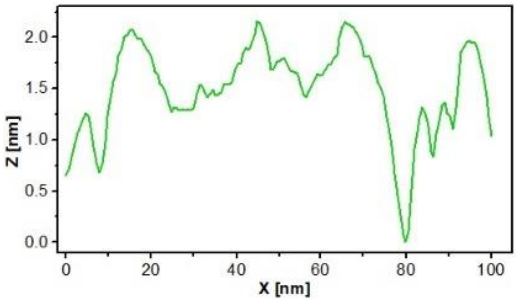

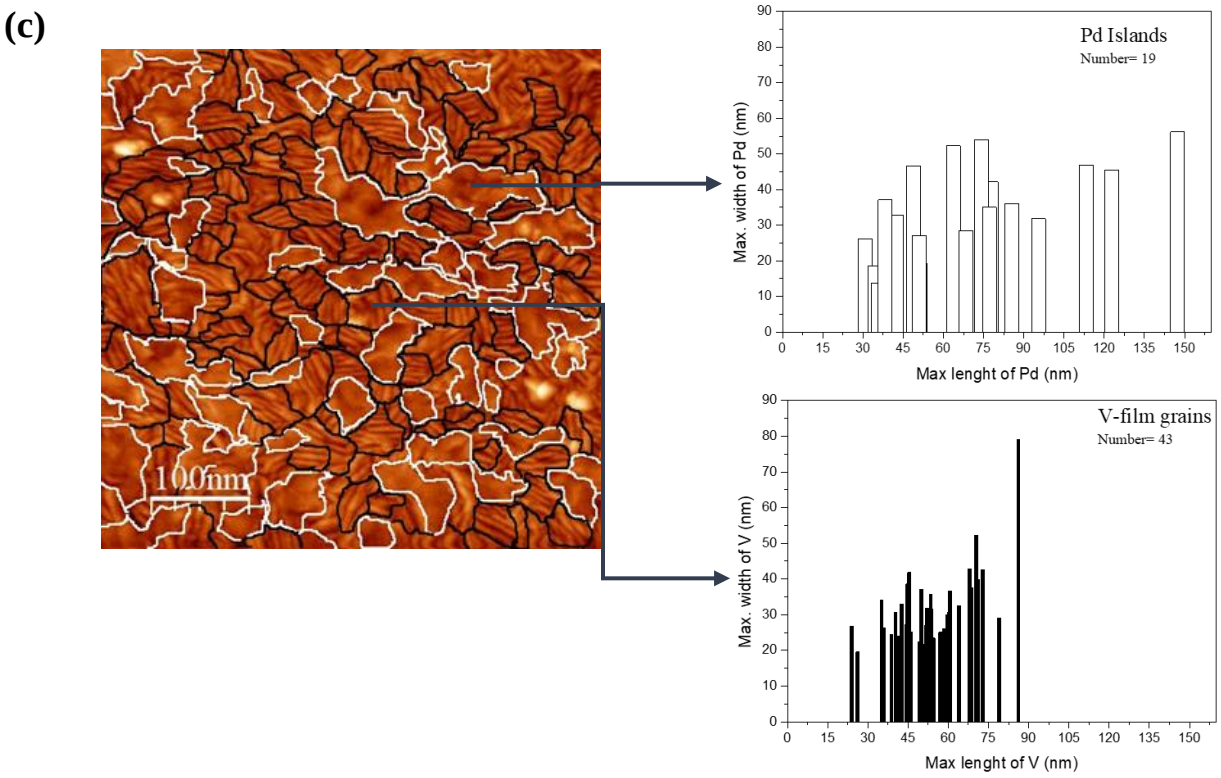

Figure 5.2.1: (a) STM-surface images and related substructure information (length, height, and width), **(b)** shows the blurred regions related to Pd particles and a line profile crossing several particles, **(c)** shows the overall distribution of V grains (bordered by black lines) and Pd particles (bordered by white lines), **(d)** presents histograms on the Pd dots size and the V film grain size distribution.

The blurred features are attributed to Pd particles, that arise from the deposited Pd as shown in Figure 5.2 (e) with a green line, and Figure 5.2.1 (b). These islands have a height of less than 2 nm while their lateral size varies from 13 to 150 nm. As will be shown later, these islands vanish upon an increase in Pd-thickness. Figure 5.2.1 (c) presents an STM-overview image of the positions of these two surface features. Black borderlines highlight the V-grains while white borderlines present the Pd-islands positions. The black boundaries are drawn by considering the ripple substructure that is interpreted as aligned inside of one V-grain.

The blurred regions are used to draw the white lines for the Pd islands. Figure 5.2.1 (d) presents the size distribution for the V-film grains and the Pd islands. Moreover, 80% of the Pd dots in the measured sample region have a maximum width between 20 nm and 55 nm and a maximum length of 30 nm -100 nm. Furthermore, 76% of the V-grains have a maximum width between 20 nm and 40 nm and a maximum length of 35 nm - 60 nm.

Figure 5.2.1 (c) confirms a higher number of V-grains which are smaller in lateral size when compared to the Pd islands.

Though these Pd islands help in measuring the surface topography, extended STM measurements are not possible for these samples: the signal gets worse with time. After two hours of measurement, the signal gets so bad that the tip doesn't get in contact anymore. This is interpreted as oxidation of the V-film which is exposed to the environment in between the Pd-islands. The environment contains a certain amount of oxygen partial pressure even under these ultra-high vacuum conditions. Thus, for extended STM measurements, especially for hydrogen-loading experiments which take more than one day, a thicker coverage of Pd is required. However, it should be kept as thin as possible, to examine the behavior of the underlying V-film.

5.3 Surface morphology of the Pd(1nm)/V(30nm)//glass

To allow for extended STM measurements and to perform hydrogen loading, the surface of the V-film is covered with 1 nm of Pd. This allows for successfully measuring for the longer periods of up to three days. But, because of the Pd coverage, the grain boundaries and the surface topography of the V-film become less visible in the STM.

(a) Without hydrogen loading

A sample in the as-deposited state is shown in Figure 5.3 (a) with 400×400 nm^2 and (b) with 150×150 nm^2 frame size. Related to the green and red lines in Figure 5.3 (a), the line profiles are shown in (c). The topography of the surface features with V-ripples shows heights of less than 2 nm. Related to the green and red lines in Figure 5.3 (b) we can see the width of 6 nm - 8 nm (green line) and visible lengths between 20 nm and 35 nm, as shown in (d). The 1 nm Pd deposited on the sample shows features with heights in the 2 nm range and with widths between 50 and 100 nm approximately covering the surface, as shown in 5.3 (d). The surface appearance is in line with the interpretation given in part 5.2, as the blurred regions increase because of the increased amount of Pd, while the ripple structure of the V-grains becomes less visible.

The grain size of the vanadium is not expected to change by the presence of the Pd coverage, thus the vanadium grains vary between 20 nm and 40 nm in width and 35 nm and 60 nm in length (see chapter part 5.2).

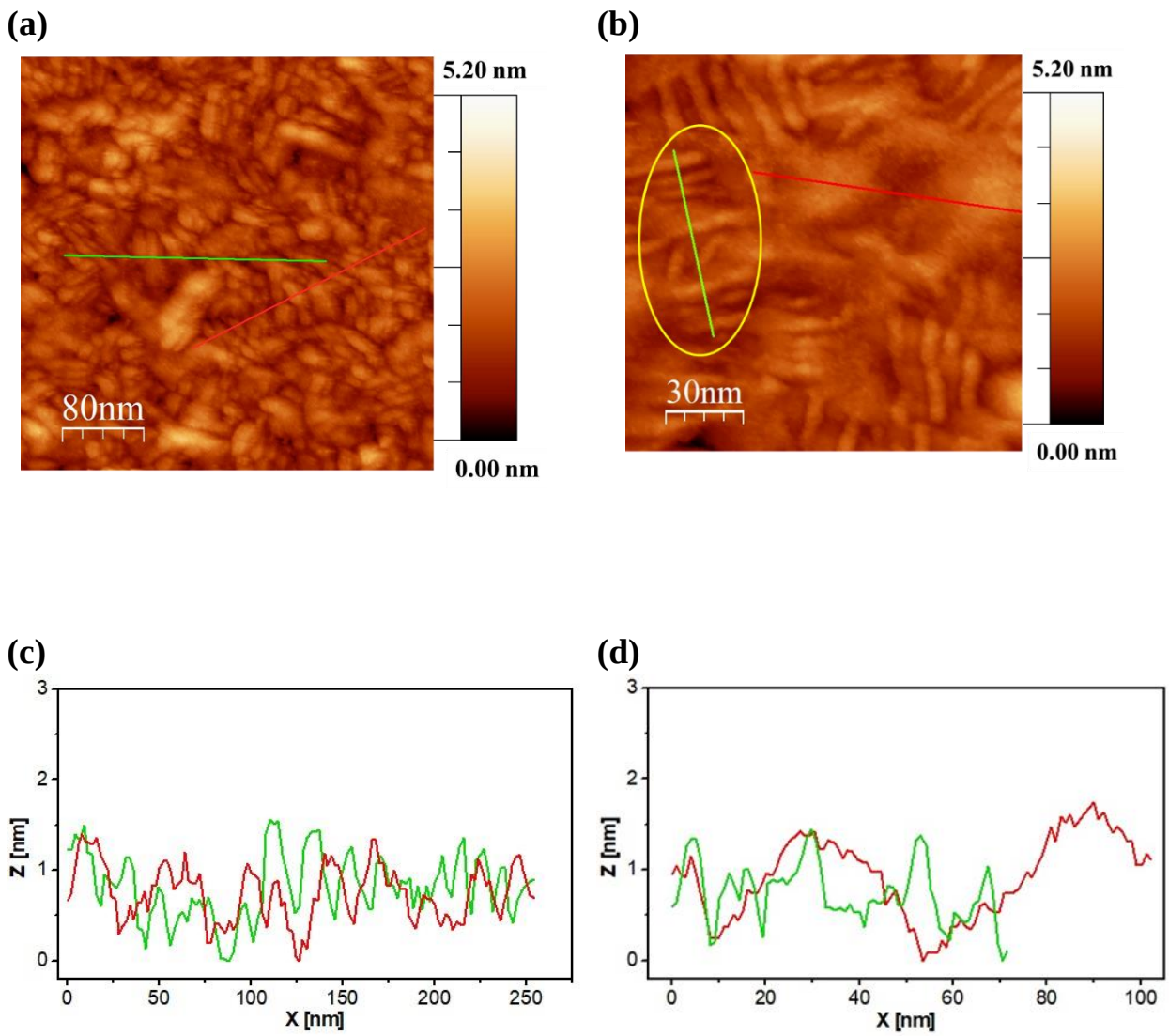

Figure 5.3: STM images of **(a)** of 400 × 400 nm^2 part showing the modulated V surface structure, and **(c)** showing the line profile of image a), the surface topography including the blurred Pd particles. Figures **(b)** and **(d)** focus on the local surface topography of the V grains and the Pd particles, respectively. The circle highlights the V surface oscillation of about ~7 nm.

(b) After hydrogen gas exposure at p_H = 8.3× 10^{-4} mbar, 30 min

The sample described above in its as-deposited state is loaded by applying 8.3× 10^{-4} mbar hydrogen partial pressure. This pressure is slightly below the pressure of hydride formation for the bulk system, in the solid solution phase. It leads to changes in the surface topography, as can be seen in Figure 5.3.1. It may be noted that as this is close to the gas discharge region, the STM measurement was done at lower pressure, but directly after the loading (see chapter 3). The two different surface features related to the Pd islands, and the V-grains are no more distinguishable in the way described

before. The observed surface features have heights of 3.5 nm - 4 nm and are broader than as deposited sample features. The blurred Pd regions are not observed anymore. This suggests the possibility of surface alloying between Pd and V. The related line profiles are shown in Figures 5.3.1 (c) and (d). Humps of 100 nm - 350 nm (length) and 200 nm (width), with feature sizes ranging from 30 nm to 40 nm in diameter and heights between 1 nm and 3.5 nm are observed (see Figure 5.3.2 (a) and (b). These humps are much larger than the size of the initial grains. It is interesting to note here that these features still show a ripple-like substructure, see Figure 5.3.1 (a). Even though the substructure still exists, its changings in its dimension. This can be seen more clearly in Figure 5.3.1 (b) and (d).

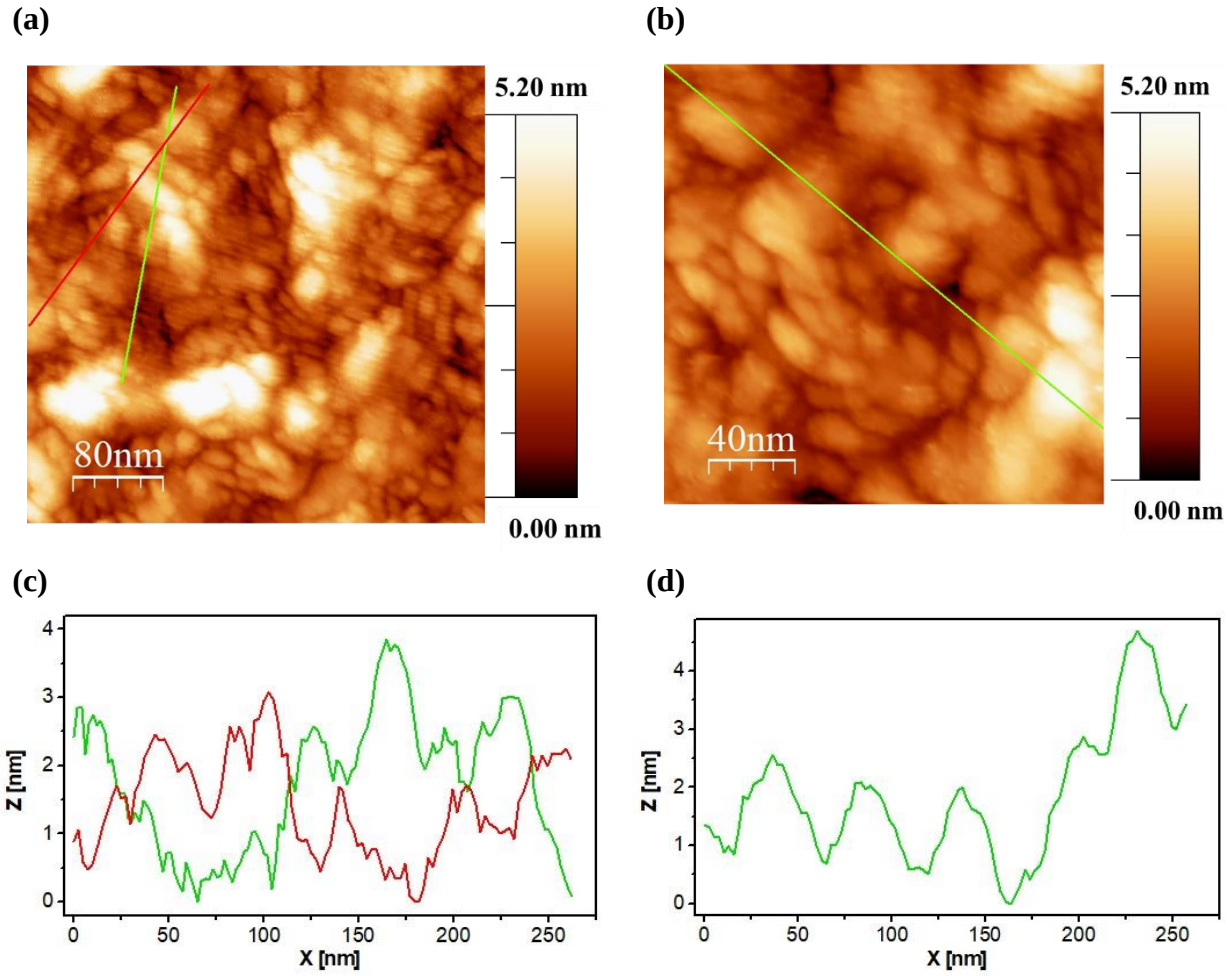

Figure 5.3.1: STM measurements of Pd(1nm)/V(30nm)//glass **(a)** showing the V-surface topography oscillations remain after hydrogen loading at 8.3 × 10^{-4} mbar hydrogen pressure (400×400 nm^2 frame size). **(b)** shows the sample surface at 200×200 nm^2 scale. **(c)** and **(d)** present the related line scans of the surface topography which develops after hydrogen loading.

The white lines, shown in Figure 5.3.2 (a), border the humps. To measure the extent of changes, traces of the hump boundaries are shown in Figure 5.3.2 (a), with a chosen region presented in different color scales as shown in part (b). The details of the sizes of the humps are given in table in Figure 5.3.2 (b). The STM image in Figure 5.3.2 (b) shows the selected sample position (with selected humps to be measured) from the bigger surface region, shown in Figure 5.3.2 (a). The mean size of the topography humps is 198 (±20) nm in length, 128 (±10) nm in width, and 3.4 (±0.3) nm in height. Thus, the hump's height is about double the height of any of the surface features of the unloaded sample, about seven times the size of the V-grains, and three-time the size of the Pd deposits in lateral size, compared to the unloaded sample.

(a)

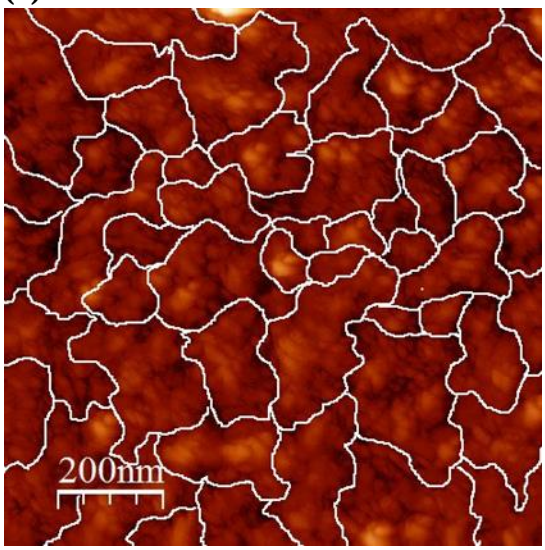

(b)

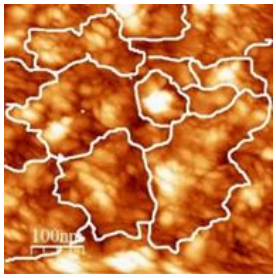

Number	Length nm	width nm	Height nm
1	343	169	3-3.7
2	204	194	
3	200	170	
4	249	200	
5	101	85	
6	200	117	
7	148	45	
8	100	33	
9	240	135	
averge size	**198 (±20)**	**128 (± 10)**	

Figure 5.3.2: (a) shows the STM image of the Pd(1nm)/V(30nm)//glass sample, after hydrogen loading at 8.3×10^{-4} mbar hydrogen pressure. Surface humps are outlined by white lines, for the 1×1 μm^2 region. **(b)** The selected area of a 500×500 nm^2 frame presented with different color scales for better visibility of the internal micro-structure, showing the grains for measuring the sizes. The relative sizes are given in the table.

Figures 5.3.3 (a) and (b) depict the two states and corresponding 3D view of sample (a) without hydrogen and (b) in the loaded state. These images show typical surface topographies, but not the same position (see chapter 3). After loading, the small surface ripples are merged and broadened. Thus, the hydrogen uptake results in humps of similar height as the initial ripple structure. The humps have about a 2 nm height difference between the surface of the hump and the deeper valley around it.

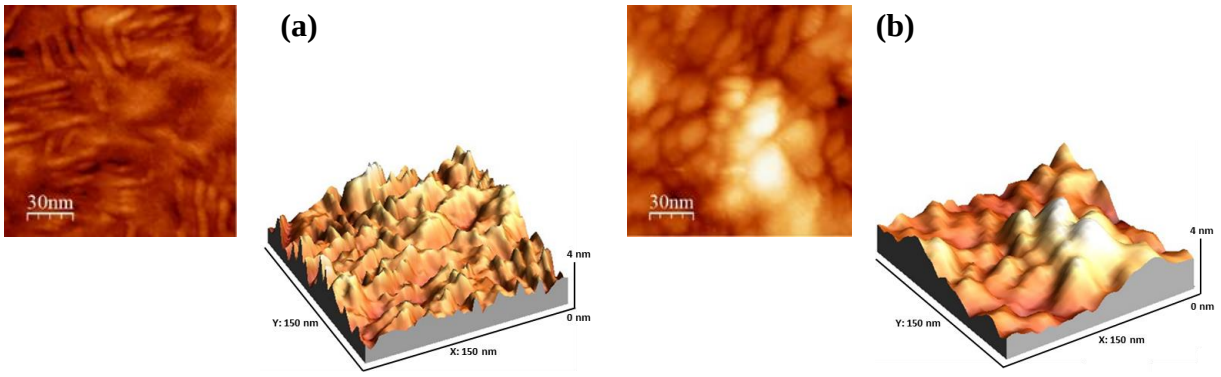

Figure 5.3.3: Surface images and 3D views of the Pd(1nm)/V(30nm)//glass sample **(a)** before hydrogen loading, and **(b)** after hydrogen exposure at 8.3×10^{-4} mbar hydrogen gas pressure, for 30 min. The 3D format visualizes that the small surface features (visible before loading in (a)) seem to be merged after the hydrogen loading (see **(b)**).

5.4 Effect of long loading time

Figure 5.4 (a) shows a similar Pd(1nm)/V(30nm)//glass sample, but it is investigated after hydrogen loading with a longer duration and with lower gas pressures. Thus, the pressure is expected to be below that required for hydride formation. The sample shows the characteristic features with ripples and blurred Pd-islands in Figure 5.4 (a), and in the line profile of Figure 5.4 (b). The surface micro-structure varies in height by 1nm - 2nm.

(a) First loading step at $p_H = 1.4\times10^{-4}$ mbar for 12 hour

Figures 5.4 (c) and (d) show the loaded state of the sample, after low-pressure loading at 1.4 mbar total pressure for 12 h in an Ar+H_2 atmosphere mixture (0.01% of H_2) or at 1.4×10^{-4} hydrogen partial pressure. This pressure is below the hydride formation pressure, of the bulk system. It is emphasized that the measurement was done after pressure reduction. After this hydrogen exposure, we see no prominent changes in the surface morphology. The related line scans shown in Figure 5.4 (b) before loading and in (d) after loading have features of the same height but get a little broader in the lateral direction, after hydrogen exposure. This indicates changes in the film surface upon hydrogen exposure.

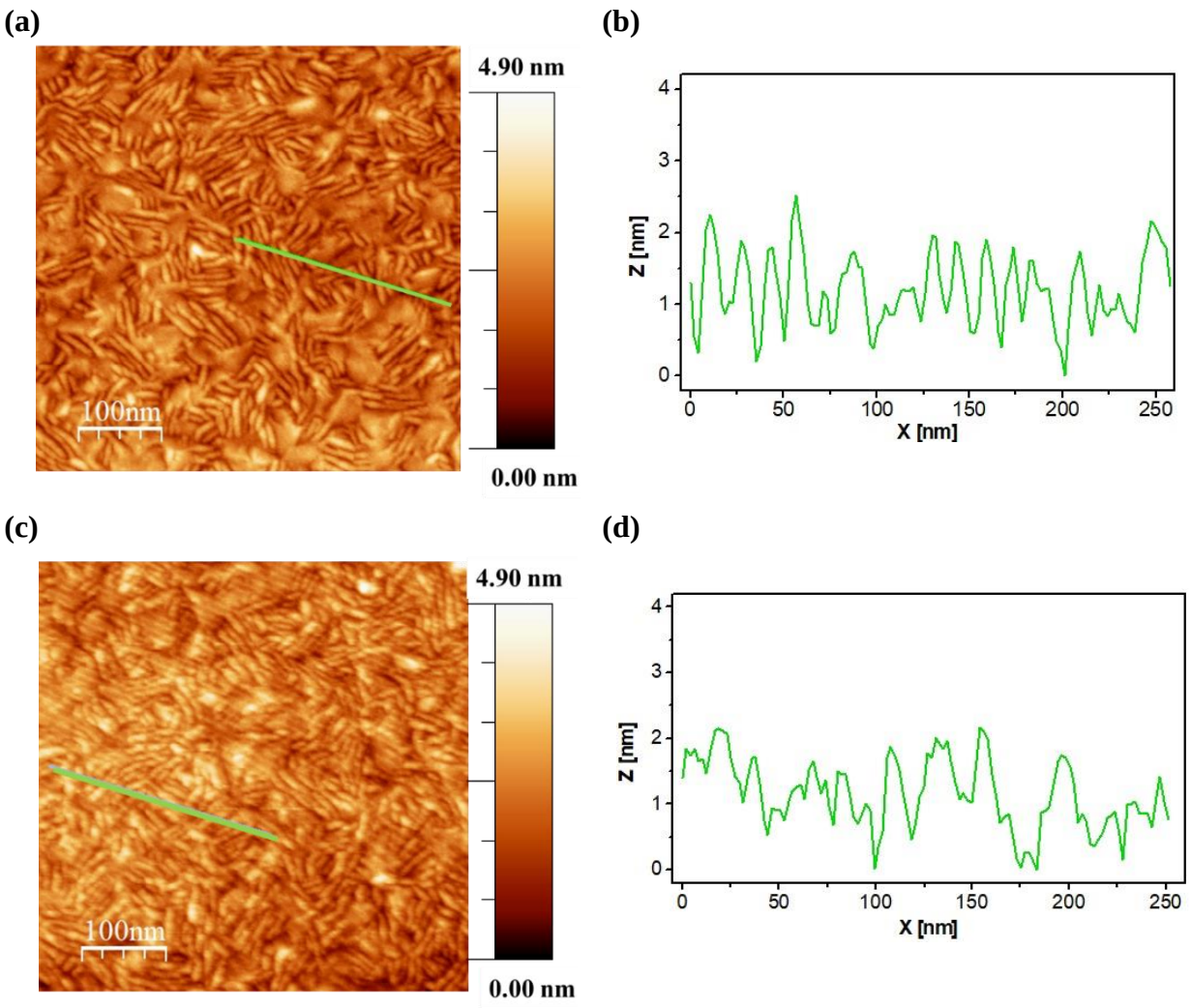

Figure 5.4: STM images of a Pd(1nm)/V(30nm)//glass sample, loaded with different time duration for low-pressure loading. **(a)** sample in the as-deposited state, **(c)** after loading done in 1.4×10^{-4} mbar pressure of H_2 for 12 hr. This results in a small change in surface, **(b)** and **(d)** line profiles show small changes in height profile.

Figure 5.4 (c) shows the diagonal periodic oscillation due to electrical noise. As the periodicity is in the same order as the surface modulation, noise filtering by Fourier transformation is not applied.

(b) Second loading step at $p_H = 1.1\times 10^{-3}$ mbar for additional two hours

Figure 5.4.1 (a) presents the initial surface topography and 5.4.1 (b) shows the related line scan. As shown in the previous paragraph, only small changes occurred after exposure to a hydrogen partial pressure of 1.4×10^{-4} mbar, for 12 hr. The second loading step is done with a total pressure of 11 mbar (Ar+0.01%H_2) or a $p_H = 1.1\text{x } 10^{-3}$ mbar hydrogen partial pressure for 2 hr. This pressure is roughly the hydride formation pressure, of the bulk system. After about 15 min. of pressure

reduction in the chamber, the STM measurements have been started. Instead of the small surface features (Ripples and Pd-islands), now comparatively large size features appear. The first observation is that the V-surface with its ripples and the Pd islands cannot be differentiated anymore, see Figure 5.4.1 (d) and (g). The height profile shows small humps ranging up to 3.5 nm (see Figure 5.4.1 d), (e). In the lateral direction hump (grain) sizes of 50 nm - 170 nm are measured.

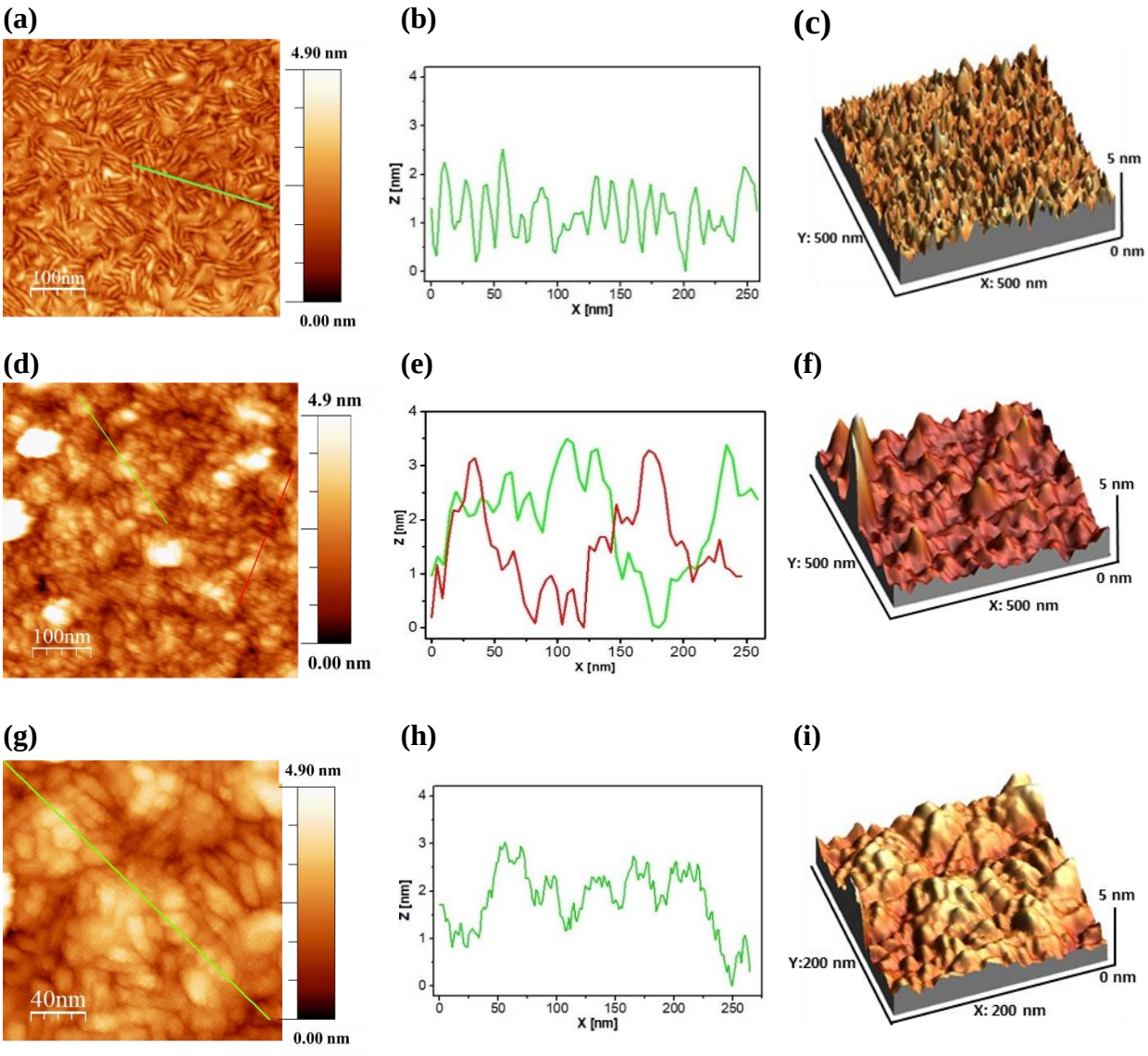

Figure 5.4.1: STM images, with (500×500 nm^2), line profiles and 3D-images of a Pd(1nm)/V(30nm)//glass sample, **(a)-(c)** in the as-deposited state and **(d)-(f)** in the loaded state after exposure to a hydrogen partial pressure of 1.1×10^{-3} mbar, for 2 hr. **(g)-(h)** shows the loaded state for a smaller frame size of 200 × 200 nm^2. The line profiles **(b), (e), (h)** and the 3D images **(c), (f), (i)** show strong surface feature changes arising due to loading.

Image (g) is taken from image (d) for better visibility of the new surface features. Comparing the line profile (b), (e), and (h) and 3D structure, (c), (f), and (i) visualize the extension of the changes. In the higher resolution image (g) small surface features (ripple of as-deposited state) visibly still exist within one hump, but now they are not aligned in parallel anymore and they expand over a broader region. The line profile (h) is showing very accurately the presence of these small height variations on top of the humps.

To see the change and development happening at the same spot is not so easy as each measurement is done after filling the chamber with hydrogen gas and then evacuating again. During this procedure, the STM measurements were paused, and the scanning tip was retracted back by one coarse step so that the sample could be loaded with hydrogen. Subsequent pressure reduction and reapproaching the tip to the surface commonly result in a sample position completely off from the previous working position (for details see chapter 3). However, markers or special surface features can be used to find the original frame position, again. To take advantage of this knowledge two large features (visible as white dots) are taken as markers in Figure 5.4.2 (a) before hydrogen loading and (d) after hydrogen loading. This allows for monitoring the surface at the same sample location.

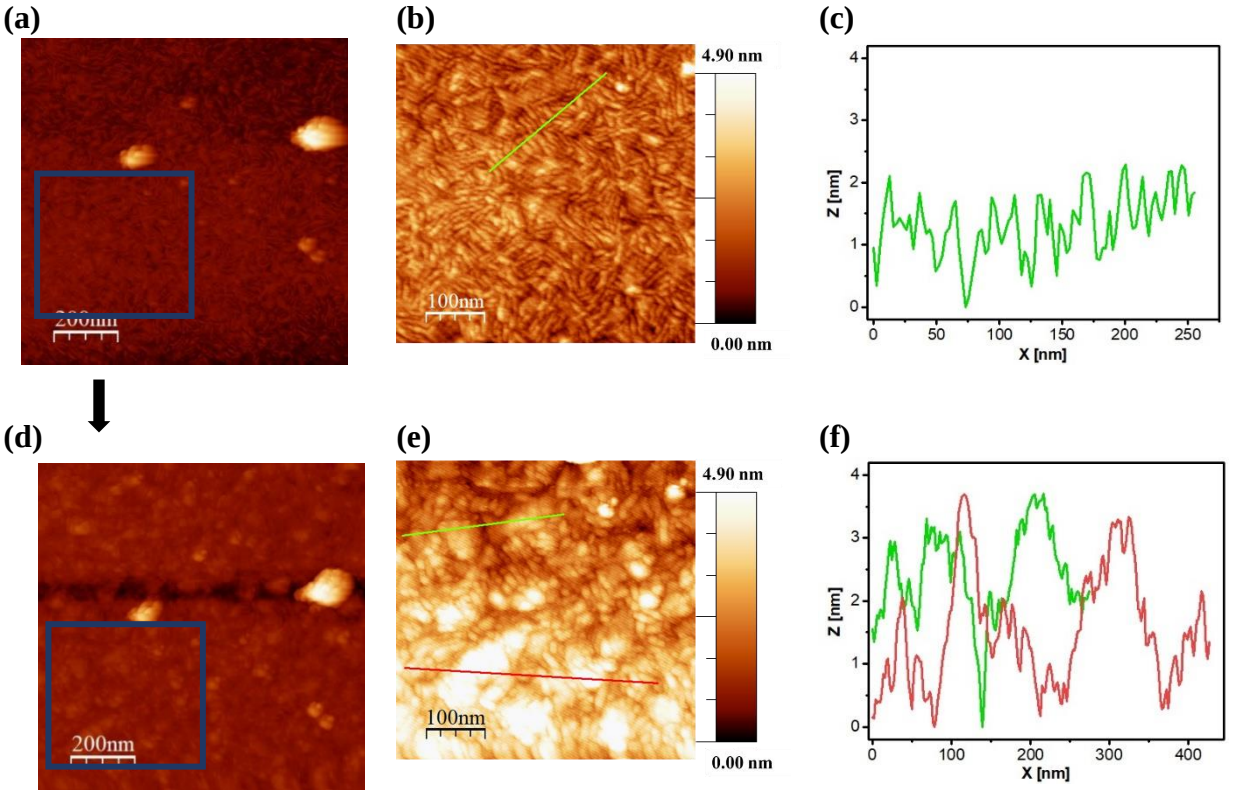

Figure 5.4.2: STM images **(a)** and **(d)** with 1 x 1 μm^2 frame, and a selected position **(b)** and **(e)** with 500 ×500 nm^2 frame size as well as line profiles **(c)** and **(f)** taken on a Pd(1nm)/V(30nm)//glass, after loading in 1.4×10^{-4}mbar hydrogen partial pressure for 12 hr and 1.1×10^{-3} mbar hydrogen partial pressure for more than 2 hr. The surface morphology changes visibly after an increase in hydrogen partial pressure from 1.4×10^{-4}mbar to 1.1×10^{-3} mbar.

Figure 5.4.2 (a)-(c) presents, how the sample surface after the loading was done at $p_H = 1.4\times 10^{-4}$mbar partial pressure of H_2, and d)-f) at $p_H = 1.1x\ 10^{-3}$ mbar partial pressure of H_2. As the scan was done with a large frame of size $1\times1\mu m^2$ and two large features were present, it becomes possible to observe the same spot. Figures 5.4.2 (b) and (e) are taken from the square area highlighted in Figures 5.4.2 (a) and (d), respectively. Some bright spots appear after the higher-pressure exposure. The surface features are visibly changing from 1.5 nm -2.0 nm height difference to 3 nm -3.5 nm height difference. Thus, the surface roughness now increases by increasing the height difference. Even though small surface ripples still persist, they appear now on a broader scale with a 50 nm-100 nm of the range of the width. This can be clearly seen in the line scans presented in parts (c), and (f).

At a pressure of 1.1×10^{-3} mbar, the sample surface changes from a very uniform ripple topography to a surface showing larger heights and lower valleys. The extent of these changes depends on the exposure time and pressure value. As will be shown in the following part, it is also affected by the thickness of the Pd coverage.

5.5 Surface morphology of Pd(8nm)/V(30nm)//glass

To protect the vanadium surface from oxidation for more longer durations and to allow for even more extended STM measurements, a coverage of 8 nm Pd was deposited on top of the vanadium film. This allowed us to successfully perform STM measurements running for more than one week. However, as the Pd film covers the vanadium surface, grain boundaries and the surface topography features of the V-film are expected to become even less visible. But the loading kinetics is expected to get faster and possibly more uniform because of the more closed Pd-layer.

(a) Surface development before hydrogen loading

Figure 5.5. shows the surface topography of the Pd(8nm)/V(30nm)//glass sample, presented by STM images, line profiles, and 3D images. The upper row shows a large field of view, while the lower row shows zoomed-in results. Figure 5.5 (b) presents the line profile of the sample, showing surface topographies having lateral sizes between 8 nm and 25 nm and a height variation of 2 nm. This resembles the height variation of the vanadium surface topography shown in Figure 5.2.

By looking more closely, the modulated surface topography of the vanadium results in a periodic assembly of Pd islands, as shown in Figure 5.5 (e). When crossing the islands in the direction

shown in part (d), a periodic line profile can be seen. Also, the underlying vanadium modulation seems to be visible, providing ripple-like features.

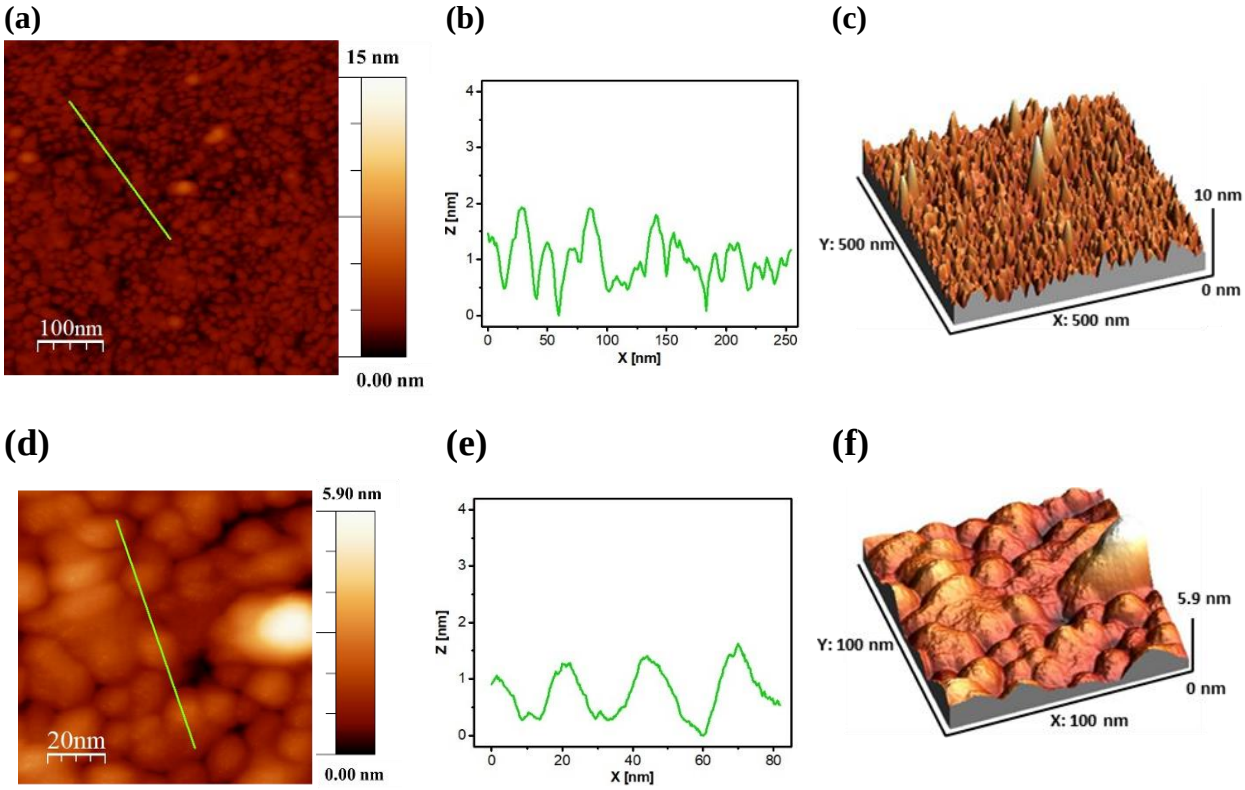

Figure 5.5: STM measurement on Pd(8nm)/V(30nm)//glass sample**. (a)** as-deposited state. **(b)** line profile showing, surface feature height profile variations in the range of 2 nm. **(c)** 3D demonstration. **(d)** zoom in on figure (a). A line profile depicting the symmetry of the underlying features in **(e)** and **(f)** shows a 3D view.

Figure 5.5 (c) presents the 3D format, showing the surface topography more clearly. The enlarged 3D format is shown in Figure 5.5 (f). In total, the Pd 8nm coverage has formed individual islands following the underlying symmetry of the V-films ripple topography. As the measurements are possible for even one week, it can be concluded that there exists a protective layer of Pd below the Pd islands. This hints a Stransky-Krastanov-like growth of the Pd coverage.

(b) After hydrogen gas exposure at $p_H = 6.7\times10^{-2}$ mbar

STM measurements on the Pd(8nm)/V(30nm)//glass sample, loaded with a high hydrogen pressure as compared to other samples are shown in Figure 5.5.1. This pressure is exerted above the hydride formation pressure of the bulk system. The morphological change is large compared to all other measured samples (see Figure 5.5.1 (a) where the maximum color scale ranges over 20 nm). The

overall appearance has changed and now surface topographies with a height difference between 8 nm and 15 nm are visible, as presented in the line profiles in Figure 5.5.1 (b), (e). Large valleys and elevated areas have appeared. While surface topography on the elevated areas has height changes between 6 nm and 7 nm, the valley-to-island change is in the range of 15 nm. To compare, before hydrogen exposure, the surface showed a uniform height variation below 2 nm in difference, and a width of 8 nm - 25 nm, the so-called ripple structure. This ripple structures still exists after hydrogen loading as the same lateral dimensions of 8 nm - 25 nm width are still visible, but now sitting on top of the different regions accompanied by a larger surface height change. This is exemplarily visible in the green line profiles (b) and (e) highlighted with black arrow.

(c) Long-term unloading after hydrogen gas exposure at $p_H = 6.7\times10^{-2}$ mbar

The (ir)reversibility of the massive surface change is studied by running long-time STM measurements at about 1×10^{-9} mbar background pressure. Here, hydrogen unloading of the vanadium film is expected to occur.

Figure 5.5.1 presents an STM measurement on the Pd(8nm)/V(30nm)//glass sample after hydrogen loading at 6.7×10^{-2} mbar hydrogen pressure, with STM images, line profiles, and 3D representation of surface topography, directly after loading (a-c), after 12 hr (d-f) and after 7 days (g-i). Even after 12 hr of unloading in the UHV system, the huge height variations still exist, as shown in Figure 5.5.1 (d). In some parts in Figure 5.5.1 (d) the small ripple features are still visible; they are highlighted by the red line scan (2). The blue line scan (3) in Figure 5.5.1 d) shows 13 nm height change from one elevated part to a reduced area. Such an abrupt height change (step) was not observed in the sample directly after loading and, therefore, is here attributed to sample unloading. The remaining ripple structures are detected on top of both parts. These remaining ripple structures are visible, especially in the green line profile (1).

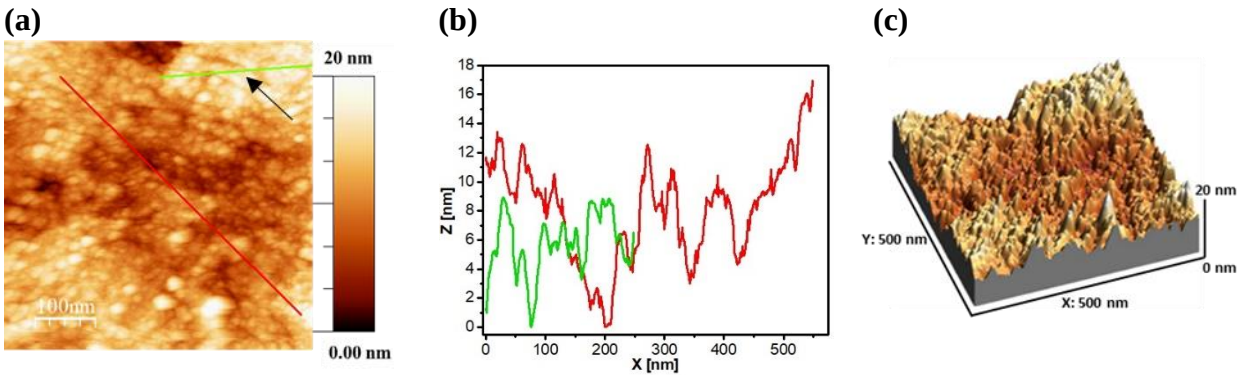

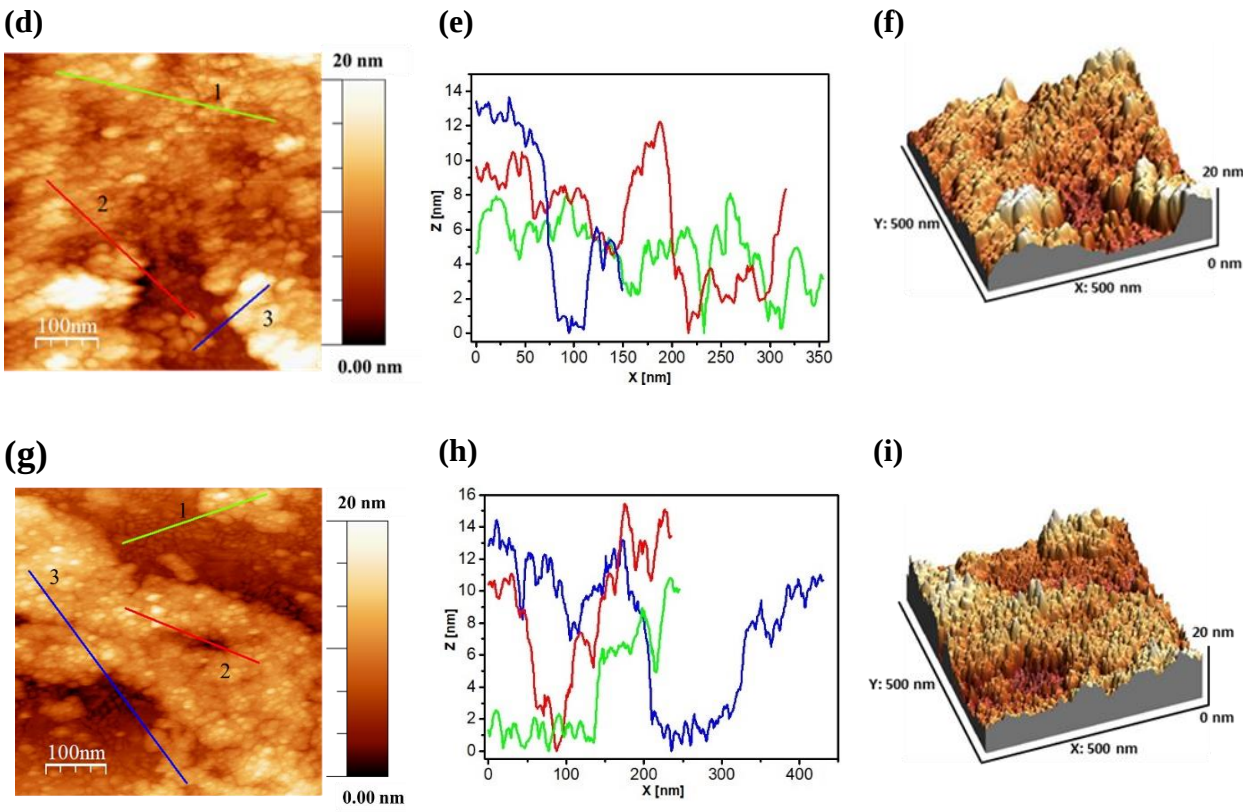

Figure 5.5.1: STM measurement on Pd(8nm)/V(30nm)//glass hydrogen loading for 6.7 × 10^{-2}mbar hydrogen pressure **(a)** sample loaded with 6.7 × 10^{-2} mbar hydrogen partial pressure, **(b)** line profile showing feature height profile variations with hydrogen loading, **(c)** 3D demonstration of surface morphology, **(d)** After 12 hr of unloading in UHV conditions, **(e)** line profile showing feature height profile variations, **(f)** 3D demonstration of surface morphology, **(g)** sample after 7 days in unloading state, **(h)** corresponding line profile and **(i)** the corresponding 3D view.

Figure 5.5.1 (g) is recorded after 7 days of unloading the sample in the UHV STM chamber. As already mentioned, it is not possible to measure at the same sample position, so part (g) shows a different position. However, even after 7 days the height variation on the sample surface is similar to the height variation after 12 h (see Figures 5.5.1 (h) and (e). Possibly, the number of these height variations is increased, as a larger part of the image shows height-reduced areas. This is difficult to judge because of the limited size of the frame. Again, the two surface features are visible in the line profiles. While the green (1) and the blue line profile (3) show remaining ripple surface features in the valley with 2 nm height variation, large abrupt height changes are detected leading to 14-15 nm height. The red line profile (2) shows remaining ripple surface variations on the elevated areas.

Comparison of Figure 5.5.1 (a) showing the initial scale of surface changes, with Figures 5.5.1 (d) and (g) shows the step transition from a wavy surface topography to the one with elevated areas

accompanied by valleys with deep pockets (steps). The presence of the surface topography was verified by performing forward and backward scans (see chapter 3).

The images show a very rough surface, after 12 hr of reduced pressure. The line profiles give details of about 10 nm steps between the valleys and the hills. This height change is very large, considering only the 30 nm film thickness of the initial vanadium film. However, they confirm hydrogen release from the vanadium film.

Figure 5.5.2 presents the surface development after 12 h of unloading, with different resolutions. The first image (a) is taken at 12 h with an image size of 500×500 nm^2, the second image (b) is taken after 12 h 40 min with an image size of 1×1 μm^2, and the third image (c) is taken after 13 h 20 min with an image size of 2×2 μm^2 and (d) taken after 14 h with an image size of 2×2 μm^2.

(a) after an additional 10 min

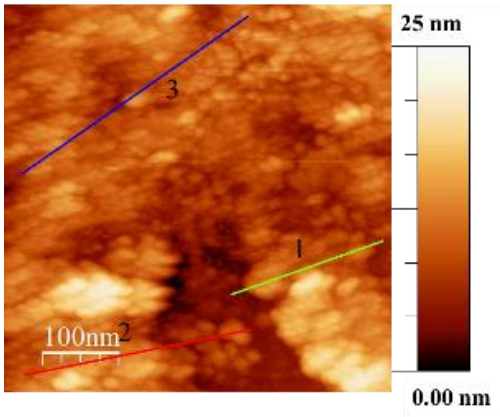

(a)I

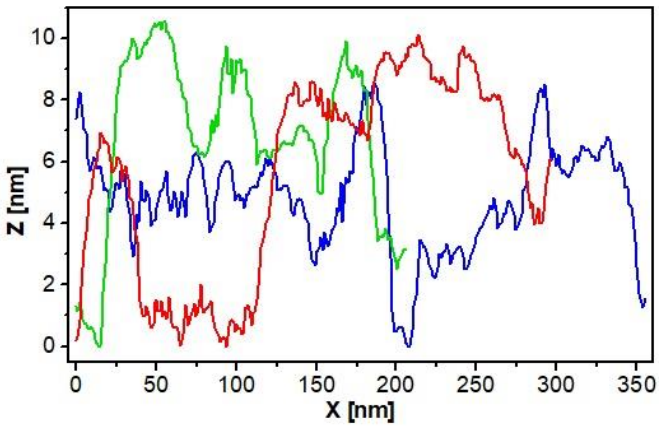

(b) after additional 40 min

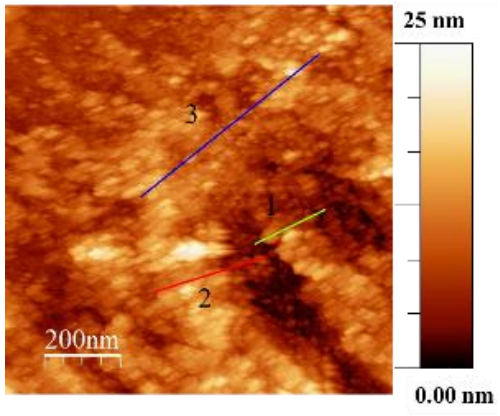

(b)I

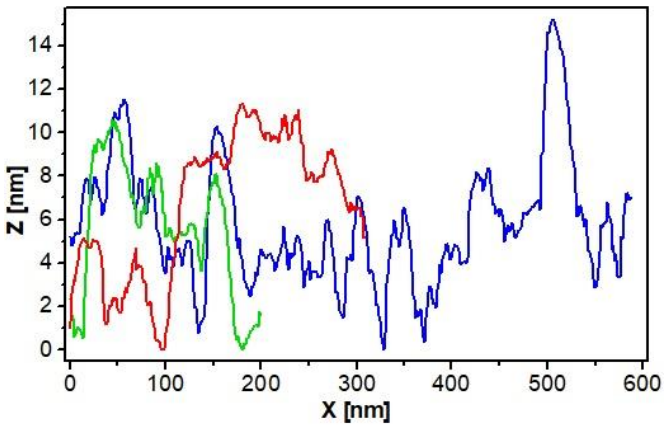

(c) after additional 1 h 20 min **(c)I**

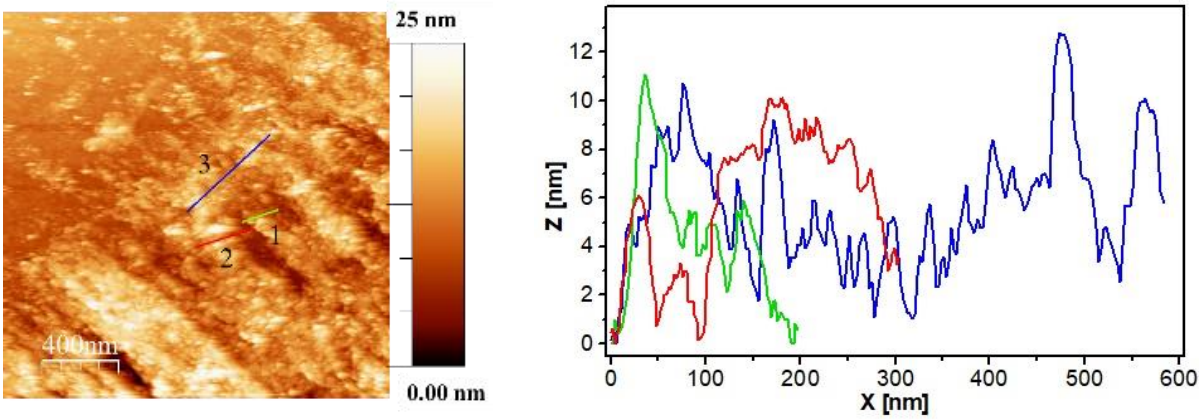

(d) after additional 2 h **(d)I**

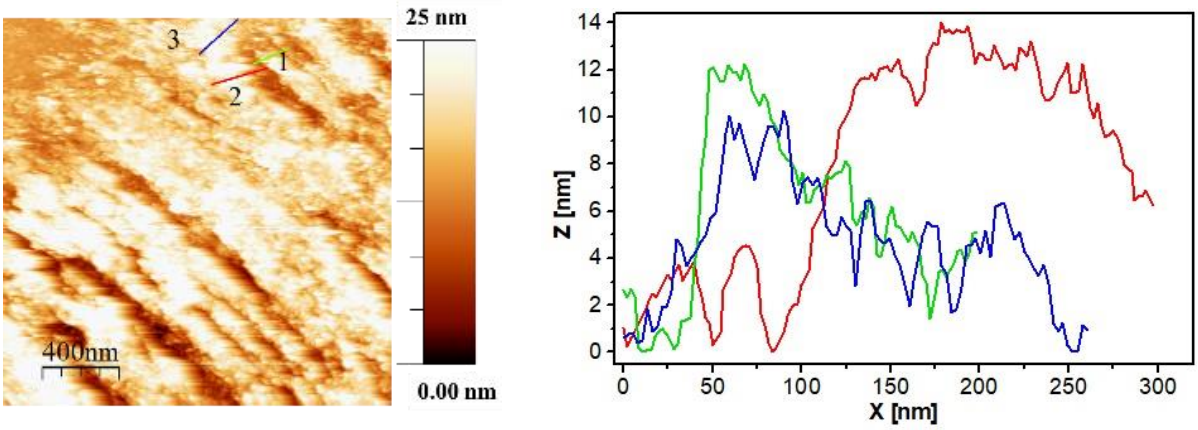

Figure 5.5.2: Present development of the same feature with time, line profile **(a) I**, **(b) I**, **(c) I**, and **(d) I**, are showing the feature of 10 nm height. With each measurement, the frame size is enlarged while focusing on a few features' time evolution as line profiles are taken by best approximation on the same positions.

Three different positions (marked by (1) green line, (2) red line, and (3) blue line) are chosen for the line profiles. The slight differences between the profiles may result from small variations in the chosen position and are here not considered proof for hydrogen release, after 12 h.

In all images, the red line profile verifies the existence of the same feature with almost the same height difference. The green line profile matches mostly the image in (a) I and (b) I. The longest line scan (blue line) also shows similarities to (b) I and (c) I. Due to a drift in position with increasing scan area, it was not possible to locate precisely all the parts of the selected positions. But, due to the larger scan area, large surface changes can be seen as accompanied by deep valleys. Striped valley surface topography is detected in this region. The surface topography is not straight

and should span over many different grains, as the grains are considered to be rotated against each other in lateral orientation (fiber texture, see chapter 3). The surface topography confirms massive material transport ranging over many grains.

It is suggested here that this massive material transport, which is induced by hydrogen absorption, results from grain sliding. Details will be discussed in the following chapter.

Chapter 6

Discussion

The results obtained from hydrogenography, STM, Stress, and EMF measurement are discussed in this chapter. Herein, the findings of the H uptake in V-films will be addressed, including the irreversible changes observed by STM and the effect of the interlayer on the H uptake. The combination of all results will also lead to a better understanding of the behavior of the patterned samples.

6.1 Precipitation and growth of the hydride phase under the influence of interface layers

6.1.1 Effect of interlayer on EMF of the sample

This part of the discussion summarizes the EMF measurement results presented in sections 4.2.1 to 4.2.7 in chapter 4 and gives phase boundaries details. Most of the EMF measurements are done with similar parameters like current density, loaded area, concentration steps, and V-films thickness. The only exception is the 5 nm Pd-dot sample which includes smaller loading steps.

Figure 6.1.1 presents all EMF curves with different interlayers in one graph. As visible in Figure 6.1.1, the presence of different interlayers results in different EMF curves of the hydrogen-loaded V-films. At low concentrations, slight deviations from the expected linearity (in this type of representation) are observed (also demonstrated in Table. 6.1.1 as starting EMF value). These slight deviations might originate from differences in the sample microstructure and are not the topic of further investigation, here.

Three different kinds of study results are presented here: (1) the effect of the Pd interlayer compared to the PC interlayer, (2) the effect of interlayer thickness on the overall mechanical stress state, and (3) the effect of an interlayer pattern.

Figure 6.1.1 presents the isotherms of the sample with no-interlayer in black, 5 nm Pd interlayer in blue, and 7 nm Pd interlayer in red. The isotherm of the sample with the 20 nm PC interlayer is plotted in green. These samples develop differently during hydrogen loading, as shown in chapters 4.1.2, 4.1.3, 4.1.4, and 4.1.7. According to the light-microscopy studies, the V-film with no-interlayer does not buckle and stayed adhered to the glass substrate from $c_H = 0$ H/V to fully loaded $c_H = 1$ H/V, see Figure 4.1.2.1(a). The samples with Pd interlayers remained adhered to the glass substrate for concentrations below $c_H = 0.4$ H/V for 7 nm Pd, and below $c_H = 0.3$ H/V for 5 nm Pd, subsequently. They start to buckle with further H-loading, see Figures 4.1.3.1(a), and 4.1.4.1(a). While the sample with a 7 nm Pd interlayer gets fully buckled, the sample with a 5 nm Pd interlayer shows areas that do not buckle, in the regarded field of view. The sample with a 20 nm PC interlayer is already buckled in the as-deposited state, see Figure 4.1.7.1(a). However, this sample remains

intact up to full loading of $c_H = 1$ H/V, as confirmed by the EMF graph and the related microscopical images.

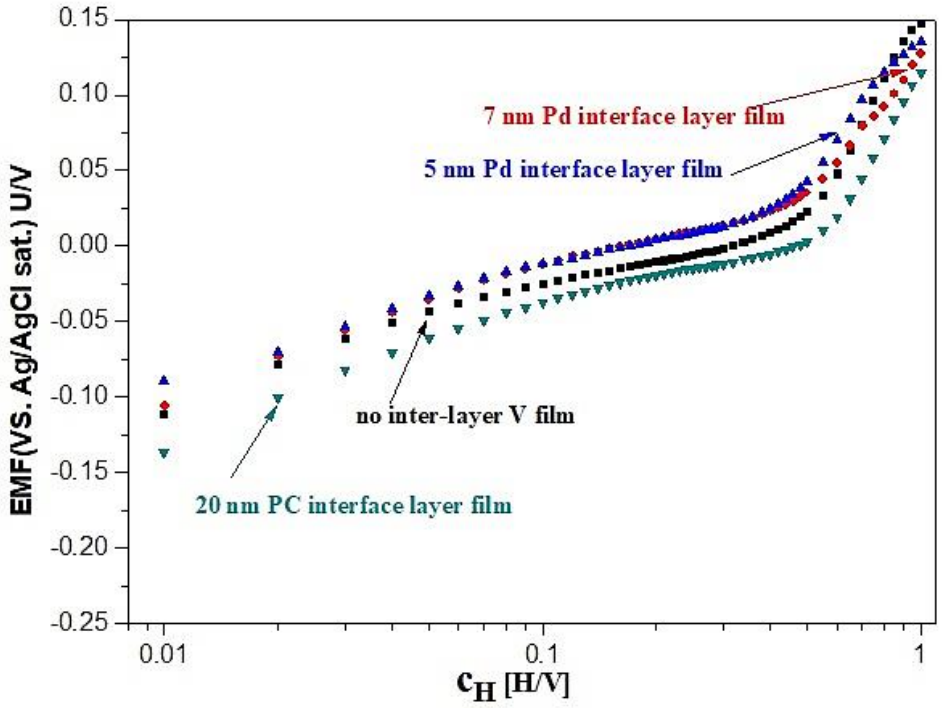

Figure 6.1.1: Isotherms (EMF curves) of 30 nm V-films with different interlayers, for comparison. Pd (red and blue) and PC (green) interface layers of different thicknesses are plotted with respect to the V film (black) containing no-interlayer, thus being directly deposited on the glass substrate.

The samples with Pd interlayer (blue and red) show higher EMF values or have a 20 mV upward plateau shift when compared to the "no-interlayer V-film" sample (black). The EMF-curves of the Pd interface layer thickness 5 nm and 7 nm are mainly identical. The only difference is a change in the plateau end value which is slightly larger for the 7 nm sample and has the larger H-solubility in the hydride phase. This may be due to the additional H-uptake in the slightly thicker Pd-layer. And possibly the smaller lattice parameter of Pd compared to V creates higher stress values in the sample with a thicker Pd interface layer. But these effects should also change the plateau height which is not observed here. Therefore, we consider this effect negligible for our interlayer thicknesses.

Table: 6.1.1 Phase boundaries extracted from the EMF measurement of different interface layers.

Sample Pd(15 nm/V(30nm)/	Starting EMF	α-phase limit [H/V]	EMF value [V]	Two-phase limit [H/V]	EMF value [V]	Miscibility gap width [H/V]

//Glass	**-0.11**	**0.08**	**-0.03**	**0.48**	**0.019**	**0.40**
Pd(7nm) layer //Glass	**-0.11**	**0.09**	**-0.015**	**0.38**	**0.021**	**0.29**
Pd(5nm) layer//Glass	**-0.08**	**0.08**	**-0.017**	**0.42**	**0.03**	**0.34**
PC (20nm) //Glass	**-0.13**	**0.06**	**-0.055**	**0.48**	**0.012**	**0.42**

To confirm this, the width of the plateau region was calculated for the samples as shown in Table 6.1.1, where Pd(15nm)/V(30 nm)/Pd(7nm) layer//glass has an α-phase limit α = 0.09 H/V and two-phase limit β = 0.38 H/V. Pd(15nm)/V(30 nm)/Pd(5nm) layer//glass has an α-phase limit α = 0.08 H/V and two-phase limit β = 0.42 H/V. The two-phase region widths come out to be 0.29 H/V for 7 nm Pd and 0.34 H/V for the 5 nm Pd interface layer, respectively, see Table 6.1.1. The film with no-interlayer has a larger two-phase region width than the films with a 5 nm or 7 nm Pd-interlayer. Interestingly, the two-phase region width of the V-film with no-interlayer resembles that of the film with a PC interlayer. This indicates that the V-film with no-interlayer effectively releases mechanical stress. However, in comparison to all other samples, the V-film with 20 nm PC interlayer has the widest plateau. Figure. 6.1.2. graphically summarizes these results.

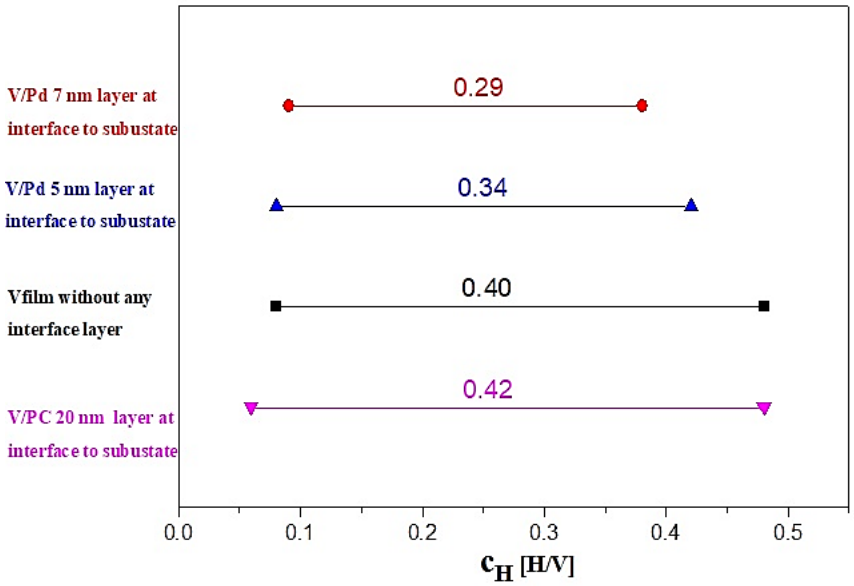

Figure 6.1.2: EMF curve two-phase region (miscibility gap) comparison of no-interlayer vanadium film with different thickness Pd interlayer.

According to Figure 6.1.1, the EMF-curves of the V-film with different Pd interlayers cross at high potentials: the EMF of the V-film with 7 nm Pd interlayer increases more slowly, thereby crossing the EMF curve of the V-film with 5 nm interlayer. This effect accounts for the onset of Pd-hydride formation, in the thinner film.

The EMF curves of different samples shown in Figure 6.1.1 also differ in their absolute voltage values. In comparison to other samples, the V-film with 20 nm PC interlayer provides the lowest EMF voltages, for all H-concentrations. As this film is detached right before any hydrogen loading, it is in a relatively free state and its intrinsic stress value can be considered as low. According to Wagner's thermodynamical approach [121], this generally results in a low EMF value and low plateau EMF.

To further validate this argument, the width of the two-phase regions of this sample is compared to the width of the V-film with no-interlayer. While the first film was deposited on the amorphous polymer (PC) substrate, the latter was deposited on the amorphous glass substrate. So, both V-film microstructures are based on a similar type of substrate, just with completely different mechanical stiffness. As shown in Table 6.1.1 and Figure 6.1.2, the V-film type Pd(15nm)/V(30nm)/PC(20nm) layer//glass two-phase region width is 0.42 H/V, while that of the V-film with no-interlayer is 0.40 H/V. This difference is small, but also in agreement with the expectations of Wagner's thermodynamical approach. Therefore, lower mechanical stress results in a wider two-phase region width.

According to the EMF curves in Figure 6.1.1, both V-films deposited on Pd interlayers have higher EMF and plateau values when compared to the two other V-films. It should be taken into account that the Pd interlayers offer a crystalline basis for the V-film growth. There exists a lattice constant difference between Pd and V, and there might be a lattice relation. The involved lattice matching might result in intrinsic mechanical stress. This intrinsic stress could explain the increase in the EMF values, compared to the V-film with the PC interlayer.

Thus, it can be summarized that the PC interlayer lowers the mechanical stress in the sample while the Pd interlayer increases the intrinsic stress state of the sample when compared to the V-film that is directly adhered to the glass substrate. Different intrinsic stress levels can be achieved by changing the interlayer type and, possibly, its thickness.

To analyze the effect of an interlayer modulation on the sample behavior, mixed adhesion samples were created with Pd or PC dots (refer to sections 4.1.5 and 4.1.6 chapter 4). Figure 6.1.3 shows the related EMF curves, in comparison to the EMF curve of the V-film with no-interlayer. The EMF curves of samples provide different initial EMF voltages and different behavior above c_H = 0.55 H/V, separating them in different directions. However, all of the EMF curves provide the same plateau EMF values. The initial difference in the EMF values may be attributed to a different initial defect density.

It may be noteworthy that the EMF curve obtained for the sample with Pd dots initially has smaller loading steps. This results in lower EMF values compared to the two other samples.

The EMF of the vanadium sample with 5 nm PC dots shows a plateau value (even a little bit higher) which is similar to the sample with no-interlayer. Regarding the sample morphology, the vanadium sample with 5 nm PC dots does not have a full interlayer structure, but rather an oval PC shape distribution (see chapter 4 part 4.1.6 and Figure 4.1.5). Thus, this sample has regions similar to the vanadium sample with no-interlayer (places where no PC dot is deposited) and regions similar to vanadium with a 20 nm PC interlayer (places where 5 nm PC dots are deposited). Additionally, the sample has boundary regions where the 5 nm PC dots end. This should result in a bending of the V- film grown on top of it. From the EMF measurement, it can be concluded that the effect of these 5 nm PC dots on the stress release during hydrogen loading is not that strong, but the adhered regions of the sample including the boundary regions of the dots combine in a stress state that is equivalent to that of the vanadium film with no-interlayer. At higher concentrations, the EMF plateau of the vanadium film on the PC dots interlayer is lower than that of the vanadium film with no-interlayer, as the latter does not buckle and cannot release the stress that strong. The vanadium film deposited on PC dots shows buckling.

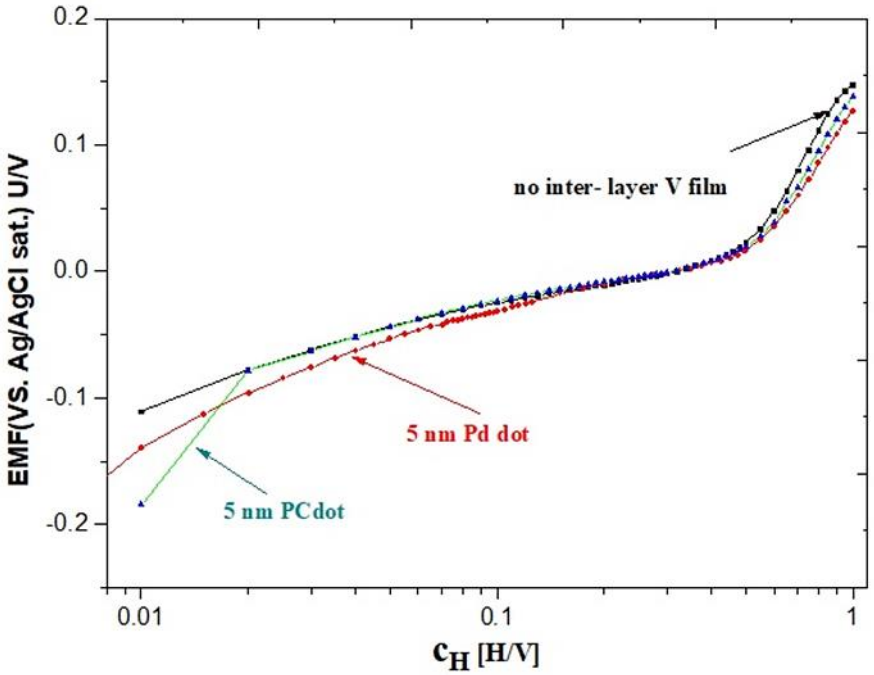

Figure 6.1.3: EMF curves obtained during hydrogen loading of vanadium with no-interlayer (black), and samples with patterned adhesion, namely Pd dots (red) or PC dots (green).

To further explain the behavior of these samples, the thermodynamical DOS model (see chapter 4.4) is fit to the EMF and available stress data, in collaboration with Stefan Wagner. The DOS model provides different site occupation energies for the samples with different interlayers. For the interstitial sites, energy -14 kJ/mol results for the vanadium film with no-inter-layer. For the vanadium film with PC interlayer, the site energy becomes even slightly more negative and is -15

kJ/mol. For the vanadium film with a Pd interlayer, the fit gives a site energy of -13 kJ/mol. These results relate to the different heights of the EMF curves, in the low concentration ranges. Based on these results, for the pattern samples with Pd-dots, the hydrogen should preferentially occupy the interstitial sites in the vanadium film on the no- interlayer regions, and for higher chemical potentials, the interstitial sites in the vanadium film on the Pd-dots. For the pattern samples with PC-dots, the hydrogen should first fill the vanadium interstitial sites on the PC-dot regions and then the sites on the no-interlayer regions.

The hydrogen site energies of the vanadium "grain boundaries" also differ, according to the fit (see chapter 4.4). They are predominantly negative for the vanadium on the 20 nm PC interlayer. Maybe this hints at different kinds of grain boundaries in V for the stress-free (PC) films when compared to the stressed V-films (no-interlayer and Pd interlayer). The related part in the EMF curve can be found at low concentrations. For more detailed information, this part has to be measured in more detail, and for lower concentrations.

Table: 6.1.2 Presenting the Phase boundary extracted from the EMF measurement of no-interlayer vanadium film with mixed adhesion samples.

Sample Pd(15nm)/V(30nm)/	Starting EMF	Alpha phase limit [H/V]	EMF value [V]	Two phase limit [H/V]	EMF value [V]	Miscibility gap width [H/V]
//glass	-0.11	0.08	-0.03	0.48	0.019	0.40
/Pd(5nm) dots//glass	-0.21	0.05	-0.53	0.5	0.017	0.45
/PC(5nm) dots//glass	-0.075	0.09	-0.023	0.48	0.019	0.39

The width of the two-phase region is plotted in Figure 6.1.4, using data from Table 6.1.2. Figure 6.1.4 shows that the vanadium films on Pd dots patterned adhesion samples have the widest two-phase width of 0.45 H/V. Here, this is considered as resulting from the small loading concentration steps. The plateau widths of the vanadium film with no-interlayer and that on the PC patterned adhesion samples (PC dots) have 0.40 H/V and 0.39 H/V and are considered to behave similarly.

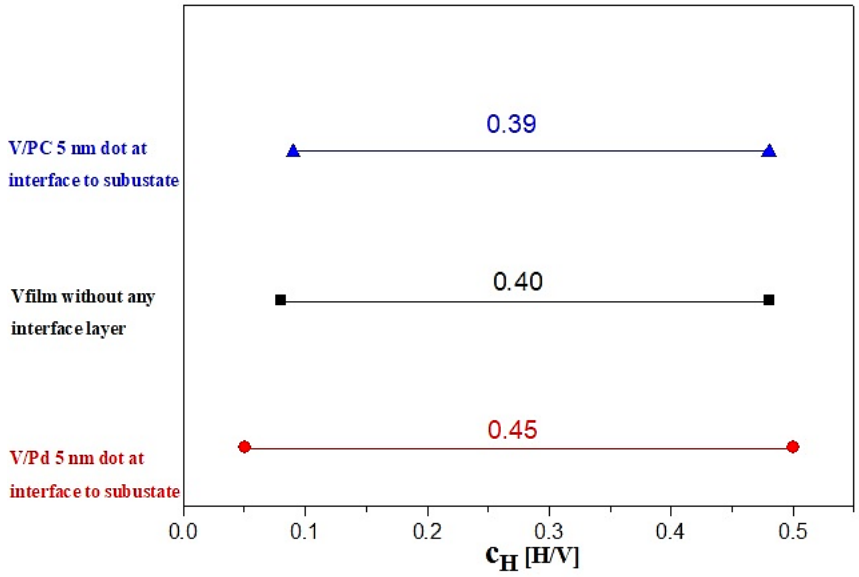

Figure 6.1.4: EMF two-phase region (miscibility gap) widths comparison of no-interlayer vanadium film with patterned adhesion samples, 5 nm PC dots at the interlayer and 5 nm Pd dots at the interlayer.

The EMF curve of the V-film with the PC pattern resembles that of the V-film with no-interlayer. Thus, the behavior seems to be dominated by the adhered part of the film. Therefore, the sample with the PC pattern has a much higher stress state than the sample with the PC interlayer.

The EMF curves in Figure 6.1.3 meet in the higher concentration plateau region. The samples containing dots are buckled from the beginning for PC and buckled above 0.125 H/V for Pd, respectively. But they both mainly contain vanadium directly grown on the glass (Si-O) substrate. Thus, the curves seem to be governed by the EMF behavior of this part. (Note: the EMF for Pd is artificially lowered because of the smaller step size)

6.2 STM measurements

The STM measurements in chapter 5 allow for studying the surface morphology of the V-film and how the morphology changes upon hydrogen absorption. As a reminder, these measurements were done by gas phase loading, and the 30 nm vanadium films were directly deposited on the native oxide on top of flat Si substrates. So, all the STM samples resemble the films with no-interlayer on glass substrates. Thus, the obtained hydrogen-induced morphology changes pertain to the samples (regions) that are directly deposited on the glass substrate.

The STM images of the intrinsic surface of the nanocrystalline V-films (Figure 5.2 (a)-(b)) show a ripple-like morphology that was not quoted in the literature before. But a similar kind of ripple surface, the “faceting staircase growth“ is observed by LEED pattern for very thin homoepitaxially

growing V (320 K) on V(110) single crystals and Fe grown on W(110) substrates and few other bcc metals films, see Figure 6.2 (a) and (b) [122, 123] Figure 6.2 (a) Figure configured from LEED pattern, presents a V-film with 10 Å ripple height where H denotes the number of staircases of height Hd_Z, d_Z presents the spacing of the adjacent atomic rows with angle α that corresponds to the inclination of the facets with respect to the V-film plane (inclination of staircases in real space). Figure 6.2 (b) presents the growth of the "staircase" (example for a Fe thin film, see [122], where D represents the number of atomic layers. This mode of growth is explained by layer-restricted diffusion (LRD). The LRD growth is determined by an energy barrier that prevents the hopping of an atom from one atomic plane to another atomic plane, in combination with free diffusion of the atom within an atomic plane. This kind of growth is shown in one specific crystal direction (in this case in [1-10] direction with d_{110} as the spacing). Thus, this kind of facetted growth acts as a model for sample growth with an anisotropic sticking probability of the atoms at the steps, being high on the steps with the edges along [1-10] and low on the steps along [001].

We suggest that the observed morphology of the nanocrystalline vanadium films (see Figure 6.2 (c) can be explained with the model discussed above. The dimension of the surface morphologies in study 6.2 (a) with widths of about ~4 nm and heights of 1 nm is very close to our results shown in Figure 6.2 (c), with widths of about ~6 nm and heights of about ~1.2 nm. Thus, we conclude that the nanocrystalline V-films of this work have ripple structures with anisotropically elongated ripples present in the preferred growth directions.

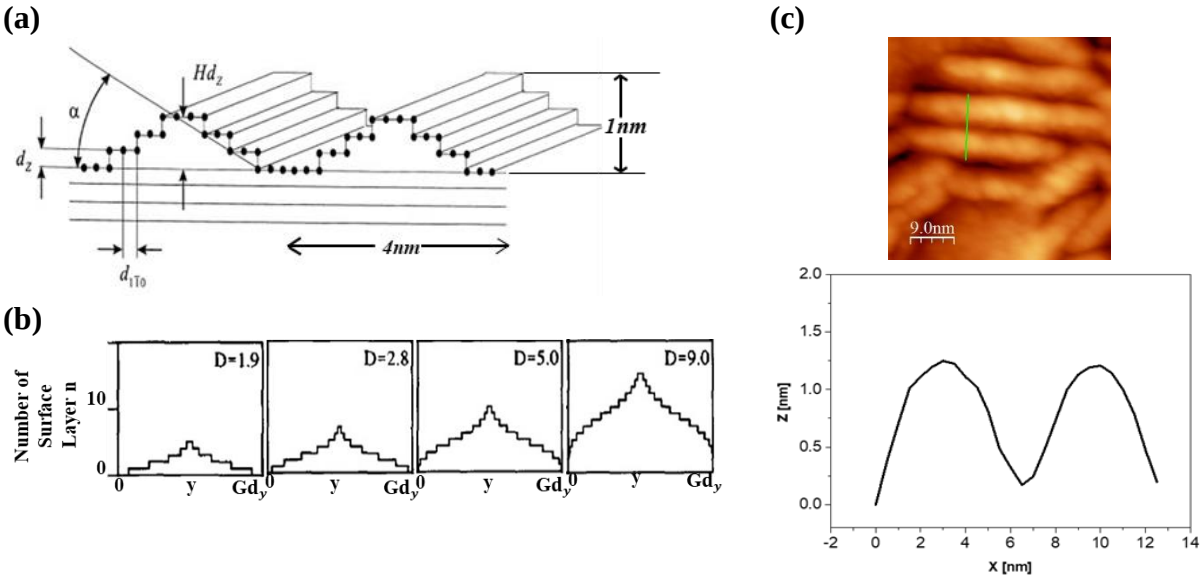

Figure 6.2: (a) Sketch of faceted surface growth observed for a 10 Å V-film [122], **(b)** cross-section of surface structure in a one-dimensional periodic model, calculated for Fe (110) [123]. Part **(c)** represents the STM image and a line scan of the surface morphology of a 30 nm V-film, to compare the surface features. Figure 6.2 (a) reprinted from permission [122] and Figure 6.2 (a) reprinted from permission [123]. copyright 1993, 1998 Elsevier.

Different thicknesses of Pd cover layers are tested to observe the sample surface, and then to fully measure the sample surface morphology development upon hydrogen loading. It is confirmed that a small amount of Pd (0.16 nm) is needed to successfully measure the V-film surface morphology even though the film is deposited under UHV conditions and directly measured in the STM, without breaking the UHV conditions. But it takes about 30 min to shift the film from the growth chamber into the STM measurement chamber and to properly mount it in the STM. During this time, the sample surface gets oxidized. Thus, Pd is needed to prevent vanadium surface oxide formation. In chapter 5 (Figure 5.2) it is observed that to see surface features of V in the STM, a deposition of 0.16 nm Pd on the V-film is enough. Figure 5.2 (a - e) presents the observed ripple structures in 2D and 3D formats and as line profiles. The V-film within the grains shows the symmetric ripple-like structure having lengths of 25 nm - 35 nm, widths of about 6 nm - 10 nm, and heights below 2 nm, see Figure 5.2 (d), 5.2.1 (a). Also visible are the (foggy appearing) Pd islands with approximately 13 to 150 nm in width and 2 nm in height, see 5.2 (e) 5.2.1 (b).

For better oxidation protection and successful extended measurements over a period of time required for hydrogen loading studies, a slightly thicker layer of Pd (1 nm) is deposited on the vanadium surface, see part 5.3. In the as-deposited condition the vanadium sample surface still shows the surface ripples with the typical length, width, and height, see Figure 5.3 (a)-(d).

After hydrogen gas exposure at $p_H = 8.3\times10^{-4}$ mbar for 30 min hydrogen partial pressure (Figure 5.3.1), the V-surface ripple morphology undergoes a change in its height from 2 nm to 3.5 nm - 4 nm and also becomes broader, see the line profile 5.3.1(c) and (d). It is informed that all STM measurements were performed after hydrogen exposure (see Chapter 3, section 3.5.1). When we compare Figure 5.2.1 (c) where two different kinds of surface features are clearly distinguishable, with Figure 5.3.2 (a), we observe no more 'blurred-appearing' Pd islands. After hydrogen exposure, the surface is clearly modified with new surface morphologies with elevated regions bordered by valleys having lengths between 100 (± 20) nm and 350 (± 20) nm, widths ranging from 30 (± 10) nm to 200 (± 10) nm and heights between 3 (± 0.3) nm - 3.7 (± 0.3) nm. So, the average topography hump is 198 (±20) nm in length, 128 (± 10) nm in width, and 3.4 (±0.3) nm in height, see Figure 6.2.1. This disappearance of the 'blurred' Pd regions and the morphology change is interpreted as Pd diffusion on the vanadium surface and possible alloying with the vanadium, in the presence of hydrogen. Also, the ripple structure has a large surface area. Because of surface energy reduction, vanadium atom surface diffusion is expected to lead to surface smoothing. Thus, the observed changes might be attributed to surface atom diffusion, stimulated by the presence of hydrogen atoms.

According to the Pd-V phase diagram, the solubility of Pd in V and the solubility of V in Pd is large. See appendix A.7 for the Pd-V phase diagram [124].

Slow loading (of a different sample) with a slightly lower pressure of $p_H = 1.4\times10^{-4}$ mbar for 12 hours (see 5.4 (a) and (c)) results in minor changes of the surface morphology, see 5.4 (b) and (d) where the line profiles show small changes in height.

Subsequent loading to a higher pressure of $p_H = 1.1\times10^{-3}$ mbar hydrogen partial pressure, for 2 hours, results in broader features. This is shown in Figure 5.4.1 (d) and (g). The pressure is comparable to the $p_H = 8.3\times10^{-4}$ mbar of the other sample.

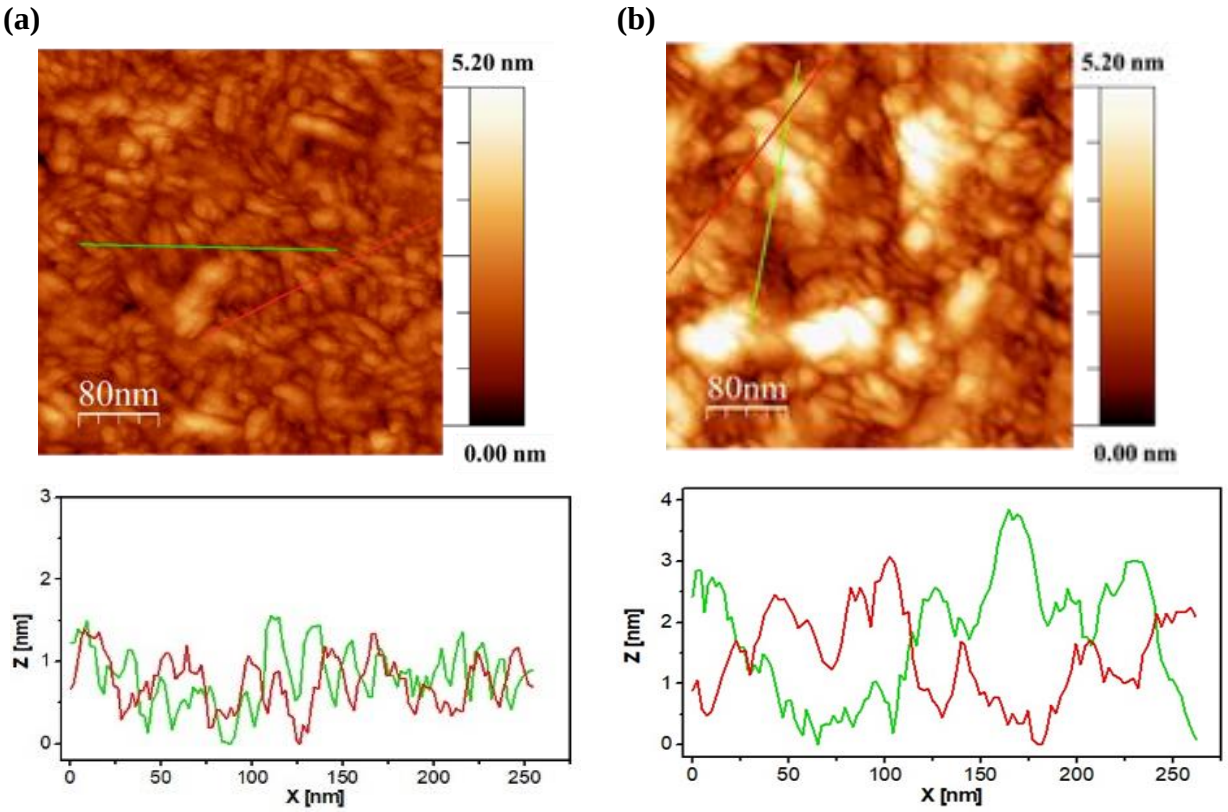

Figure 6.2.1: (a) As-deposited state of sample loaded at $p_H = 8.3\times 10^{-4}$ mbar **(b)** After hydrogen loading.

For this sample measured with a large frame size of $1\times1\mu m^2$ and the existence of two large surface markers, it becomes possible to observe the same spot before and after hydrogen exposure. The images shown in Figures 5.4.2 (b) and (e) are taken from the square area of images (a) and (d), respectively. At the very same position, features are changing from 1.5-2.5 nm height to 3-3.5 nm height. Even though the small surface modulation still exists, line scans appear on broader widths of 50 nm - 100 nm, when we compare line scans 5.4.2 (c) and (f).

Thus, for a 30 nm V-film a pressure above $p_H = 8.3\times 10^{-4}$ can be applied to see surface morphology changes due to hydrogen loading.

To allow for even more extended STM measurements, the surface of vanadium was covered with 8 nm of Pd. This helps in successful STM measurement for three days, offers more uniform

hydrogen absorption in the V-film, and seems to prevent surface oxide formation. But, the initial grain boundaries and the surface ripple topography of the underlying V-film are not clearly visible, see Figure 5.5 (a). The initial ripple morphology seems to be covered by a Pd-layer which still shows surface modulations of Pd-islands. Figure 5.5 (b) presents the line profile of the sample, showing modulations with a lateral size of 20 nm and with a height of 2 nm, see Figure 5.5 (d) and (e). Figures 5.5 (c) and (f) show the 3D presentation of the surface.

If the sample is exposed to a high hydrogen partial pressure of $p_H = 6.7\times10^{-2}$ mbar, large morphological changes are detected, compared to any other sample measured, see Figure 5.5.1 (a). This pressure is well above the phase transition pressure and allows for fast sample loading. The new surface morphology has heights of 8 nm and 15 nm, as shown in Figure 5.5.1 (b). Furthermore, Figure 5.5.1 (e) presents the related line profile. Large valleys and hills are visible. While hills have height changes of 6 nm to 7 nm, the valley-to-island height change is in the range of 15 nm.

This height change is unexpectedly high. Assuming linear elastic lattice expansion upon hydrogen absorption in the 30 nm V-film gives a maximum height increase of $d \times \alpha_H \times \Delta c_H = (30\ \text{nm} \times 0.13 \times 1) = 4$ nm, where d is the film thickness, α_H is the V film lattice expansion coefficient (see chapter 2), and $\Delta c_H = 1$ H/V for the fully loaded film, that is theoretically achievable. When a Pd layer of 1 nm is deposited, the height of the surface features increases from 2 nm to 3.5-4 nm. This change is still in line with linear elastic lattice expansion. Morphology changes in width are stronger in this case as compared to the height changes (see discussion before). But the strong surface morphology changes ranging up to 6 nm or even 15 nm cannot be explained by linear elastic expansion.

The STM unloading experiments in Chapter 5, Figure 5.5.1 (d) and (g) and Figure 5.5.2, have shown that the surface morphology changes mainly persist, thereby confirming massive irreversible material transport to the sample surface. So, irreversible processes are responsible for surface topography changes. Figure 6.2.2 shows the surface modifications by hydrogen absorption in a 25 nm Nb film [125], and in comparison, to that of the 30 nm V films. For the 25 nm Nb film, the surface topography changes are in the range of 1-1.5 nm while for the V-film, surface topography changes of 6 to 15 nm are observed [see Figure 6.2.2 line scans (d) and (e)].

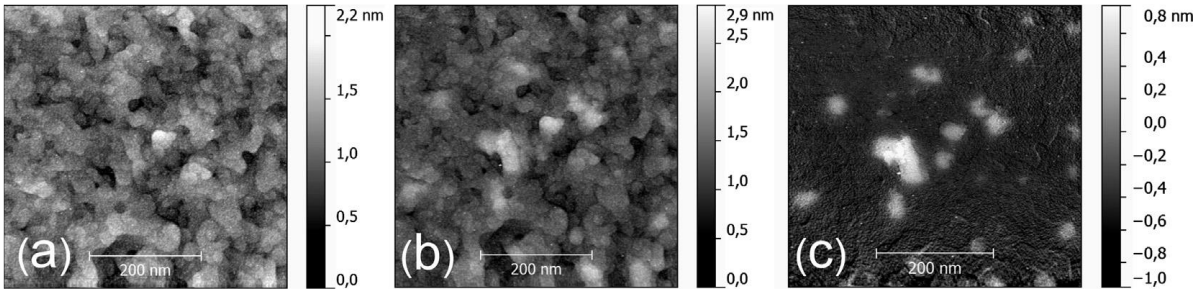

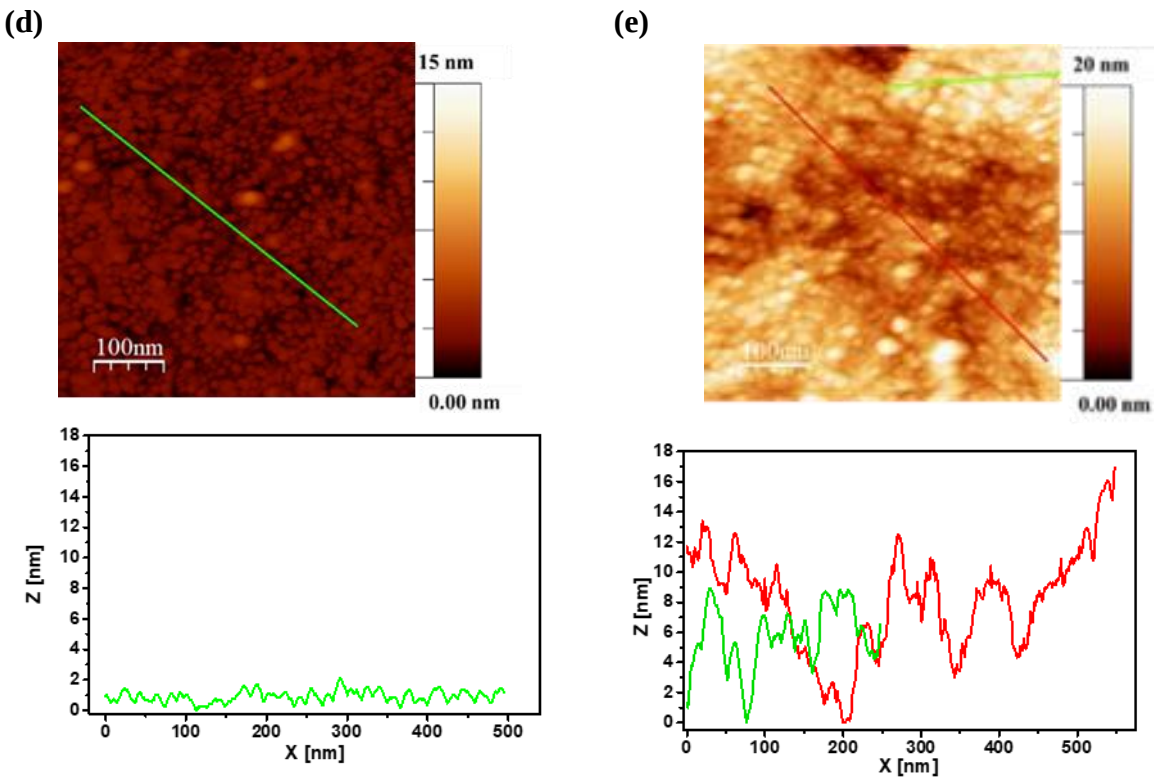

Figure 6.2.2: Surface changes observed by STM measurements on 25 nm Nb film and 30 nm V film upon hydrogen loading, **(a)** Nb surface before hydrogen loading **(b)** during hydrogen loading at $p_H = 8\times10^{-7}$ mbar for t = 500 min, **(c)** presents the difference image. **(d)** 8 nm Pd cover 30 nm V-film before hydrogen loading **(e)** V-film after hydrogen loading at $p_H = 6.7 \times 10^{-2}$ mbar. Images **(a)**, **(b)**, and **(c)** were taken from [125].

The surface morphology changes are also larger than what has been seen when dislocations are generated. Most of these studies have been performed on epitaxial films with large single crystalline regions in the range of several micrometers. For epitaxial Nb-H, Burlaka reported maximum hydride heights in the range of what is expected for linear elastic expansion, though not many changed occur even by dislocation presence. The new morphology detected for the vanadium films suggests massive material transport on account of the presence of the nanocrystalline grains. It is here suggested that grains can slide under high compressive stress which is in the GPa range. Thus, possible interpretations of the observed surface changes of these V-films upon H-loading are plastic deformation due to dislocation formation and grain sliding. Both mechanisms result in in-plane stress release. As the grain size in these V-films is small, the grain sliding mechanisms may play a significant role.

6.3 Result of stress measurement

The hydrogen-induced stress has been determined by in-situ stress measurements, described in section 4.3.1 of chapter 4. The focus was on evaluating the effect of different hydrogen loading current densities leading to different stress states, during the electrochemical H-loading. These measurements, as shown in Figure 4.3.1.1 (a), relate to Pd (15nm)/V(30nm)//glass sample (black curve with j= 0.65 A/m^2, red curve with j= 0.2 A/m^2, blue j= 0.064 A/m^2). Thus, the obtained results relate to the no-interlayer sample parts.

As shown in section 4.3.1.1, the stress curves strongly depend on the loading current density. The maximum compressive stress and the final stress value attained with full H-loading (c_H =1 H/V) reached in the sample by applying different current densities are summarized in Table 6.3. Data in the table show that with a smaller current density, the sample can reach higher values of maximum compressive stress, at a certain medium H-concentration. With further loading, the sample releases stress. This stress is so strong that even the final stress value is below the maximum stress value. The sample with j= 0.2 A/m^2 current density shows the strongest stress release.

Table 6.3 Effect of different amounts of current density on the hydrogen-related compressive stress in 30 nm vanadium on the glass substrate.

Current density A/m^2	Maximum compressive stress [GPa]	c_H at maximum compressive stress [H/V]	Final stress value at c_H =1 H/V [GPa]
j= 0.65	**-0.9**	**0.80**	**-0.7**
j= 0.2	**-1.1**	**0.35**	**-0.1**
j= 0.064	**-1.6**	**0.96**	**-1.6**

Continuous and step-wise H-loading (using similar parameters shows several comparable stress developments, especially for smaller concentrations (see Figure 4.3.1.2 (a)). In the shown example, the loading current for both samples is 100 μA. The current density differs just because of small differences in the sample area. We suggest considering this as rather similar current densities. Table 6.3.1 shows that the maximum and the final stress values are not much different for both types of loading. But in detail, the initial stress development is slightly steeper for the continuous loading. It bends upon plastic processes and even turns backward at concentrations above 0.8 H/V, see Figure 4.3.1.2 (a). This backward trend is not observed for the step-wise loading, though EMF curve bending can be seen.

This suggests the role of plastic processes of different velocities and origins. Even though the same current density is used, applying continuous loading seems to stimulate a plastic process with strong stress release ability. During step-wise loading, hydrogen gets enough time to redistribute itself and slow plastic processes can act. We suggest that plastic deformation by dislocation formation and movement sets in at lower mechanical stress, though it is a slow process. Such

deformation is found for many different samples upon gas phase loading and here, upon ECL loading. Plastic deformation by grain sliding sets in at higher mechanical stress but is a faster process. It can be only observed for higher driving forces and nanocrystalline samples.

Table 6.3.1 Effect of different loading processes on stress

Type of loading processes	Current density [A/m^2]	Maximum compressive stress [GPa]	c_H at maximum compressive stress [H/V]	Final stress value at c_H=1 H/V, [GPa]
Step-wise loading	**0.7**	**-0.8**	**0.85**	**-0.8**
Continuous loading	**0.65**	**-0.9**	**0.8**	**-0.7**

The related EMF curves given in Figure 4.3.1.2 (b) show a different plateau width, for the two loading modes. As a reminder, the plateau pressure value is artificially different, because of the addition of the applied voltage in the continuous loading mode. This non-equilibrium situation is also affecting the plateau width.

Hysteresis cycle

The sample reversibility behavior has already been discussed in part 4.3.1.3 of chapter 4 for the continuously loaded samples. These samples remained completely adhered to the substrate after the first loading and subsequent unloading. The vanadium in the film is transformed into the hydride phase during the loading cycle and returns to the solid solution after the complete unloading of the sample. A stress hysteresis was found: the sample went into the compressive stress state upon H-absorption, Figure 4.3.1.3 (a), (b); these changes non-linearly depend on c_H. During the first loading [1], see Figure 6.2.3 the initial stress increase was highest, and massive stress release was detected above about c_H=0.4 H/V by upward bending. This curve behavior was already discussed before see section 4.3.1.3, two different stress release mechanisms (formation of dislocations and predominately grain sliding) were suggested. Subsequent unloading (black curve in unloading cycle part) leads to tensile stress of +1.7 GPa at c_H=0 H/V. This finding confirms strong vanadium transport to the sample surface upon hydrogen loading. This missing material turns the film into a state with tensile stress, after unloading.

This is in accordance with the STM observations, where the nanocrystalline V-films show strong material transport upon hydrogen uptake.

The first loading cycle (also see black curve in Appendix A.5) has a wide-open loop and shows the highest residual stress. With the second [2] loading cycle (red curve), the loop gets smaller but remains open. It implies that the end value does not meet the starting value of the previous cycle. After the second loading cycle, all measured loops ([3]- [6]) are almost closed, see Figure 4.3.1.3 (a) and (b). The shape of the cycle's hysteresis resembles each other. With increasing loading cycle number, the required work for the full cycle decreases, as can be seen by the decreasing area of the hysteresis loops.

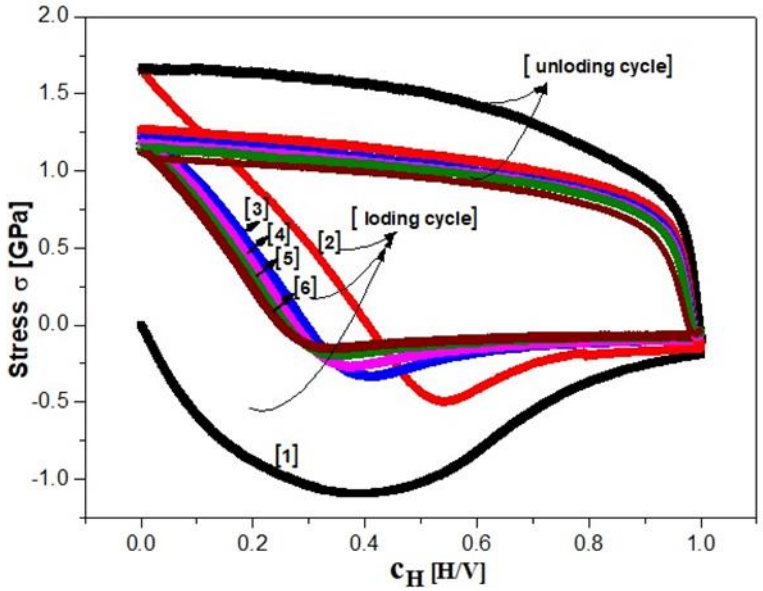

Figure 6.2.3: Stress hysteresis observed during multiple loading and unloading cycles with continuously loaded done for Pd(15nm)/V(30nm)//glass sample using current density j= 0.2 A/m^2.

The compressive stress developing during the loading branch is released subsequently during the unloading branch. Thus, the sample is in the tensile stress state after each unloading state. For this nanocrystalline V-film in all repeated loading branches, a nearly linear increase in compressive stress is observed. Maximum compressive stress is reached between c_H = 0.20 H/V and c_H = 0.55 H/V for cycles presented in Figure 6.2.3. At higher concentrations, the stress curve bends upward due to stress relaxation causing a dip in the stress curve. With a further increase in H concentration, no further change in stress is noticed.

Further, the STM findings reveal the behavior of compressive stress development and relaxation that observed as dip in stress measurements (Figure 6.2.3). In addition to defect generation and relaxation processes, strong morphology changes occur in vanadium films at maximum compressive stress.

The hysteresis as well as the dip get smaller with every cycle. With unloading, the sample reaches a tensile stress state, but with subsequent loading the maximum compressive stress value decreases and further decreases with each loading cycle. Because of this reason, the dip appears due to the rise of maximum compressive stress and its relaxation goes on decreasing with each cycle. The dip's shift to regions of lower H-concentration suggests easier stress release or material softening because plastic deformation sets in at lower mechanical stress.

6.4 Effect of interlayer on the optical measurements

After gaining knowledge of different stress release mechanisms, we can focus on the effect of the interlayers. As explained in section 4.1 in chapter 4, different interlayers give rise to different states of mechanical stress, ranging from quasi-zero mechanical stress (detached (buckled), as deposited on PC interlayer) to strong stress (adhered, no-interlayer, see sections before 6.4 of this chapter). Optical measurements offer valuable insights into details, see chapter 4 results section from 4.1.1 to 4.1.7.

From the point of view of optical measurements, the following two important aspects emerge are:

(1) All the samples are covered with a 15 nm Pd cap protective layer.

(2) The optical behavior observed upon hydrogen loading of palladium is opposite to that of vanadium loading (sections 4.1.1 and 4.1.2). From optical transmission spectra and EMF data, it can be concluded that from 50 loading steps ranging from $c_H = 0$ H/V up to $c_H = 1$ H/V, generally the last 3 to 4 loading steps are influenced by the palladium loading and can be neglected, when focusing about the vanadium information.

It is noteworthy here that reflection images are less sensitive to hydrogen loading concentration, giving predominantly visual information about the sample appearance and the presence of buckles. Transmission images are more sensitive to hydrogen loading, as the image brightness is governed by Beer-Lambert's law (more details can be found in Chapter 3). Transmission graphs can be extracted from the transmission images. Thus, we will discuss different interlayer sample measurements by focusing on these three pieces of information, reflection images, transmission images and transmission intensity diagrams.

6.4.1 Reflection images

Details about the buckle formation are visible in the reflection images. The reflection images on Pd(15nm)/V(30nm)//glass with no-interlayer show a uniform surface which with loading from $c_H = 0$ H/V up to $c_H = 1$ H/V shows no such drastic change [see Figure 4.1.2 (a)]. Only some surface features already presented in the initial state of the sample, get darker with hydrogen loading.

The reflection images of the Pd(15nm)/V(30 nm)/Pd(7nm or 5nm) layer//glass with of 7 nm (see Figure 4.1.3.1) and 5 nm (see Figure 4.1.4.1) Pd interlayer show the microscopic surface feature in as-deposited state at $c_H = 0$ H/V. With hydrogen loading, changes like buckles start appearing at $c_H = 0.4$ H/V for the 7 nm Pd interlayer and $c_H = 0.3$ H/V for the 5 nm Pd interlayer. At $c_H = 0.95$ H/V for the 7 nm buckle, detachment is completed while for the 5 nm buckle, it is almost completed at $c_H = 1$ H/V, as still some area is not completely buckled, in the frame of view.

This detachment is in line with the studies on the 30 nm Pd film which shows buckle formation due to H-loading at c_H = 0.16 H/Pd (see section 4.1.1 in chapter 4). Further hydrogen loading results in an increase in buckle area and more buckles are created all across the sample. Till c_H = 0.44 H/Pd, different buckle areas appear and grow, but above c_H = 0.44, H/Pd they merge, and their growth dominates. The whole sample (in the field of view) is covered with buckles at concentrations of c_H = 0.79 H/Pd. This confirms buckle (or interface crack) formation at the palladium/substrate interface.

The concentration for buckle formation for the 5 nm and 7 nm Pd interlayers is higher than that for the 30 nm Pd film. This might be related to a higher strain energy density, which is present in the Pd film when compared to the vanadium film. It should be considered that the concentration for the Pd interlayers accounts for H/V, but for the Pd film, it is H/Pd.

In accordance with these results and as discussed in section 4.1.5 of chapter 4, the sample with a 5nm Pd dot pattern as interlayer Pd(15nm)/V(30nm)/Pd(5nm) dots //glass shows a uniform surface in the reflection image at c_H = 0 H/V, showing no signs of the Pd dots. At c_H = 0.125 H/V, small buckles become visible. At c_H = 0.7 H/V, buckle formation is completed in the Pd dot pattern area and the Pd-dot positions are nicely visible. The remaining part of the sample that is not covered by Pd dots shows no sign of buckle formation. Expectedly, it behaves like a no-interlayer sample.

The vanadium film on the 5 nm Pd dot pattern started buckle formation at $c_{H\ \mathbf{5nm\ dot}}$ = 0.125 H/V in comparison to $c_{H\ \mathbf{5nm\ layer}}$ = 0.3 H/V for the vanadium film with 5 nm Pd interlayer, though both had the same film thickness. The buckled state of the Pd dot sample was completed at $c_{H\ \mathbf{5nm\ dot}}$ = 0.7 H/V and thus, much earlier than the Pd interlayer sample with $c_{H\ \mathbf{5nm}\ \text{layer}}$= 1 H/V. This early completion is suggested here is because of the different surface morphology (flat glass and Pd-dots on flat glass). Therefore, stress release is different even in the same kind of material. The bending of the V-film at the edges of the 5 nm dots may also affect the stress release mechanism of the V-film.

Reflection images of PC interlayer of 5 nm PC-dots Pd(15nm)/V(30nm)/PC (5nm) dots//glass are shown in section 4.1.6 of chapter 4. Reflection images of 20 nm PC-layer samples (Pd(15nm)/V(30nm)/PC(20nm) layer//glass) can be found in chapter 4, section 4.1.7. For both samples, delamination and folding of the whole sample already exist at c_H = 0 H/V, in the PC-covered regions. Thus, for the vanadium film on a 5 nm Pd dot pattern, the dots are already visible at c_H = 0 H/V.

With loading, the existing features for both types of samples get darker (see Figures 4.1.6.1 and 4.1.7.1). With H-loading of the vanadium on the 5 nm PC dot pattern, the dotted area gets darker. With increasing the H-content in the sample, the circumference buckles and gets widened. The remaining area of this sample with no PC coverage stays adhered to the substrate for concentration range from c_H = 0 H/V to c_H = 1 H/V. Vanadium on the 20 nm PC interlayer was totally bucked from the beginning and covered with small wrinkles. These wrinkles get bigger and broader in size and darker in color, with increasing hydrogen concentration.

Thus, the reflection images allow for judging the adhesion state of the sample before and during loading.

6.4.2 Transmitted light intensity changes in adhered vanadium films

Transmission images and spectra allow for gaining information about the hydrogen concentration of the sample. The transmission of the vanadium and the palladium cap layer were found to develop in different directions, upon H-loading. In all the samples both effects are recorded simultaneously. The pure 30 nm Pd layer shows an intensity peak at i_t = 124 in the as-deposited state [see Figure 4.1.1.1(b)]. With hydrogen loading, this peak decreases in the area while staying at the same position. Simultaneously, a new peak appears at higher transmitted intensity. A peak with a shoulder emerges between i_t = 125 to 155 at c_H = 0.99 H/Pd showing two-phase regions. According to the reflection image shown in Figure 4.1.1.1(a), buckle formation starts at c_H = 0.16 H/Pd. The initial peak i_t = 124 disappears at c_H = 0.69 H/Pd, while the new peak only remains. It presents the hydride phase. The film is fully buckled at c_H = 0.79 H/Pd.

The vanadium film with no-interlayer (Pd(15nm)/V(30nm)//glass) film stayed adhered to the substrate till fully loaded (see Figure 4.1.2.2). The related light transmission goes darker with hydrogen loading from c_H = 0 H/V to c_H = 1 H/V, as shown in transmission images and transmission spectra (Figures 4.1.2.1 and 4.1.2.2). The peak present at i_t= 66 for c_H = 0 H/V moves towards lower intensity till i_t= 56 for c_H = 0.7 H/V. Results of this optical response of the vanadium film upon the hydrogen uptake in current research corroborate the results documented by Hjörvarsson et. al. [98]. Above c_H = 0.8 H/V, the peak shifts toward higher intensity because of the loading of the Pd-cap layer.

According to the stress measurement, this kind of sample is expected to develop the maximum compressive stress in the range of -0.9 GPa while at a fully loaded state c_H = 1 H/V sample can have a final compressive stress state of about -0.7 GPa which is lower than the intermediate value (see section 6.3 and Table 6.3.1). It suggests very effective stress release on account of different loading conditions). According to the STM measurements on similar kinds of samples the theoretical expansion for a 30 nm V-film in the fully loaded state c_H = 1 H/V, is expected to be only 4 nm (see section 5.5 of chapter 5 and section 6.2 of the present chapter). STM measurements reveal a massive material transport to the sample surface. Morphology changes are found, as high as 15 nm from the deep valley-to-hilly island [see Figure 5.5.1 (a)]. Further, when the adhered V-film is loaded with hydrogen, the stress release strongly depends on the current density (see section 6.3). According to the discussion there, strong compressive stress can lead to massive material transport to the film surface and local film thickness increase. As Lambert-Beer's law also contains the sample thickness as a parameter, this thickness increase might additionally decrease the light transmission of the sample. In addition to this for vanadium, it is experimentally observed that the

imaginary part of the dielectric constant increases with hydrogen absorption resulting in a transmission decrease (see chapter 2 section 2.5.1).

To conclude, the darkening of the transmission signal upon hydrogen loading contains this added effect of sample thickness change (see Figure 4.1.2.2). Both concentration and thickness change act in the same direction for the transmitted light intensity.

6.4.3 Transmitted light intensity changes in detached vanadium films

The vanadium deposited on the 20 nm PC interlayer (Pd(15nm)/V(30nm)/PC(20nm) layer//glass is completely buckled in the as-prepared state [see section 4.1.7 and Figure 4.1.7.1 (a)]. Although the sample is buckled, it remains intact and EMF measurements are possible (see Figure 4.2.7). This sample has the lowest EMF values. Due to buckle formation, the transmission pixel intensities in Figure 4.1.7.2 do not provide much information. The peak is comparably broad. This is attributed to the scattering disturbance at the buckled film surface which is not possible to avoid. The transmitted light intensity fluctuates between c_H = 0.0 H/V and c_H = 0.5 H/V, with a peak position at i_t = 57 and i_t = 55, respectively. The c_H value between 0.5 H/V and 1 H/V peak almost stays pinned to the same position. The concentration-related intensity shift seems to be overshadowed by the buckle morphology effect.

As this kind of sample is already buckled in the initial state, only a small amount of compressive stress is expected to appear upon hydrogen loading in the tiny regions which may be adhered to the substrate, if any. Thus, the effect of massive material mass transport is not expected, for this sample.

6.4.4 Transmitted light intensity changes in samples with varying adhesion conditions

The vanadium films deposited on Pd interlayers, Pd(15nm)/V(30nm)/Pd(7nm) layer//glass and Pd(15nm)/V(30nm)/Pd(5nm) layer//glass are fully adhered in the initial state (see sections 4.1.3 and 4.1.4). But they buckle at higher hydrogen concentrations.

The related EMF curves show a higher chemical potential (see Figure 6.1.1) for the 5 nm Pd and the 7 nm Pd interlayer sample, when compared to the sample no-interlayer. According to the approach of Wagner et al. [121] the sample Pd interlayer samples should contain a higher compressive stress state. This is in accordance with the expectations, as the Pd-samples are strongly buckled, after H-loading.

The images in Figure 4.1.3.1 (a) show that the 7 nm Pd interlayer sample starts to grow small dark buckle spots at c_H = 0.4 H/V. At c_H = 0.8 H/V rapid growth appears and at c_H = 0.95 H/V the V-film is fully buckled. The sample with the 5 nm Pd interlayer looks uneven in the as-deposited state. This film shows small dark centers getting darker at c_H = 0.3 H/V. Above the concentration

of c_H = 0.65 H/V, the H/V buckle region appears to grow. This film is not fully buckled, c_H = 1 H/V, in the frame of view. By looking at the EMF graph at higher concentrations in Figure 6.1.1, it appears that the 5 nm Pd interlayer V-film has a higher EMF value compared to the 7 nm Pd interlayer V-film. That may be the result of the fully buckled state in the 7 nm Pd interlayer V-film.

The related transmission pixel intensity diagrams (for the 7 nm Pd interlayer, see Figure 4.1.3.2, and for the 5 nm Pd interlayer see Figure 4.1.4.2) behave similarly to those of the sample with no-interlayer shown in Figure 4.1.2.2. Except for a few details, all samples get darker with hydrogen loading, and the intensity moves towards lower intensity values. Only the intensities of the last few concentration steps move in the opposite direction due to the Pd cap-layer loading effect. The sample with the 5 nm Pd interlayer shows a small additional peak in Figure 4.1.4.2 which is explained by the dark spot present on this sample surface. For the sample with the 7 nm Pd interlayer shown in Figure 4.1.3.2, the starting peaks are pinned to the same position between c_H = 0.0 H/V to c_H = 0.25 H/V.

Therefore, it is suggested that both the samples with 7 nm Pd and 5 nm Pd interlayer are in a higher compressive stress state, as for both the samples the EMF shifts to higher values and both samples buckle with increasing hydrogen content. While for the sample with a 7 nm Pd interlayer, the hydrogen-induced stress results in full buckling which is not achieved for the sample with a 5 nm Pd interlayer; it is also detectable by the higher EMF value at higher hydrogen concentration (see Figure 6.1.1).

Both samples are adhered up to a concentration of c_H = 0.6 H/V and show strong buckling above this concentration. The stress measurement of the adhered film, Figure 4.3.1.1 (a) shows that after a certain hydrogen concentration (c_H ~ 0.2 H/V), the increases in the curve (black and red) stress are reduced, and thus, the film releases stress. So, it is suggested that samples in the adhered condition (of up to c_H = 0.6 H/V) develop stress follow by strong relaxation. This strong relaxation is detected by STM measurements in the form of massive material transport, leading to height changes, see sections 5.5 and 6.2. This is also expected to happen in the samples deposited on the Pd interlayer. Thus, Figures 4.1.3.2 and 4.1.4.2 show movement of the transmitted intensity signal strongly toward the darker intensity values. This is interpreted, again, as a double effect of increasing hydrogen concentration and partial thickness increase on the optical transmission signal.

Mixed adhesion samples with Pd dots and PC dots

The patterned samples with 5 nm Pd or 5 nm PC dots, namely Pd(15nm)/V(30 nm)/Pd(5nm) dots//glass and Pd(15nm)/V(30 nm)/PC(5nm) dots//glass are different in appearance in the as-deposited state (see sections 4.1.5 and 4.1.6). As the optical microscopes used for Pd and PC measurements are different, the exact intensity value is incomparable and only the relative change is considered here. The transmission images are given in Figures 4.1.5.1 (b) and 4.1.6.1 (b).

As discussed before, the sample containing PC dots is locally already there in a buckled state and the sample with Pd dots is not, see reflection images Figures 4.1.5.1 (a) and 4.1.6.1 (a). The

adhesion energy between the vanadium film and PC is very small. This results in film detachment above a certain mechanical stress or above a certain hydrogen concentration. The optical transmission changes with hydrogen loading differing between the adhered part of the sample, which stays adhered throughout the whole measurement, and the part that buckles due to the presence of the dots (PC or Pd).

With this information in mind, it can be seen that the transmission image shown in Figures 4.1.5.1 (b) and 4.1.6.1 (b), both the samples have a similar appearance at c_H = 0 H/V (as-deposited condition) and display no buckling effect (which is observed in the PC-dots region by images taken in reflection mode). Thus, here, the transmission signal does not get interfered by film buckling.

Due to the difference in total thickness and the metal character of the added Pd, the Pd dot regions appear darker than the rest of the regions of the sample (see Figure 4.1.5.1 (b). The (stronger) peak position at c_H = 0 H/V in the adhered part is i_t= 131 (grey scale intensity) and in the Pd dot part is i_t= 104 (grey scale intensity) (see appendix Figure A.8). The PC dots are transparent for visible light. Therefore, the PC sample shows a uniform transmission intensity. Figures 4.1.6.3 (a) and (b) show a constant peak position at c_H = 0 H/V at around i_t= 112 (grey), for the adhered and the buckled sample part, respectively.

The Pd dot area becomes visible with the hydrogen loading of the Pd-dot sample. As the vanadium layer of the Pd dot sample gets loaded with hydrogen (see Figure 4.1.5.1 (b)), the sample gets darker. Results of the optical reflection measurement clarify that at around c_H = 0.125, H/V buckles start to nucleate (Figure 4.1.5.1 (a)). In the optical transmission from c_H = 0.2 H/V onward bulking can be observed. It is clearly seen from the transmission pixel intensity diagrams that the sample shows V-film-like characteristics by getting darker upon hydrogen loading (Figure 4.1.5.3 (a) and (b).

The vanadium film deposited on the PC dot shows an increased buckle area upon hydrogen loading (Figure 4.1.6.1 (b)). The transmission pixel intensity diagrams (see Figure 4.1.6.2 (a)) show changes happening with hydrogen loading. Very Smooth loading results in peak position intensity shift from i_t= 112 to i_t= 97 (greyscale intensity), for the adhered sample part. The buckle sample part shows almost no change in the initial transmitted intensity from c_H = 0.0 H/V to c_H = 0.25H/V. The peak only gets broader. Above this concentration, the peak shifts to i_t= 105 at c_H = 0.7 H/V.

Figures 6.4.3 **(**a) and (b) show the relative change in the pixel intensity for the sample containing Pd and PC dots, with respect to the hydrogen concentration. The relative change is determined from the peak position of Figure 4.1.5.2 (b), appendix Figure (A.8), 4.1.6.2 (a), and 4.1.6.2 (b). The relative change is given in percentage and refers to the initial peak position at c_H = 0.0 H/V, in the sample. Figure 6.4.3 shows the relative intensity change for the adhered part in the sample with Pd dots and PC dots. The adhered parts show the maximum relative change of 14.5% for Pd and 13.4%, for PC respectively, appearing at c_H = 0.8 H/V. That the maximum values are reached in both samples at the same concentration, and they represent the fact that the adhered part just shows the V-film effect. Here, the V-film is directly adhered to the glass substrate, for both samples. The result, therefore, supports the expectations.

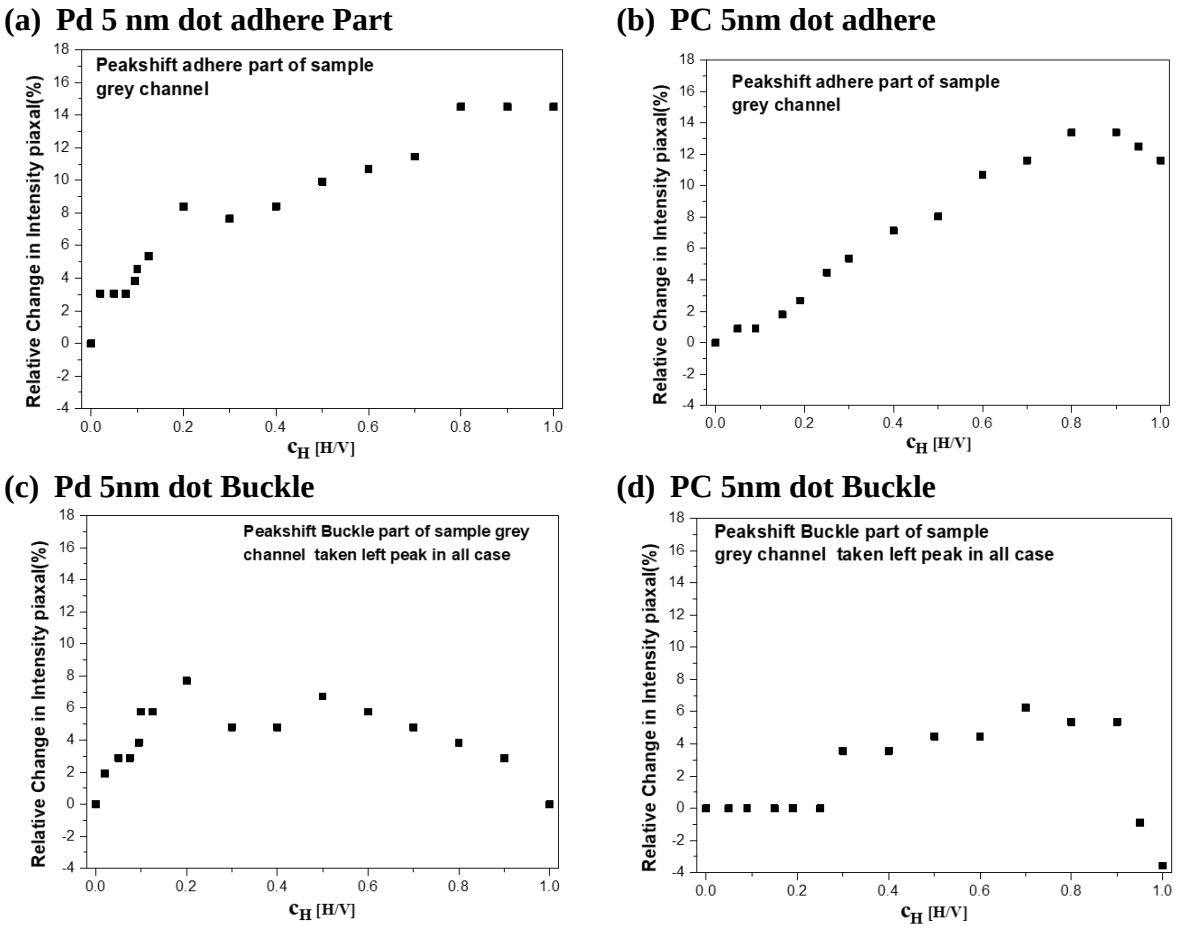

Figure 6.4.3: Relative change of the peak position of the transmitted light pixel intensity as a function of the concentrations, for the patterned vanadium sample having Pd dots and PC dots of 5 nm thickness, **(a) (b)** for the adhered sample part **(c) (d)** for the buckled sample part. All values are related to the initial peak position of each sample.

The dot parts of the samples experience a maximum shift of 6.7% for Pd and 6.3% for PC, at c_H = 0.5 H/V and c_H = 0.7 H/V, respectively. This dot part of the sample contains contributions from the interlayer, from the buckle formation, and is an outcome of the dot circumference that adds bending to the V-film. Thus, due to all these effects, less symmetry appears in the buckle part behavior, and that is also expected as this part has PC and Pd as interlayers.

The relative intensity change is much stronger for the adhered part than that for the dot part of the samples. This is contrary to the expectations, as the adhered part is considered to be the part exposed to higher hydrogen-induced stress. This assumption is based on results obtained by our group on niobium, palladium, and other metal films. Film detachment happens in the dot regions that are considered low-stress regions. According to findings by Wagner et al. [44] on hydrogen-

loaded Nb-films, regions with low mechanical stress form hydrides at lower chemical potentials; thus, they contain higher hydrogen concentrations at the sample chemical potentials as adhered regions. Wagner et al. confirmed this for Nb films by using hydrogen microscopy. Based on these studies, the (buckled) dot region should contain a higher hydrogen concentration than the adhered surrounding. Transferring this result to vanadium, the dot-region transmitted intensity should appear darker than that of the surrounding adhered region. This finding contradicts the findings in the transmitted light-intensity images (Figure 6.4.3). Here, the relative intensity change is stronger for the adhered region. This can be understood by combining the reported results and considering the massive material transport happening in regions exposed to high stress: the adhered sample parts. These regions contain information on the increase in both concentration and thickness. The massive increase in thickness influences the transmitted light intensity. Lambert-Beer's law contains both contributions and the massive local thickness cannot be neglected. This now leads to the new optical behavior with a strong darkening in the adhered sample parts and a soft darkening in the dot sample parts. In total, the dot regions appear lighter than the surrounding regions.

Thus, without the knowledge of the massive material transport happening in the adhered regions, this result could have been misinterpreted by a lower hydrogen content in the dot sample part regions. To our knowledge, published hydrogenography results are interpreted only by the change in the hydrogen content in the film and do not contain additional information about any massive thickness change. The results of this thesis on patterned samples show how this issue can lead to strong misinterpretations of the sample behavior.

Chapter 7

Summary

The objective of this work was to determine the hydrogen absorption behavior of grain boundary-rich nanocrystalline vanadium (V)-thin films and determine the effect of an interface layer on the sample loading behavior. The underlying idea was to control hydride locations by using different interface layers at different positions on one sample. This aspect was addressed by using several mixed adhesion samples.

The thin films (30 nm of V, different thicknesses for Pd) and interlayers needed for this work are deposited by ion beam sputtering (IBS) on glass substrates, and PC interlayers are deposited with pulsed laser deposition (PLD). X-ray diffraction and X-ray Reflectometry measurements were used to determine the texture, film thickness, and interface roughness of the as-prepared samples. V-films are loaded with hydrogen from the gas phase as well as electrochemically. Optical transmission and reflection (hydrogenography) measurements were performed by step-wise electrochemical loading and stress measurements, mostly by continuous electrochemical loading. The EMF was measured simultaneously. Additionally, STM measurements were undertaken upon hydrogen gas exposure on selected samples for local surface modification studies.

Results of our studies reveal that the optical microscopy measurements in the reflection mode provide information on the sample morphology (adhered or buckled), and in the transmission mode, they give information on the phase distribution. Optical properties are affected by the hydrogen content. In transmission mode, V-films get darker upon hydrogen content increase confirming previous studies showing increasing imaginary parts of the dielectric constant with increasing hydrogen content. The effect is wavelength-dependent and is maximum in the green color.

While V-films stayed adhered to the glass substrates, they locally detach and buckle at different hydrogen concentrations for different interlayers. This can be understood using different adhesion energies. V-films on PC interlayers are already buckled in the as-prepared state because of the very low adhesion.

V-films grown on glass substrates do not buckle up to c_H =1 H/V. Reflection mode images of the optical microscope measurements show no phase separation, even though a two-phase field is present, according to the EMF. This can be interpreted and explained as due to the presence of nano-scale hydrides which are homogeneously distributed in the V-film.

EMF measurements on different interlayers show more details: the buckled V-H films with PC interlayer have the lowest plateau pressure in comparison to all other samples. Because of the film buckling, the PC interlayer has the lowest stress state. Even in the buckled state this sample is intact and can be loaded up to c_H = 1 H/V. All other samples show higher EMF values. There might be a lattice relation and lattice matching involved that results in intrinsic mechanical stress. Different intrinsic stress could explain the different initial EMF-values levels. Stress measurements show the

in-plane compressive stress development with increasing hydrogen content in the films. The intrinsic stress was not measured in detail.

The buckled V-H films with PC interlayer have a wide two-phase region. The V-H films with Pd interlayer of 7 nm or 5 nm thickness show a two-phase region width of only 0.29 H/V and 0.34 H/V and, thus, a narrowed two-phase region. In comparison, V-H films with no-interlayer have a two-phase field width of 0.40 H/V which is close to that of V-H films with a PC interlayer. This indicates that V films with no-interlayer Pd(15nm)/V(30nm)//glass, have an effective stress relaxation mechanism.

Both V-films, with PC interlayer and with no-interlayer, are deposited either on an amorphous polymer over the glass or directly on the amorphous glass. Therefore, they may possess a similar microstructure, even though the mechanical stiffness of the PC layer or the glass substrate differs. Pd interlayers provide a crystalline basis for the V-film growth. Here, the lattice mismatch and a lattice relation can lead to intrinsic stress. That may explain the higher EMF of the V-film deposited on the Pd interlayer compared to the other (no-) interlayers.

STM measurements were performed on V-films with no-interlayer. The capping Pd layer, required for dissociative chemisorption of hydrogen gas molecules and oxidation protection, was tried to be kept as small as possible to allow for observations of changes in the V-film. It was observed that the V-film surface oxidizes with time and a Pd layer ranging from 0.16 nm to 8 nm was required, depending on how long the measurement needed to be run. STM images of the intrinsic surface of the nanocrystalline V-films show ripple-like morphologies, having lengths of 25 nm - 35 nm, widths of about 6 nm - 10 nm, and heights less than 2 nm. The 0.16 nm Pd required to perform these measurements forms Pd islands of 13 to 150 nm in width and 2 nm in height. Also, for a thicker Pd coverage of 1 nm surface ripples with the typical length, width, and height are visible.

The hydrogen gas pressure needed for hydride formation for bulk at room temperature was expected to be above 10^{-5} mbar or slightly higher. Hence, different pressure regimes with different loading durations were checked. Hydrogen exposure in the STM was experimentally challenging, as the gas discharge region of the STM is in this range (10^{-3} mbar-10 mbar). Thus, gas mixtures were used, and post-loading studies were performed.

Hydrogen gas exposure at $p_H = 8.3 \times 10^{-4}$ mbar for 30 min, results in ripple morphology changes in height from 2 nm to 3.5 nm - 4 nm, and width and the separate Pd islands disappear. New surface morphologies appear with elevated regions bordered by valleys with average topography humps of 200 (±20) nm in length, 130 (± 10) nm in width, and 3.4 (±0.3) nm in height. Longer exposure durations do not change the new topography. Lower pressure exposure ($p_H = 1.4 \times 10^{-4}$ mbar, 12 h) does not show the new surface morphology. Thus, $p_H = 8.3 \times 10^{-4}$ mbar or pressure higher than this can be used to see surface morphology changes.

Hydrogen gas exposure at $p_H = 6.7 \times 10^{-2}$ mbar allows for faster sample loading. Here, an 8 nm Pd cover was used, but the initial grain boundaries and the surface ripple topography of the underlying V-film were still detectable by the surface. After hydrogen loading, a completely new surface

topography was detected. Elevated areas with heights of about 7 nm and low valley-like areas having valley-to-island height changes in the range of 15 nm were measured. This is an unexpected high topography modulation with respect to the initial V-film thickness of 30 nm. It is suggested that hydrides form at this pressure leading to high mechanical stress.

A maximum height increase of 4 nm by pure lattice expansion is calculated by using linear elastic theory on a 30 nm V-film and hydrogen uptake of c_H = 1 H/V. Also, surface changes due to dislocation are not expected to this extent. It is suggested that this effect is related to the nanocrystalline nature of the samples leading to grain boundary sliding under high stress upon hydrogen uptake.

The stress development in continuous and step-wise loading, as well as the effect of the current density on the stress development and its reversibility, was measured for this kind of sample. The stress development in V-films upon the different process of hydrogen uptakes (continuous and step-wise loading) gives similar behavior for lower concentrations, maximum stress, and final stress state resulting in values close enough to each other. But the initial stress increase is slightly steeper for continuous loading. This curve bends suggesting plastic processes and even turns backward with a positive slope. This effect is not present in step-wise loading. This is interpreted with the time-dependency, due to enough time available for hydrogen to redistribute itself and, also, for stress-driven diffusion of lattice atoms.

Different current densities during continuous hydrogen loading of the same kind of film result in different stress developments. According to the stress developments, two different regimes were found and attributed to two different release mechanisms acting with different velocities: dislocation formation and grain sliding. Dislocation formation was attributed to the well-known behavior of reduced stress increase with a negative slope, and grain sliding accounted for stress release with an even positive slope. Interestingly, the sample loaded with medium current density j= 0.2 A/m^2 shows the strongest stress release with strong positive slope curve parts and the lowest final stress value.

Cyclic loading and unloading of a V-film with no-interlayer (j= 0.2 A/m^2) show a wide hysteresis. With increasing cycle number, the hysteresis area decreases. Hydrogen loading results in compressive stress, and hydrogen unloading results in tensile stress in the film. During loading, a maximum change occurs in the compressive stress curve, after which the curve bends upwards producing a dip in the curve. These dips and the upward bending are again attributed to grain sliding processes, Further loading cycles result in a reduced compressive stress development and a smaller dip and, thus, a smaller hysteresis area. This means that both stress release processes get less active with larger cycle numbers. The strong tensile stress state detected after unloading, supports the massive material transport towards the film surface which was found in the STM measurements.

Optical reflection measurements showed that V-films with no-interlayer stayed adhered to the substrate, while films on Pd or PC interlayers buckled. For PC interlayers the film was buckled right after deposition. For Pd interlayers, film buckling occurs at high hydrogen concentrations. This was attributed to the larger adhesion between Pd and V when compared to PC and V. While

this V-film on PC is in a very low-stress state, the V-film on the Pd interlayers is exposed to increasing compressive stress upon hydrogen uptake. This can explain the buckling of the V film with the Pd interlayer at high hydrogen concentrations. A slight thickness dependency is also found, the 7 nm Pd interlayer V-film gets fully buckled while the 5 nm Pd interlayer V-film does not.

The information from stress, STM, EMF, and optical measurements on thin films allowed us to interpret the unexpected results of mixed interlayer samples, especially the optical darkening of the hydrogen-loaded V-film in the no-interlayer regions with respect to the brighter V-film in the dots regions. For many films, the optical change was attributed via Lambert-Beer's law solely to the hydrogen content. This can be interpreted in a lower H-content in the buckled region, which is opposite to the expectations.

Mixed adhesion samples were prepared by using 5 nm thin and about 1 mm wide PC or Pd dots (see chapter 4 section 4.1.5, 4.1.6 and Figures 4.1.5.1, 4.1.6.1), having combinations of regions with V-film with no-interlayer and regions with PC or Pd interlayers. EMF measurements resemble those of V-films with no-interlayer and are not strongly affected by the Pd or PC pattern. This was supported by the thermodynamical DOS model (see chapter 4 section 4.4) that could be fitted to the available EMF and stress measurement data, in collaboration with Dr. Stefan Wagner.

When the V-film with mixed adhesion Pd dots 5 nm pattern is compared with V-film with Pd interlayer 5 nm, the buckling starts at the very low concentration of $c_H = 0.125$ H/V. For the V-film on the Pd dot pattern, buckle formation is completed in the Pd dot pattern area at $c_H = 0.7$ H/V. Buckle formation is not completed for the V-film on the 5 nm Pd interlayer, till $c_H = 1$ H/V. This suggests a patterning effect on the sample buckling, possibly because of V-film bending at the edges of the 5 nm thick dots.

The V-film with mixed adhesion 5 nm PC pattern and the V-film with 20 nm PC interlayer buckle in an as-deposited state, at the locations of the PC interlayer. The PC mixed adhesion pattern samples have two different regions: the buckled PC dot region and the adhered region that acts like the film with no-interlayer. With hydrogen loading, the buckle regions of both samples get darker, and bigger buckle folds are found. The rest of the V film has no PC interlayer and, thus, stays adhered to the substrate from $c_H = 0$ H/V to $c_H = 1$ H/V. This part appears lighter when compared to the buckled region in reflection mode. This region resembles the V film with no-interlayer.

For the V-film with no-interlayer (Pd(15nm)/V(30nm)//glass), the optical transmission goes darker with the increasing hydrogen content from $c_H = 0$ H/V to $c_H = 1$ H/V, presented in transmission images and transmission spectra (Figures 4.1.2.1 and 4.1.2.2). This sample stays adhered at all concentrations and the stress measurement for such a sample shows maximum compressive stress of -0.8 GPa (loading). STM measurements show massive material transport and morphology changes in the range of 15 nm, after hydrogen loading.

The V-film on the PC dots resembles the V-film on the PC interlayer. Transmission spectra of this sample do not interfere with buckle formation much. Because of the slight attachment to the substrate, this type of sample is not expected to develop large compressive stress. Thus, no massive

material transport upon grain sliding is expected for this sample. The film thickness should remain the same.

For the mixed adhesion Pd dot samples, the dot region resembles the V-film on Pd interlayers. EMF measurements on the V-films and applying Wagner et al. [121] model to them, show higher compressive stress when compared to the V-film with no interlayer. Transmission pixel intensity diagrams show a shift towards lower intensity for the 5 nm Pd interlayer and constant intensity for the 7 nm Pd interlayer, respectively. As these V-films buckle above c_H = 0.6 H/V, they develop strong compressive stress upon hydrogen uptake, resulting in stress release and massive material transport. Thus, the transmission signal gets affected and shifts toward lower intensity, due to thickness change in addition to hydrogen concentration change.

Transmission images for both types of mixed adhesion samples show similar appearance and constant brightness in the initial state. The dot regions (even when buckled) are (mainly) not visible in transmission. The transmission pixel intensity of the region outside the dot resembles that of the V-film with no-interlayer and gets darker upon hydrogen loading.

Selected transmission spectra analysis for the buckled and adhered area of the mixed adhesion samples showed similar behavior as the related thin films. The V-film on the adhered part of the PC dots sample shows no-interlayer-like characteristics while the buckled part shows only a small shift in the peak position towards lower intensity. For both mixed adhesion samples (Pd and PC), the maximum relative change of transmission intensity in the no-interlayer part gives a change of 14.5% and 13.4%, by plotting the peak intensity with respect to the concentration at c_H = 0.8 H/V with respect to c_H = 0 H/V. In the dot part, the maximum relative change of transmission intensity is 6.7% and 6.3% for c_H = 0.5 H/V and c_H = 0.7 H/V, respectively. Certainly, the dot part behavior of the sample contains contributions of the interlayer (Pd or PC), thereby affecting the transparency difference with hydrogen loading and buckle formation. All these effects result in different behavior of the buckle part.

Thus, the lighter appearance of the V-film on the buckled dot parts compared to the adhered parts can be attributed to thickness changes related to the massive material transport via grain sliding in the nanocrystalline V-films. As massive material transport only happens in the adhered parts, this affects the optical transmission on top of the hydrogen content. Lambert-Beer's law contains contributions of both thickness and hydrogen content. Thus, the surrounding adhered regions get much darker, mimicking a higher hydrogen content, if the thickness change by massive material transport is overlooked. Simple transmission signal changes upon hydrogen concentration were observed for epitaxial Nb, Pd, and other metal films [44]. Massive thickness changes were not reported for these films, just glide steps resulting from dislocations appearing at the film surface. But nanocrystalline vanadium films show massive material transport upon hydrogen loading, which originates from grain sliding. The transmission signal contains information on hydrogen uptake as well as thickness changes. This effect has to be considered when interpreting light-intensity data, especially on nanocrystalline thin films, using the Lambert-Beer law for hydrogen concentration determination.

List and details of Appendices

A1. Pd(15nm)/V(30nm)//glass detailed concentration range

Figure A.1 presents the transmission pixel intensity diagrams of Pd(15nm)/V(30nm)//glass (no-interlayer). As mentioned in section 4.1.2, Figure A.1 shows the whole concentration range from c_H = 0 H/V to c_H = 1 H/V. The right-hand side of the graph represents the concentration scale of the electrochemical loading with the step size of 0.01 between c_H = 0 H/V to c_H = 0.3 H/V, 0.02 between c_H = 0.3 H/V to c_H = 0.5 H/V and 0.05 between c_H = 0.5 H/V to c_H = 1 H/V, as shown by Figure A.1. In section 4.1.2, the curve at the concentration step c_H = 0.55 H/V is replacing c_H = 0.6 H/V. As mentioned, this shifting effect does not originate from the optical change in the sample itself, but from some disturbance during the measurement

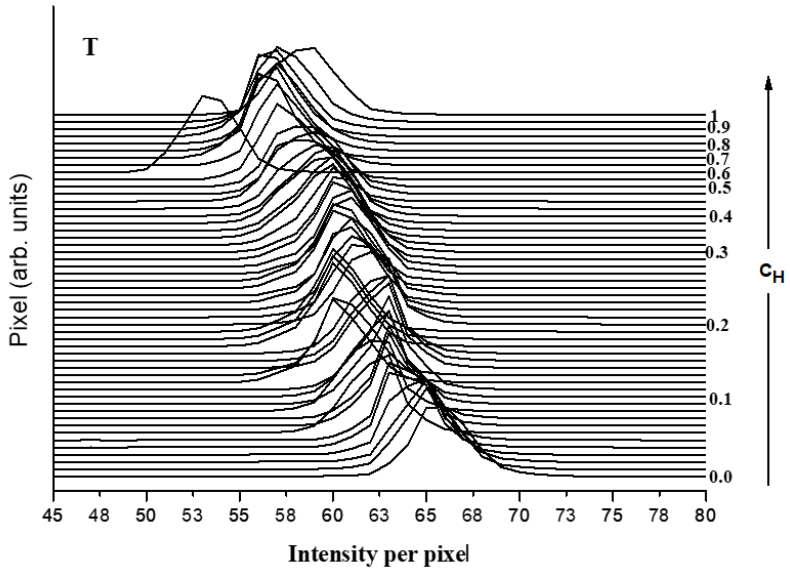

Figure A.1: Transmission pixel intensity diagrams of the Pd(15nm)/V(30nm)//glass with complete concentration range.

A2. EMF of first and second loading of Pd(15nm)/V(30nm)/Pd(7nm) layer //glass

Difference of -0.03 V in the EMF signal between the first and second loading arise due to different initial stresses in the sample before the first and the second loading cycle. Before the first loading, the sample has an intrinsic compressive stress state, due to deposition conditions. During the first loading, the sample gets more in-plane compressive stress, as shown by the stress measurement. It also releases these stresses through stress-relaxation processes. Unloading of the sample shows tensile stress development. All this results in different stress conditions. Thus, result in a lowering of the plateau pressure and are observed by the measurement shown in Figure A.2.

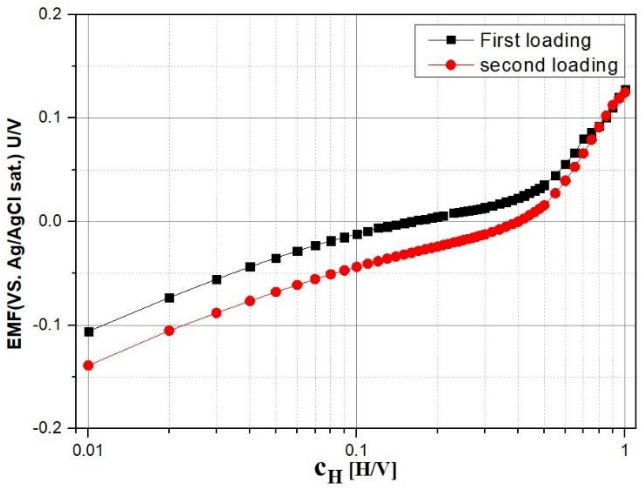

Figure A.2: First and second loading curve of Pd(15nm)/V(30nm)/Pd(7nm) layer //glass, measured during electrochemical hydrogen loading.

A.3. Adhere and buckle transmission of mixed adhesion samples with Pd dots

Mixed adhesion sample Pd(15nm)/V(30nm)/Pd(5nm) dots//glass dots develop buckles above c_H = 0.125 H/V, as can be seen from in reflection mode images. As discussed in chapter 4, buckles do not (strongly) affect the transmission signal, Figure A.3 presents pixel intensity diagrams focus on three concentrations (0.095, 0.1, and 0.125 H/V), that are shifted to the right by no known physical phenomenon. Therefore, these pixel intensity diagrams are shifted back to the left with a constant value.

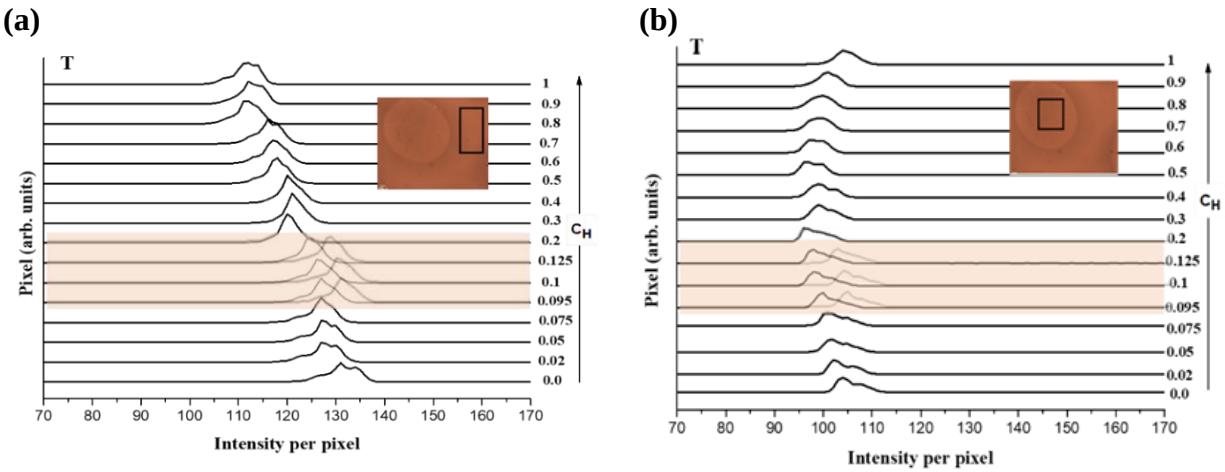

Figure A.3: Transmission pixel intensity diagrams of the Pd(15nm)/V(30 nm)/Pd(5nm) dots//glass film. **(a)** The adhered part of the sample. **(b)** The buckle part of the sample.

The coloured area of the pixel intensity diagrams of the adhered and the buckled part show this change. Figure 4.1.5.3 (b) shows the corrected version of adhered part of Figure A.3

A.4. Mixed adhesion samples with PC dots

The sudden shift at 0.1 H/V and 0.2 H/V (see Figure A.4) is judged to be an artificial intensity jump and does not originate from a change in the sample itself but from some random disturbance. Thus, to present the physical effects of hydrogen absorption, the neighbouring diagrams are plotted (for example c_H = 0.09 H/V (replacing those at 0.1 H/V) and c_H = 0.19 H/V (replacing those at 0.2 H/V), as presented in Figure A.4.

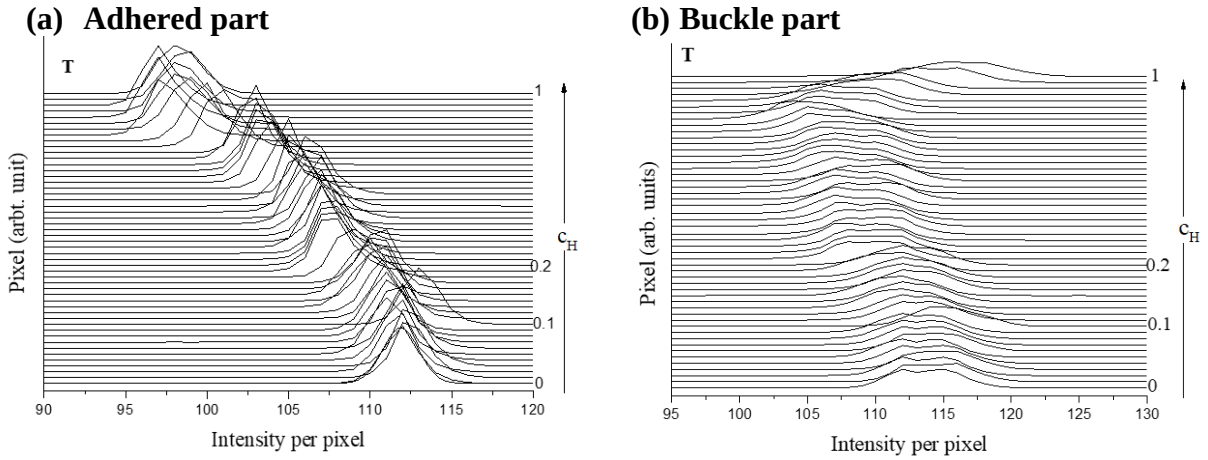

Figure A.4: Transmission pixel intensity diagrams of the Pd(15nm)/V(30 nm)/PC (5nm) dots//glass film presenting all concentration steps taken during the measurement, for the **(a)** adhered part and the **(b)** buckled part.

A.5. First and second loading and unloading cycle of Pd(15nm)/V(30nm)//glass sample

Given below are the six hysteresis cycles of hydrogen loading and unloading of the Pd(15nm)/V(30nm)//glass sample. Figure A.5 included the starting 1st (loading and unloading indicated with black color) and 2nd (loading and unloading indicated with red color) cycle. First loading and unloading show an open hysteresis. During unloading, high tensile stress develops in the sample resulting in the opening. This effect decreases with continuous loading and unloading cycles. The second cycle shows a distorted hysteresis because the first unloading results in larger tensile stress than the second unloading.

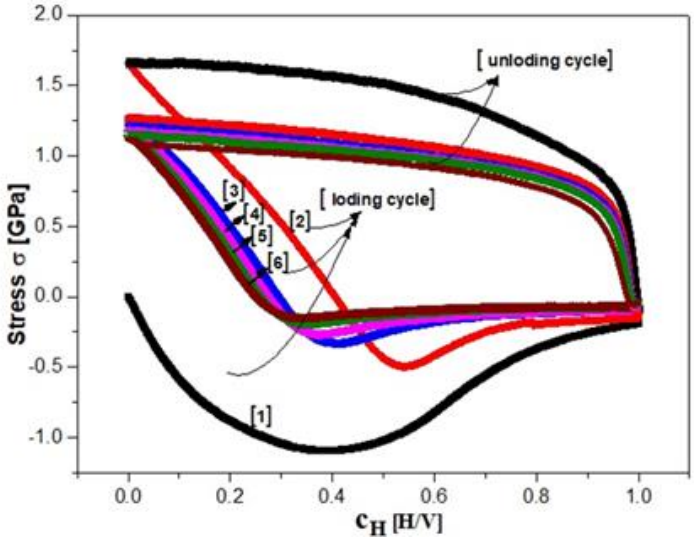

Figure A.5: 1st, 2nd, and higher loading and unloading cycles resulting in stress hysteresis, as observed on Pd(15nm)/V(30nm)//glass.

A.6 Pressure-composition isotherm of V-H system

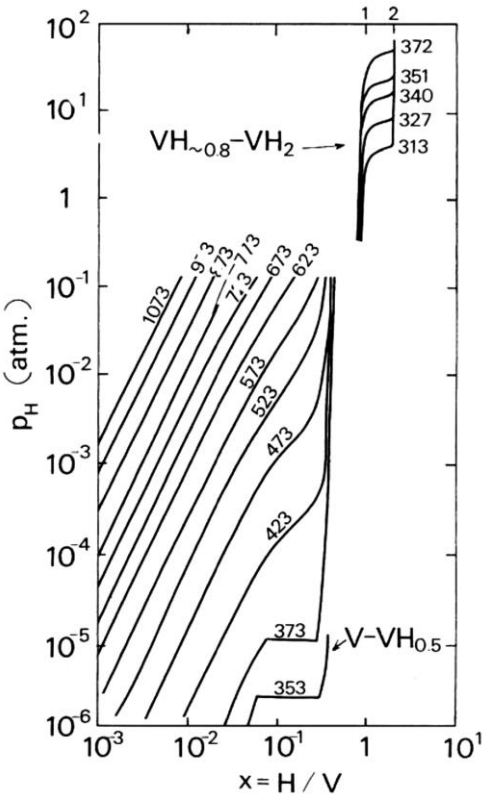

Figure A.6: Pressure-composition-isotherms of V-H plotted for different temperatures (K). Reprinted from [13]. copyright 2005 Springer Nature.

A.7 Phase diagram of the Pd-V system

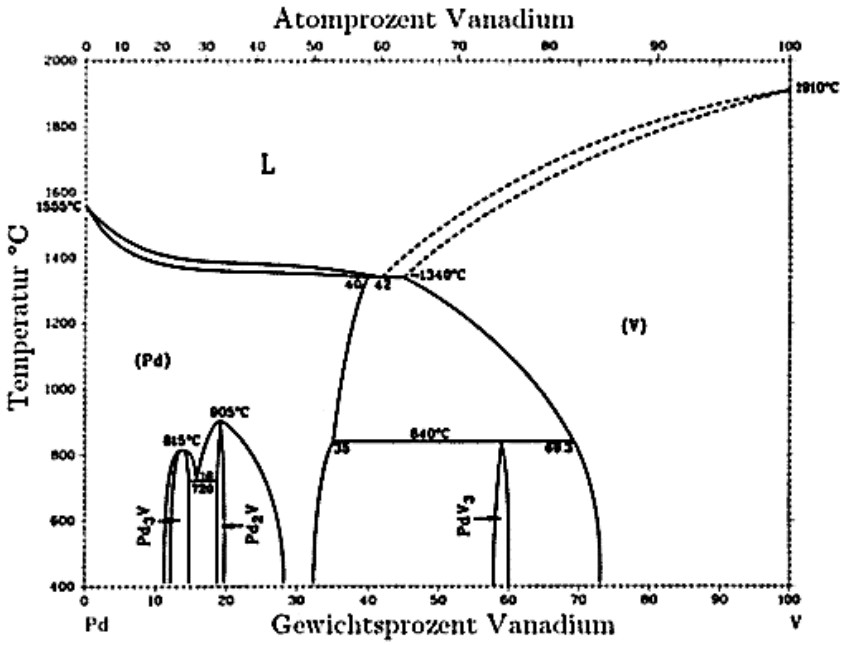

Figure A.7: Presents the phase diagram of the Pd-V system. Reprinted from [124]. copyright 1992 Springer Nature.

A.8 Transmission pixel intensity diagrams of the mixed adhesion Pd dots sample buckle region

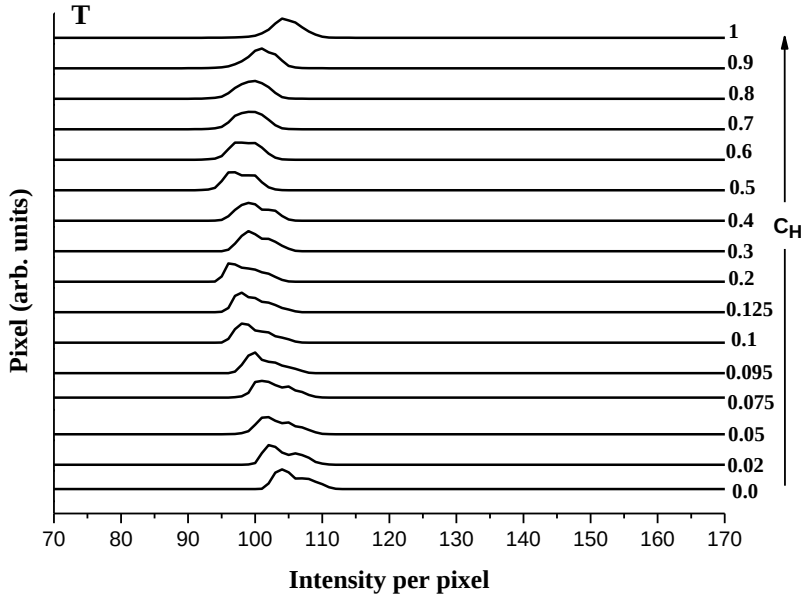

Figure A.8: Transmission pixel intensity diagrams of buckle part of the Pd(15nm)/V(30 nm)/Pd(5nm) dots//glass film .

A.9. Transmission pixel intensity diagrams of thicker V-films

Figure A.9. presents the transmission intensity diagram of 50 nm and 70 nm film, as with the new light microscope [described in chapter 2] it was possible to probe thicker films as well. With the new microscope, transmission images look more smoother, and 50 nm V-film behaves similarly to as seen for 30 nm V-film. On the other hand, the hydrogen loading effect on 70 nm film show changes at high concentrations in the transmission intensity diagram

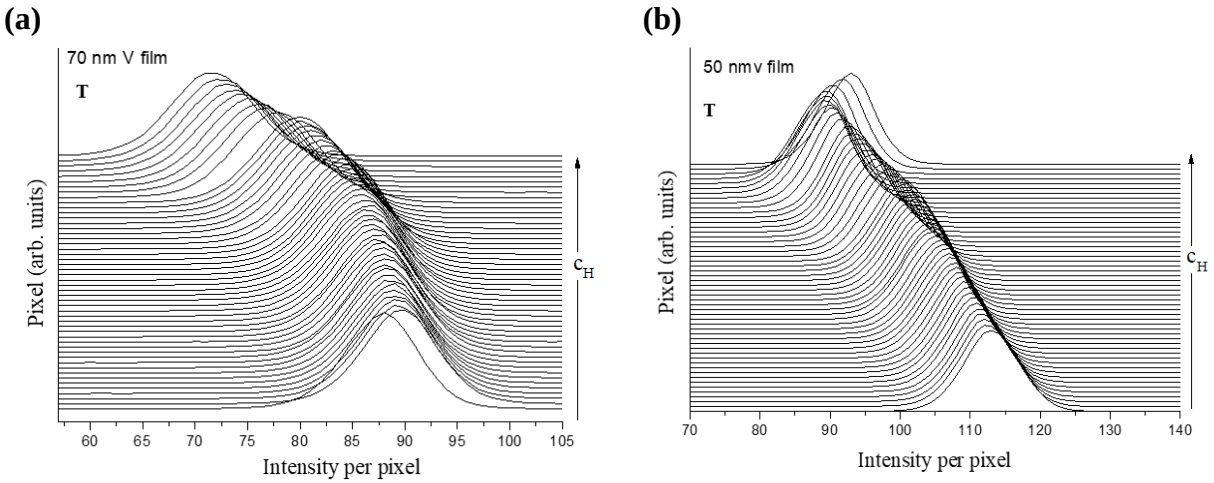

Figure A.9: The transmission intensity diagrams of **(a)** a 70 nm and **(b)** a 50 nm film. With the Leica 1750 light microscope (described in chapter 2), it was possible to probe thicker films, as well. With the Leica 1750 microscope, transmission images look smoother. The 50 nm V-film behave similar to 30 nm V-film while 70 nm V-film show till 1 H/V intensity shifting toward low intensity.

Bibliography

[1] B. Lomborg, "The World Is Mostly Run On Fossil Fuels (81%)," Linkedin, 19 Feb 2018. [Online]. Available: https://www.linkedin.com/pulse/world-mostly-run-fossil-fuels-81-bjorn-lomborg.

[2] A. Zervos, "RENEWABLES 2018 GLOBAL STATUS REPORT REN21," National Technical University of Athens, Athens, 2018.

[3] "Global Trends in Renewable Energy Investment 2018," Frankfurt School of Finance & Management gGmbH 2018, Frankfurt, 2018.

[4] "Hydrogen from renewable power: Technology outlook for the energy transition," International Renewable Energy Agency, Abu Dhabi, 2018.

[5] J. A. Dean, Langes hand book of Chemistry, Fifteenth Edition, McGraw-Hill Professional, 1998.

[6] N. G. Hörmann, A. Grossa and P. Kaghazchi, "Semiconductor–metal transition induced by nanoscale stabilization," *Phys. Chem. Chem. Phys.,* vol. 17, no. 8, pp. 5569-5573, 2015.

[7] A. Pundt and R. Kirchheim, "HYDROGEN IN METALS: Microstructural Aspects," *Annual Review of Materials Research,* vol. 36, pp. 555-608, 2006.

[8] U. Laudahn, A. Pundt, M. Bicker, U. v. Hülsen, U. Geyer, T. Wagner and R. Kirchheim, "Hydrogen-induced stress in Nb single layers," *Journal of Alloys and Compounds,* Vols. 293-295, pp. 490-494, 1999.

[9] W. S. Slaughter, The Linearized Theory of Elasticity, Boston: Springer Science + Business Media, Birkhäuser Boston, MA, 2002.

[10] B. Hjörvarsson, G. Andersson and E. Karlsson, "Metallic superlattices: quasi two-dimensional playground for hydrogen," *Journal of Alloys and Compounds,* Vols. 253-254, pp. 51-57, 1997.

[11] S. Olsson, "Phase transition and phase transformation of hydrogen in quasi-2D lattices," Uppsala University, Uppsala, 2003.

[12] K. Nörthemann, "Wasserstoffabsorption in epitaktischen Niobschichten: eine STM-Studie," Uni-Goettingen, Göttingen, 2006.

[13] Y. Fukai, The Metal-Hydrogen System, Heidelberg: Springer Berlin, 2005.

[14] G. Alefeld and J. Völkl, Hydrogen in Metals I, Heidelberg: Springer Berlin, 1978.

[15] X. Xin, R. Johansson, M. Wolff and B. Hjörvarsson, "Hydrogen in vanadium: Site occupancy and isotope effects," *Phys. Rev. B,* vol. 93, no. 13, p. 134107, 2016.

[16] S. Wagner, "Dünne Palladium-Wasserstoff-Schichten als Modellsystem: Elektrischer Widerstand und Thermodynamik struktureller Phasenübergänge unter elastischen und mikrostrukturellen Zwangsbedingungen," Georg-August-Universität Göttingen, Göttingen, 2014.

[17] I. P. Jain, Y. K. Vijay, K. L. Malhotra and K. S. Uppadhyay, "Hydrogen storage in thin film metal hydride—a review," *International Journal of Hydrogen Energy,* vol. 13, no. 1, pp. 15-23, 1988.

[18] S. Wagner and A. Pundt, "Quasi-thermodynamic model on hydride formation in palladium–hydrogen thin films: Impact of elastic and microstructural constraints," *International journal of hydrogen energy,* vol. 41, no. 4, pp. 2727-2738, 2016.

[19] S. Wagner, T. Kramer, H. Uchida, P. Dobron, J. Cizek and A. Pundt, "Mechanical stress and stress release channels in 10–350 nm palladium hydrogen thin films with different micro-structures," *Acta Materialia,* vol. 114, pp. 116-125, 2016.

[20] J. Bloch, J. Pejova, J. Jacob and B. Hjörvarsson, "Hydrogen-vanadium system in thin films: Effect of film thickness," *Physical Review B,* vol. 82, no. 24, p. 245428, 2010.

[21] G. Andersson, B. Hjörvarsson and P. Isberg, "influence of compressive biaxial strain on the hydrogen uptakeof ultrathin single-crystal vanadium layers," *PHYSICAL REVIEW B,* vol. 55, pp. 1174-1781, 1997.

[22] G. Andersson, P. H. Andersson and B. Hjörvarsson, "Effects of varying compressive biaxial strain on the hydrogen uptake of thin vanadium (001) layers," *Journal of Physics: Condensed Matter,* vol. 11, no. 35, p. 6669, 1999.

[23] D. G. Westlake, "A geometric model for the stoichiometry and interstitial site occupancy in hydrides (deuterides) of LaNi5, LaNi4Al and LaNi4Mn," *Journal of the Less Common Metals,* vol. 91, no. 2, pp. 275-292, 1983.

[24] A. Magerl, B. Berre and G. Alefeld, "Changes of the elastic constants of V, Nb, and Ta by hydrogen and deuterium," *Physica status solidi (a),* vol. 36, no. 1, pp. 161-171, 1976.

[25] T. Schober, "Electron microscopy of hydride precipitates in niobium," *Scripta Metallurgica,* vol. 7, no. 10, p. 1119, 1973.

[26] B. J. Makenas and H. K. Birnbaum, "Phase changes in the niobium-hydrogen system. I. Accommodation effects during hydride precipitation. Technical report," *Acta Metallurgica,* vol. 28, no. 7, pp. 979-988, 1980.

[27] A. J. Maeland, "Investigation of the Vanadium—Hydrogen System by X-Ray Diffraction Techniques12," *J. Phys. Chem.,* vol. 68, no. 8, pp. 2197-2200, 1964.

[28] T. Schober and A. Carl, "A differential thermal analysis study of the vanadium–hydrogen system," *physica status solidi (a),* vol. 43, no. 2, pp. 443-449, 1977.

[29] G. Alefeld and J. Völkl, Hydrogen in Metals II, Springer-Verlag Berlin Heidelberg GmbH, 1978.

[30] Y. Fukai and S. Kazama, "On the constitution of β-VHX," *Scripta Metallurgica,* vol. 9, no. 10, pp. 1073-1076, 1975.

[31] H. Asano, I. Abe and Hirabawashi, "A calorimetric study of the phase transformation of vanadium hydrides VH0.06–VH0.77," *Acta Metallurgica,* vol. 24, no. 1, pp. 95-99, 1976.

[32] W. Pesch, "Strukturen und Phasenumwandlungen im Vanadium-Wasserstoff und Vanadium-Deuterium-System," Rhei-nisch-Westfaelische Technische Hochschule, Aachen, 1982.

[33] H. Wenzl, "Ordered and disodered hydrogen interstitials in Niobium, Tantalum and Vanadium crystals: Structures and Phase diagrams," *Journal de Physique Colloques,* vol. C7, pp. 221-222, 1977.

[34] H. Sugimoto, "Mechanism of Stabilization of the β Phase of Vanadium-Hydrogen System," *Journal of the Physical Society of Japan,* vol. 58, no. 8, pp. 2592-2599, 1984.

[35] Y. Noda, K. Masumoto, S. Koike, T. Suzuki and S. Sato, "X-ray crystallographic study of tetragonal and monoclinic B1-V2H," *Acta Cryst. B,* vol. 42, no. 6, pp. 529-533, 1986.

[36] S. Takano and T. Suzuki, "Electron-optical study of $beta$-hydride and hydrogen embrittlement of vanadium," *Acta Met.,* vol. 22, no. 3, pp. 265-274, 1974.

[37] R. E. Marsh, "On the Structure and Twinning of monoclinic β-V2H*," *Acta Cryst. B,* vol. 43, no. 5, pp. 415-416, 1987.

[38] A. Pundt, *Nanoskalige Metall-Wasserstoff-Systeme,* Göttingen: Georg-August-Universität Göttingen, 2005.

[39] F. D. Manchester, V. San-Martin and V. Pitre, "The H-Pd (hydrogen-palladium) System," *Journal of Phase Equilibria,* vol. 15, no. 1, pp. 62-83, 1994.

[40] P. F. Miceli, H. Zabel, J. A. Dura and C. P. Flynn, "Anomalous lattice expansion of metal-hydrogen thin films," *Journal of Materials Research,* vol. 6, no. 5, pp. 964-968, 1991.

[41] R. Gemma, "Hydrogen in V-Fe thin films and Fe/V-Fe multi-layered thin films," Göttingen University, Göttingen, 2011.

[42] S. C. Jain, A. H. Harker and R. A. Cowley, "Misfit strain and misfit dislocations in lattice mismatched epitaxial layers and other systems," *Philosophical Magazine A,* vol. 75, no. 6, pp. 1461-1515, 1997.

[43] R. Kirchheim, "Interaction of hydrogen with external stress fields," *Acta Metallurgica,* vol. 34, no. 1, pp. 37-42, 1986.

[44] S. Wagner, M. Moser, C. Greubel, K. Peeper, P. Reichart, A. Pundt and G. Dollingerb, "Hydrogen microscopy – Distribution of hydrogen in buckled niobium hydrogen thin films," *International Journal of Hydrogen Energy,* vol. 38, no. 31, pp. 13822-13830, 2013.

[45] J. Weissmüller and C. Lemier, "On the size dependence of the critical point of nanoscale interstitial solid solutions," *Philosophical Magazine Letters,* vol. 80, no. 6, pp. 411-418, 2000.

[46] J. Weissmüller, "Thermodynamics of Nanocrystalline Solids," in *NANOCRYSTALLINE METALS AND OXIDES Selected Properties and Applications*, Boston, KLUWER ACADEMIC PUBLISHERS, 2001, pp. 1-40.

[47] R. Koch, "The intrinsic stress of polycrystalline and epitaxial thin metal films," *Journal of Physics: Condensed Matter,* vol. 6, no. 45, pp. 9519-9550, 1994.

[48] R. Koch, "Intrinsic stress of epitaxial thin films and surface layers," in *Growth and Properties of Ultrathin Epitaxial Layers*, Elsevier Science, 1997, pp. 448-489.

[49] T. Scharf, J. Faupel, K. Sturm and H. Krebs, "Intrinsic stress evolution in laser deposited thin films," *Journal of Applied Physics,* vol. 94, no. 7, pp. 4273-4278, 2003.

[50] H.-U. Krebs, M. Weisheit, J. Faupel, E. Süske, T. Scharf, C. Fuhse, M. Störmer, K. Sturm, M. Seibt, H. Kijewski, D. Nelke, E. Panchenko and M. Buback, "Pulsed Laser Deposition (PLD) -- A Versatile Thin Film Technique," in *Advances in Solid State Physics*, Heidelberg, Springer-Verlag Berlin, 2003, pp. 505-518.

[51] M. F. Doerner and W. D. Nix, "Stresses and deformation processes in thin films on substrates," *Critical Reviews in Solid State and Materials Sciences,* vol. 14, no. 3, pp. 225-268, 1988.

[52] J. A. Thornton, J. Tabock and D. W. Hoffman, "Internal stresses in metallic films deposited by cylindrical magnetron sputtering," *Thin Solid Films,* vol. 64, no. 1, pp. 111-119, 1979.

[53] M. Pletea, W. Brückner, H. Wendrock and R. Kaltofen, "Stress evolution during and after sputter deposition of Cu thin films onto Si (100) substrates under various sputtering pressures," *Journal of Applied Physics,* vol. 97, no. 5, p. 054908, 2005.

[54] T. Scharf, J. Faupel, K. Sturm and H.-U. Krebs, "Pulsed laser deposition of metals in various inert gas atmospheres," *Applied Physics A volume,* vol. 79, no. 4-6, pp. 1587-1589, 2004.

[55] S. Wagner and A. Pundt, "Mechanical stress impact on thin Pd1−xFex film thermodynamic properties," *Applied Physics Letters,* vol. 92, p. 051914, 2008.

[56] R. Kirchheim and A. Pundt, "Hydrogen in Metals," in *Physical Metallurgy (Fifth Edition)*, Elsevier, 2014, pp. 2597-2705.

[57] D. Sander, "The correlation between mechanical stress and magnetic anisotropy in ultrathin films," *Reports on Progress in Physics,* vol. 62, no. 5, pp. 809-858, 1999.

[58] U. Laudahn, *Spannungen und Dehnungen von mit Wasserstoff beladenen Nb-Einfach- und Pd-Nb-Vielfachschichten,* Göttingen: Georg-August-Universität Göttingen, 1998.

[59] J.-M. Zhang, Y. Zhang, K.-W. Xu and V. Ji, "Young's modulus surface and Poisson's ratio curve for cubic metals," *Journal of Physics and Chemistry of Solids,* vol. 68, no. 4, pp. 503-510, 2007.

[60] L. D. Landau and E. M. Lifshitz, Theory of Elasticity, Course of Theoretical Physics, Oxford: Butterworth-Heinemann, 1986.

[61] V. Burlaka, *Critical thicknesses in Nb-H thin films: coherent and incoherent phase transitions, change of precipitation and growth modes and ultrahigh mechanical stress,* Göttingen: Georg-August-Universität Göttingen, 2015.

[62] J. F. Nye, Physical Properties Of Crystals: Their Representation by Tensors and Matrices, USA: Oxford University Press, 2002.

[63] N. W. Ashcroft and N. D. Mermin, Solid State Physics, Orlando: Harcourt College Publishers, 1976.

[64] H.-J. Kowalsky, Lineare Algebra (De Gruyter Lehrbuch), Berlin: De Gruyter, 1974.

[65] G. Fischer, Lernbuch Lineare Algebra und Analytische Geometrie, Springer Spektrum, 2012.

[66] D. I. Bolef, "Elastic Constants of Single Crystals of the bcc Transition Elements V, Nb, and Ta," *Journal of Applied Physics,* vol. 32, no. 1, pp. 100-105, 1961.

[67] M. Hamm, *Hydrogen diffusion and hydride formation in grain boundary rich magnesium,* Göttingen: Georg-August-Universität Göttingen, 2019.

[68] E. Nikitin, "Controlled delamination of metal films by hydrogen loading," Georg-August-Universität Göttingen, Göttingen, 2008.

[69] M. Dornheim, *Stresses, strains and position of phase boundaries in thin Nb- and Y-films during H-loading and -unloading,* Göttingen: Georg-August-Universität Göttingen, 2002.

[70] A. Pundt, "Hydrogen in Nano-sized Metals," *Advanced Engineering Materials,* vol. 6, no. 1, pp. 11-21, 2004.

[71] Y. Li, A. J. Bushby and D. J. Dunstan, "The Hall–Petch effect as a manifestation of the general size effect," *Proceedings of the Royal Society A,* vol. 472, no. 2190, pp. 1-17, 2016.

[72] M. Turwitt, G. Elssner and G. Petzow, "MANUFACTURING AND MECHANICAL PROPERTIES OF INTERFACES BETWEEN SAPPHIRE AND NIOBIUM," *Journal de Physique Colloques,* vol. 46, pp. C4-123_C4-127, 1985.

[73] K. H. Hansen, T. Worren, S. Stempel, E. Lægsgaard, M. Bäumer and H.-J. Freund, "Palladium Nanocrystals on Al2O3: Structure and Adhesion Energy," *Physical Review Letters,* vol. 83, no. 20, pp. 4120-4123, 1999.

[74] W. Rosenhain and D. Ewen, "The Intercrystalline Cohesion of Metals," *Journal of the Institute of Metals,* vol. 10, no. 2, p. 119, 1913.

[75] W. Rosenhain and J. C. Humfrey, "The Tenacity, Deformation, and Fracture of Soft Steel at High Temperatures," *Journal of the Iron and Steel Institute,* vol. 87, pp. 219-271, 1913.

[76] I. Adlakha and K. N. Solanki, "Critical assessment of hydrogen effects on the slip transmission across grain boundaries in α-Fe," *Proceedings of the Royal Society A,* vol. 472, no. 2185, pp. 1-16, 2016.

[77] C. M. Hu, C. M. Lai, P. W. Kao, N. J. Ho and J. C. Huang, "Quantitative measurements of small scaled grain sliding in ultra-fine grained Al–Zn alloys produced by friction stir processing," *Materials Characterization,* vol. 61, no. 11, pp. 1043-1053, 2010.

[78] M. F. Ashby and R. A. Verrall, "Diffusion-Accommodated Flow and Superplasticity," *Acta Metallurgica,* vol. 21, no. 2, pp. 149-163, 1972.

[79] J. I. Avila, R. J. Matelon, R. Trabol, M. Favre, D. Lederman, U. G. Volkmann and A. L. Cabrera, "Optical properties of Pd thin films exposed to hydrogen studied by transmittance and reflectance spectroscopy," *Journal of Applied Physics,* vol. 107, no. 2, p. 023504, 2010.

[80] R. J. Matelon, J. I. .Avila, U. G. Volkmann, A. L. Cabrera, E. H. Morales and D. Lederman, "Substrate effect on the optical response of thin palladium films exposed to hydrogen gas," *Thin Solid Films,* vol. 516, no. 21, pp. 7797-7801, 2008.

[81] A. L. Cabrera, J. I. Avila and D. Lederman, "Hydrogen absorption by metallic thin films detected by optical transmittance measurements," *International Journal of Hydrogen Energy,* vol. 35, no. 19, pp. 10613-10619, 2010.

[82] R. Griessen, I. Giebels and B. Dam, "Optical properties of metal-hydrides: switchable mirrors," Vrije Universiteit, Amsterdam, 2004.

[83] R. Gremaud, M. Gonzalez-Silveira, Y. Pivak, S. d. Man, M. Slaman, H. Schreuders, B. Dam and R. Griessen, "Hydrogenography of PdHx thin films: Influence of H-induced stress relaxation processes," *Acta Materialia,* vol. 57, no. 4, pp. 1209-1219, 2009.

[84] A. T. M. van Gogh, D. G. Nagengast, E. S. Kooij, N. K. Koeman, J. H. Rector, R. Griessen, C. F. J. Flipse and R. J. J. G. A. M. Smeets, "Structural, electrical, and optical properties of La1-zYzHx switchable mirrors," *Physical REview B,* vol. 62, no. 19, p. 195105, 2001.

[85] E. Shalaan, H. Schmitt and K.-H. Ehses, "On the optical properties of gadolinium hydride systems," *Thn solid films,* vol. 489, no. 1-2, pp. 330-335, 2005.

[86] E. S. Kooij, A. T. M. v. Gogh and R. Griessen, "In Situ Resistivity Measurements and Optical Transmission and Reflection Spectroscopy of Electrochemically Loaded Switchable YH x Films," *Journal of The Electrochemical Society,* vol. 146, no. 8, pp. 2990-2994, 1999.

[87] R. Gremaud, C. P. Broedersz, D. M. Borsa, A. Borgschulte, P. Mauron, H. Schreuders, J. H. Rector, B. Dam and G. R, "Hydrogenography: An Optical Combinatorial Method To Find New Light-Weight Hydrogen-Storage Materials," *Advanced Materials,* vol. 19, no. 19, pp. 2813-2817, 2007.

[88] R. Gremauda, M. Slaman, H. Schreuders, B. Dam and R. Griessen, "An optical method to determine the thermodynamics of hydrogen absorption and desorption in metals," *Applied Physics Letters,* vol. 91, no. 23, p. 231916, 2007.

[89] J. N. Huiberts, R. Griessen, J. H. Rector, R. J. Wijngaarden, J. P. Dekker, d. G. D. G. and N. J. Koeman, "Yttrium and Lanthanum hydride films with switchable optical properties," *Nature,* vol. 380, no. 6571, pp. 231-234, 1996.

[90] C. Perrotton, R. J. Westerwaal, N. Javahiraly, M. Slaman, H. Schreuders, B. Dam and P. Meyrueis, "A reliable, sensitive and fast optical fiber hydrogen sensor based on surface plasmon resonance," *Optics Express,* vol. 21, no. 1, pp. 382-390, 2013.

[91] M. Born and E. Wolf, Principles of Optics: Electromagnetic Theory of Propagation, Interference and Diffraction of Light, Cambridge: Cambridge University Press, 1999.

[92] H. Kuzmany, Solid-State Spectroscopy: An Introduction, Heidelberg: Springer Berlin, 1998.

[93] M. A. Ordal, L. L. Long, R. J. Bell, S. E. Bell, R. R. Bell, R. W. Alexander and C. A. Ward, "Optical properties of the metals Al, Co, Cu, Au, Fe, Pb, Ni, Pd, Pt, Ag, Ti, and W in the infrared and far infrared," *Applied Optics,* vol. 22, no. 7, pp. 1099-1119, 1983.

[94] A. Remhof and Borgschulte, "Thin-Film Metal Hydrides," *ChemPhysChem,* vol. 9, no. 17, pp. 2440-2455, 2008.

[95] K. J. Palm, J. B. Murray, T. C. Narayan and J. N. Munday, "Dynamic Optical Properties of Metal Hydrides," *ACS Photonics ,* vol. 5, no. 11, pp. 4677-4686, 2018.

[96] Y. Fukai, S. Kazama, K. Tanaka and M. Matsumoto, "Hydrogen-induced states in VH x and VD x observed by soft X-ray emission spectroscopy," *Solid State Communications,* vol. 19, no. 6, pp. 507-509, 1976.

[97] J. Prinz, "Hydrogen in thin metal films as seen by electron and light scattering," Karlsruhe Institute of Technology & Uppsala University, Karlsruhe, 2010.

[98] J. Prinz, G. K. Pálsson, P. T. Korelis and B. Hjörvarsson, "Combined light and electron scattering for exploring hydrogen in thin metallic films," *Applied Physics Letters,* vol. 97, no. 25, p. 251910, 1997.

[99] T. Scharf and K. HU, "In situ mechanical spectroscopy of laser deposited films using plasma plume excited reed," *Review of Scientific Instruments,* vol. 77, no. 9, pp. 93901-93905, 2006.

[100] F. Döring, "Minimizing thermal conductivity in laser deposited multilayers," Uni-Goettingen, Gottingen, 2017.

[101] R. Kirchheim and R. B. McLellan, "Electrochemical Methods for Measuring Diffusivities of Hydrogen in Palladium and Palladium Alloys," *Journal of The Electrochemical Society,* vol. 127, no. 11, pp. 2419-2425, 1980.

[102] R. Kircheim, Hydrogen solubility and diffusivity in defective and amorphous metals, Progress in Material Science, 1988.

[103] P. W. Atkins and M. J. Clugston, Principles of Physical Chemistry, Pitman, 1982.

[104] A. Baldi, B. D. M. H. Schreuders, J. H. Rector, T. Atmakidis, M. J. W. Bakker, H. A. Zondag, W. G. J. van Helden, B. Dam and R. P. Griessen, "Mg–Ti–H thin films as switchable solar absorbers," *International Journal of Hydrogen Energy,* vol. 33, no. 12, pp. 3188-3192, 2008.

[105] M. Born and E. Wolf, Principle of Optics, Cambridge University Press, 2002.

[106] Y. Pivak, R. Gremaud, K. Gross, M. Gonzalez-Silveira, A. Walton, D. Book, H. Schreuders, B. Dam and R. Griessen, "Effect of the substrate on the thermodynamic properties of PdHx films studied by hydrogenography," *Scripta Materialia,* pp. 348-351, 2009.

[107] Y. Pivak, H. Schreuders, M. Slaman, R. Griessen and B. Dam, "Thermodynamics, stress release and hysteresis behavior in highly adhesive Pd–H films," *International Journal of Hydrogen Energy,* pp. 4056-4067, 2011.

[108] J. Kürschner, S. Wagner and A. Pundt, "Delamination-supported growth of hydrides in Pd thin films studied by electrochemical hydrogenography," *Journal of Alloys and Compounds,* vol. 593, pp. 87-92, 2014.

[109] G. G. Stoney, "The tension of metallic films deposited by electrolysis," *Proceedings of the Royal Society of London,* vol. 82, no. 553, pp. 172-175, 1909.

[110] G. Binnig, H. Rohrer, C. Gerber and E. Weibel, "Surface Studies by Scanning Tunneling Microscopy," *Phys. Rev. Lett.,* vol. 49, no. 1, pp. 57-61, 1982.

[111] C. J. Chen, Introduction to Scanning Tunneling Microscopy, New York: Oxford University Press, 1993.

[112] R. Wiesendanger, Scanning Probe Microscopy and Spectroscopy: Methods and Applications, Cambridge: Cambridge University Press, 1994.

[113] R. Bowen and N. Hilal, Atomic Force Microscopy in Process Engineering, Butterworth-Heinemann, 2009.

[114] B. D. Cullity, Elements of X-Ray Differaction, Prentice_Hall Inc., 2014.

[115] M. Yakasa, "X-ray thin-film measurement techniques," *Rigaku Journal,* vol. 26, no. 201-09, 2010.

[116] Bruker, "Diffrac-suite-software," 2015. [Online]. Available: https://www.bruker.com/products/x-ray-diffraction-and-elemental-analysis/x-ray-diffraction/xrd-software/overview/leptos.html..

[117] J. Kürschner, "Electrochemical Hydrogenography of metal thin films, Master Thesis," Georg-August-Universität Göttingen, Göttingen, 2012.

[118] P. Atkins and J. De Paula, Atkins´ Physical Chemistry, Oxford University Press, 2006.

[119] S. Wagner, P. Klose, V. Burlaka, K. Nörthemann, M. Hamm and A. Pundt, "Structural Phase Transitions in Niobium Hydrogen Thin Films: Mechanical Stress, Phase Equilibria and Critical Temperatures," *ChemPhysChem,* vol. 20, no. 14, pp. 1890-1904, 2019.

[120] J. M. Rosamilia, A. J. Abys and B. Miller, "Electrochemical hydrogen insertion into palladium and palladium□Nickel thin films," *Electrochimica Acta,* vol. 36, no. 7, pp. 1203-1208, 1991.

[121] S. Wagner and A. Pundt, "Hydrogen as a probe for defects in materials: Isotherms and related microstructures of palladium-hydrogen thin films," *AIMS Materials Science,* vol. 7, no. 4, pp. 399-419, 2020.

[122] T. Nawrath, H. Fritzsche and H. Maletta, "Growth modes of vanadium and iron on V(110) single crystals," *Surface Science,* vol. 414, no. 1-2, pp. 209-220, 1998.

[123] M. Albrecht, H. Fritzsche and H. Gradmann, "Kinetic facetting in homoepitaxy of Fe(110) on Fe(110)," *Surface Science,* vol. 294, no. 1-2, pp. 1-9, 1993.

[124] H. Baker, Introduction to Alloy Phase Diagrams, USA: ASM International Handbook Committee , 1992.

[125] V. Burlaka, S. Wagner and A. Pundt, "In-situ STM and XRD studies on Nb–H films: Coherent and incoherent phase transitions," *Journal of Alloys and Compounds,* vol. 645, no. 1, pp. S388-S391, 2015.

Acknowledgements

On this occasion first and foremost, I would like to thank with all my heart to Prof. Astrid Pundit for her supervision, support, and patience during this work. Her strong motivation and confidence in me, help me to reach this point.

With great joy and gratitude like to thank my work, co-supervisor Prof. Dr. Reiner Kirchheim and Prof. Cynthia A. Volkert. I like to thank you again for taking the time to be a part of the defense committee member. With that, I would like to thank the other defense committee members for their time and patience: Prof. Dr. Michael Seibt, Prof. Dr. Hans-Christian Hofsäss, and Prof. Dr. Martin Wenderoth.

The members of the Hydrogen in Metals Group: R Gemma, H.T. Uchida, C. Izawa, for there their guidance and their support. Especially I also thank H.T. Uchida for his support in starting of this research work. Also, the literature database created by him help me immensely. Jantje Lina Schommartz helped a lot in the initial days of my learning, a lot of thanks to her. I further thank Martin Deutges for helping me during any computer programming problem, I came across.

Like to thank V. Burlaka to make me learn the working of the STM system with great patience while writing his thesis. Also would like to thank S. Wagner for his kind feedback, helpful nature makes me comfortable to discuss experimental work without any hesitation. Also, like to thank him for the theoretical model work he has done for this work. I would also like to thank Philipp Klose, Felix Jung, Magnus Hamm, Niklas Teichmann, and Mari Tiegel for their suggestion during group discussions. I would like to thank Bachelor student Felix Maischner that I was allowed to be supervised.

Special thanks to Marian Bongers for helping me with XRD, XRR, and AFM measurements. My group members were all finished with their work, and I felt a bit alone, but Marian was always ready to help or guide me with work-related discussions or things that are bothering me, such as bureaucratic regulations in Germany. I feel strong in the presence of all these nice souls.

I wish to acknowledge Florian Döring for preparing PC thin film using PLD for my work. Special thanks to Tobias Schulz, he is the key to solving any problem related to lab equipment. I want to extend my deep gratitude toward him for working so many hours and solving so many issues. Also, all other technicians of the institute: Michael Malchow, Karin Ahlborn, Kerstin Born, Frank Köhler, and all members of the electronic workshop, thank you so much for always being helpful and friendly, irrespective of how many times I visited you.

I owe my deep gratitude to Karin Haake, Regina Wunderlich, Phuong Quan me, and Christina Kuba for their help and support for all the administrative things. Especially like to wish heartfelt thanks to Christina Kuba for all your help in some of the most challenging times with administrative help and kind words to make it through. I like to apologise to all staff working in Institutes that make things running, and also to the people that in any way supported me, I can not list all of you

by name, please accept my deep gratitude. I would also like to thank all my dear friends who encouraged and supported me in all circumstances.

Last but not least, I like to thank my mother Munash Tyagi, My father S.B. Tyagi, My Bother Amit Tyagi, My sister-in-law Parul Tyagi and My sister Pooja Tyagi. I have no words to explain all the love and support I have received during the last few years.

In the last, I would like to thank DFG for their financial support through Project **PU131/9-2.**